Pairing and Superfluidity in Strongly Interacting Fermi Gases

by

Christian H. Schunck

Diplom, Physik (2003)
University of Heidelberg

Submitted to the Department of Physics
in partial fulfillment of the requirements for the degree of

Doctor of Philosophy

at the

MASSACHUSETTS INSTITUTE OF TECHNOLOGY

June 2008

Author ....
Department of Physics
May 22, 2008

Certified by..
Wolfgang Ketterle
John D. MacArthur Professor of Physics
Thesis Supervisor

Accepted by..
Thomas J. Greytak
Professor of Physics, Associate Department Head for Education

Pairing and Superfluidity in Strongly Interacting Fermi Gases

by

Christian H. Schunck

Submitted to the Department of Physics
on May 22, 2008, in partial fulfillment of the
requirements for the degree of
Doctor of Philosophy

Abstract

This thesis describes experiments with superfluid spin mixtures of ultracold fermionic ^{6}Li atoms. The properties of the strongly interacting gas are studied in the crossover regime between Bose-Einstein condensation (BEC) of two-body bound molecules and a Bardeen-Cooper-Schrieffer (BCS) superfluid of pairs bound by many-body interactions. We obtain the homogeneous phase diagram of the two-component gas with resonant interactions. As a function of temperature and spin polarization the phase diagram shows first and second order phase transitions that merge at a tricritical point. At zero temperature a first order phase transition from a superfluid with equal spin populations to a mixed normal phase is observed at a critical spin polarization known as the Chandrasekhar-Clogston limit of superfluidity.

Pairing correlations in the superfluid and normal phase are studied with radio-frequency (rf) spectroscopy. A signature of strong correlations is observed above the critical temperature but also at spin polarizations where superfluidity is quenched even at zero temperature. Significant limitations for the interpretation of these experiments due to final state interactions are overcome by the creation of new superfluid spin mixtures. The asymmetric rf dissociation spectra of the new mixture allow us to determine the spectroscopic pair size in the crossover regime. The size of the resonantly interacting pairs is found to be on the order of, but smaller than the interparticle spacing. Rf spectra of the majority component in an imbalanced system show a signature of thermally excited quasiparticles and by comparison to the minority spectra reveal changes in the nature of the binding as a function of spin polarization.

Thesis Supervisor: Wolfgang Ketterle
Title: John D. MacArthur Professor of Physics

To my wife Alessandra,
and my parents Angelika and Heiner

Acknowledgments

My time as a PhD student at MIT was an incredibly intense, exciting and thrilling experience. First and foremost this was due to the extraordinary group of people from whom I could learn and who made this work possible and enjoyable.

I would like to thank Wolfgang Ketterle for giving me the opportunity to join his group and for his advise, guidance, encouragement and support. Wolfgang's enthusiasm for physics and his ability to condense it into easily graspable ideas were a constant source of inspiration. I will cherish the memory of the many open ended brain storming sessions during group meetings.

Working in the BECI/Lithium team was simply an amazing experience. I would like to thank all members of the Lithium team, for these fantastic years, for teaching me physics and for your friendship. When I joined the group Claudiu Stan, Zoran Hadzibabic, and Subhadeep Gupta introduced me to the lithium projectas well as to life at MIT. With Claudiu I share the experience of building a *magnetic* trap, directly followed by another (non magnetic) one. I learned a lot from Claudiu's original ideas, his attention to detail and his patience. I am very glad that we stayed in contact over all the years even after he joined a group at Harvard: from the first day I set foot into MIT to the date of my thesis defense I could count on Claudiu's support.

Zoran and Deep formed a perfect duo and even graduated within the same week. They showed me how to operate the laser systems and introduced me to the "dudes". Both of them taught me lots of physics through their vivid discussions. Deep and Zoran also introduced me to the cuisine of their respective countries which I enjoyed immensely. I still remember a wonderful summer night Deep, Zoran, Claudiu and me spend on Zoran's porch discussing physics and the world beyond until many hours past sunrise.

When Martin Zwierlein re-joined the group as a graduate student I got to know an enthusiastic and brilliant physicist who would become a close friend. We spend crazy times together both inside the lab and out. In countless run nights Martin taught me an incredible amount of physics and how to "play" with the machine. It is hardly possible to describe the many memorable and unique experiences we shared together from a trip to Pasadena (with Martin singing and playing on the various Steinways scattered around in the hotel at 2 am in the morning), eating a Thanksgiving turkey at 3 am, to spontaneous parties in Boston. After finishing his PhD Martin left MIT for a year - it is great to have him back again on the hallway in a double bay office! Throughout the years we were the best customers Bertucci's could ever hope to get and I whish that everyone there will remember that the rolls should be served with butter (as well as olive oil) and be accompanied by a diet coke.

With André Schirotzek another post-diploma student became part of the team and immediately made a difference by flooding the lab not only with his boundless energy, dedication and good humor but also with an eclectic choice of music. During numerous runs we enjoyed many interesting discussions covering essentially any imaginable topic from physics, to politics, to religion, to ... etc. We survived a couple of interesting moments in the lab (for the record, André proved that a duster actually also works well as a fire extinguisher) and we were lucky to be able to attend the Enrico Fermi Summer School on ultracold Fermi gaes in Varenna together.

The fact that we had not been working with a postdoc for many years, did not scare Yong-il Shin to join our team after graduating from BEC III. We were very lucky to have him with us during the last two years. The efficiency with which Yong works in the lab is incredible, the way he uncovers new physics is elegant and beautiful and he always extended his help in a very kind and supportive way. Soon after joining the lithium project Yong got married to his wife Miye and I wish him and his family all the best for the future.

Sebastian Raupach joined the lithium lab during a time of fast paced progress. We soon became close friends and after a DAMOP meeting in Tuscon we hit the road driving through Arizona, Utah and Nevada together with Sebastian's wife Heike. Postdoc Jamie Kerman joined the lab during the same year but unfortunately stayed with us only for a short time.

Our nearest neighbors on the hallway are the members of BEC III, Aaron Leanhardt, Tom Pasquini, Michele Saba, Gyu-Boong Jo, Caleb Christensen, Ye-yeoung Lee and Jae Choi which deserve my apologies for ramping up the Feshbach fields far too often. I am especially indebted to Michele Saba for advice in numerous matters and to Jae Choi for being "just a boy".

Whenever one needs a tool BEC II is a great place to look. Jamil Abo-Shaeer, Jit Kee Chin, Johnny Vogels, Kaiwen Xu, Takashi Mukaiyama, Dan Miller, Yingmei Liu, Christian Sanner, Aviv Keshet, and Ralf Gommers deserve lots of credit for keeping their lab well organized. Jamil always knew when it was time to cheer people up and how to do it best. With Dan Miller I share the memory of many early morning coffee's in Varenna and a fantastic crawfish dinner in New Orleans. Aviv Keshet finished the new word generator just in time to help me out during the last weeks of the PhD.

The members of BEC IV Micah Boyd, Eric Streed, Gretchen Campbell, Dominik Schneble, Luis Marcassa, Patrick Medley, Jongchul Mun, David Hucul, David Weld, Hiro Miyake always had to struggle not to be left behind in building 36. Thanks to Gretchen and Micah for complaining loud when we had forgotten them once again. With Micah I spend a very relaxed OSA meeting at a pool in Tuscon and Micah, Tom and me spend two nice days exploring Barcelona together.

Many thanks to Martin's student Cheng-Hsun Wu for being a great office mate and the new members of Martin's group, Ariel Sommer and Christoph Clausen for relaxing dinners at Cosi and Bertucci's.

I would also like to thank the late Carol Costa for help in numerous occasions. It is possible that I am one of the last students in the hallway who has been encouraged by her to write the thesis acknowledgements first and I am joining the long list of students who did not listen...and at this moment I can tell her advice was in place! Ellenor Barish and Joanna Keseberg also helped whenever possible and deserve special thanks for processing receipts for probably more than a hundreds pounds of Starbucks coffee beans. Maxine Samuels was always there to help and has placed emergency orders late on Friday afternoons on more than one occasion.

My parents and my sister deserve my deep gratitude for encouraging me on my way, for their constant support and for providing me with good advice and help.

Finally, I would like to thank my wife Alessandra for her love and invaluable support during challenging times, for cheering me up, for being understanding with my work and sometimes crazy working schedule and for being patient during the last couple of months. I am looking forward to continuing our journey together in Europe.

Contents

List of Figures

List of Tables

Chapter 1

Introduction

1.1 Ultracold Fermi gases and the BEC-BCS crossover

The first superfluids of bosons and fermions were both realized in the laboratory of Heike Kamerlingh Onnes at the University of Leiden in the Netherlands. A century ago, in 1908 Onnes created the coldest temperatures on earth thus far and cooled liquified ^{4}He below the λ-point at 2.2 K into - what was later shown to be - the superfluid phase. Three years later, by using ^{4}He as a coolant, Onnes observed superconductivity in mercury, when he found that at temperatures below 4.2 K the resistivity of the metal essentially dropped to zero. At this time the concepts of quantum theory just started to emerge and the notion of "bosons" (^{4}He) and "fermions" (the electrons in the mercury) had not yet been conceived.

A century later, and again in systems cooled to the coldest temperatures on earth - now about a million times colder then in Onnes' laboratory in 1908 - the regimes of bosonic and fermionic superfluidity can be smoothly connected in experiments with ultracold atomic gases.

In between lay the introduction of Bose-Einstein statistics in 1924/25 and the formulation of Fermi-Dirac statistics in 1926 which was first applied to electrons in a metal by Arnold Sommerfeld in 1927. In 1939/40 Fierz and Pauli introduced the spin statistics theorem that says that bosons have integer and fermions have half integer spin. While superfluidity of bosons was connected early (London, 1938) with Bose-Einstein statistics and the phenomenon of Bose-Einstein condensation (BEC), superconductivity (i.e. superfluidity of charged fermions) remained puzzling for decades until in 1957 Bardeen, Cooper and Schrieffer (BCS) developed a full theory for the superconducting state. The discovery of the proton (Rutherford, 1918) and the neutron (Chadwick, 1932) which, together with the the electron (Thomson, 1897), are the fermionic building blocks of atoms, allowed the classification of atoms as "bosons" and "fermions": if the combined number of electron, protons, and neutrons is even, atoms have integer spin and are bosons, if total number of atomic constituents is odd, an atom has half-integer spin and is a fermion. Bose-Einstein condensation of bosonic atoms in ultracold atomic gases was observed in 1995 and the first quantum degenerate Fermi gas of fermionic atoms was created in 1999.

It is interesting to note that usually the "bosons" made the first appearance: Superfluidity of ^{4}He was realized before superconductivity of electrons in a metal and superfluidity of ^{3}He, Bose-Einstein statistics was formulated before Fermi-Dirac statistics, superfluidity of bosons was understood before superconductivity of electrons, and ultracold Bose gases were created before ultracold Fermi gases. The additional complexity involved in studying fermions both theoretically and experimentally and particularly in the context of superfluidity lies in their quantum statistics: while undistinguishable bosons can occupy the same quantum state, undistinguishable fermions must occupy orthogonal states.

Given the very different statistics bosons and fermions obey, how can the regimes of bosonic and fermionic superfluidity be related? As a tightly bound pair of two fermions has integer spin and can thus can be regarded as a boson, the idea of a connection between fermionic superfluidity and the formation of fermions pairs seems quite natural. However, due to the Coulomb repulsion between electrons it appeared impossible that electrons could form a tightly bound pair in a metal. In 1950 it was realized that there actually is a small, effectively attractive interaction between the electrons in superconductors mediated by lattice vibrations. Six years later Cooper found that for any small attractive interaction a bound state of fermions can form as a many body effect. While the idea of pair formation proved to be correct, the fermion pairs in the BCS superfluid are far from tightly bound: they are correlated in momentum space and they do not obey Bose-Einstein statistics. The BCS superfluid is not a Bose-Einstein condensate of fermion pairs. However, it was realized later that Bose-Einstein condensates of tightly bound fermion pairs can actually be described as a limit of the BCS state. This observation is the basis of BCS-BEC crossover theories, conceived and developed by Popov, Keldysh, Eagles [1], Legget [2], Noziéres and Schmitt-Rink [3], which smoothly connect the BCS limit of superfluid, many-body bound fermion pairs to the BEC limit of superfluid, two-body bound molecules.

This crossover between the well known limits of Bose-Einstein condensation and BCS superfluidity can be realized and explored in ultracold atomic gases and the studies of fermionic superfluidity in this regime are the subject of this thesis.

1.1.1 High temperature superfluidity

Fermionic superfluidity has been observed over a huge range of temperatures from more than 100 K in high-temperature superconductors, in the 1 K range for conventional superconductors, in the mK range for ^{3}He, down to 20 nK in ultracold quantum gases (as described in chapter 4 of this thesis). However, the absolute temperature scales are deceiving as fermionic superfluidity is a many-body effect and therefore depends on the density n of the surrounding fermions. An appropriate temperature scale for a comparison of the critical temperatures T_C across various systems is the Fermi temperature T_F which is proportional to the Fermi energy $k_B T_F = E_F \propto n^{2/3}$ (k_B is Boltzmann's constant). With

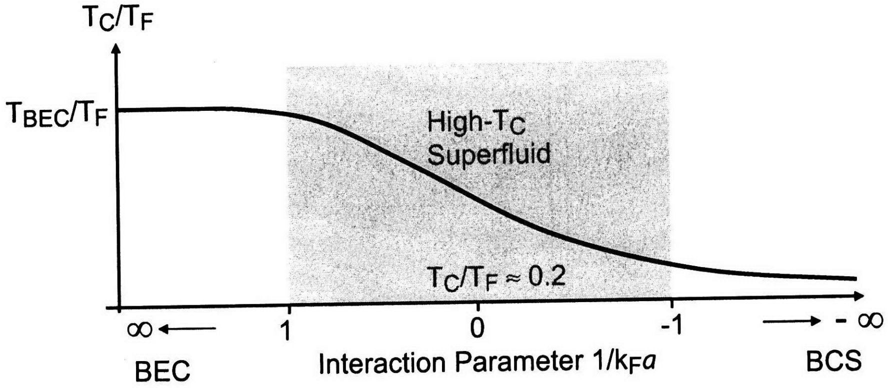

Figure 1-1: Critical temperature in the BEC-BCS crossover as a function of the interaction parameter $1/k_F a$.

this scaling T_c/T_F is as low as 10^{-8} for metallic lithium at ambient pressure, in the range of 10^{-4} to 10^{-5} for conventional superconductors, 5×10^{-4} for ^{3}He, and 10^{-2} for high-T_C superconductors.

Figure 1-1 shows the critical temperature for an ultracold Fermi gas in the BEC-BCS crossover. Here the strength of the coupling is measured by the dimensionless quantity $1/k_F a$, where k_F is the Fermi wavenumber and a the experimentally tunable s-wave scattering length. In the BCS limit T_C decays exponentially with the coupling or interaction strength: $T_c \simeq T_F e^{-\frac{\pi}{k_F a}}$, the regime where most fermionic superfluids including high T_C superconductors have been observed. On the BEC side, the large critical temperature for BEC of two-body bound molecules is approached. In between, for $-1 < 1/k_F a < 1$, lies the crossover where fermionic superfluidity in ultracold atomic Fermi gases has been realized [4]. Here the critical temperature is as high as $T_c/T_F \approx 0.2$. Scaled to the density of electrons in a metal, this critical temperature corresponds to superconductivity far above room temperature (and the melting point of the metal, too). The crossover therefore permits the study of fermionic superfluidity in a new regime - and the strongly interacting Fermi gas at 20 nK forms in fact a high-temperature superfluid.

1.1.2 The Fermion pairs

The instability of fermions with weak attractive interactions towards pair formation in a filled Fermi sea gives rise to fermionic superfluidity in the BCS limit. It is the character of these pairs that changes smoothly but -comparing the BEC and BCS limits - quite dramatically in the BCS to BEC crossover. One of the important quantities characterizing the pairs and with significant influence on the properties of the superfluid is the pair size relative to the interparticle spacing, illustrated in Fig. 1-2. In the BEC limit the fermion pairs are bound dimers, stable in isolation and small compared to the interparticle spacing.

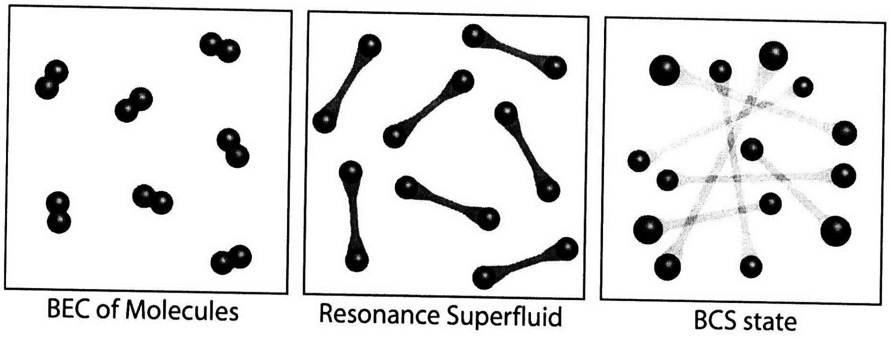

Figure 1-2: Fermion pairs in the BEC-BCS crossover.

In contrast, the pairs on the BCS side are significantly larger than the interparticle spacing and unstable in vacuum. In the crossover regime the size of fermion pairs in on the order of the interparticle spacing. The main chapters of this thesis focus either on the fermion pairs directly with rf spectroscopy experiments, or on interesting macroscopic consequences of the pairing phenomenon: by imbalancing the populations in the two strongly interacting spin states of gas superfluidity can be quenched which gives rise to an interesting and rich phase diagram.

1.1.3 Universality

At unitarity, where the scattering length a far exceeds the interparticle spacing and the interaction strength $1/k_F a$ reaches zero (in the limit of a approaching infinity, see section 3.4) the only relevant length and energy scales in the fermion system are the inverse Fermi wavenumber k_F and the Fermi energy E_F. In this regime the physics is expected to be universal [5] and not to depend on the specific properties of the fermions used in the experiment. For example the fermion pair size at unitarity should be a universal constant times $1/k_F$ (which is proportional to the interparticle spacing $n^{1/3}$), and the interaction energy a universal fraction of E_F. For this reason some of the experiments with ultracold gases could be relevant to understand properties of neutron starts and even the quark gluon plasma of the early universe although the density and temperature scales involved are vastly different.

1.2 Overview of the experiments in the BEC I lab at MIT

This section gives a short summary of the experiments that were carried out by my colleagues and me with the BEC 1 machine in the group of Wolfgang Ketterle at MIT[1].

The BEC 1 experiment has a long history and some of its parts date back to the years

---

[1] A general overview of the developments in the field are given in recent review papers cite.

well before 1995 when BEC in ^{23}Na was observed. The ultra high vacuum of the main chamber has been maintained continuously since 1996. Of course, many upgrades have been introduced since then, including a double species oven to accommodate both ^{23}Na and ^{6}Li , the laser system for ^{6}Li, a new magnetic trap, etc.

1.2.1 From strong interactions to fermion pair condensation

When I joined the BEC I lab as an undergraduate student in 2001 the first quantum degenerate cloud of ^{6}Li had been observed and the group was on the way to access a regime of strong interactions via Feshbach resonances. We soon saw first signs of the s-wave Feshbach resonance, which was used in most of the later experiments, via magnetic fields dependent losses [6]. At this time we were puzzled that these losses occurred mainly at fields closer to 700 G than to 800 G where the resonance was predicted. When I returned as a graduate student in 2003 an rf spectroscopy experiment was in progress, which studied mean field shifts in the gas as it entered the strongly interacting regime [7]. Again something "strange" seemed to be going on at fields around and above 700 G, where the mean field shifts became small and the mixture unstable. In the summer of 2003 we learned that some of these features were due to molecule formation and that surprisingly stable molecules started to form at fields above 750 G with lifetimes that could be sufficient for evaporative cooling into the quantum degenerate regime [8, 9, 10, 11]. Bose-Einstein condensation (BEC) of these molecules [2] was accomplished soon thereafter, in the fall of 2003 [12, 13, 14]. The "smoking gun" for condensation, a bimodal density distribution, could, however, not be observed in the regime of universal interactions close to the center of the Feshbach resonance and on the BCS side. Early in 2004 the JILA group introduced a rapid magnetic field ramp technique that transformed the increasingly fragile fermion pairs at unitarity and on the BCS side into more tightly bound and stabile molecules. This enabled the observation of fermion pair condensation in the whole BEC-BCS crossover at JILA and later at MIT [15, 16].

1.2.2 High temperature superfluidity

The observation of fermion pair condensation reinforced the quest to observe superfluidity in the system. Due to the strong interactions this turned out to be a challenging task since the behavior of the gas in the normal phase was in most instances qualitatively similar to the one associated with superfluids. In spring 2005 we observed vortex lattices in a rotating cloud in the entire crossover regime which demonstrated phase coherence and superfluidity of the strongly interacting system [4]. This was the starting point for most experiments discussed in this thesis.

With the new system at hand we could now set out to explore its macroscopic and microscopic properties. On the macroscopic scale we studied the stability of the superfluid

---

[2] The term "molecule" might not be appropriate since in the regime where BEC was observed many-body interactions are already important.

with regard to changes in a number of experimental parameters. In one of the first experiments we observed for how long superfluidity survived the expansion of the gas using vortices as "markers" for the superfluid region in the cloud [17]. Since the density of the system was reduced adiabatically during expansion this experiment addressed the stability of the superfluid as a function of the interaction strength (at finite temperature).

1.2.3 Macroscopic properties of the superfluid: Population imbalanced mixtures

In a second experiment we looked at the stability of the superfluid with regard to an imbalance in the populations of the two spin states from which it is formed. The questions raised by this experiment stimulated a whole series of further studies. The initial, quite playful experimental approach was to turn the knob on the Agilent frequency generator used to control the populations in the spin mixture and then to check whether vortices could be observed. This allowed us to establish superfluidity in imbalanced mixtures and to characterize the breakdown of superfluidity at the so-called Chandrasekhar-Clogston limit [18].

We soon realized that in an imbalanced mixture the superfluid phase transition could be observed directly in expansion without any magnetic field sweeps[3]: a bimodal density distribution emerged in the minority component as a function of temperature [19]. With these observations new questions about the origin of the bimodal structure and the nature of the superfluid and normal phases in imbalanced mixtures emerged. The data indicated that superfluidity at zero temperature required equal densities, leading to phase separation between the normal mixture and the superfluid. To confirm this hypothesis we had to observe phase boundaries in the trapped cloud with high spatial resolution. This was accomplished by a phase contrast imaging technique which allowed us to observe the phase transition directly in the trap [20]. Subsequently we refined this method by taking two phase contrast images of the same sample in rapid succession. Since we found the local density approximation to be valid, these two images gave immediate access to the local physics at a full range of densities and spin imbalances. The non-interacting ideal Fermi gas of the pure majority component in the spatial wings served as a reliable, ideal gas thermometer. The result was the homogeneous phase diagram of a resonantly interacting imbalanced Fermi gas, with first and second order phase transitions merging at a tricritical point [21].

Already in the first paper about population imbalanced Fermi gases we studied how the critical imbalance evolves with varying interaction strength. Due to the Chandrasekhar-Clogston limit there is no continuous crossover between different superfluid regimes as the interactions are changed. Instead, there will be at least one, but possibly a series of phase transitions involving exotic superfluids, between the limits of a Bose-Fermi mixture on the

---

[3] The observation of vortices at unitarity still required a magnetic field sweep to enhance the vortex contrast

BEC side and the (ultimately) normal gas in the BCS limit. With the newly developed techniques for the analysis of in trap density distributions we recently explored the phase diagram as a function of interaction strength and identified the Bose-Fermi mixture in the BEC limit.

1.2.4 Microscopic properties of the superfluid: Exploring pairing correlations with rf spectroscopy

In another set of experiments we studied the microscopic physics of the fermion pairs in the superfluid with radio-frequency (rf) spectroscopy. After the creation of molecular condensates the Innsbruck group had applied rf spectroscopy to a resonantly interacting Fermi gas and observed pairing correlations at low temperatures [22]. Since no clear experimental signature of the superfluid phase transitions was observed, we first started out to correlate the rf spectra with the indicators for superfluidity. This confirmed that pairing set in at a temperature larger than the superfluid transition temperature. Since we were already working with imbalanced systems we also took rf spectra above and below the critical imbalance and found that they did not show any differences. Our conclusion was that the rf spectra do not reveal the onset of superfluidity within the experimental resolution but provide evidence for pairing in a regime where the critical temperature is zero [23].

While performing this experiment we realized that we could spatially resolve what parts of the trapped cloud were resonant at a given radio-frequency. Focusing on an equal mixture and building on our experience from spatially resolving features in imbalanced clouds, we were now able to obtain "local" rf spectra, i.e. rf spectra at a given density [24]. All previous spectra were averaged over the density distribution of atoms in the trap and therefore more difficult to interpret. The spatially resolved spectrum, however, had a very narrow linewidth which appeared to be at odds with the expectations for both the BEC and BCS limits. This seemed to indicate that so-called final state interactions severely affected the rf spectra: The rf transfers atoms in one state of the initial two state spin mixture ($|\uparrow\rangle, |\downarrow\rangle$) to a third state $|3\rangle$. If this state interacts strongly with atoms in the initial state the rf spectrum does not simply reflect the pairing correlations of the initial state but the possibly complex interplay of interactions in the initial and final state. To make progress we needed an efficient handle on the final state interactions while preserving the initial state of interest.

The solution emerged from a seemingly unrelated observation. The rf experiments were associated with rapid atom losses after the rf pulse was applied. The losses appeared to involve the collision of three atoms, each of them in a different state $|\uparrow\rangle$, $|\downarrow\rangle$ and $|3\rangle$. However, this observation implied that all three two-state spin mixtures were likely to be stable! This started us to think about changing the final state interactions by exploring new strongly interacting spin mixtures. Indeed, a suitable mixture with negligible final state interactions could be created and the observed rf spectra at unitarity were dramatically different from the ones reported in the previous experiments. The essential features of the rf spectra could now be understood within a simple model and we were able to determine the fermion pair size at unitarity. The pairs turned out to be smaller than the interparticle spacing and are the smallest observed in fermionic superfluids.

With both the knowledge of the homogeneous phase diagram for imbalanced mixtures and an ideal system for obtaining spatially resolved rf spectra, we were then able to systematically study the pairing correlations in the superfluid, polarized superfluid, and mixed normal phase of an imbalanced mixture. This lead to the observation of local double peak structure in the rf spectra of the majority component - the first clear signature of quasiparticles in the superfluid.

Some of the experiments mentioned above are the subject of this thesis which is outlined in the following section.

1.3 Outline of the thesis

The main focus of this thesis are experiments with imbalanced spin mixtures and experiments probing the microscopic nature of the fermion pairs with rf spectroscopy. A few earlier publications with a somewhat different background (p-wave resonances [25], timescales related to fermion pair condensation [26] as well as the expansion of a superfluid Fermi gas [17]) will also be briefly discussed. Since a number of recent review papers are now available most of the general background will be summarized in short and primarily to establish a common language. We then proceed to discuss the new results in detail.

The thesis is organized as follows: Chapter 2 gives a a brief introduction of BEC-BCS crossover theory. In chapter 3 the new techniques and systems developed for the experiments presented in this thesis will be discussed. Chapter 4 introduces the superfluid ^{6}Li system as the starting point for the experiments. In chapter 5 the experiments leading to the observation of the phase diagram for population imbalanced mixtures will be presented. The rf spectroscopy experiments studying the fermion pairs are the subject of Chapter 6.

Publications directly related to this thesis are included in the appendices A to H.

Chapter 2

BEC-BCS crossover in ultracold atomic Fermi gases

2.1 BEC-BCS crossover

This section gives a brief summary of BEC-BCS crossover theory. The purpose is to establish the notation and to illustrate a few concepts relevant to this thesis. For extensive and detailed reviews of the topics discussed in this chapter please see references [27, 28, 29]. The discussion presented here is based on ref. [28].

The many-body Hamiltonian for a two state mixture of interacting fermions in the BEC-BCS crossover is:

$$\hat{H} = \sum_{k,\sigma} \epsilon_k c^\dagger_{k\sigma} c_{k\sigma} + \frac{V_0}{\Omega} \sum_{k,k',q} c^\dagger_{k+\frac{q}{2}\uparrow} c^\dagger_{-k+\frac{q}{2}\downarrow} c_{k'+\frac{q}{2}\downarrow} c_{k'-\frac{q}{2}\uparrow} \tag{2.1}$$

Here $c_{k\sigma}$ and $c^\dagger_{k\sigma}$ are creation and annihilation operators of a fermion with momentum k , mass m and spin $\sigma = (\uparrow, \downarrow)$ obeying the commutation relations

$$\begin{aligned} [c_{k\sigma}, c^\dagger_{k'\sigma'}]_+ &= c_{k\sigma} c^\dagger_{k'\sigma'} + c^\dagger_{k'\sigma'} c_{k\sigma} = \delta_{kk'} \delta_{\sigma\sigma'} && (2.2) \\ [c_{k\sigma}, c_{k'\sigma'}]_+ &= 0 && (2.3) \\ [c^\dagger_{k\sigma}, c^\dagger_{k'\sigma'}]_+ &= 0 && (2.4) \end{aligned}$$

Ω is the volume of the system and the coupling "constant" V_0 is given in terms of the s-wave scattering length a (for a δ function potential $V(\mathbf{r}) = V_0 \delta(\mathbf{r})$ and ignoring higher order corrections):

$$V_0 = \frac{4\pi\hbar^2 a}{m} \tag{2.5}$$

The first term of the Hamiltonian corresponds to the kinetic energy of the particles and

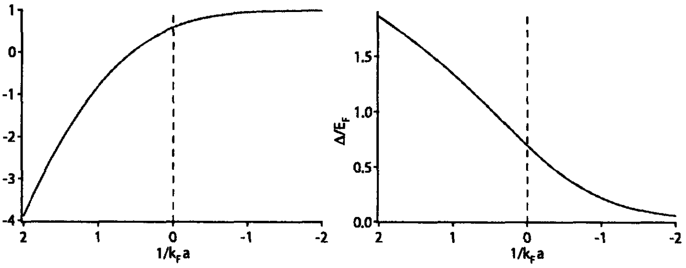

Figure 2-1: Chemical potential μ and gap Δ in the BEC-BCS crossover. In the BCS limit: $\mu \approx E_F \gg \Delta$ and $\Delta \approx \frac{8}{e^2} e^{-\frac{\pi}{2k_F|a|}}$. In the BEC limit: $\mu = -\frac{\hbar^2}{2ma^2} + \frac{\pi\hbar^2 an}{m}$ and $|\mu| \gg \Delta$. The first term in μ is the binding energy per particle in a molecule, the second one reflects density dependent molecule-molecule interactions (which the theory does not predict correctly [30]). $\Delta \propto \frac{E_F}{\sqrt{k_F a}}$ has no special significance in the BEC limit, however, Δ^2/μ is proportional to the molecular mean field $\frac{4\pi\hbar^2 na}{m}$.

$\epsilon_k = \hbar^2 k^2/2m$. The second term describes the a dependent correlation energy of the interacting fermion system and includes density fluctuations, i.e. interactions between pairs at finite momentum $\mathbf{q} \neq 0$. By neglecting these density fluctuations - which is a strong approximation for ultracold gases - one obtains the BCS Hamiltonian:

$$\hat{H} = \sum_{k,\sigma} \epsilon_k c^\dagger_{k\sigma} c_{k\sigma} + \frac{V_0}{\Omega} \sum_{k,k} c^\dagger_{k\uparrow} c^\dagger_{-k\downarrow} c_{k'\downarrow} c_{-k'\uparrow} \tag{2.6}$$

The exact solution[1] to this Hamiltonian is the BCS wave function:

$$|\Psi_{BCS}\rangle = \prod_k (u_k + v_k c^\dagger_{k\uparrow} c^\dagger_{-k\downarrow}) |0\rangle \tag{2.7}$$

with

$$\begin{aligned} v_k^2 &= \frac{1}{2}\left(1 - \frac{\xi_k}{E_k}\right) \\ u_k^2 &= \frac{1}{2}\left(1 + \frac{\xi_k}{E_k}\right) \end{aligned} \tag{2.8}$$

E_k and ξ_k depend on the gap Δ and the chemical potential μ which vary in the BEC-BCS

---

[1] The BCS wavefunction is an exact solution in the sense that it provides the correct thermodynamic quantities. There is an ongoing discussion how it is related to the the exact wavefunction for the ground state of the BCS Hamiltonian [cite Richardson, cite Ortiz].

crossover as shown in Fig. 2-1[2]:

$$\begin{aligned} E_k &= \sqrt{\xi_k^2 + \Delta^2} \\ \xi_k &= \epsilon_k - \mu \end{aligned} \tag{2.9}$$

The u_k and v_k give the probability amplitude for a pair state $c_{k\uparrow}^\dagger c_{k\downarrow}^\dagger |0\rangle$ to be empty or fully occupied, respectively and $u_k^2 + v_k^2 = 1$). Several functions involving combinations of u_k and v_k (like u_k^2, v_k^2, $u_k v_k$ and v_k/u_k) have special significance in the crossover and are important for the description of the fermion pairs as discussed in the following sections. Figure 2-2 shows their k dependence for five different interactions strengths.

2.2 Quasiparticle excitations

The BCS state describes a wavefunction of pairs. In some experiments, however, excited states with unpaired fermions will be accessed. Such unpaired fermions also emerge as finite temperature excitations. They are referred to as quasiparticles and their creation operators are given by:

$$\gamma_{k\uparrow}^\dagger = u_k c_{k\uparrow}^\dagger - v_k c_{-k\downarrow} \tag{2.10}$$

$$\gamma_{-k\downarrow}^\dagger = u_k c_{-k\downarrow}^\dagger + v_k c_{k\uparrow} \tag{2.11}$$

The BCS ground state can be regarded as the quasiparticle vacuum

$$\gamma_{k\uparrow} |\Psi_{BCS}\rangle = \gamma_{-k\downarrow} |\Psi_{BCS}\rangle = 0 \tag{2.12}$$

with excitations

$$\begin{aligned} \gamma_{k\uparrow}^\dagger |\Psi_{BCS}\rangle &= c_{k\uparrow}^\dagger (u_k^2 + v_k^2) \prod_{l \neq k} (u_l + v_l c_{l\uparrow}^\dagger c_{-l\downarrow}^\dagger |0\rangle \\ &= c_{k\uparrow}^\dagger \prod_{l \neq k} (u_l + v_l c_{l\uparrow}^\dagger c_{-l\downarrow}^\dagger |0\rangle \qquad (2.13) \\ & \qquad (2.14) \end{aligned}$$

where a pair ($\mathbf{k}\uparrow$,$-\mathbf{k}\downarrow$) is removed and a single fermion in $\mathbf{k}\uparrow$ added.

The energy cost for adding a quasiparticle relative to the chemical potential has two contributions: the kinetic energy $\xi_k = \epsilon_k - \mu$ required to add a particle with momentum $\mathbf{k}$ and the loss in pairing energy of the BCS state which can be shown to be $E_k - \xi_k$ [28].

---

[2] Δ and μ have to be determined simultaneously from the gap equation $\Delta = -\frac{V_0}{\Omega} \sum_k u_k v_k = -\frac{V_0}{\Omega} \sum_k \frac{\Delta}{2E_k}$ and from the number equation for the total particle density $N/\Omega = 2 \int \frac{d^3k}{(2\pi)^3} v_k^2$.

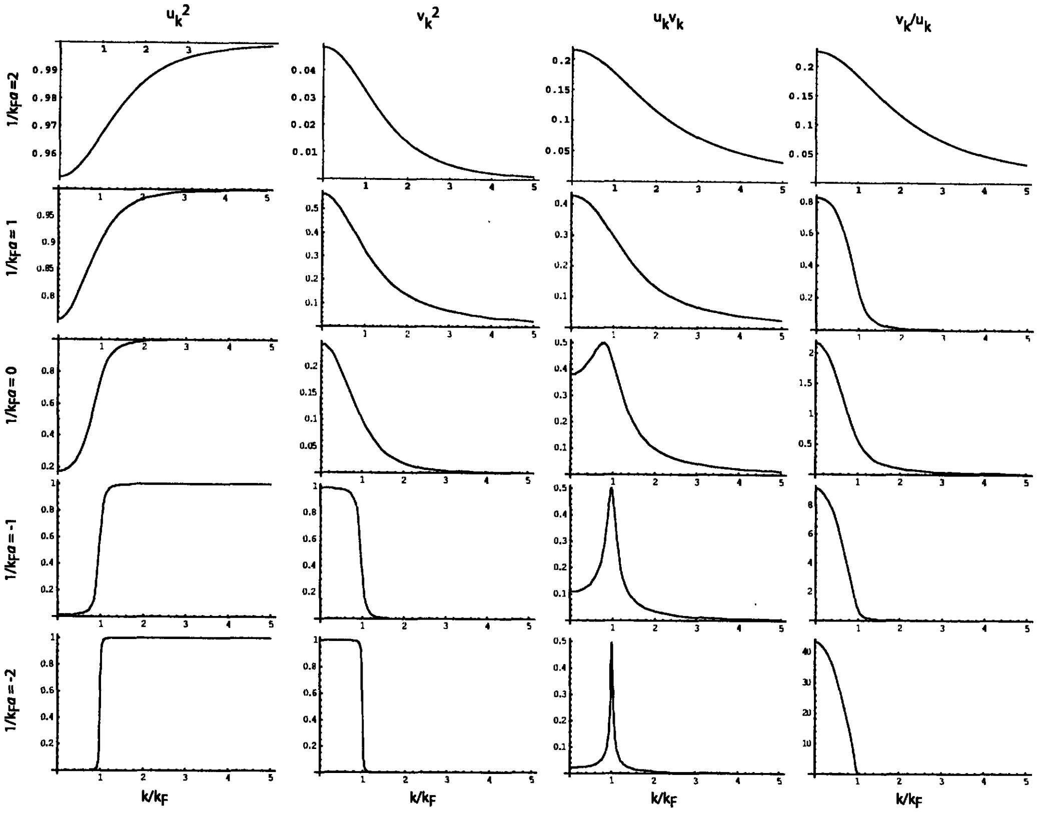

Figure 2-2: v_k and u_k in the BEC-BCS crossover. Plotted are u_k^2, v_k^2, $u_k v_k$ and v_k/u_k for four different interaction strengths. $v_k^2 \propto n$ and $u_k^2 = 1 - v_k^2$. In the BEC limit $u_k \to 1$ and $v_k \to 0$ for $k \to 0$ whereas in the BCS limit $u_k \to 0$ and $v_k \to 1$ for $k < k_F$. $u_k v_k = \langle \Psi_{BCS} | c_{k\uparrow}^\dagger c_{-k\downarrow}^\dagger | \Psi_{BCS} \rangle$ is the two-point correlation function, or the "Cooper pair" wave-function in k space. In the BCS limit this function is sharply peaked around the Fermi momentum k_F whereas in the BEC limit momentum states from $k = 0$ to $k > k_F$ contribute to the wavefunction with monotonously decreasing weight. The BCS pair wavefunction suggest another form for the pair wavefunction in k-space: v_k/u_k. This is (up to a normalization factor) the k-dependent pre-factor of the pair creation operators $c_{k\uparrow}^\dagger c_{-k\downarrow}^\dagger$ in the BCS state. The identification of v_k/u_k as the pair wavefunction is based on the interpretation of the BCS state as N/2 identical particles. The function v_k/u_k is similar to $u_k v_k$ in the BEC limit. In the BCS limit, however, v_k/u_k carries more weight at low momentum components and sharply falls off to zero around k_F. The function v_k/u_k is relevant in rf spectroscopy experiments. The plots are based on the following values for μ and Δ: 1) $1/k_F a = 2$, $\mu \approx -4E_F$ and $\Delta \approx 1.9E_F$; 2) $1/k_F a = 1$ $\mu \approx -0.8E_F$ and $\Delta \approx 1.3E_F$; 3) $1/k_F a = 0$ $\mu \approx 0.6E_F$ and $\Delta \approx 0.7E_F$; 4) $1/k_F a = -1$ $\mu \approx 0.95E_F$ and $\Delta \approx 0.2E_F$; 5) $1/k_F a = -2$ $\mu \approx 0.997E_F$ and $\Delta \approx 0.046E_F$.

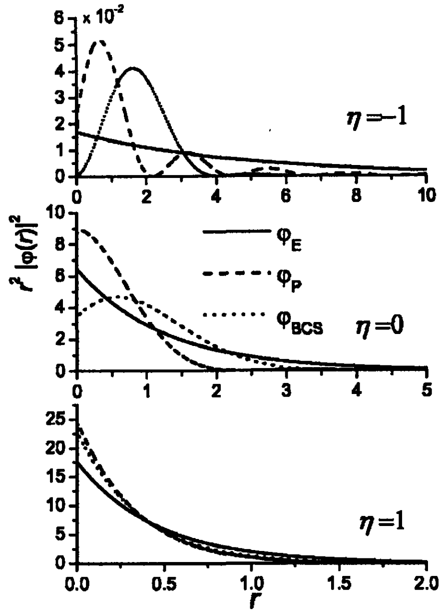

Figure 2-3: Spatial pair wavefunctions ϕ_E (from the mathematically exact solution of the BCS Hamiltonian), ϕ_P and ϕ_{BCS} for three different interaction strengths (here $\eta = 1/k_F a$ and r is measured in units of $1/k_F$). Reprinted from ref. [31].

The total energy cost is therefore E_k, with a minimal value either given by the gap Δ for $\xi_k = \mu > 0$ or if $\mu < 0$ on the BEC side by $\sqrt{\mu^2 + \Delta^2}$ for $k = 0$.

2.3 Fermion pair wavefunction

The formation of fermion pairs is a prerequisite for fermionic superfluidity and many properties of the superfluid are related to the stability of these pairs. This becomes especially apparent in the BEC-BCS crossover where the pairs change from tightly bound molecules to large and many-body bound Coper pairs.

The molecules in the BEC limit can be described straightforwardly in terms of a pair wavefunction $\phi_m(r) \propto e^{-r/b}/r$, where b is the size of the molecule. The situation is more complex in the BCS limit, where there are several potential "candidates" for the pair wavefunction. In Fig. 2-2 the k-dependence of two of them ($v_k u_k$ and v_k/u_k) is plotted for different interactions strengths. The first function is the two-point correlation function $\langle \Psi_{BCS} | c^\dagger_{k\uparrow} c^\dagger_{-k\downarrow} | \Psi_{BCS} \rangle = u_k v_k$ which is peaked at k_F indicating that most of the correlations are maintained by the pairs on the Fermi surface. The second one is based on the BCS wavefunction, suggesting v_k/u_k as the wavefunction of the $N/2$ equal pairs. A third one are the wavefunctions obtained from the mathematically exact solution of the BCS Hamiltonian which describe $N/2$ different pairs [31].

The spatial wavefunctions can be obtained as the Fourier transform of $u_k v_k$ and u_k/v_k:

$$\phi_P(\mathbf{r}) = \int \frac{d^3k}{(2\pi)^3} u_k v_k e^{i\mathbf{kr}} = \frac{1}{2}\int \frac{d^3k}{(2\pi)^3}\frac{\Delta}{E_k} e^{i\mathbf{kr}} \tag{2.15}$$

$$\phi_{BCS}(\mathbf{r}) = \int \frac{d^3k}{(2\pi)^3}\frac{v_k}{u_k} e^{i\mathbf{kr}} = \int \frac{d^3k}{(2\pi)^3}\frac{\Delta}{E_k+\xi_k} e^{i\mathbf{kr}} \tag{2.16}$$

The spatial wavefunctions are plotted for three different values of $k_F a$ in Fig. 2-3. All wavefunctions decay exponentially as a function of distance everywhere in the crossover and become identical in the BEC limit. Since $u_k v_k$ as well as v_k/u_k show sharp features in the BCS limit at the Fermi wavenumber k_F (a peak and an edge, respectively) their Fourier transforms on the BCS side show a modulation around $1/k_F$.

It depends on the experiment which pair wavefunction appears most naturally. In rf spectroscopy experiments, that will be discussed in the next section, the rf excitation affects fermions at all k and therefore the wavefunction v_k/u_k appears naturally in the description. The two-point correlation function based on $u_k v_k$ is best used to describe excitations at the Fermi surface.

2.4 Rf excitation of fermion pairs

Rf spectroscopy is a powerful tool to study the microscopic properties of the fermion pairs in the BEC-BCS crossover. Important quantities that can - at least in principle - be obtained by this technique are the binding energy of the pairs, the pair size and possibly a characteristic temperature for pair formation.

In the rf spectroscopy experiments atoms in one state of the two state $(\uparrow,\downarrow)$ mixture (here chosen to be $|\uparrow\rangle$) are transferred into an unoccupied third state $|3\rangle$ (see Fig. 2-4). If the mixture is non interacting the rf transition occurs at an excitation energy $\hbar\omega_{rf}$ equal to the atomic hyperfine energy $\hbar\omega_{hf}$ as it would be the case in *absence* of atoms in state $|\downarrow\rangle$ (see also Fig, 2-4 a).

In the following we assume that the initial state is interacting and described by the crossover wavefunction. The rf excitation can then "break" a pair resulting in a quasiparticle in the initial state plus a free particle in state $|3\rangle$. Since the momentum of the rf photon is negligible the rf excitation only changes the internal state of the atom and preserves its momentum. To transfer an atom from state $|\uparrow\rangle$ to state $|3\rangle$ the rf photon must provide the kinetic energy of the transferred particle ϵ_k as well as the energy $E_k - \mu$ required for creating the quasiparticle in addition to $\hbar\omega_{hf}$ (Fig. 2-4 b):

$$\hbar\omega_{rf} = \hbar\omega_{hf} + \epsilon_k + E_k - \mu \tag{2.17}$$

It is convenient to express all energies relative to the bare hyperfine energy and therefore

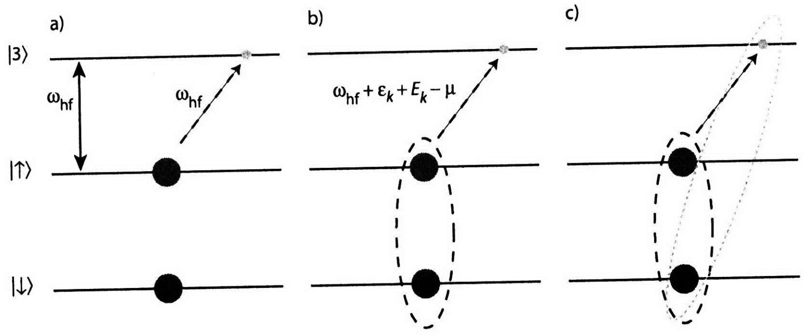

Figure 2-4: Schematic illustration of rf spectroscopy. Rf spectroscopy in fermions requires a three level system since so called clock shifts are absent both in coherent [7] as well as incoherent [32] two state fermionic spin mixtures. a, in the absence of interactions the rf is resonant with the bare "atomic" transition at $\hbar\omega_{rf}$. b) If the initial state is interacting the frequency response changes. c) In the discussion in the text we neglect "final state interactions". Such interactions can have a significant impact on the rf spectrum. Final state interactions will be discussed in detail in chapter 6

we define $\omega \equiv \omega_{rf} - \omega_{hf}$ so that

$$\hbar\omega = E_k + \xi_k \tag{2.18}$$

The minimum or threshold energy required for an rf excitation $E_{th} = \hbar\omega_{th}$ is given by $\hbar\omega_{th} = \hbar\omega(k=0) = \sqrt{\mu^2 + \Delta^2} - \mu$. In the BEC limit E_{th} approaches the molecular binding energy $2|\mu| = \hbar^2/ma^2$ and in the BCS limit $E_{th} \to \Delta^2/2E_F$ which is the condensation (binding) energy of a fermion pair.

Here we have assumed that atoms in the final state $|3\rangle$ do not interact with atoms in the initial states. In their most dramatic form such interactions can suppress pair dissociation but instead lead to so-called bound-bound transitions between pairs (as schematically illustrated in Fig. 2-4 c). The effect of such interactions will be discussed in detail in chapter 6).

The rf operator is given by:

$$H_{RF} \propto \sum_k c^\dagger_{k3} c_{k\uparrow} + h.c. \tag{2.19}$$

where only the first part contributes since state $|3\rangle$ is initially empty. It is convenient to express $c_{k\uparrow}$ via quasiparticle creation and annihilation operators as $c_{k\uparrow} = u_k\gamma_{k\uparrow} + v_k\gamma^\dagger_{-k\downarrow}$. With that we have

$$\begin{aligned} H_{RF}\,|\Psi_{BCS}\rangle &\propto \sum_k c^\dagger_{k3}(u_k\gamma_{k\uparrow} + v_k\gamma^\dagger_{-k\downarrow})\,|\Psi_{BCS}\rangle && (2.20)\\ &= \sum_k v_k c^\dagger_{k3}\gamma^\dagger_{-k\downarrow}\,|\Psi_{BCS}\rangle && (2.21)\end{aligned}$$

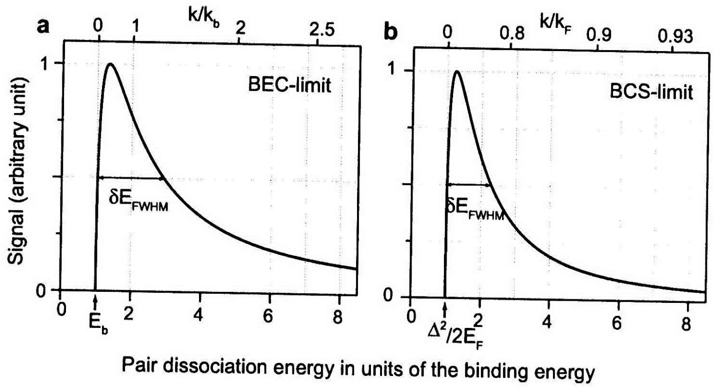

Figure 2-5: Rf spectra in the BEC and BCS limit.

The complete rf spectrum can be obtained with Fermi's Golden Rule [28] and is proportional to

$$I(\omega) \propto \rho(\epsilon_k)\frac{v_k^2}{u_k^2}|_{\epsilon_k=\epsilon(\omega)} \tag{2.22}$$

Here $\rho(\epsilon) \propto \sqrt{\frac{2m\epsilon_k}{\hbar^2}}$ is the density of states and v_k/u_k is proportional to the fermion pair wavefunction in the BCS state (see Fig. 2-2). Both $\rho(\epsilon_k)$ and v_k^2/u_k^2 have to be evaluated at the photon energy which can be obtained from 2.18 as

$$\epsilon(\omega) = \frac{\omega - \omega_{th}}{2\omega}(\hbar\omega + \hbar\omega_{th} + 2\mu)$$

With that we find

$$\frac{v_k^2}{u_k^2}|_{\epsilon_k=\epsilon(\omega)} = \frac{\Delta^2}{\hbar\omega^2}$$

and

$$I(\omega) \propto \frac{\sqrt{\omega - \omega_{th}}\sqrt{\omega + \omega_{th} + 2\mu/\hbar}}{\omega^{5/2}} \tag{2.23}$$

The rf spectra in the BEC and BCS limits are very similar (see Fig. 2-5): the spectral response rises steeply around ω_{th} and falls off as $\omega^{-3/2}$ for large ω. The second factor in the nominator reduces to $\sqrt{\omega}$ in the BEC limit for molecular dissociation and approaches $\sqrt{\omega + 2E_F/\hbar}$ in the BCS limit, where the Fermi energy enters as a new energy scale. Compared to the BEC limit this leads to a smaller ratio between spectral linewidth and threshold energy. The dissociation lineshape in the BEC limit is given by:

$$I_m \propto \frac{\sqrt{\omega - \omega_{th}}}{\omega^2} \tag{2.24}$$

This lineshape is, in fact, quite generic. By introducing an additional frequency offset ω_0

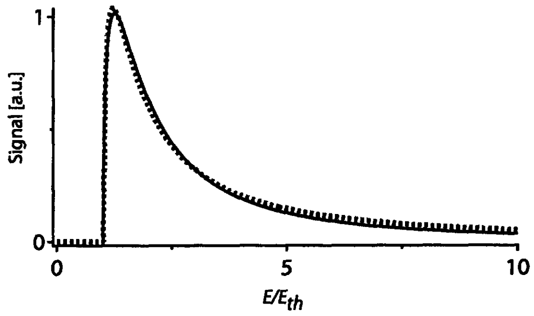

Figure 2-6: Generic rf lineshape. Simulated rf dissociation lineshape in the BCS limit for $\Delta \ll E_F$ (black solid line) with a fit based on I_{gen} (dashed red). $E = \hbar\omega$ is given in units of E_{th}.

we can define:

$$I_{gen} = const. \frac{\sqrt{\omega - \omega_{th}}}{(\omega - \omega_0)^2} \tag{2.25}$$

Figure 2-6 shows that a simulated rf spectrum in the BCS limit is well fit by I_{gen}. This implies that in the presence of uncalibrated shifts to the pair dissociation threshhold it is virtually impossible to distinguish experimentally between BEC and BCS pair dissociation lineshapes. In the experiments the onset of rf spectrum may be indeed be subject to possibly small, but unknown shifts due to Hartree terms [33, 7].

Chapter 3

The Experiment: Atoms, apparatus and techniques

This chapter gives a brief overview over the experiment and experimental techniques. Our experiments are carried out in a gas of ultracold ^{6}Li atoms. The experimental setup and most techniques have been discussed in a number of previous publications and PhD theses. We will often refer to the Varenna notes [28] which provide a detailed review of this work. Below we will focus on some newer developments, specifically the creation of two new superfluid spin mixtures in ^{6}Li and spatially resolved imaging techniques.

3.1 ^{6}Li

^{6}Li consists of three protons, three neutrons and three electrons and is therefore a fermion. The hyperfine structure of the ^{6}Li ground state is shown in fig. 3-1. All experiments discussed here are carried out in two state mixtures of atoms in the three lowest ^{6}Li hyperfine states which are labeled in the order of increasing energy as $|1\rangle$, $|2\rangle$ and $|3\rangle$.

3.2 Equipment

The major equipment involved in the preparation of a strongly interacting ^{6}Li gas in our experiments involves:

- an ultrahigh vacuum system
- a double species oven creating a combined ^{23}Na and ^{6}Li atomic beam [34, 35]
- the laser systems for ^{23}Na and ^{6}Li providing the photons for laser cooling and imaging the atoms [36, 37]
- a high current coil assembly (magnetic trap) for trapping the atoms and for generating external magnetic fields up to 1000 G [36, 38]

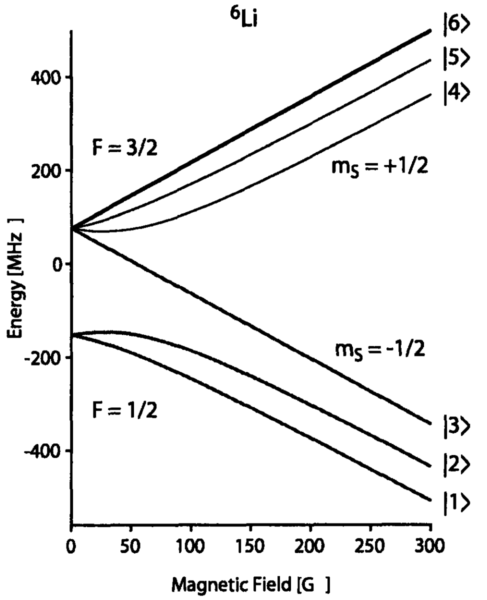

Figure 3-1: Hyperfine structure of the ^{6}Li ground state. The hyperfine splitting at zero field between the $F = 3/2$ and $F = 1/2$ levels is 228 MHz (F is the total - nuclear plus electron - spin and a good quantum number at low field, m_S (m_I) are the projections of the electron (nuclear) spin on the z-axis and a good quantum numbers at high fields). During sympathetic cooling with ^{23}Na in the magnetic trap ^{6}Li is in the stretched state $|6\rangle$. The experiments described in this thesis are carried out in two state spin mixtures of the three lowest hyperfine states (shown in red). At fields larger than 300 G the typical splitting between these states is 80 MHz.

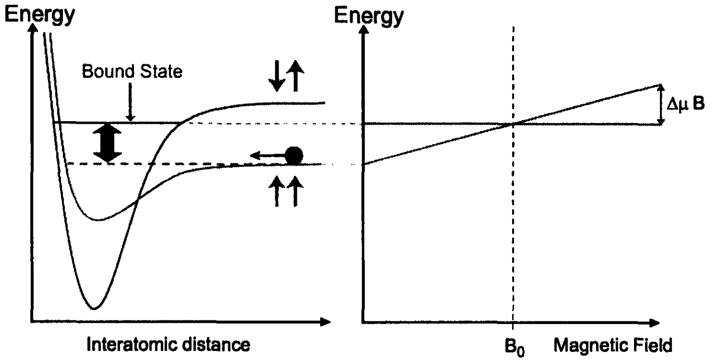

Figure 3-2: Singlet and triplet potentials for two scattering atoms depending on the spin configuration of the valance electrons. If the atoms scatter, for example, in the triplet potential (the "open channel") they cannot access the continuum states of the singlet potential (the "closed channel"). A Feshbach resonance arises when a bound state in the singlet potential is tuned into resonance with the scattering atoms via an external magnetic field.

- a 1064 nm infrared laser for creating the optical trap in which the various spin mixture are realized and the experiments are carried out [39].

Detailed descriptions of these components and associated equipment are given in the above references. Further references and information can also be found in [40].

3.3 Preparation of ultracold ^{6}Li fermions

After pre-cooling in a magneto optical trap (MOT) ^{6}Li is sympathetically cooled with bosonic ^{23}Na in a magnetic trap resulting in a pure sample of typically $30 \cdot 10^6$ quantum degenerate ^{6}Li atoms at a temperature of $T/T_F = 0.3$. The sympathetic cooling with ^{23}Na is necessary since the collisions required for rethermalization would "freeze out" in a pure, spin polarized gas of ^{6}Li atoms at temperatures below 6 mK. In this regime p-wave collisions are energetically suppressed and s-wave collisions are forbidden for identical fermions. A detailed summary of the cooling procedure and optical trapping together with further references are given in [41, 39, 28].

3.4 Creation of superfluid spin mixtures

3.4.1 Inducing strong interactions: Feshbach resonances

The observation of fermionic superfluidity in ultracold Fermi gases and the exploration of the BEC-BCS crossover are based on the ability to tune the interaction strength $1/k_F a$. The inverse Fermi wavenumber $1/k_F$ under typical experimental conditions is on the order of $10000a_0$, and typical scattering lengths do not exceed $100a_0$. These conditions do not

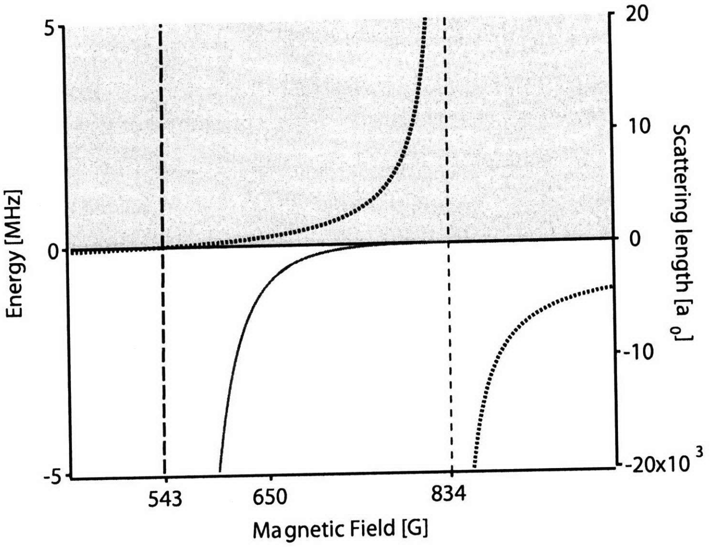

Figure 3-3: Feshbach resonance in ^{6}Li for the lowest two hyperfine states $|1\rangle$ and $|2\rangle$ in the s-wave channel. Shown in red (solid) is the binding energy of the bound molecular state in the singlet potential as it approaches the zero energy threshold at $B_{12} = 834$ G. The continuum of scattering states is shaded in grey. The blue dashed line shows the s-wave scattering length as a function of the magnetic field. The scattering length is positive on the "BEC side", where the bound molecular state exists in the potential, negative on the "BCS side" and diverges "at "resonance" (834 G). Apart from the broad resonance at 834 G the (1,2) mixture exhibits a narrow s-wave resonance at 543 G (thick dashed line).

permit the observation of superfluidity at experimentally attainable temperatures nor do they provide a sufficient tuning range for the interactions to observe crossover physics. The crossover regime can be accessed experimentally via Feshbach scattering resonances that allow the adjustment of the s-wave scattering length as a function of an externally applied magnetic field B. Feshbach resonances emerge when a molecular bound state in the "closed channel" of the interatomic potential is brought into resonance with atoms colliding in the "open channel" (see Fig. 3-2). The energy of the bound state relative to the energy of the scattering atoms can be controlled by an externally applied magnetic field B.

Figure 3-3 shows the $B_{12} = 834$ G Feshbach resonance in ^{6}Li. At fields below B_{12} the binding energy of weakest bound state in the singlet potential [1], approaches the resonances as $\hbar^2/ma^2$ where a is the s-wave scattering length. This bound molecular state is strongly coupled to the continuum of scattering states shifting the resonance from the uncoupled threshhold at 543 G by about 300 G to 834 G. Such a huge shift is unusual as is the large background scattering length of $-2100a_0$ at high fields. Both is due to an virtual state in

---

[1] The quantum numbers are $X^1\Sigma_g^+$, $v = 38$. This state has two total nuclear spin projections $I = 0$ and $I = 2$. Here we refer to the state with $I = 2$. The $I = 0$ state gives rise to a second resonance close to 543 G.

the ^{6}Li triplet potential just in the continuum of scattering states. At fields above the B_{12}, where a is negative, no bound molecular state exists.

The Feshbach resonance gives rise to the dispersive shape of the s-wave scattering length (shown in Fig. 3-3), and therefore allows the tuning of the interaction parameter $1/k_F a$ over a large range from negative to positive values. For $1/k_F a > -1$ the superfluid phase transition can be reached at experimentally accessible temperatures. All experiments discussed in this thesis were performed in the vicinity of "broad" Feshbach resonances, where the effective range of the interaction potential is small compared to the inverse Fermi wavevector. In this regime the specifics of the molecular state in the closed channel do not affect the physics and at unitarity the inverse Fermi wavenumber is the only relevant length scale. See ref.[28] for an extensive discussion of Feshbach resonance and the relevant energy scales.

Feshbach resonances appear to be the ideal "tool" to manipulate atoms and access strong interactions. However, when Feshbach resonances were first observed in bosonic ^{23}Na [42] they were found to be associated with rapid and strong losses [43]. In contrast to bosons, fermion pairs were found to be stable in the vicinity of the Feshbach resonance which is a direct consequence of the Pauli principle [30]. Only this stability made the experiments described in the following chapters of the thesis possible.

3.4.2 Feshbach resonances in ^{6}Li

In the three two state mixtures of the three lowest hyperfine states in ^{6}Li four s-wave [6, 7, 10, 44] and three p-wave [45, 25] resonances have been observed at magnetic fields between 0 and 1000 G. One additional p-wave resonance is predicted at 225 G [46]. Table 3.1 gives the resonance locations and widths. Most experiments in ^{6}Li have been carried out in the vicinity of the broad (1,2) resonance at 834 G. Recently we have also created superfluids in the (1,3) and (2,3) spin combinations around the (1,3) and (2,3) Feshbach resonances respectively (see figure 3-4 and chapter ??). The preparation of the superfluid spin mixtures for all three cases will be discussed in the next section.

3.4.3 Three superfluid mixtures

^{6}Li is sympathetically cooled in the stretched state $|6\rangle$. The cloud is then transferred into an optical trap. A low magnetic bias field is applied and the atoms are transferred into state $|1\rangle$ via an adiabatic Landau-Zener sweep across the single photon $|6\rangle \rightarrow |1\rangle$ hyperfine transition at 228 MHz (further details are given in [28]). The optically trapped sample in state $|1\rangle$ is the starting point for creating the various superfluid spin mixtures.

States	Wave	B [G]	Width [G]
$(1,1)$	p	159.1	< 0.4
$(1,2)$	p	185.1	< 0.2
$(2,2)$	p	214.9	< 0.4
$(1,3)$	p	225	
$(1,2)$	s	543.3	< 0.4
$(1,3)$	s	690	≈ 120
$(2,3)$	s	811	≈ 220
$(1,2)$	s	834	≈ 300

Table 3.1: Feshbach resonances in the lowest three hyperfine states of ^{6}Li . The resonances are sorted in the order of increasing magnetic field. The first three p-wave resonances were reported in [45, 25]. The fourth p-wave resonance has been predicted [46] but has not yet been observed. The three lowest s-wave resonances have a huge width and all three of them have now been used to create fermionic superfluids (see chapter ??). The width and position of these resonances has been reported in [44].

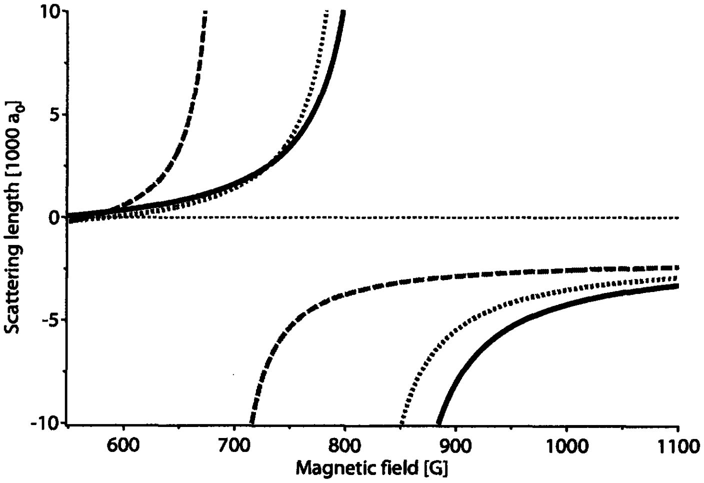

Figure 3-4: Broad s-wave Feshbach resonances in ^{6}Li (calculation by A. Simoni [46] based on the data in ref. [44]). Except for our most recent rf spectroscopy experiments all studies in the strongly interacting regime with ^{6}Li were carried out in vicinity of the (1,2) Feshbach resonance at 834 G (solid black line). However, also around the (1,3) resonance at 690 G (dashed blue) and the (2,3) resonance at 811 G stable fermionic superfluids in the respective spin mixtures can be created.

(1,2) Mixture

To produce the superfluid in the (1,2) system the magnetic field is ramped to values in the vicinity of the (1,2) Feshbach resonance at 834 G. At this field a non-adiabatic Landau-Zener sweep around the $|1\rangle$ to $|2\rangle$ transition frequency of about 80 MHz is applied, creating an equal mixture of atoms in state $|1\rangle$ and $|2\rangle$. The mixture is then evaporatively cooled by lowering the trap depth of the optical trap in several seconds to about 1 μK.

(2,3) Mixture

The preparation of a (2,3) superfluid follows essentially the same procedure as described for the (1,2) mixture. The only difference is that instead of applying a Landau Zener transfer that creates an equal (1,2) mixture, the atoms are adiabatically transferred into state $|2\rangle$ followed by a second non-adiabatic sweep that creates an equal (2,3) mixture.

(1,3) Mixture

The (1,3) mixture is prepared around 568 G, where both a_{12} and a_{13} are small. First an equal (1,2) mixture is created with a non-adiabatic Landau-Zener rf sweep. The atoms in state $|2\rangle$ are then transferred into state $|3\rangle$ with an adiabatic Landau-Zener sweep, yielding an equal (1,3) mixture. To access the strongly interacting regime the magnetic field is adjusted in about 100 ms to fields close to the (1,3) Feshbach resonance at 690 G where the system is evaporatively cooled into the superfluid phase.

3.4.4 Population imbalance

The probability for transferring atoms via a Landau-Zener sweep from state $|a\rangle$ to $|b\rangle$ is given by:

$$P_{|a\rangle\rightarrow|b\rangle} = 1 - \exp(-2\pi\frac{\Omega_R^2}{\dot{\omega}})$$

If $\dot{\omega} \gg \Omega_R^2$ the rf sweep is adiabatic and the transferred fraction from $|a\rangle$ to $|b\rangle$ approaches 100%. A smaller transfer can be accomplished by performing a non-adiabatic sweep and choosing appropriate values for either $\dot{\omega}$ by adjusting the sweep time or Ω_R by adjusting the rf power. The Landau-Zener sweep is a coherent process. The initial state after the transfer is therefore a coherent superposition and not yet the desired incoherent mixture of distinguishable atoms in state $|a\rangle$ and $|b\rangle$. Decoherence, however, occurs within about ten milliseconds after the sweep due to the motion of the atoms in the externally applied inhomogeneous magnetic field.

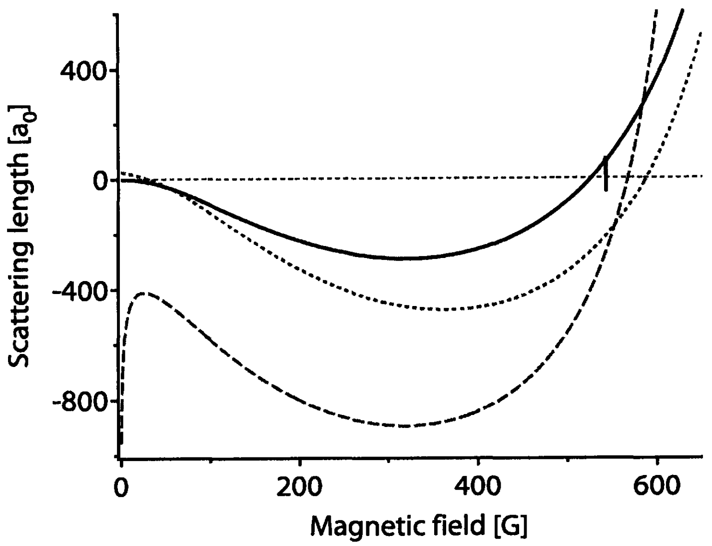

Figure 3-5: *s*-wave scattering length at fields below 600 G in ^{6}Li (calculation by A. Simoni [46] based on the data in ref. [44]): a_{13} (dashed blue), a_{23} (dotted red) as well as a_{12} (black solid). The zero crossings of the scattering length are at magnetic fields of about: 527 G ($a_{12} = 0$), 568 G ($a_{13} = 0$), and 588 G ($a_{23} = 0$). The minima of the scattering length are at about 320 G (where $a_{12} = -290a_0$ and $a_{13} = -895a_0$) and 363 G (where $a_{23} = -476a_0$). The narrow *s*-wave resonance in the (1,2) mixture at 543 G is also indicated.

3.4.5 Stability

All three mixtures show lifetimes at unitarity that exceed 10 seconds. This is surprising since one would expect that close to a Feshbach resonance where interactions of the atoms at short distances are enhanced, inelastic collisions are facilitated as well. The potentially bad, inelastic two-body collisions are dipolar- and spin relaxation. Dipolar relaxation involves the transfer of angular momentum from the relative motion of the atoms to the electrons and nuclei. Spin relaxation occurs when angular momentum is exchanged between electrons and nuclei without affecting the relative motion of the atoms.

Both processes are forbidden for fermions if the internal state of two the outgoing atoms is identical. In this case anti-symmetrization requires an odd (ex. *p*-wave) outgoing spatial wave, whereas the incoming spatial wavefunction is *s*-wave. Inelastic spin relaxation processes are therefore excluded. Also dipolar relaxation is not allowed since this process can only connect spatial waves of the same parity.

The (1,2) mixture with only one possible exothermic relaxation process $(1,2) \rightarrow (1,1)$ must therefore be stable. For the (1,3) and (2,3) mixtures the allowed exothermic collisions are $(1,3) \rightarrow (1,2)$, $(2,3) \rightarrow (1,3)$, and $(2,3) \rightarrow (1,2)$. For all processes spin relaxation is not possible since the *z*-projection of the total angular momentum is not conserved. However, dipolar relaxation is allowed with an outgoing *d*-wave in the final state. Since the initial state is s-wave, the released energy in the relaxation process occurring at small distances must be sufficient to overcome the d-wave barrier. We can estimate the height of this barrier as

$$V(r_{\mathrm{max}}) = -\frac{C_6}{r_{\mathrm{max}}^6} + \frac{6\hbar^2}{2\mu r_{\mathrm{max}}^2} \tag{3.1}$$

with $r_{\mathrm{max}} = \left(\frac{C_6 \mu}{2\hbar^2}\right)^{\frac{1}{4}}$. Here $C_6 \approx 1393$ a.u. (1 a.u.$= 9.57344 \times 10^{-26}$ J nm^6) is the coefficient of the ^{6}Li van-der-Waals potential and $\mu = m_{\mathrm{Li}}/2$. We find $V(r_{\mathrm{max}}) \approx 600$ MHz which is large compared to the 80 MHz Zeeman splitting between the hyperfine levels. This might compensate for any collisional enhancement of dipolar relaxation close to the Feshbach resonance. The observed lifetimes are consistent with typical dipolar relaxation rates on the order of 10^{-15} cm^{-3} s^{-1}.

3.4.6 Comparison of the mixtures

What is the "mixture of choice" for experiments? Since all three s-wave resonances are broad, universality requires that at unitarity the mixtures show exactly the same behavior. For most experiments it is therefore not important which mixture is chosen. Until our realization of the two new superfluid mixtures, all experiments in ^{6}Li have been carried out in the (1,2) system.

Even at unitarity, however, the choice of the mixtures matters in experiments involving a third state. This is the case in rf spectroscopy experiments where one drives rf transition from the initial mixture to a third state. Here it is desirable that the final state interacts only weakly with the initial one. The (1,3) mixture (with $|2\rangle$ as the final state) fulfills this requirement but not for the (1,2) and (2,3) systems (with $|3\rangle$ and $|1\rangle$ as the final states, respectively). The (1,3) mixture is indeed the right choice for rf spectroscopy experiments (see chapter 6).

One noticeable difference between the three large s-wave resonances is their width which differs by almost a factor of three between the (1,3) and (1,2) resonances. The smaller width of the (1,3) resonance together with its location at lower magnetic fields might be of some advantage if one would like to access the more weakly interacting regime on the BCS side at lower externally applied magnetic fields (at 1000 G $a_{13} = -2560 a_0$, which is comparable to $a_{12} = -2580 a_0$) at 1500 G).

At fields below the broad s-wave resonances the (1,3) mixture is also very interesting (see figure 3-5). At 320 G the s-wave scattering length $a_{13} = -895 a_0$ which should allow for efficient evaporation. In optical traps providing tight radial confinement with trap frequencies in the kHz range values of $k_F a_{13} \approx -1$ might be within experimental reach. This could be sufficient to enter the superfluid regime at experimentally attainable temperatures. By increasing the magnetic field one can change the interactions from attractive to repulsive which is interesting for the observation of antiferromagnetism in an optical lattice.

Apart from the two-state mixtures, a one-state "mixture" of atoms in state $|1\rangle$ and a three-state mixture of atoms in states $|1\rangle$, $|2\rangle$, and $|3\rangle$ show some promise. In a pure sample of $|1\rangle$ atoms the p-wave resonance close to the 160 G could be used to form p-wave molecules. Since only fermions in the ground state are involved, these molecules might be reasonably stable and there could be an opportunity to create a superfluidity with p-wave pairing. Very recently the creation p-wave molecules at the three lowest p-wave resonances in ^{6}Li has been reported together with measurements of their elastic and inelastic collision rates [47].

The ternary mixture shows lifetimes exceeding 30 ms within a broad range of magnetic fields and for strong interactions. If this mixture proves to be sufficiently stable [48] future work could focus pairing competition in multi-component Fermi gases and spinor Fermi superfluids (with analogies to quark matter) [49, 50, 51, 52, 53].

3.5 The harmonic trap as a feature: Spatially resolved 3D density distributions in imbalanced mixtures

The ability to reconstruct the three dimensional (3D) density distribution of the trapped atomic gas was crucial for many of the experiments discussed in this thesis. Usually, the harmonic confinement of the atoms leads to experimentally determined quantities that are averaged over the density distribution of atoms in the trap. For the purpose of obtaining quantities at a given density a box potential appears to be more suitable.

If it is possible, however, to obtain spatially resolved 3D densities the trap actually actually becomes a great feature (under the assumption that the local density approximation is valid). This is the case in our system, where a single harmonically confinement sample allows us to observe the behavior of the gas for whole range of local densities and spin polarizations. In imbalanced mixtures the harmonic confinement also provides an ideal gas thermometer by spatially separating the non-interacting wings of the majority component from the strongly interacting mixed system.

Complete information about the 3D density $n(x, y, z)$ can be obtained from images of the atoms. We assume that the imaging light E_0 propagates into the y direction entering and existing the cloud at the same x and z coordinates. The transmitted light E_t will be attenuated and phase shifted according to: $E_t = tE_0e^{i\phi}$, where t is the transmission coefficient and ϕ is the phase shift.

In most experiments we were interested in situations where the two components of the gas $|\uparrow\rangle$ and $|\downarrow\rangle$ had different density distributions $n_\uparrow(x, y, z)$ and $n_\downarrow(x, y, z)$ (caused for example by a global population imbalance, or a radio-frequency pulse that selectively removed atoms in one component). To obtain both $n_\uparrow$ or $n_\downarrow$ several problems needed to be addressed.

Both t and ϕ do not directly depend on n but on the column density $n_c(x, z) = \int n(x, y, z)dy$ due to line-of-sight integration along the y direction. Therefore the 3D density distributions need to be reconstructed form n_c using the so-called inverse Abel transformation as detailed below.

In order to obtain information about both $n_\uparrow$ and $n_\downarrow$, two images of the cloud need to be taken separately. In principle this could be done by using light resonant with atoms in state $|\uparrow\rangle$ and $|\downarrow\rangle$ for the first and second image, respectively. Resonant light, however, will be absorbed which leads to heating of the cloud and therefore a potentially blurred second image. Signal to noise considerations make absorption imaging even more undesirable. The imaging signal has to be particularly sensitive to the difference $n_\uparrow - n_\downarrow$ since abrupt features in this quantity clearly indicate changes in the behavior of the system and possibly phase transitions. As absorption images only contain information about $n_\uparrow$ or $n_\downarrow$ separately, they do not provide this sensitivity. Especially if $n_\uparrow$ and $n_\downarrow$ are both large and fluctuating this will lead to large fluctuations in $n_\uparrow - n_\downarrow$. The solution was to use phase contrast imaging, a dispersive imaging method sensitive to the phase shift ϕ of the transmitted light.

3.5.1 Phase contrast imaging

For phase contrast imaging off-resonant light at large detunings $\delta \gg 1$ is used, with δ measured in units of the natural linewidth of ^{6}Li ($\Gamma_{\mathrm{Li}} = 6$ MHz). In this limit absorption can be neglected, $t \approx 1$ and $\phi = -n_c\sigma_0/\delta$ where $\sigma_0 = \frac{3}{2\pi}\lambda^2$ is the resonant cross section[2]. Since ϕ is linear in n_c we would like the recorded intensity on the CCD camera to be linear in ϕ as well.

Any dispersive imaging method requires that the scattered and phase shifted light is separated from the transmitted light. The simplest solution is to block the unscattered light in the Fourier plane of the imaging system where it comes to a focus. The recorded intensity is then proportional to $|E_0e^{i\phi} - E_0|^2 \propto 1 + \phi^2/2$ for $\phi \ll 1$, which depends quadratically on ϕ. The situation can be modified by not blocking, but instead just phase shifting the unscattered light. For a phase shift of $\pm\pi/2$, one finds for the intensity in the limit $\phi \ll 1$, $|E_0e^{i\phi} + E_0(e^{\pm i\pi/2} - 1)|^2 \propto 1 + 2\phi$, which shows the desired linear dependency on ϕ and therefore n_c.

Let ν be the probe frequency of the imaging beam and $\nu_\uparrow^0$ and $\nu_\downarrow^0$ the optical resonance frequency for the atoms in state $|\uparrow\rangle$ and state $|\downarrow\rangle$ respectively. The optical signal is therefore proportional to:

$$\frac{n_{c,\uparrow}}{\nu - \nu_\uparrow^0} + \frac{n_{c,\downarrow}}{\nu - \nu_\downarrow^0}$$

Choosing $\nu = \nu_{1/2} = (\nu_\uparrow^0 + \nu_\downarrow^0)/2$ as shown in figure 3-6, the optical signal directly reflects the density difference $n_{cl} = n_{c,\uparrow} - n_{c,\downarrow}$. With this choice for the imaging frequency atoms in state $|\uparrow\rangle$ cause exactly the opposite phase shift from atoms in state $|\downarrow\rangle$ and any common mode signal cancels out. In principle this can be verified in an equal mixture,

---

[2] Valid for a two level atom in the rotating wave approximation.

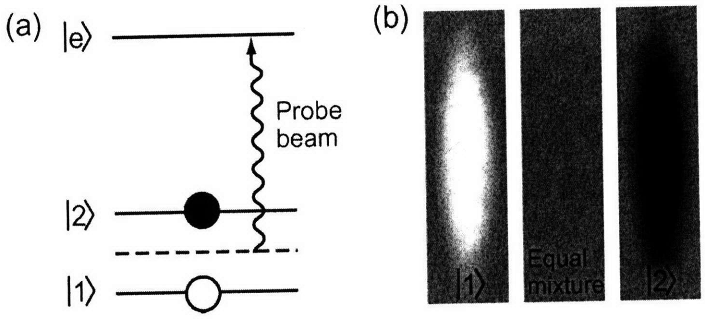

Figure 3-6: Phase contrast imaging of the density difference of two spin states. a) Schematics of the imaging setup. b) Phase contrast images of a spin polarized sample in state $|1\rangle$ (left), $|2\rangle$ (right), or an equal mixture (center). The phase shift of the light for the two spin states has the opposite sign and cancels for an equal mixture.

where no phase contrast signal should be observed. In practice, the imaging frequency ν_0 is determined experimentally by canceling the phase contrast signal for an equal mixture. We find that ν_0 usually deviates from $v_{1/2}$ by about 1 to 2 MHz probably due to imperfections in the imaging setup.

For the second phase contrast image the imaging frequency is detuned from ν_0 by one or two natural linewidths. The image then reflects the weighted density difference $n_{c2} = \alpha_\uparrow n_{c,\uparrow} - \alpha_\downarrow n_{c,\downarrow}$. To determine the coefficients $\alpha_\uparrow$ and $\alpha_\downarrow$ we use highly imbalanced clouds with atoms in state $|\uparrow\rangle$ and $|\downarrow\rangle$ as the majority component, respectively. (Describe in more detail.) An example of the two phase contrast images, together with cuts through the column densities $n_{c1}(0,z)$ and $n_{c2}(0,z)$ are shown in fig. 3-7 (a-c). The column densities $n_{c,\uparrow}$ and $n_{c,\downarrow}$ can now be determined from n_{c1} and n_{c2} as $n_{c,\uparrow} = (\alpha_\downarrow n_{c1} - n_{c2})/(\alpha_\downarrow - \alpha_\uparrow)$ and $n_{c,\downarrow} = (\alpha_\uparrow n_{c1} - n_{c2})/(\alpha_\downarrow - \alpha_\uparrow)$. In the next step the 3D densities $n_\uparrow$ and $n_\downarrow$ are reconstructed from $n_{c,\uparrow}$ and $n_{c,\downarrow}$.

3.5.2 Inverse Abel transformation

The inverse Abel transform can be applied to obtain a 3D density distribution from line-of-sight integrated images for systems with cylindrical symmetry[3]. The details of the trapping potential used in our experiments are given below. In short, the trap is cigar shaped and the two transverse trapping frequencies are equal to better than 2%. The criterium of cylindrical symmetry is therefore met to a sufficiently high degree. The inverse Abel transformation is given by:

---

[3] The inverse Abel transformation is a special case of the so-called inverse Radon transformation, which does not require cylindrical symmetry, but the knowledge of line-of-sight integrated distributions for an infinite number of angles. The cylindrical symmetry reduces this requirement to one distribution obtained from line-of-sight integration along an axis perpendicular to the symmetry axes.

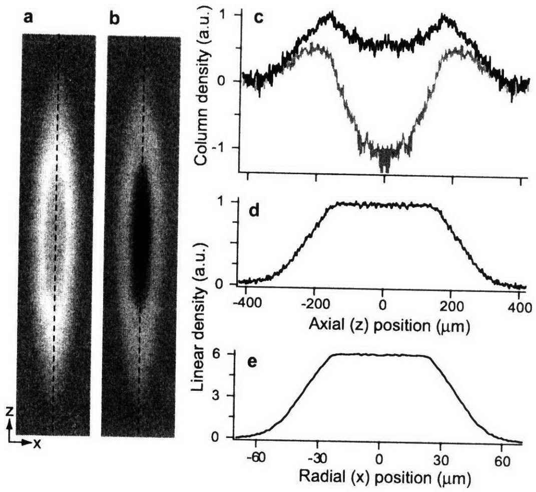

Figure 3-7: Double phase contrast imaging: density difference a) and weighted density difference b) of an imbalanced cloud. (c) Column density difference (black) and weighted column density difference (red) along the dashed lines of the phase contrast images. d) and e): radially and axially intergrated column density difference. The profiles show a flat top distribution indicating that the local density approximation is valid.

$$n(r, z) = -\frac{1}{\pi} \int_r^\infty \mathrm{d}x \frac{1}{\sqrt{x^2 - r^2}} \frac{\mathrm{d}n_c(x, z)}{\mathrm{d}x}$$

As one would expect, the transformation depends on the derivative of column density n_c, which causes the inverse Abel transformation to be very sensitive to noise. An excellent signal to noise ratio for n_c is therefore required. Any "kinks" in the density profiles will cause jumps in the density distribution after the transformation. Averaging the column density profiles along elliptical equipotential lines $\lambda^2 x^2 + z^2 = r^2$, where λ is the aspect ratio of the trapping potential, helps to reduce noise. The averaging has to be performed with carefully chosen restrictions to avoid washing out sharp features caused, for example, by phase boundaries [21].

3.5.3 Trapping potential

Here we describe the trapping configuration for typical experimental conditions after preparation of the strongly interacting sample, i.e. at magnetically applied bias fields in the range of 700 to 900 G and after evaporation in the optical trap. We specifically state the parameters relevant for the experiments based on *in situ* imaging. The trapping potential is cigar shaped, with an aspect ratio $\lambda \sim 6$. The confinement of the atoms is only to first order harmonic and due to a combined optical and magnetic potential. The optical trap is generated by a 1064 nm gaussian laser beam with a waist w of about 125 μm, creating a trapping potential $V_o(\rho, z) = U_0 e^{-(2\rho^2/w^2)}$, with $\rho = \sqrt{x^2 + y^2}$. The magnetic potential provides essentially all of the axial confinement along with some weak radial anti-trapping: $V_m(\rho, z) = \frac{m\omega_z^2}{2}(-\frac{\rho^2}{2} + z^2)$. The combined potential is then by

$$V(\rho, z) = U_0 \exp\left(-\frac{2\rho^2}{w^2}\right) + \frac{m\omega_z^2}{2}\left(-\frac{\rho^2}{2} + z^2\right) \tag{3.2}$$

yielding a trap depth of

$$U = \frac{1}{4}\omega_r^2 w^2 \left[1 - \frac{\omega_z^2}{2\omega_r^2} \ln\left(1 + \frac{2\omega_r^2}{\omega_z^2}\right)\right] \tag{3.3}$$

Here ω_r is the radial trapping frequency in the central harmonic region of the potential. Typical values of ω_r, ω_z and U are: $\omega_r \sim 2\pi \times 130$ Hz, $\omega_z \sim 2\pi \times 23$ Hz and 2 μK respectively. Typical Fermi energies are on the order of 1 μK. Therefore $U \sim E_F$ and the anharmonicities of the trapping potential in the radial direction (for $\rho \sim w$) affect the spatial wings of the trapped cloud. While the overall confinement is predominantly harmonic, the effects of anharmonicities must still be considered when information is obtained from the spatial wings of the cloud. An important example concerns the temperature determination from the non-interacting wings of the majority cloud in an imbalanced gas.

3.5.4 LDA and doubly integrated density difference profiles

As we have pointed out above, spatially resolved imaging techniques turn the harmonic confinement of the atoms into a feature since the images provide a "cut" through the physics in the cloud at various densities. An important requirement, however, is that the local density approximation (LDA) is valid, i.e. that all relevant quantities at a given point (ρ, z) in the trapping potential (here assumed to be axially symmetric as in the experiment) depend only on the *local* value of $V(\rho, z)$. It turns out that imbalanced clouds actually provide a way to check the validity of the LDA for their description. As we will discuss later in this thesis the superfluid core in an imbalanced mixture has *equal* densities in the zero temperature limit (at the expense of a *larger* density imbalance in the normal outer regions of the cloud). Here we will show that this leads to a characteristic "flat top" distribution of doubly integrated density difference profiles in an imbalanced mixture if the confinement is harmonic and the LDA applies.

In an axial symmetric harmonic trap, equipotential shells are given by ellipses $\lambda^2\rho^2 + z^2 = c$; here $\lambda = \omega_r/\omega_z$ is the aspect ratio, $\rho^2 = x^2 + y^2$ as above, and c is a constant. If the local density approximation is valid, the densities on the elliptical shells are constant and depend only on the value of c. The doubly intergrated density difference profile with $\Delta n = n_\uparrow - n_\downarrow$ is then given by:

$$\Delta n_{dbl}(z) = \int_0^\infty \rho \Delta n(\lambda^2\rho^2 + z^2) d\phi d\rho = \frac{\pi}{\lambda^2} \int_{z^2}^\infty \Delta n(a) da \tag{3.4}$$

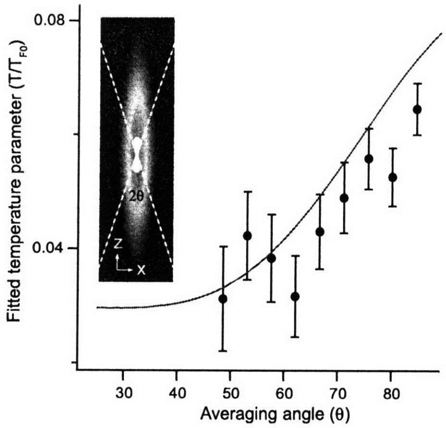

Figure 3-8: Effect of anharmonicities on the in situ temperature determination. The temperature of the cloud was determined for various angles θ of the averaging sector. For larger values of θ, spatial wings at larger values of ρ contribute and the radial anharmonicities become increasingly important in the averaged profile. This results in a broadening of the spatial wings and consequently higher value of the fitted temperature. The red line shows the results of a simulation using the same parameters as the experiment ($\lambda = 6.15$, $T_{F0} = 1$ μK and the trap depth $U/k_B = 2$ μK.

The density difference $(n_\uparrow - n_\downarrow)$ is zero in the balanced superfluid core up to a certain critical $\lambda^2\rho^2 + z^2 \equiv a_c^2 > z^2$. So for $z < a_c$ we have:

$$\Delta n_{dbl}(z < a_c) = \frac{\pi}{\lambda^2} \int_{a_c^2}^{\infty} \Delta n(a) da = const \tag{3.5}$$

Figure 3-7 d) and e) indeed show the flat top distribution of the doubly integrated density difference profiles, demonstrating that the LDA and harmonic confinement are good approximations for our system.

3.5.5 Temperature determination

The absolute temperature of strongly interacting Fermi gases is difficult to determine since the exact relation between the density distribution of the atoms and the temperature of the system is not known. A comparison with theory is limited to the assumptions underlying the theoretical description and their accuracy.

For a balanced mixture in the strongly interacting regime the temperature has been determined as the derivative of entropy with energy [54] which resulted in temperatures averaged over a certain range. Furthermore some assumptions and approximations had to be made with regard to the energy and entropy measurements [54].

To obtain the local temperatures in the trapped, imbalanced cloud we therefore have to rely on a different temperature calibration. Usually, when there is the need to characterize

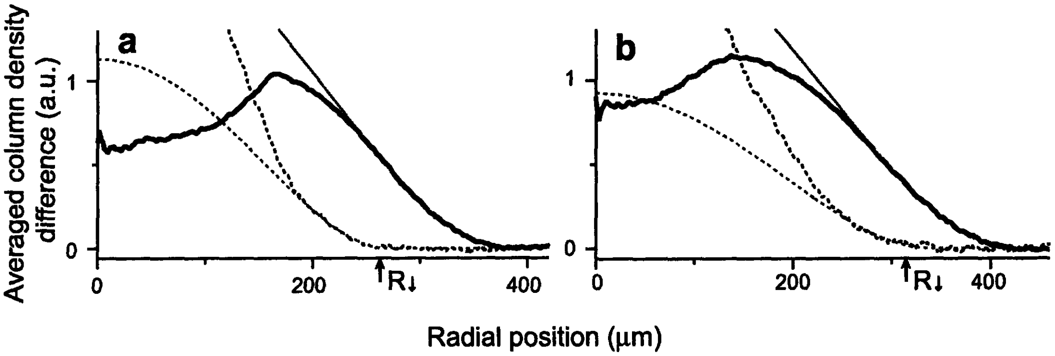

Figure 3-9: In situ temperature determination. The relative temperature $T' = T/T_{F0}$ is determined from the outer region ($r > R_\downarrow$) of the averaged column density difference profile (black line) fitted to a finite temperature Fermi-Dirac distribution in a harmonic trap (red line). The radius of the minority cloud $R_\downarrow$ was determined from a fit of the wing profile of the minority component (black dashed line) to a zero temperature Thomas-Fermi distribution (red dashed line). a, T' = 0.03(1) and δ = 44(4)% b, T' = 0.08(1) and δ = 46(4)%.

a system with unknown properties, it is helpful to bring it in contact with a simpler, well understand system for calibration. In imbalanced mixtures such a situation arises naturally since the spatial wings of the majority cloud (where the minority density has dropped to zero) constitute a non-interacting ideal Fermi gas in equilibrium with the interacting cloud. In other words the majority wings can serve as an ideal gas thermometer, an idea that was first applied in ref. [19]. In this experiment, however, the temperature was determined by a fit to the wings of the *expanded* majority cloud after release from the trap. For small imbalances this lead to an overestimate of the temperature (of not more than 20%) due to the collisional dynamics during expansion.

For an *in situ* temperature calibration expansion dynamics poses of course no a problem, instead the trap anharmonicities have to be taken into account. To obtain the low noise profiles required for an accurate temperature calibration, the column density profiles are averaged along lines of constant $(\lambda^2\rho^2 + z^2)$. For a full average, the trap anharmonicities which affect the wings of the majority cloud, lead to a systematic overestimate of the temperature. This systematic shift can be controlled by restricting the averaging range to small angles where only small values of ρ contribute and the trap asymmetry only has a negligible influence (see Fig. 3-8).

As shown in Fig. 3-9 the temperature of the system can then be obtained from a fit to the outer wing of the majority cloud, i.e. to the region $r > R_\downarrow$ where the density of the minority has dropped to zero. Here $R_\downarrow$, the radius of the minority cloud, is determined from a zero-temperature Thomas-Fermi fit to the wing profile of the minority component[4].

---

[4] See ref. [28] for an extensive discussion on the quantitative analysis of density distributions

The fit to the majority cloud yields the relative temperature

$$T' \equiv T/T_{F0} = \frac{k_B T}{\frac{\hbar^2}{2m}(6\pi^2 n_0)^{2/3}} \tag{3.6}$$

where $k_B T_{F0}$ the Fermi energy of a non-interacting, zero temperature, harmonically trapped Fermi gas with central density n_0 and the same density distribution in the outer wings as the majority cloud. The local temperature $T'_{\mathrm{local}}(r)$ can then be defined with the density of the majority cloud $n_\uparrow(r)$:

$$T'_{\mathrm{local}}(r) = \frac{T}{T_{F\uparrow}(r)} = \frac{k_B T}{\frac{\hbar^2}{2m}(6\pi^2 n_\uparrow(r))^{\frac{2}{3}}} = \frac{T}{T_{F0}}\left(\frac{n_0}{n_\uparrow(r)}\right)^{\frac{2}{3}} \tag{3.7}$$

Chapter 4

Creating and exploring a high temperature superfluid of ultracold ^{6}Li atoms

This chapter gives a brief summary of the experiments that lead to the observation of high temperature superfluidity. See ref. [28] for an extensive review.

4.1 Fermion pair condensation

An important step on the way to superfluid Fermi gases was the creation of the conceptually simplest fermion pairs: the weakly bound "molecules" on the BEC side of the Feshbach resonance [55, 8, 9, 10]. The stability of these molecules came as a surprise since Feshbach associated molecules from bosonic atoms were too short lived to reach thermal equilibrium in the quantum degenerate regime [56, 57, 58]. The molecules created from fermionic atoms, however, were protected from decay into lower lying states by Fermi statistics [30] and showed lifetimes which exceeded 10 s in the (1,2) mixture of ^{6}Li. With such favorable lifetimes direct evaporation from a two component (1,2) mixture into a Bose-Einstein condensate of weakly bound fermion pairs proved possible (Fig. 4-1) [13, 14]. In ^{40}K molecular lifetimes were considerably shorter (100 ms) and the observation of BEC relied on a sweep across the Feshbach resonance [12].

The observation of fermion pair condensation in the entire BEC-BCS crossover was achieved a few month later (see figure 4-2) [15, 16]. Close to resonance and on the BCS side bimodal density profiles could not be observed in situ. Here the chemical potential μ becomes comparable to $k_B T_c$ and the condensate does not spatially separate from the thermal cloud. The solution was a rapid non-adiabatic magnetic field sweep across the Feshbach resonance towards lower magnetic fields shortly after the optical trapping potential is turned off. This sweep transfers the many-body bound fermion pairs into stable molecules

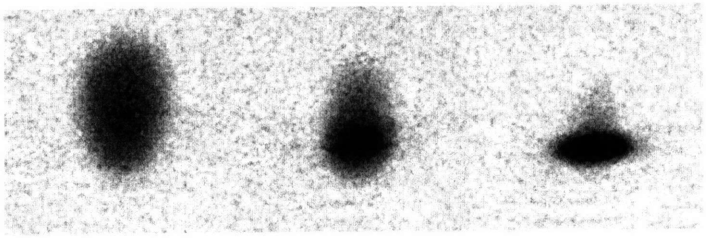

Figure 4-1: Phase transition: Fermion pair condensation on the BEC side at 770 G. As the temperature is lowered a bimodal density distribution emerges in a gas of weakly bound $^6Li_2$ molecules, the hallmark of Bose-Einstein condensation.

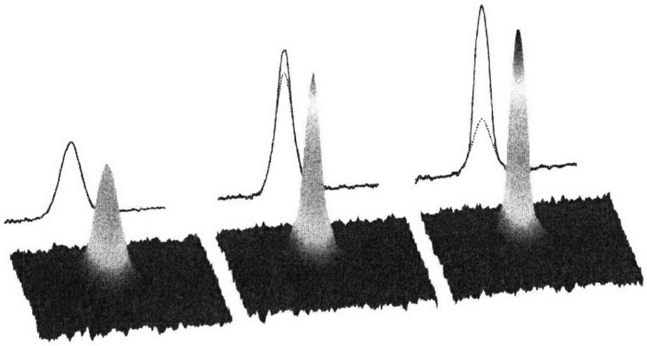

Figure 4-2: Phase transition: Fermion pair condensation at unitarity. The observation of bimodal density distribution in the strongly interacting regime required a rapid magnetic field ramp to the BEC side of the Feshbach resonance. Fermion pair condensates could then be observed as a peak of condensed, zero momentum pairs surrounded by a cloud of thermal molecules.

while preserving their center of mass momentum. The interaction energy of the pairs is lowered by up to 2 orders of magnitude as the molecular scattering length between the pairs is drastically reduced. After further expansion the momentum distribution of the pairs before the sweep can be observed: the condensed, zero momentum pairs are now clearly separated from the thermal finite momentum pairs.

With the "rapid ramp" technique the "phase diagram" of fermion pair condensation in the BEC-BCS crossover shown in Fig. 4-3 was obtained. Note that the rapid ramp method is an excellent qualitative indicator for the onset of fermion pair condensation but very difficult to interpret quantitatively due to the complicated dynamics during the magnetic field sweep. For example the relation between the observed condensate fraction and the original one is not well understood [59, 60, 61, 62].

The rapid ramp methods gives rise to an important concern: could the observed pair condensates be created during the rapid ramp and not result from a pair condensate in the

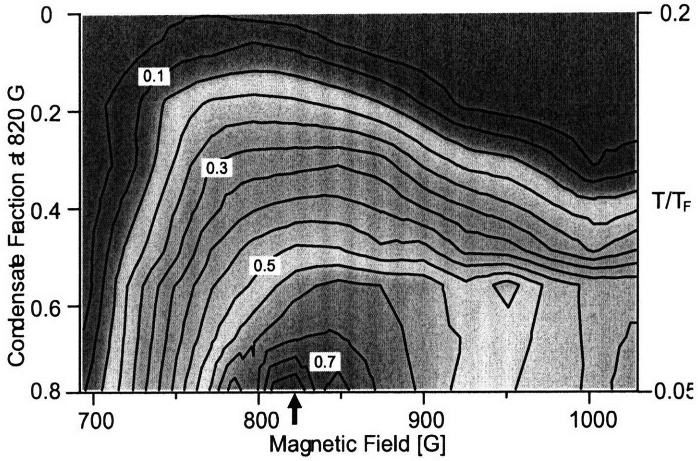

Figure 4-3: "Phase diagram" of fermion pair condensation. Condensates are observed in the entire crossover regime. The highest condensate fractions are obtained close to resonance. The decreasing condensate fraction on the BCS side is due to the decreasing interaction strength in this regime. The sharp decay of the condensate on the BEC side is caused by heating owing to vibrational relaxation of the molecules.

initial state? While the experiments provided some evidence that such concerns were not justified we decided to explicitly study the relevant timescales [26].

4.1.1 Timescales

The condensates detected after the rapid ramp can be expected to reflect condensation of the original fermion pairs if the ramp is fast compared to the many-body physics leading to the formation of a fermion pair condensate. The formation dynamics of the condensate can be studied by observing the relaxation of the system in response to a fast change in the interaction strength. By periodically changing the interactions via a magnetic field modulation on the BCS side of the Feshbach resonance and monitoring how the measured condensate fraction adjusted to this perturbation the relaxation time of the fermion pair condensate could be determined [26]. Figure 4-4 shows the delayed response of the fermion pair condensate to the magnetic field modulation. The relaxation time is more than an order of magnitude larger than the time required to cross the Feshbach resonance with the rapid ramp.

In later experiments we have actually seen direct signs of the phase transition at unitarity in high resolution images of expanding clouds of an equal mixture [28]. The column density profiles showed small deviations from an ideal Thomas-Fermi profile close to the critical temperature. However, these very faint features could have hardly been interpreted as signatures of pair condensation without the dramatic changes revealed by the rapid ramp method or the observation of superfluidity via vortex lattices which is the subject of the

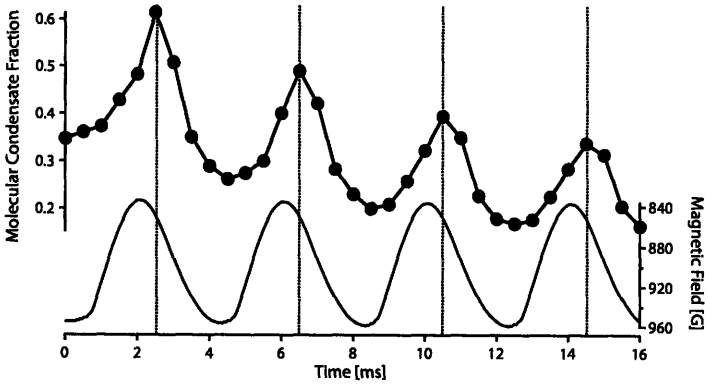

Figure 4-4: Relaxation of a fermion pair condensate. Shown is the response of the condensate fraction to a modulation of the external magnetic field on the BCS side of the Feshbach resonance. The higher the magnetic field the smaller is the interaction strength and the smaller is the expected steady state condensate fraction (see Fig. 4-3). The response of the fermion pair condensate to a modulation of the magnetic field (and therefore the interaction strength) is delayed by about 500 μs. This is about 130 times the unitarity limited collision time $\hbar E_F^{-1}$ and large compared to the 10 μs long magnetic field ramp through the Feshbach resonance.

following sections.

4.2 High temperature superfluidity

The observation of fermion pair condensation did not demonstrate superfluidity in ultracold Fermi gases. Although in three dimensions superfluidity and condensation usually occur together, the observation of long range phase coherence and superfluid flow are necessary to establish superfluidity. For example the formation of a quasi condensates can occur in systems that have not yet reached full three dimensional equilibrium and therefore do not exhibit superfluidity.

A number experiments showed features that were consistent with superfluidity but did not provide sufficient prove as the strongly interacting normal phase often showed at least a qualitatively similar behavior. Examples are superfluid hydrodynamics (probed in expansion [63] and via collective oscillations [64, 65]), pair formation [22], or a measurement of the heat capacity of the gas [66]. An experiment that is directly sensitive to the emergence of a macroscopic wavefunction (and therefore long range phase coherence and superfluid flow) is to rotate the gas. Since the flow field of a superfluid is rotation free the superfluid can contain angular momentum only in the form of quantized vortices. The observation of ordered and stable vortex lattices in a rotating gas is therefore a "smoking gun" for superfluidity. Note that classical vortices can spontaneously form in the normal phase. However, in this case the vortices are not an equilibrium property of the system, they are not quan-

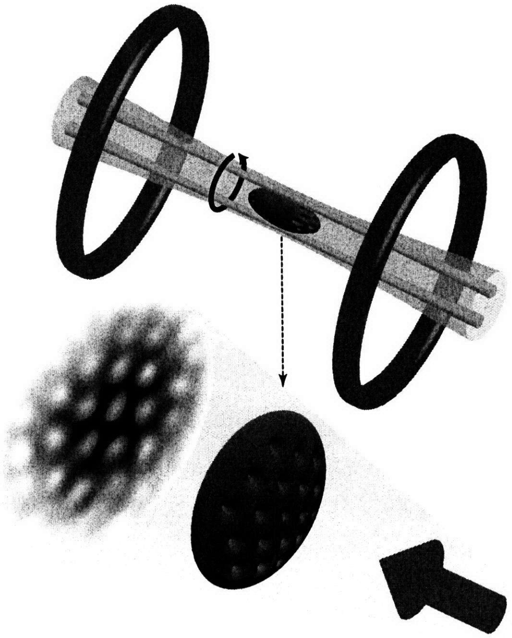

Figure 4-5: Schematics: process of vortex creation. Angular momentum is imparted onto the gas with the help of two rotating stirring beams (in green), that create an repulsive potential for the atoms. The atoms are confined in an optical dipole trap (in pink) with additional axial confinement provided by the magnetic field generated by the circular coils shown in blue. The stirring beams excite a surface mode of the superfluid that decays via the formation of vortices. The vortices penetrate into the superfluid and arrange themselves in a triangular Abrikosov lattice, a process that takes several 100 ms after the stirrer is turned off. The vortex cores are too small to be imaged in situ. Therefore the optical trap is switched off and the gas is allowed to expand before imaging. The expansion serves as a (non-linear) magnifying glass for the vortices. To enhance the vortex contrast and to stabilize the fermion pairs during expansion the magnetic field is usually switched to lower fields after the optical trap is turned off.

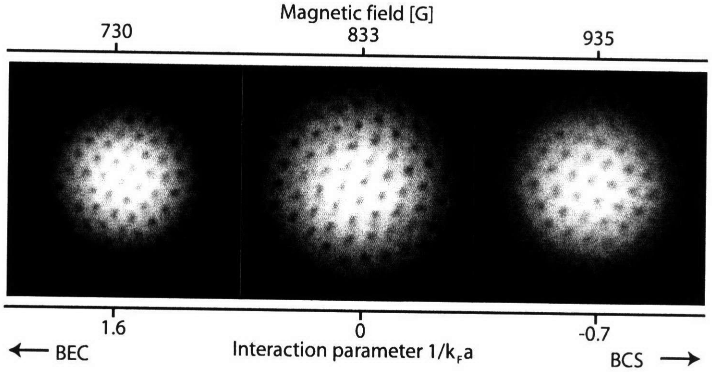

Figure 4-6: Observation of vortex lattices in a rotating superfluid in the BEC-BCS crossover.

tized and they decay due to finite viscosity. In rotating atomic Bose-Einstein condensate as well as rotating superfluid ^{4}He and ^{3}He the observation of vortex lattices was regarded as unambiguous proof of superfluidity.

Rotating the ultracold fermion gas in the optical trap and observing the vortices required a considerable effort the details of which are documented in Martin Zwierlein's PhD thesis [39] and in [28]. The experimental procedure is illustrated and summarized in Fig. 4-5. Figure 4-6 shows the vortex lattices observed in the BEC-BCS crossover. This established phase coherence and superfluidity for strongly interacting gases of fermions and for molecular gases of weakly bound molecules.

The observation of vortices at resonance and on the BCS side was not possible in situ. In a narrow window on the BEC side stirring, equilibration and expansion could be performed at the same magnetic field. In general, however, the final step of the process - the expansion of the vortex lattice - had at least in part to take place on the BEC side: On resonance and further in the strongly interacting regime on BCS side (where $k_F a < -1$) the size of the vortices is essentially given by $1/k_F$ which is on the order of 0.2 μm for typical values of k_F. This size is smaller than the resolution one could reasonably hope to achieve with imaging light resonant with the ^{6}Li atoms at a wavelength of 0.67 μm. During expansion at a stationary magnetic field the vortex size will at best increase as the condensate radius [28]. In addition the vortex contrast on resonance and on the BCS side is reduced as E_F/Δ due to quantum depletion which leads to a finite density of non-coherent atoms inside the vortex cores. During expansion on the BCS side the fraction of atoms inside the core will even increase further. Finally superfluidity will cease if the density of the system drops below a critical value during expansion (for finite temperature and interaction strength).

These problems can all be solved with a sweep to the BEC side where the superfluid is stabilized, the size of the vortices relative to the condensate radius increases and quantum depletion is drastically reduced. The only requirement is that the condensate density at the time of the magnetic field sweep is still sufficiently high for the condensate to adjust to the change of interaction strength.

Since the observation of vortex lattices in the crossover relies in part on a magnetic field sweep the concern that the system became superfluid during the sweep and the vortex lattices formed afterwards has to be considered. However, the time required for vortices to crystalize in a regular vortex lattice is several 100 ms [1]and more than an order of magnitude larger than the duration of the sweep and the remaining expansion on the BEC side of about 10 ms. The equilibrated, triangular vortex lattices observed in the experiments cannot have formed in this short time frame and in particular not in a cloud expanding at the speed of sound.

As mentioned above, superfluidity can break down during expansion on the BCS side of the resonance: as the density decreases in expansion T/T_c increases and superfluidity will eventually be lost. We have studied the stability of the expanding fermionic superfluid on resonance and the BCS side as a function of density and interaction strength. This experiment is the subject of the next section.

4.3 Superfluid expansion of a rotating Fermi gas

From preceding discussion the ultimate fate of an expanding superfluid on the BCS side at finite temperature is known: the gas will turn normal. But how long can superfluidity survive the expansion and at what densities or interaction strengths will superfluidity break down?

These questions can be addressed quite elegantly by releasing the gas from the trap and delaying the sweep to the BEC side for a variable BCS expansion time t_{BCS}. If the superfluid turns normal during the BCS expansion the vortex core will fill in quickly and disappear. Therefore the vortices can be used as "markers" for the superfluid regions in the expanding cloud [17].

Figure 4-7 shows the expansion of the superfluid gas for a fixed total, but variable BCS expansion time at 910 and 960 G. The presence of vortices indicates that the superfluid initially survives the expansion. Vortices are lost first in the lower density wings of the cloud and finally in the central region. The total BCS expansion time until superfluidity is lost depends on the initial interaction strength. The "healthier" the system starts out, (i.e. the larger the initial $k_F|a|$) the longer the superfluid survives the expansion. Figure 4-8 demonstrates that superfluidity is lost at a critical $k_F a \sim -0.8$ independently of the initial interactions strength or the magnetic field.

The most plausible explanation for the breakdown of superfluidity is that the cloud turns normal during expansion. As the cloud expands T/T_F stays constant while T/T_c increases. We can estimate the critical $k_F a$ by equating $1 \equiv \frac{T}{T_c} = \left(\frac{T}{T_F}\right)\left(\frac{T_F}{T_c}\right) = 1.76\left(\frac{T}{T_F}\right)\left(\frac{E_F}{\Delta}\right)$ with $\Delta = \frac{2}{e}^{7/3} E_F e^{-\pi/2k_F|a|}$ which is valid in the BCS limit for $k_F|a| \leq 1$. For our lowest

---

[1] This is independent of temperature and interaction strength and holds for atomic BECs as well.

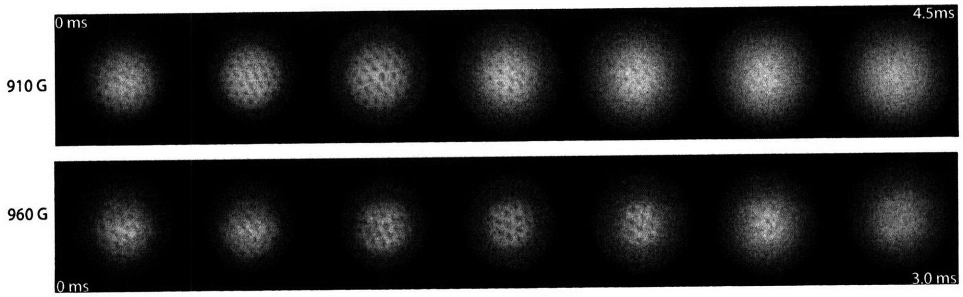

Figure 4-7: Superfluid expansion of the rotating gas. Shown are absorption images for different expansion times on the BCS-side of the Feshbach resonance at 910 G (0.0, 1.0, 2.0, 3.0, 3.5, 4.0, and 4.5 ms) and 960 G (0.0, 0.5, 1.0, 1.5, 2.0, 2.5, and 3 ms), before the magnetic field was ramped to the BEC-side for further expansion. The total expansion time remained constant. The vortices served as markers for the superfluid parts of the cloud. Superfluidity survived the expansion for several milliseconds and was gradually lost from the low density edges of the cloud towards its center. The field of view of each image is 1.2 mm × 1.2 mm.

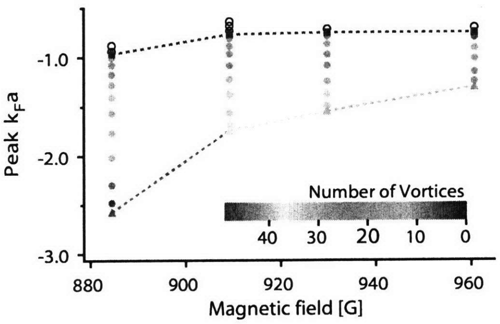

Figure 4-8: Central interaction strength $k_F a$ during superfluid expansion. The triangles indicate the initial $k_F a$ of the trapped superfluids which decreases as $|a|$ decreases for higher magnetic fields. During expansion vortices survived up to a critical interaction strength of $k_F a = -0.8 + / - 0.1$ (squares) almost independent of of the magnetic field (or scattering length a). Filled circles correspond to partially superfluid, open circles to normal clouds. The observed number of vortices is color coded.

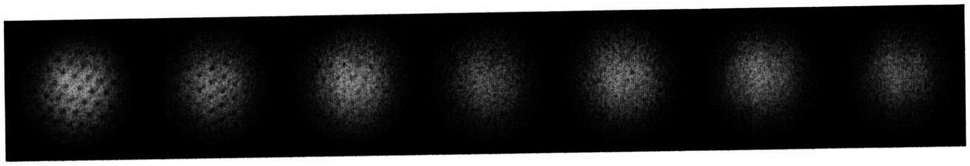

Figure 4-9: Expansion at unitarity. Shown are absorption images after a fixed total time-of-flight, but for different expansion times on resonance (2, 2.5, 3, 3.5, 4, 5, and 6 ms) before the magnetic field was swept to the BEC-side for further expansion. While the gas remains superfluid the vortex contrast is lost gradually across the whole cloud from about 15% to 3% after 2 and 5 ms of expansion on resonance respectively. Vortices could still be detected at densities as low as 1.2×10^{11} cm^{-3} in the wings of the expanded cloud. At this point the cloud size had increased by more than a factor of four and the peak density had dropped by a factor of 17 compared to in traps values. The field of view of each image is 1.2 mm ×1.2 mm.

estimated temperatures of $0.05T_F$ this gives $k_F a = -0.9$ close to the observed value.

Also the increasing size of the fermion pairs for decreasing density could in principle lead to the observed loss of superfluidity. If the size of the pairs exceeds the interparticle spacing the sweep methods which relies on the efficient transfer of correlated fermion pairs into molecules might fail. We will consider these issues when we discuss our determination of the fermion pair size in the strongly interacting regime. Note, however, that the loss of vortices in the cloud due to an increasing pair size would likely be more gradual and not lead to the sharp boundaries between superfluid and normal regions seen in the experiment (see Fig. 4-7).

Could superfluidity be quenched due to rapid rotation? When the size of the vortex cores becomes comparable to the separation between the vortices, superfluid flow is expected to break down as superconductivity in type II superconductors at the critical field H_{c2}. Since the size of the vortex cores depends exponentially on $k_F a$ the effects of rotation might not be negligible. However, in ref. [67] it is found that the superfluid should be stable in the strongly interacting regime at all rotation frequencies.

So far we have focused on the breakdown of superfluidity on the BCS side. At resonance $T_c/T_F = const.$ and therefore the gas should remain superfluid during expansion. Indeed Fig. 4-9 shows that vortices are not lost after the gas is released from the trap. However, the vortex contrast decreases uniformly across the cloud with increasing resonant expansion. The low densities the gas reaches during expansion could prevent the vortex cores to adjust quickly enough to the high contrast and larger size they would have in equilibrium on the BEC side after the sweep.

In this experiment we have observed vortices at densities as low as 1.2×10^{11} cm^{-3}, demonstrating fermionic superfluidity in a system 100 million times more dilute than air and at a temperature of less than 20 nK. At the other extreme fermionic superfluidity in neutron stars is expected to occur at temperatures of 10 billion K and densities nearly 20 orders of magnitude higher than in air. Even higher temperatures and densities exist in the quark gluon plasma of the early universe. Although this state of matter is not a superfluid, recent experiments demonstrated that it shows very small viscosity similar to normal but strongly interacting ultracold Fermi gases [63, 68]. It is amazing to see that systems under such extremely conditions share universal properties.

Chapter 5

Superfluidity and phase separation in strongly interacting Fermi gases with density imbalance

5.1 Introduction

The creation of high-temperature superfluid in fermionic gases allows the study fermionic superfluidity in an entirely new regime. An interesting way to get insight into the new system is to study its stability against a change of parameters that can ultimately quench superfluidity. In the previous chapter we have looked at the stability of the superfluid many-body state as a function of the interaction strength. An even more powerful approach is to break a symmetry of the superfluid state and to observe the response of the system. In ultracold Fermi gas this can be easily achieved by creating an imbalance in the number of atoms in the two hyperfine states that form the superfluid. The first experiments with strongly interacting imbalanced Fermi gases established superfluidity in these system [18] and lead to the direct observation of the superfluid phase transition at unitarity [19]. Furthermore the so-called Chandrasekhar-Clogston limit of superfluidity which gives the critical population imbalance for a first order quantum phase transition from the superfluid to the normal phase was established [18]. These experiments were based on data obtained from the gas after expansion. A more detailed characterization of the superfluid and normal phases was carried out by observing the trapped gas *in situ* with the methods described in chapter 3 [20]. This lead to the determination of the homogenous phase diagram of a strongly interacting Fermi gas at unitarity as a function of temperature and spin polarization [21]. The phase diagram proved to be very rich with first and second order phase transitions that merge at a tricritical point. In the last part of the chapter we will discuss imbalanced Fermi gases in the BEC-BCS crossover.

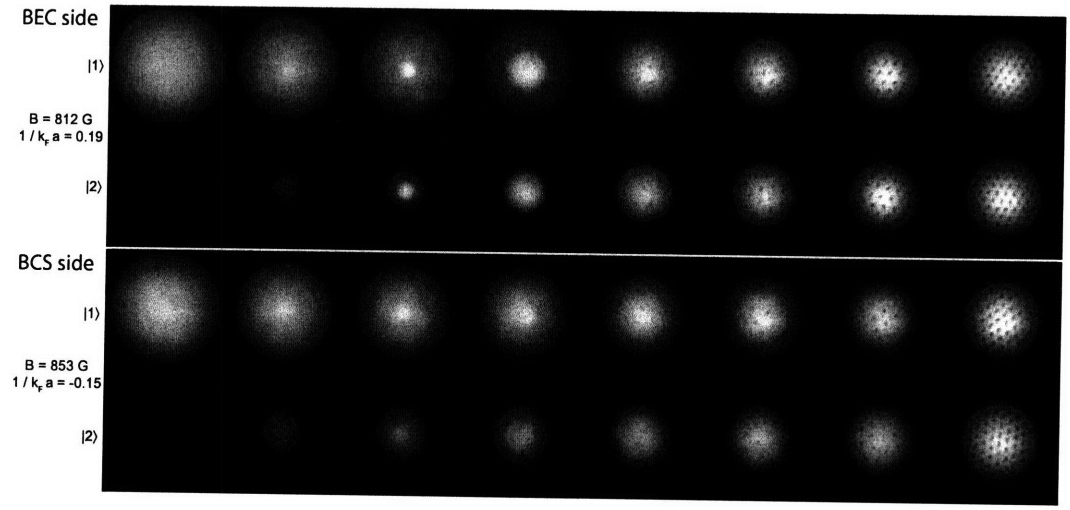

Figure 5-1: Superfluidity in imbalanced Fermi gases. The presence of vortex lattices in the rotating gas demonstrates the stability of the superfluid against substantial imbalances in the strongly interacting regime. Superfluidity breaks down at a population imbalance $\delta_{N,c} = \frac{N_\uparrow - N_\downarrow}{N_\uparrow + N_\downarrow}$ of about 75%. This is known as the Chandrasekhar-Clogston (CC) limit of superfluidity. For the 812 G (853) data δ_N was from left to right 100%, 90%, 80%, 62%, 28%, 18%, 10% and 0% (100%, 74%, 58%, 48%, 32%, 16%, 7% and 0%).

5.2 Superfluidity and direct observation of the superfluid phase transition in imbalanced Fermi gases

5.2.1 Breakdown of superfluidity: The Clogston-Chandrasekhar (CC) limit

The standard BCS theory describes fermionic superfluidity in a two component fermion mixture with the same mass, chemical potentials and particle numbers and the Fermi energies of the two components are equal. Although pairing costs kinetic energy there is a gain in potential energy of $(1/2)\rho_F\Delta^2$ (where $\rho_F \equiv \rho(E_F)/\Omega = \frac{1}{4\pi^2}(\frac{2m}{\hbar^2})^{3/2}\sqrt{E_F}$) which makes the formation of superfluid pairs favorable even for arbitrarily small attractive interactions. The creation of an imbalance in the spin populations ($N_\uparrow > N_\downarrow$) leads to different Fermi energies of the two components. Since in the imbalanced system the Fermi energies are then not at "eye level" there is in an additional energy cost for the formation of superfluid pairs. In a simple $T = 0$ model one can assume that superfluidity requires equal densities. The imbalanced system may then form an equal density superfluid in one part of the volume and a normal mixture at a local imbalance that is larger than the global one in the other part of the volume. This requires the superfluid to expel majority atoms which costs kinetic energy. If this energy cost exceeds the superfluid stabilization energy superfluidity is quenched. This is known as the Chandrasekhar-Clogston (CC) limit of superfluidity [69, 70].

Assuming that $\delta_N = \frac{N_\uparrow - N_\downarrow}{N_\uparrow + N_\downarrow} \ll 1$ one can show [28] that the CC limit is reached at a critical density difference $\Delta n = \frac{N_\uparrow - N_\downarrow}{2\Omega}$ of

$$\Delta n_c = \frac{\rho_F \Delta}{\sqrt{2}} \tag{5.1}$$

It is convenient to define the parameter h proportional to the chemical potential difference between the two components $h = \frac{\mu_\uparrow - \mu_\downarrow}{2}$. For definiteness we assume $\Delta \ll E_F$, $E_F = \mu = \frac{\mu_\uparrow + \mu_\downarrow}{2}$ and $h \ll \mu$. With that we have[1]:

$$\begin{aligned} \Delta n &= \frac{1}{12\pi^2}\left(\frac{2m\mu}{\hbar}\right)^{\frac{3}{2}}\left[\left(1+\frac{h}{\mu}\right)^{\frac{3}{2}} - \left(1-\frac{h}{\mu}\right)^{\frac{3}{2}}\right] && (5.2) \\ &\approx h\rho_F && (5.3) \end{aligned}$$

In terms of h the CC limit is therefore reached when

$$h_c \approx \frac{1}{\sqrt{2}}\Delta \tag{5.4}$$

Similarly one finds for the critical population imbalance

$$\delta_{N,c} \approx \frac{3}{2}\frac{\Delta}{\mu} \tag{5.5}$$

The above discussion assumed a homogenous system. However, the gases we are studying are trapped in a harmonic potential and therefore the densities $n_\uparrow(\mathbf{r})$, $n_\downarrow(\mathbf{r})$, the chemical potentials $\mu_\uparrow(\mathbf{r})$, $\mu_\downarrow(\mathbf{r})$ and the gap $\Delta(\mathbf{r})$ vary spatially. Note that in chapter 3 we have demonstrated that the local density approximation is valid for our system.

In the following we will use global as well as local quantities. Most importantly the population imbalance δ_N is a global quantity since it is based on the total number of minority and majority atoms in the trap. We will refer to the *local* population imbalance as the "*spin polarization*":

$$\sigma(\mathbf{r}) = \frac{n_\uparrow(\mathbf{r}) - n_\downarrow(\mathbf{r})}{n_\uparrow(\mathbf{r}) + n_\downarrow(\mathbf{r})} \tag{5.6}$$

5.2.2 The experiment: Superfluidity and the CC limit at unitarity

Superfluidity in population imbalanced Fermi gases was established with the same methods as in equal mixtures by rotating the gas and observing vortex lattices [18] (see figure 5-1). Vortices are always found within the parts of the cloud that also show the presence of a fermion pair condensate. In very small fermion pair condensates no vortices have been observed as it is difficult to nucleate them in small condensates surrounded by large thermal clouds. We therefore conclude that the presence of a fermion pair condensate shows that the system is superfluid and assume that fermion pair condensation is a more sensitive indicator

---

[1] With $n = \frac{1}{6\pi^2}\left(\frac{2m\mu}{\hbar^2}\right)^{\frac{3}{2}}$ and $\mu_\uparrow = h + \mu$ and $\mu_\downarrow = h - \mu$

for the onset of superfluidity than vortices. Careful measurements of the emergence of fermion pair condensation as a function of imbalance and temperature [19] demonstrated a critical population imbalance at unitarity of $\delta_{N,c} = 74(5)\%$ for an harmonically trapped gas. This value agrees with results from more recent quantum Monte-Carlo calculations [71].

5.2.3 Bimodal density profiles: Direct observation of the superfluid phase transition at unitarity

As we have mentioned in the previous chapter the density profiles of a balanced mixture at unitarity show only very subtle signs of the superfluid phase transition (see Fig. 5-2 a-c). Bimodal density distributions, the hallmark of BEC for weakly interacting Bose gases, were only revealed after a rapid ramp to the BEC side of the Feshbach resonance that suddenly reduced the chemical potential of the condensate relative to the thermal cloud [15, 16].

In imbalanced mixtures this situation changes dramatically: At low temperatures the minority component develops a dense central core inside a thermal cloud which is directly visible at unitarity and the BCS side (Fig. 5-2 e-f). Rapid ramp experiments confirm that the emergence of bimodal density profiles on resonance coincides with the superfluid phase transition. The density profiles of the minority component therefore reveal the superfluid phase transition without the quantitatively poorly understood magnetic field sweeps [19].

What phenomenon leads to the emergence of a bimodal density distribution in the minority cloud? To gain insight into this question we studied the normal to superfluid phase transition as a function of population imbalance at the lowest temperatures. Figure 5-3 correlates the emergence of bimodal density profiles, i.e. the onset of superfluidity, with an *estimate* of the central densities of minority and majority component[2]. The data suggest that superfluidity indeed sets in when the densities of minority and majority become equal. The densities profiles also show that the superfluid core is surrounded by a mixed, imbalanced normal gas. Only in the wings of the cloud is a pure gas of majority atoms observed.

One explanation for the bimodal density distribution of the minority component is phase separation: the superfluid of equal densities ($T = 0$) spatially separates from the mixed normal component giving rise to a first order phase transition and a discontinuity in the density profile of the minority cloud. We have actually used this phase separation scenario, first suggested by XXX in 2004 [72], when motivating the CC limit.

The characterization of the superfluid and normal phases including the determination of phase boundaries requires the knowledge of the *in situ* density profiles of both majority and minority components. A detailed description of the experimental techniques required to obtain these profiles including phase contrast imaging and the important aspects of temperature calibration has been given in chapter 3. In the following we will focus on the

---

[2] Since the column density profiles were obtained after expansion a precise reconstruction of the central densities in the trapped cloud was not possible

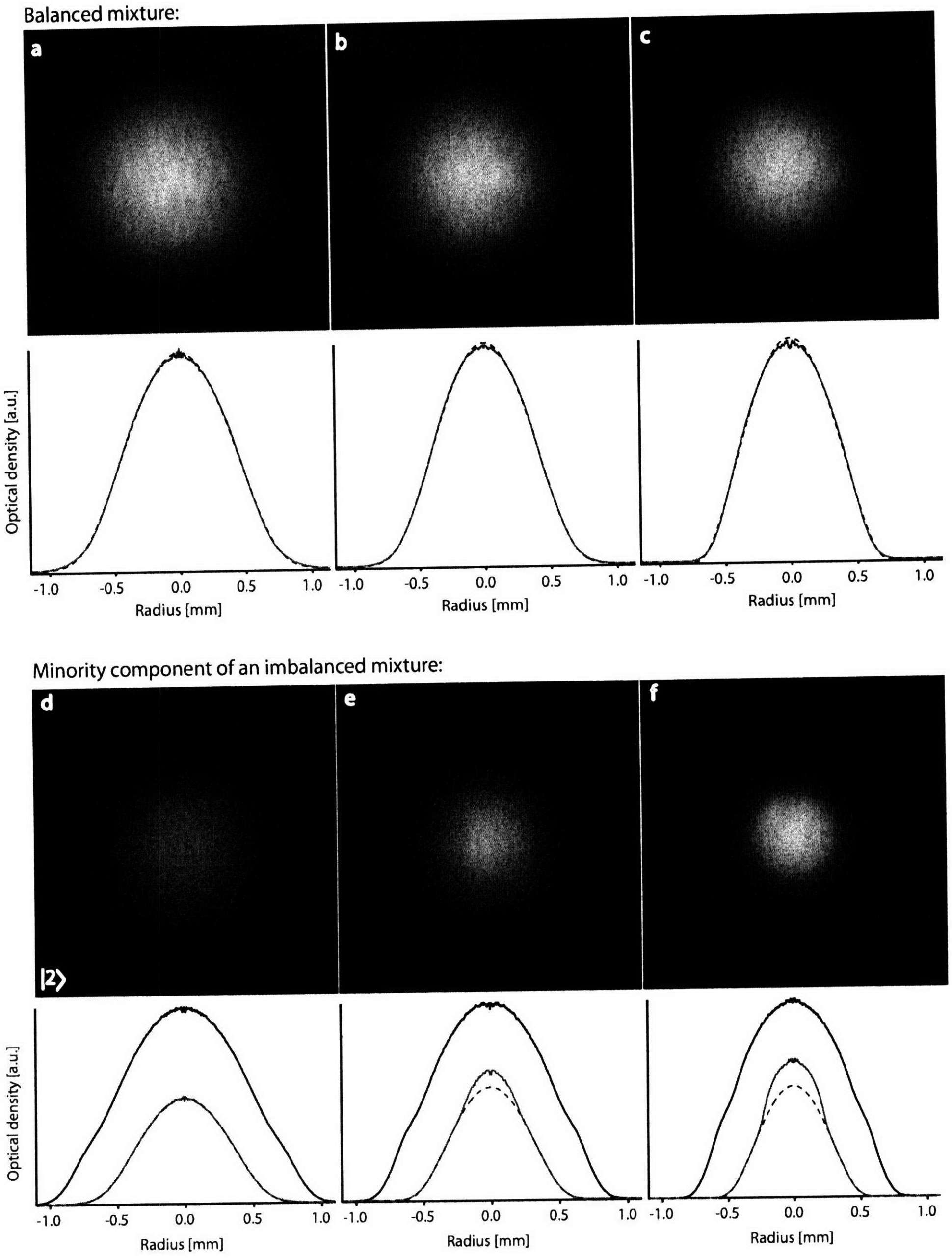

Figure 5-2: Direct observation of the superfluid phase transition at unitarity in the minority component of an imbalanced mixture. When a balanced gas is cooled through T_c the density profiles do not change significantly (a-c). In contrast, the minority component of an imbalanced mixture clearly shows a bimodal density distribution below T_c (d-f). The density profiles of the majority component (shown in blue) are considerably less affected by the onset of superfluidity. Only a careful analysis of the density profiles for the balanced gas and the majority component in the imbalanced case reveals small changes as a function of temperature which can be attributed to the superfluid phase transition. See refs. [19] and [28] for details.

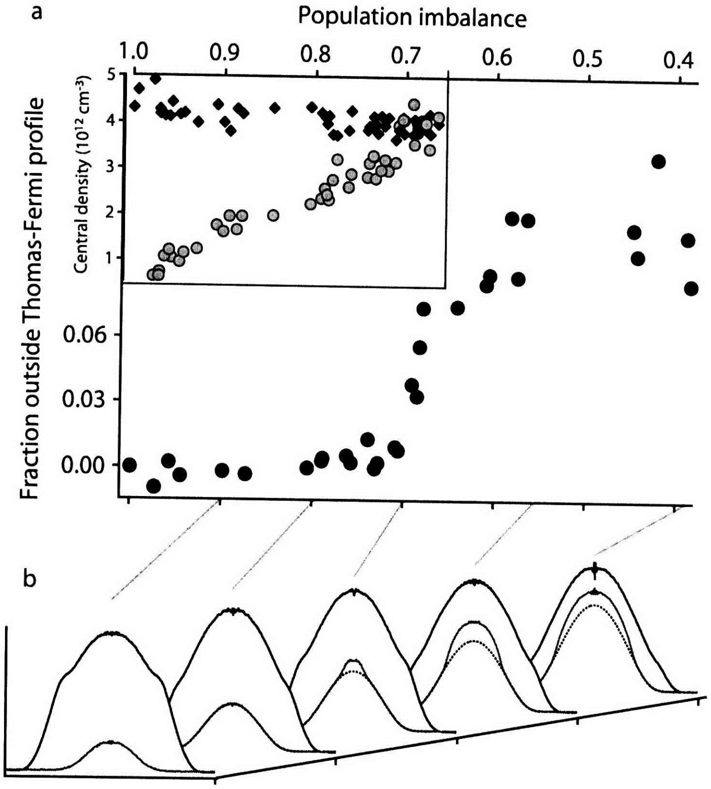

Figure 5-3: Emergence of bimodal density distributions: a consequence of phase separation? As the population imbalance decreases the CC limit is approached and at δ_c the minority cloud becomes bimodal (b). The onset of bimodality/superfluidity is measured by the fraction outside of a Thomas-Fermi profile fitted to the wings of the cloud. At the critical imbalance δ_c this quantity suddenly increases (a). The inset in (a) gives an estimate of the central densities of the minority and majority clouds. As the imbalances decreases the minority density increases until it reaches the almost constant majority density at δ_c. This observation provides evidence for a phase separation scenario where a superfluid of equal densities (at $T = 0$) is spatially separated from a normal mixed cloud of unequal densities.

the density profiles to answer the new questions raised by the experiments:

- Does superfluidity at zero temperature require equal densities?
- Is there phase separation between a balanced superfluid and the mixed normal phase at T=0?
- What is the phase diagram of the system at finite temperature?

5.3 Probing the nature of the superfluid: The homogeneous phase diagram

5.3.1 Density profiles in a harmonic trap

Due to the confinement of the gas in an optical trap which provides an approximately harmonic trapping potential $V(\mathbf{r})$ the chemical potentials of minority ($\downarrow$) and majority ($\uparrow$) component vary spatially as

$$\mu_\uparrow(\mathbf{r}) = \mu_{\uparrow 0} - V(\mathbf{r}) \tag{5.7}$$

$$\mu_\downarrow(\mathbf{r}) = \mu_{\downarrow 0} - V(\mathbf{r}) \tag{5.8}$$

Here $\mu_{\uparrow 0}$ and $\mu_{\downarrow 0}$ are the global chemical potentials. The total chemical potential $\mu(\mathbf{r})$ and the chemical potential difference h are given by

$$\mu(\mathbf{r}) = \frac{\mu_\uparrow(\mathbf{r}) + \mu_\downarrow(\mathbf{r})}{2} \tag{5.9}$$

$$h = \frac{\mu_\uparrow(\mathbf{r}) - \mu_\downarrow(\mathbf{r})}{2} = \frac{\mu_{\uparrow 0} - \mu_{\downarrow 0}}{2} = const \tag{5.10}$$

The ratios $\eta(\mathbf{r}) = \mu_\downarrow(\mathbf{r})/\mu_\uparrow(\mathbf{r})$ and $h/\mu(\mathbf{r})$ vary spatially over the trapped sample and provide a cut through the homogenous phase diagram (since the local density approximation is valid).

In a harmonic trapping potential $V(r) \propto r^2$ (Fig. 5-4 a) the chemical potentials of majority and minority components can be expressed as:

$$\mu_\uparrow(r) = \mu_{\uparrow 0}\left(1 - \frac{r^2}{R_\uparrow^2}\right) \tag{5.11}$$

$$\mu_\downarrow(r) = \mu_{\uparrow 0}\left(\eta_0 - \frac{r^2}{R_\uparrow^2}\right) \tag{5.12}$$

Here $R_\downarrow$ and $R_\uparrow$ mark the radii where the densities of minority and majority component become zero respectively and $\eta_0 = \mu_{\downarrow 0}/\mu_{\uparrow 0} = R_\downarrow^2/R_\uparrow^2$.

Figure 5-4 b) schematically shows the density distributions of majority and minority components in a harmonic trapping potential. We assume that the phase separation sce-

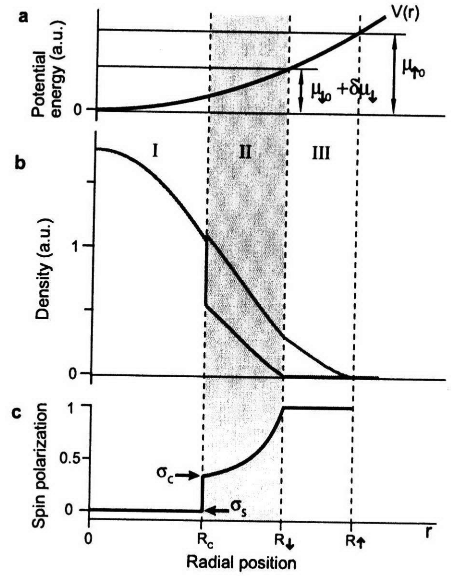

Figure 5-4: Schematics of density profiles in the harmonic trap assuming phase separation between a balanced superfluid and an normal mixed region. As a function of radius from the trap center three distinct regions can be identified: I) balanced superfluid, II) partially polarized normal gas, III) fully polarized normal gas. See the text for a discussion. $\mu_{\uparrow 0}$ and $\mu_{\downarrow 0}$ are the global chemical potentials, $\delta\mu_{\downarrow}$ measures the shift for the minority component due to interactions.

nario between a balanced superfluid and a partially polarized normal gas yields a correct description of the system at T=0. The experiments described in the following sections will show that the observed density profiles indeed have a similar structure.

In the center of the cloud (region I) one expects the balanced ($n_\downarrow = n_\uparrow$) superfluid (at T=0). At finite temperature this region can have a small polarization due to thermally excited quasiparticles. According to equation 5.4 with a spatially varying $\Delta(\mathbf{r})$ the CC limit is reached when $h_c \approx \Delta(R_c)$. At $r = R_c$ the minority density suddenly jumps to lower densities, indicating a sharp boundary between the superfluid and the partially polarized normal phase. This is a consequence of phase separation which is associated with a first order phase transition [72]. At radii $R_\downarrow < r < R_\uparrow$ the gas is fully polarized: only majority atoms are present. This part of the cloud can serve as an ideal gas thermometer and also yields an absolute density calibration.

The jump in the density of the minority cloud at $r = R_c$ corresponds to a sudden change in the local polarization σ. The maximum polarization of the stable superfluid is given by σ_s and the minimum polarization of the stable normal gas by σ_c. For $\sigma_s < \sigma < \sigma_c$ the gas is unstable. Of particular interest for the comparison between theory and experiments are the value of the critical polarization σ_{c0} at T=0 (the CC limit) and the polarization and temperature where $\sigma_s = \sigma_c$, which corresponds to a tricritical point in the phase diagram.

5.3.2 Central density difference and superfluidity: finite vs zero temperature

In a first experiment we obtained phase contrast images that (after 3D reconstruction) showed the density difference $n_\uparrow(\mathbf{r}) - n_\downarrow(\mathbf{r})$ [20]. The *in situ* phase contrast images directly reveal how the superfluid core emerges inside the trapped Fermi gas as the temperature decreases (Fig. 5-5). While the rapid ramp and vortex experiments described in the previous chapter were required to independently establish that this is signature of the superfluid phase transition it is very satisfying to finally observe the onset of superfluidity so dramatically without further "ado".

From images like the ones in Fig. 5-5 the three dimensional central density difference $n_\uparrow(0) - n_\downarrow(0)$ was reconstructed and then correlated with the independently measured onset of fermion pair condensation (see Fig. 5-6). This demonstrated that in the $T = 0$ limit the superfluid is balanced (see Fig. 5-6) while at finite temperature the superfluid is polarized (the yellow shaded region in Fig. 5-6 b)). If $T > 0$ the superfluid can tolerate a certain access of majority atoms in the form of quasiparticle excitations.

Importantly, the central density difference shows a very different behavior at $T \sim T_c, \delta \ll \delta_c$ compared to $T \ll T_c, \delta \sim \delta_c$. In the first limit the onset of condensation occurs at a finite central density difference which smoothly decreases to zero (Fig. 5-6 b)). This is a signature of a second order phase transition. The onset of superfluidity around the critical imbalance, however, is associated with a rapid drop of the central density difference to zero,

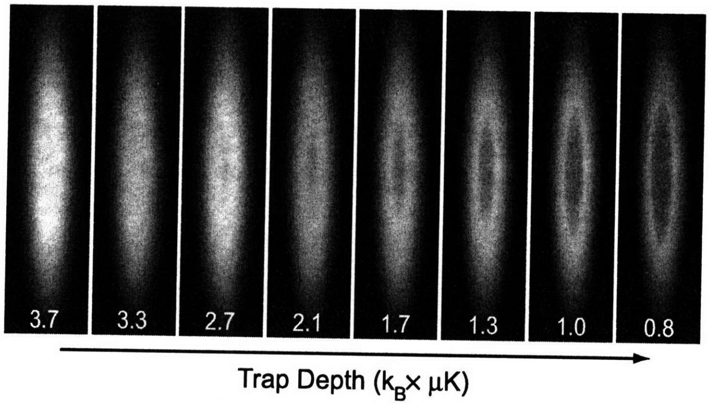

Figure 5-5: In situ observation of the superfluid phase transition: Emergence of phase separation at unitarity. Shown are phase contrast images of the density difference $n_\uparrow - n_\downarrow$ ($\delta_N = 56\%$). As the temperature (final trap depths for evaporation) decreases a superfluid core forms inside the cloud. The field of view for each image is 160 μm × 940 μm.

a discontinuous feature typical for first order phase transitions. A phase diagram of the imbalanced superfluid at unitarity is therefore expected to show both first and second order phase transitions. Since the experiment described here was only sensitive to $n_\uparrow(\mathbf{r}) - n_\downarrow(\mathbf{r})$ we could not yet extract quantities like $\mu(\mathbf{r})$ and $\sigma(\mathbf{r})$ which are required to fully characterize the phase diagram.

5.3.3 Analysis of in situ density profiles

To map out the phase diagram of an imbalanced superfluid at unitarity $n_\uparrow$ and $n_\downarrow$ have to be known separately. According to the discussion in section 5.3.1 the first order phase transition may then be characterized by determining $\sigma_s(T/T_{F\uparrow})$ and $\sigma_c(T/T_{F\uparrow})$ from the jump in $n_\downarrow$ at the phase boundary between the mixed normal and the superfluid phase. Here we define $T/T_{F\uparrow} \equiv T'_{\text{local}}(R_c)$, see section 3.5.5.

This was achieved in an improved experiment where a second phase contrast image, yielding a weighted density difference $\alpha n_\uparrow(\mathbf{r}) - \beta n_\downarrow(\mathbf{r})$, was taken shortly after the first image with $\alpha = \beta = 1$ (see chapter 3). From the two images the three dimensional densities $n_\uparrow(r)$ and $n_\downarrow(r)$ as well as the spin polarization $\sigma(r)$ were obtained. Figure 5-7 shows $n_\uparrow(r)$ and $n_\downarrow(r)$ at $T' = 0.03$. In the density profiles the three regions from the schematic profile of figure 5-4 can be clearly identified: the balanced superfluid in the center (I) a mixed normal region (II) and the wings of the cloud where only majority atoms are present (III). At the interface of region I and II the minority density changes abruptly, the signature of the first order phase transition. The corresponding spin polarization $\sigma(r)$ is displayed in Fig. 5-8 i). From $\sigma(r)$, σ_c and σ_s were determined as $\sigma_c = \sigma(R_c)$, $\sigma_s = \sigma(R_c - 0.05R_\uparrow)$. Here R_c is given by the kink in the column density difference profile (Fig. 5-8 a-c)). The

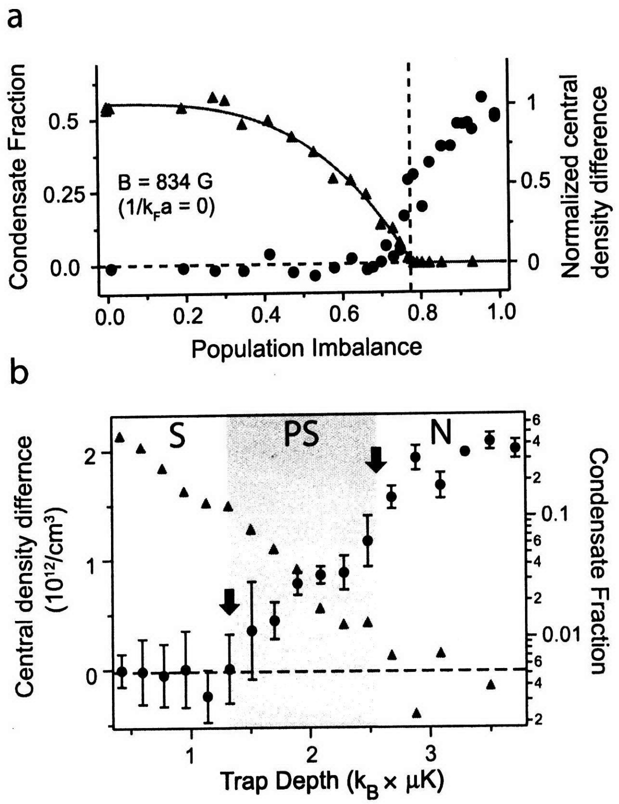

Figure 5-6: First order vs second order phase transition: Correlation of the central density difference with the formation of a fermion pair condensate. (a) At low temperatures the onset of fermion pair condensation (red triangles) as a function of the population imbalance is associated with a sharp drop in the central density difference (filled circles), indicating a first order phase transition. (b) As a function of temperature three regimes can be identified: i) An imbalanced normal (N) state at high temperatures. ii) For intermediate temperatures fermion pair condensation emerges at a finite central density difference ($n_\uparrow(0) - n_\downarrow(0) > 0$) which gradually drops to zero as the temperature decreases with decreasing trap depth. In this regime the superfluid is polarized (PS). iii) A balanced superfluid (S) at the lowest temperatures. The smooth decrease in the central density difference as superfluidity sets in (see the yellow shaded region in the figure) is typical for a second order phase transition.

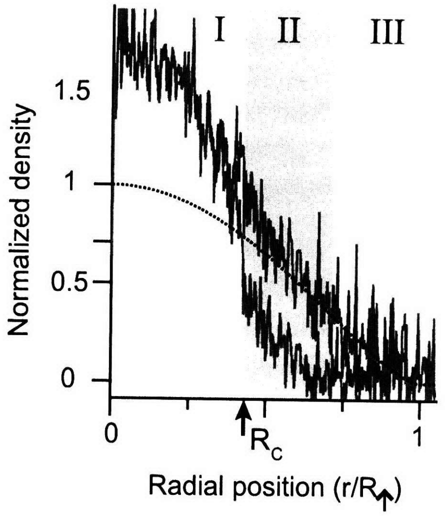

Figure 5-7: $n_\uparrow$ (red, upper trace in region II and III) and $n_\downarrow$ (blue, lower trace in region II and III) at the lowest temperature ($T' = 0.03$). The dashed line is a zero temperature Thomas-Fermi fit to the non-interacting wings of the majority component. The three regions indicated in the schematic profile of Fig. 5-4 can be clearly identified.

definition of σ_s prevents σ_c and σ_s to become equal at high temperature and is therefore a lower bound for the maximum polarization of the superfluid. By determining σ_s and σ_c as a function of temperature (see Fig. 5-8 i-l) the phase boundary between the superfluid and normal phase can be traced at low temperature until $\sigma_c \approx \sigma_s$, where the jump in σ disappears. From the previous experiment we already know that at higher temperatures the superfluid phase transition is second order without sharp features in the density profiles. In this regime we have used the rapid ramp method to determine the onset of superfluidity and then evaluated the central density difference for the same parameters. The combined data give the critical lines in the homogeneous phase diagram of an imbalanced Fermi gas at unitarity shown in Fig. 5-9.

5.3.4 The phase diagram

The phase diagram is quite rich: the thermodynamically unstable region for $\sigma_s < \sigma < \sigma_c$ gives rise to the first order phase transition observed in the density profiles. At higher temperatures the superfluid to normal transition is second order. The first and second order critical lines meet at a tricritical point. The phase diagram shows two further points of interest the critical temperature T_{c0} at zero imbalance and the critical spin polarization σ_{c0} at zero temperature. In the absence of a theory for the critical line between the superfluid and normal phases, we have applied a linear fit to the data points. This extrapolation suggest that $(\sigma_{tc}, T_{tc}/T_{F\uparrow}) \approx (0.2, 0.07)$, $\sigma_{c0} \approx 0.36$ and $T_{c0} \approx 0.15$ (the constraint on T_{c0}

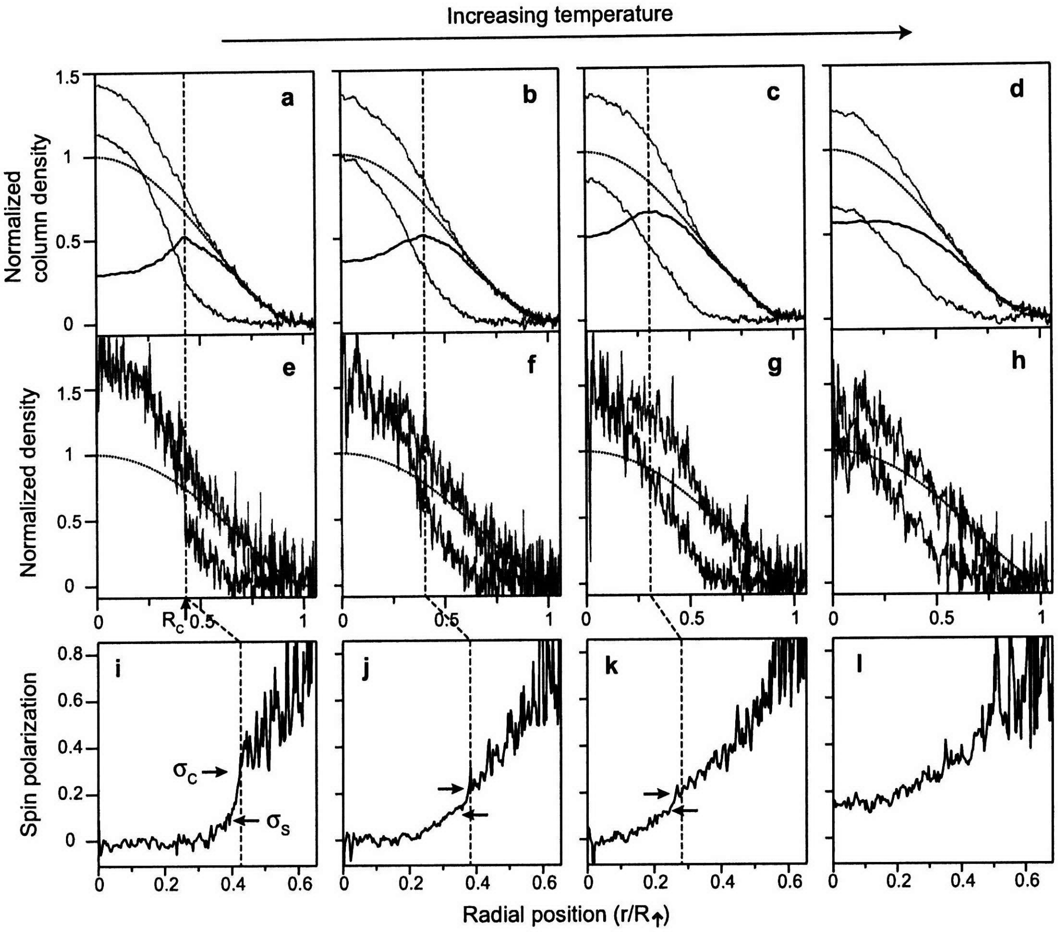

Figure 5-8: Temperature dependence of $n_{c,\uparrow}$, $n_{c,\downarrow}$, $n_\uparrow$, $n_\downarrow$ and $\sigma(r)$. Shown are the density profiles for four different temperatures T' given by: 0.03(1) (a,e,i); 0.05(2) (b,f,j); 0.07(1) (c,g,k); 0.10(1) (d,h,l). T' was determined as discussed in section 3.5.5. As the temperature increases the jump in $\sigma(r)$ decreases until it vanishes in i). Note that beyond the analysis presented in this section, the density profiles allow the determination of the zero-temperature equation of state in a polarized Fermi gas [73].

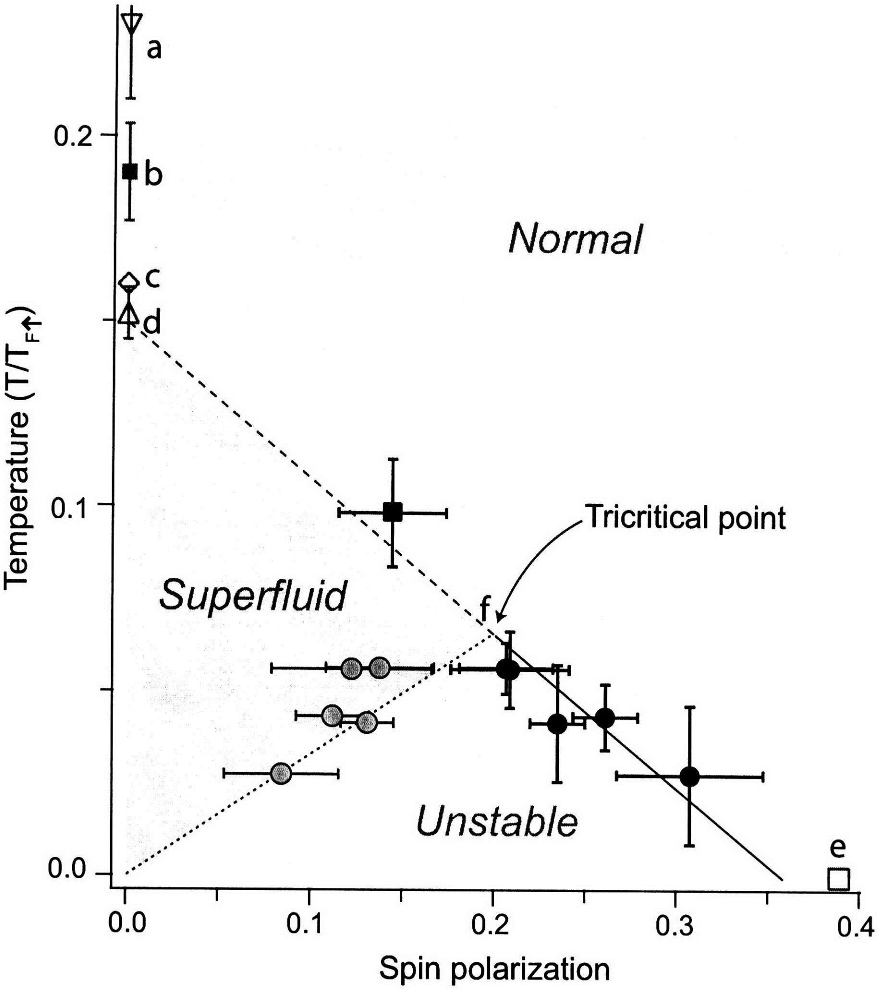

Figure 5-9: Homogeneous phase diagram at unitarity. The filled black (grey) circles give the experimentally determined values for σ_c (σ_s) and trace the phase boundary of the thermodynamically unstable region $\sigma_s < \sigma < \sigma_c$. The critical line at temperatures above T_{tc} (black square) was determined by the onset of fermion pair condensation. Note that for small population imbalances a reliable fit to the non-interacting wings of the majority cloud for temperature calibration was not possible and therefore no further data yielding a stronger constraint for T_{c0} could be obtained. The phase diagram also shows several theoretical (and one experimental) predictions for $T_c, 0$ and σ_{c0}: a) ref. [74]; b) ref. [54], the original data have been scaled by $\sqrt{\xi}$ with $\xi = 0.42$ from ref.[75]; c) ref. [76]; d) ref. [77]; e) ref. [71]; f) The location of the tricritical point in the diagram has recently been obtained theoretically in ref. [78] and is found to be $(\sigma_{tc}, T_{tc}/T_{F\uparrow}) = (0.24, 0.06)$ in good agreement with our experimental determination.

is not very strong as the in situ temperature calibration could not be performed for small populations imbalances).

The values for both T_{c0} and σ_{c0} have been the subject of long standing debates. With regard to T_c a number of approaches [74, 77, 76] (including two Quantum Monte Carlo calculations) and one measurement [54] obtained different results within a range of 0.15 to 0.23 of local T/T_F. Our extrapolation seems to favor rather the lower critical temperatures.

The critical σ_{c0} has been discussed controversially for more than two years. While all our previous observations [18, 19, 20] and Monte Carlo calculations [71] were consistent with a low $\sigma_{c0} < 0.4$, a number of theoretical studies obtained values for σ_c exceeding 0.9 [75, 79, 80, 81, 82, 83]. Furthermore experiments of the Rice group [84, 85] were considered to be consistent with a large $\sigma_{c0} > 0.9$.

The results presented here clearly confirm a $\sigma_{c,0} < 0.4$ and rule out considerable higher values. This is a dramatic consequence of the strong interactions already in the normal phase which stabilize an imbalanced normal two-state mixture relative to the balanced superfluid one. The importance of these interactions is a qualitative feature of strongly interacting Fermi gases and theories that obtained high values for the CC limit did not capture this physics appropriately. For example Bogliubov-de Gennes theory includes interactions only in the form of pairing correlations in the superfluid phase. The stability of the mixed normal phase at T=0 at unitarity has first been demonstrated theoretically in ref. [86] based on very general arguments and was further supported in ref. [87] and by Monte Carlo calculations [71, 88, 89].

The interpretation of the experiments at Rice is still an open issue. While surface tension and finite size effects [90, 91] seem to play an important role in these experiments[3], they cannot explain an apparently higher Clogston limit but should rather lead to a further reduction compared to the value established in our experiments. Further experiments are necessary to gain a better understanding of these effects and their relation to superfluidity.

So far we have considered the critical line separating the superfluid from the normal phase. However, there is another interesting point in the phase diagram which is the crossing of the critical line σ_s with the σ axis at $T = 0$. If this crossing occurs at a finite value of σ the superfluid can tolerate a finite polarization even at $T = 0$. While the data do not permit an accurate extrapolation to zero temperature there is another way to address this question. As illustrated in figure 5-10, the answer is simply determined by the relative magnitude of Δ and h_c. If $h_c > \Delta$ excess fermions would have a lower energy in the superfluid as polarized quasiparticle than in the mixed normal phase and the superfluid at $T = 0$ should show a finite polarization. From the in situ profiles we find that $h_c \approx 0.95\mu$ [21]. Since $\mu < \Delta$ at unitarity as shown in [76, 75, 92] this implies $h_c < \Delta$ and therefore we can conclude that the superfluid at $T = 0$ is unpolarized and balanced.

---

[3] The experiments were carried out in very elongated traps and with comparatively low atom numbers.

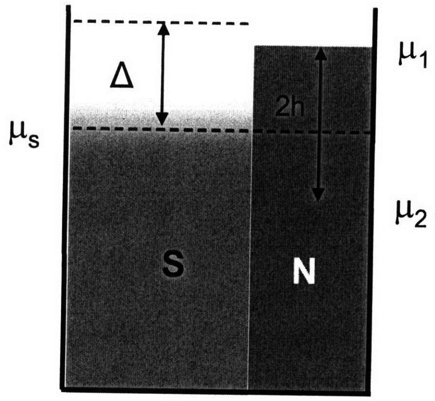

Figure 5-10: Δ vs h at T=0. Only if $\Delta < h_c$ can the superfluid be polarized at zero temperature. The experiment provides evidence that this is not the case and the superfluid is balanced.

5.4 Changing the interactions: From a Bose-Fermi mixture to exotic superfluids?

In the previous sections we considered the imbalanced gas with universal interactions at unitarity. Imbalanced mixtures on the BEC and BCS side of the resonance are, however, of great interest in themselves and here we will give an overview of our experiments studying these systems [18, 19, 20, 93]. With the phase diagram at unitarity in mind, an important goal of experiments in imbalanced mixtures is to obtain the three dimensional phase diagram of strongly interacting fermions as a function of temperature, imbalance, and interaction strength (see Fig. 5-11).

In the BEC limit the imbalanced system is a weakly interacting Bose-Fermi mixture of bosonic dimers and unpaired fermions. This mixture can be described within mean field theory using a Bose-Fermion scattering length a_{bf} to capture the atom-dimer interactions and a Bose-Bose scattering a_{BB} for the dimer-dimer interactions. The value of a_{bf} has been predicted more than fifty years ago in the context of neutron-deuteron scattering to be $a_{bf} = 1.18a$ [94], but has not been experimentally confirmed since then. The Bose-Bose scattering length $a_{bb} = 0.6a$ has been obtained about five years ago [30] and studies in balanced Fermi gases were found to be consistent with this value [95, 96].

As the interactions increase towards unitarity an interesting situation emerges: close to resonance, fermion pairs - that are weakly bound and stable bosonic molecules in isolation - cannot undergo Bose-Einstein condensation if they are imbedded in a Fermi sea of majority atoms at a sufficiently high spin polarization. This is just a consequence of the CC limit that increases from zero in the BCS limit to $\sigma_{c0} \sim 0.4$ at unitarity and eventually reaches 1 at a critical point on the BEC side. In the following we will determine this critical interaction strength.

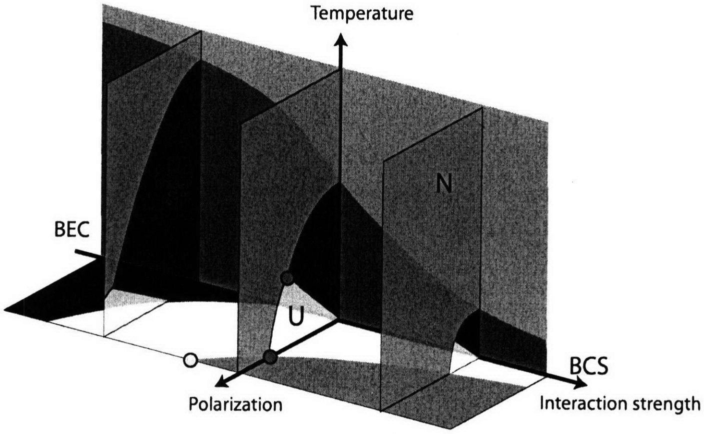

Figure 5-11: Schematic illustration of a three dimensional, homogeneous phase diagram of a strongly interacting Fermi gas with spin imbalance as a function of polarization, temperature and interaction strength. The normal (N, green), superfluid (SF, blue) and unstable (U,white) regions in the phase diagram are color coded. In the previous section we have determined the tricritical point at unitarity (red circle) and the critical spin polarization (blue circle) [21]. The yellow circle marks the critical point on the BEC side, where the normal mixed phase disappears and fermion pairs will start to condensate at T=0 irrespective of the spin polarization of the sample (see section 5.4.1). The phase diagram does not show possible states of exotic superfluids discussed in the text.

In the BCS limit the imbalanced gas will ultimately become normal. There are, however, several suggestions for exotic superfluid phases like the breached pair or Sarma state [97, 98], the Fulde-Ferrel-Larkin-Ovchninikov (FFLO) state [99, 100, 101, 102] or a state with a deformed Fermi surface [103] that can stabilize the superfluid close to the CC limit on the BCS side. So far none of this phases have been observed in ultracold Fermi gases.

5.4.1 The CC limit as a function of interaction strength

Figure 5-12 shows that the CC limit occurs at increasingly high imbalances as the interactions become stronger from the BCS to the BEC side [18, 19, 20]. To precisely determine how the critical imbalance approaches unity on the BEC side we will again take full advantage of spatially reconstructed density profiles which are displayed in Fig. 5-13.

At 834 G we observe the density profiles and spin polarizations as discussed in the previous section. In the center of the cloud ($r < R_c$) is the balanced superfluid, at intermediate radii ($R_c < r < R_\downarrow$) we find the mixed normal region and for $R_\downarrow < r < R_\uparrow$ the minority density is zero. As in the previous experiments the non-interacting wings of the majority cloud for $r > R_\downarrow$ provide an absolute temperature and density calibration. The extend of the mixed normal region (shaded in blue) is largest on the BCS side and decreases with increasing interaction strength and critical spin polarization. It disappears when $R_\downarrow$ becomes

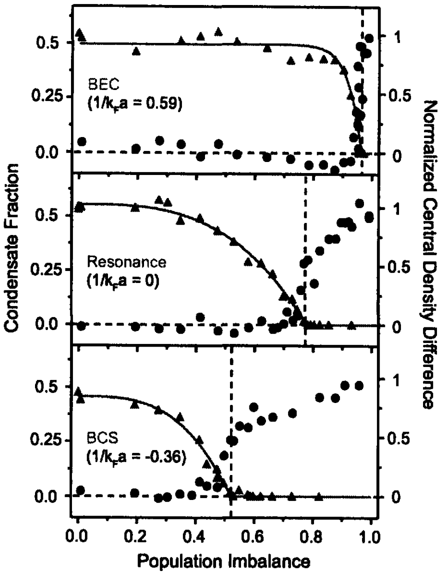

Figure 5-12: CC limit in the crossover determined via the onset of fermion pair condensation and correlated with the central density difference in the cloud. Note that the x-axis refers to the global population imbalance δ_N and not the spin polarization σ. At unitarity the CC limit occurs at $\delta_{Nc} \approx 0.75$ and $\sigma_c \approx 0.4$.

equal to R_c at a critical interaction strength $1/(k_{F\uparrow}a)_c$. For larger interaction strength no mixed normal region exists, implying that all minority atoms are fully paired and that these pairs can undergo Bose-Einstein condensation independently of the spin polarization of the sample. Therefore one may argue that at this point the pairs fulfill the minimum requirement to be called "bosonic" and that the two spin state fermion mixture can now be justifiably called a "Bose-Fermi" mixture, though still strongly affected by interactions.

In the regime where $R_\downarrow$ approaches R_c it becomes increasingly difficult to determine σ_c directly from the density profiles with high precision (see Fig. 5-14 a). Another good measure for the extend of the normal mixed phase is the ratio κ of the chemical potential of the majority component at $R_\downarrow$ and R_c:

$$\kappa = \frac{\mu_\uparrow(R_\downarrow)}{\mu_\uparrow(R_c)} = \frac{R_\uparrow^2 - R_\downarrow^2}{R_\uparrow^2 - R_c^2} \tag{5.13}$$

The smaller the value of κ, the larger is the normal mixed region and κ approaches unity when $R_\downarrow = R_c$. The linear extrapolation of κ to unity yields the critical interactions strength $1/(k_{F,\uparrow}a)_c = 0.71(5)$.

The density profiles of the spin mixture reveal even more details about the system. On the BEC side above the critical interaction strength $1/(k_{F,\uparrow}a)_c$ both the Bose-Bose and Bose-Fermi scattering lengths can be extracted [93]. The observed values of $a_{bf} = 1.23(3)a$

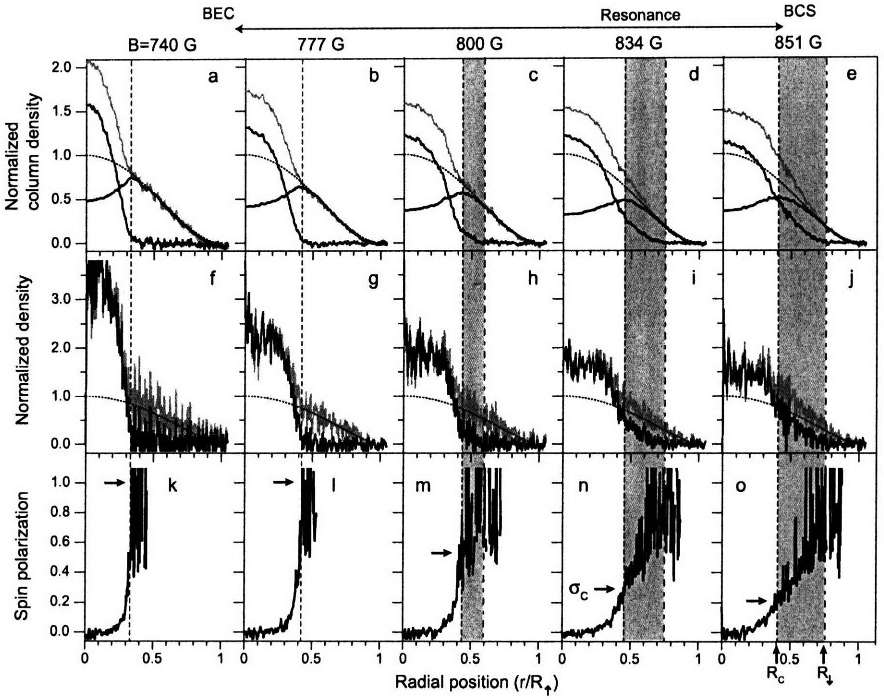

Figure 5-13: Density profiles and spin polarization ($n_{c,\uparrow}$, $n_{c,\downarrow}$, $n_\uparrow$, $n_\downarrow$ σ) of a trapped Fermi mixture as a function of interaction strength (green: majority, blue: minority, black: difference). The black dotted line is a zero-temperature Thomas-Fermi distribution fit to the wings of the majority component ($r > R_\downarrow$). $R_\uparrow$, $R_\downarrow$ (dashed dot lines), and R_c (dashed lines) are the radii of the majority, the minority cloud, and the superfluid core, respectively. The critical polarizations σ_c at the phase boundary $r = R_c$ are indicated by the right arrows. The values for $R_\uparrow$ (in μm), $R_c/R\uparrow$, and $R_\downarrow/R_\uparrow$ were respectively: for (a,f,k), 381, 0.33, 0.33; for (b,g,l), 380, 0.33, 0.33; for (c,h,m), 362, 0.35, 0.59; for (d,i,n), 371, 0.44, 0.72; for (e,j,o), 367, 0.41, 0.76. $T/T_{F0} \leq 0.05$ and $T_{F0} \approx 1.0$ μK.

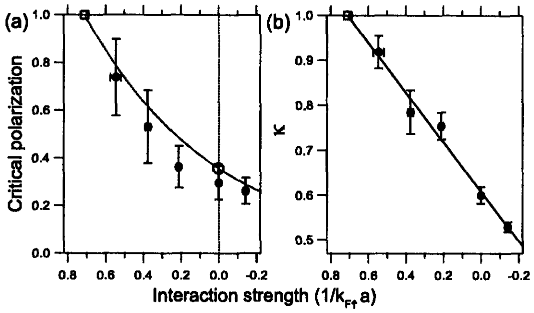

Figure 5-14: Phase diagram of the partially polarized normal phase in the crossover regime. (a) The critical polarization σ_c as a function of the interaction strength $1/k_{F\uparrow}a$ at the phase boundary. (b) κ as a function of the interaction strength. The critical $1/(k_{F\uparrow}a)_c$ for $\sigma_c = 1$ (red square) is found by linear extrapolation of κ to unity. The red solid line is a guide to the eye for the critical line that exponentially connects $(1/(k_{F\uparrow}a)_c = 0.71, \sigma_c = 1)$ and the critical value on resonance $(1/k_{F\uparrow}a = 0, \sigma_{c0} = 0.36)$ (as determined experimentally [21]), indicated by the red open circle.

and $a_{bb} = 0.55(1)a$ are close to the theoretical predictions [94, 30]. The Bose-Bose scattering length actually starts to increase (from its exact value of 0.6) in the vicinity of the critical interaction strength. Interestingly, if beyond mean field effects via the Lee, Huang and Yang (LHY) correction [104] are included in the model [4], the value of a_{bb} remains constant up to $1/(k_{F,\uparrow}a)_c$, implying that mean field theory plus the LHY correction yields a good description even of strongly interacting Bose-Fermi mixtures. With the determination of a_{bf} a prediction made in the context of neutron-deuteron scattering fifty years ago, has now be tested with ultracold atoms. This stresses again the universality of interacting fermion systems and shows the power of the tools provided by atomic physics to study them.

---

[4] The effects of the LHY correction which reduces the compressibility of the Bose gas has previously been observed in strongly interacting Fermi gases via an upshift of the radial compression mode frequency [105].

Chapter 6

Pairing correlations of fermions in the superfluid and the normal phase

In the previous chapters we have discussed the superfluid properties and the phase diagram of strongly interacting Fermi gases with (and without) population imbalance. This has provided us with insights into the properties of the strongly interacting gas on a macroscopic scale. We now proceed to address the underlying physics at a microscopic level by studying the fermion pairs.

Pair formation is the prerequisite for condensation and superfluidity in fermionic superfluids. The fermion pairs play a central role in BEC-BCS crossover [1, 2, 3] and show a very different behavior in both limits with important ramifications for the superfluid systems. In the BEC limit the fermion pairs are tightly bound molecules, small compared to the interparticle spacing and stable in isolation. The molecules start forming around temperatures T^* well above the critical temperature T_c for Bose-Einstein condensation. In the BCS limit the fermion pairs are weakly bound, large compared to the interparticle spacing and unstable in isolation. Here the pairs form only once the system undergoes the superfluid phase transition.

With the realization of a crossover superfluid fermionic pairing can be studied in a new regime. In particular at resonance the high temperature superfluid is expected to show universal behavior with the only relevant energy and length scales given by E_F and $1/k_F$, respectively. The comparison between BEC and BCS limits points to some of the interesting questions about the resonantly interacting pairs: Do pre-formed pairs exist at temperatures $T* > T_c$? What is the pair size compared to the interparticle spacing? Further questions concern imbalanced systems: do fermion pairs also exist at imbalances $\delta > \delta_c$ i.e. in a regime where $T_c = 0$ or is the phase transition as a function of spin polarization associated with "Pauli Pair Breaking" [106, 107, 108]? To summarize these questions we would like to understand where in the phase diagram of fig. 5-9 fermion pairs are present and to investigate their nature. The "tool" employed for these studies is radio-frequency (rf) spectroscopy.

Rf techniques provide access to the hyperfine structure of atoms and are widely used in atomic physics from precision spectroscopy in atomic clocks to evaporative cooling in ultracold atomic gases or as an output coupler for atom lasers [109, 110]. As discussed in chapter 2 signatures of pairing correlations in rf spectroscopy experiments are a characteristic pair dissociation lineshape and shifts of the rf transition line with regard to the bare atomic line. Such interaction shifts are often referred to as "clock shifts" since they are the dominant source of systematic errors for atomic clocks. While being a vice for precise clocks, these shifts are a great feature to study and understand correlations in interacting systems.

In this chapter we will follow the progress made in rf spectroscopy experiments of strongly interacting fermions over the past years and will address a number of the fundamental questions with regard to pairing as we go along. In the course of the experiments we realized, however, that so-called final state interactions severely affected the rf spectra obtained in the standard (1,2) mixture. The results of these experiments have therefore to be interpreted with caution. We then realized a new superfluid spin mixture where final state interactions are negligible. This was decisive for finally being able to easily interpret the observed rf spectra in terms of pair dissociation and to determine the size of the fermion pairs at unitarity. In ongoing experiments imbalanced mixtures were studied enabling the spectroscopic observation of quasiparticles.

6.1 The Innsbruck experiment: A signature of pairing in the crossover

The first rf spectroscopy experiments with ultracold fermions have been carried out at JILA [33] and MIT [7] even before molecules and fermion pair condensation were observed. These experiments demonstrated the effects of attractive and repulsive interactions in the gas by studying mean field shifts. Shortly afterwards the JILA group published rf dissociation spectra of the newly created weakly bound molecules [55].

A first signature of pairing in the many-body regime was observed by the Innsbruck group [22] in 2004. We will discuss the Innsbruck results in some detail to motivate the questions we have addressed in our subsequent experiments. In the Innsbruck experiment the initial state is a (1,2) mixture of ^{6}Li atoms and the rf is tuned around the $|2\rangle$ to $|3\rangle$ transition. The spectra are obtained by monitoring losses in state $|2\rangle$ after the rf is applied.

Let us first consider the rf spectra for weakly interacting molecules on the BEC side of the Feshbach resonance shown in Fig.6-1. At high temperatures (fig.6-1a) only unbound atoms are present and the spectrum shows no shift from the bare atomic transition line (i.e.

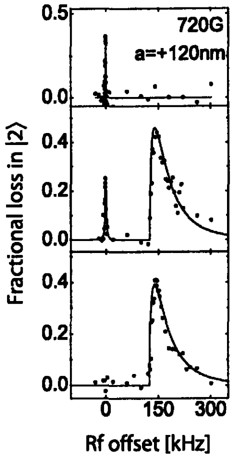

Figure 6-1: Rf spectra on the BEC side of the 834 G Feshbach resonance reported by the Innsbruck group [22]. The three spectra were obtained for different temperatures. At high temperatures no molecules have formed only the "atomic" peal is visible. As the temperature is lowered molecules start forming and a molecular peak emerges. The peak is located at higher radio frequencies due to the additional energy required to break the molecule. At the lowest temperatures all atoms are paired into molecules and the molecular peak is the only remaining feature in the spectrum. The gap between the atomic peak and the onset of the asymmetric molecular peak corresponds to the molecular binding energy. Reprinted from [22].

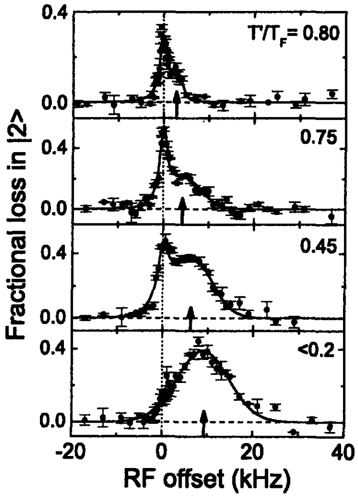

Figure 6-2: Rf spectra close to unitarity at 837 G reported by the Innsbruck group [22]. Again the spectra were obtained at different temperatures and show the emergence of a double peak structure similar the molecular spectra on the BEC side. Note that the pairing peak is fairly symmetric in contrast to the molecular dissociation peak in the spectra of fig 6-1. Reprinted from [22].

the $|2\rangle$ to $|3\rangle$ transition in the absence of atoms in state $|1\rangle$). As the temperature is lowered (1,2) molecules start forming and a second, asymmetric peak emerges in the spectrum at higher frequencies (fig.6-1b). At the lowest temperatures all atoms form molecules and the molecular or "pairing" peak is the only remaining feature in the spectrum (fig.6-1c). The molecular dissociation spectrum spectrum is characterized by the sharp increase of the signal at a threshold value and a slow decay at high energy, the typical features of molecular dissociation spectra that were discussed in chapter 2.

The spectra obtained in the Innsbruck group close to unitarity are shown in figure 6-2. As a function of temperature they display a similar behavior as the molecular spectra in the BEC limit: at high temperatures the system responds at the atomic transitions frequency, as the temperature is lowered a pairing peak emerges and at the lowest temperatures only this peak remains in the spectrum. There are, however, certain differences: the onset of the pairing peak occurs at the frequencies of the atomic transition and the pairing peak appears to be fairly symmetric. Furthermore the shift of the rf peak at unitarity was found to be proportional to the Fermi energy.

The emergence of a double-peak structure in the rf spectra and the shifted spectral response at the lowest temperature made a strong case for the formation of fermion pairs at unitarity. The Innsbruck rf spectra were also regarded as a key indication for superfluidity in the strongly interacting regime (before superfluidity was established via the observation of vortex lattices [4] about a year later).

We were motivated to revisit rf spectroscopy of strongly interacting fermions in part by questions the Innsbruck experiment had left open and also by new questions that emerged from the creation of imbalanced mixtures:

- *Rf spectroscopy, pair formation and the superfluid phase transition.* Since no signature for the superfluid phase transition was observed in the experiment [22] the connection between the observed rf spectra, pair formation and superfluidity remained unclear.
  - Do the rf spectra indicate the normal to superfluid phase transition?
  - Do pre-formed pairs exist in the normal phase above T_c?
- *Effects of the trapping geometry.* At unitarity fermion pairs form due to many body interactions and consequently the response of the system to the rf pulse is density dependent. Since the experiments are carried out in a harmonic trapping geometry the observed spectra show the response averaged over the density distribution of trapped cloud.
  - In the BEC limit molecules and unbound atoms coexist locally. Is the double peak structure at unitarity an artifact of the trapping geometry or does it imply the local coexistence of fermion pairs and unbound atoms?

  - Does inhomogeneous broadening prevent a clear observation of a gap between the atomic line and the onset of the pairing peak?

- *Effect of final state interactions and interpretation of the spectral lineshape.* The early MIT experiment [7] demonstrated the absence of mean field shifts in the (1,2) mixture at magnetic fields beyond 700 G and temperatures on the order of T_F. This was attributed to the fact that all interactions between atoms in states $|1\rangle$, $|2\rangle$, and $|3\rangle$ are simultaneously unitarity limited[1]. However, this also implies strong interactions in the final state which any detailed interpretation of the spectra needs to take into account.
  - The pairing peak at unitarity is fairly symmetric in contrast to the pair dissociation spectra expected in the BEC and BCS limits. Is this a consequence of final state interactions?

- *Pairing correlations at imbalances above the CC-limit* The CC-limit is also referred to as the "Pauli pair breaking" limit [106, 107, 108].
  - Is the CC limit associated with pair dissociation?
  - Does rf spectroscopy reveal the normal to superfluid phase transition as a function of imbalance at very low temperatures?

- *Majority versus minority spectra* The correlation between the spectra of minority and majority components can give important information about the nature of the pairs.
  - Are the pair dissociation spectra of minority and majority component the same or are they different? How does this depend on the phase of the system?
  - Will the majority spectrum show "local" double peaks i.e. two peaks at a given density? In other words can rf spectroscopy distinguish between paired and unpaired majority atoms at a finite spin polarization?

This collection of questions indicates that the research in this area both experimentally and theoretically is a major frontier. Issues as fundamental as what should be called a "pair" in the many-body regime are still under debate. In the following we will describe our experiments that were designed to address some of these questions.

The two experiments we will discuss first [23, 20] have been carried out in the standard (1,2) mixture of ^{6}Li as was the Innsbruck experiment. However, as already mentioned above we have demonstrated in later studies [111] that final state interactions severely affected all rf spectra obtained from this mixture in the strongly interacting regime [22, 23, 24]. Since the experiments in the (1,2) mixture have motivated the later experiments we will

---

[1] The exact range of magnetic fields where the interactions are unitarity limited depends on the densities involved. For the typical densities in the center of the trapped gas at 834 G $1/k_F a_{ij} \leq 1$ where ij refers to state $|i\rangle$ and $|j\rangle$.

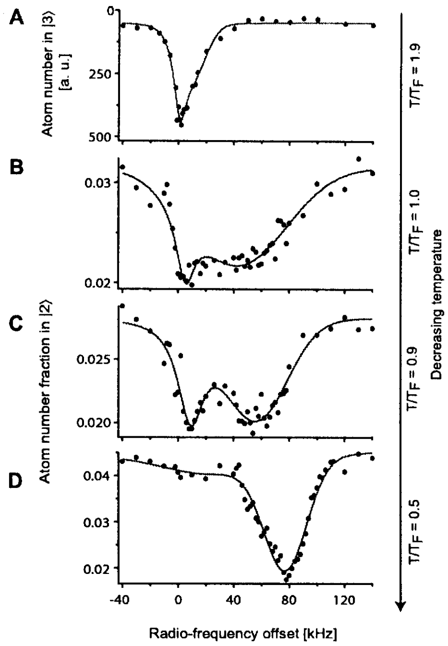

Figure 6-3: Rf spectra of the minority component in a highly imbalanced superfluid ($\delta_N \sim 0.9$), well above CC limit of superfluidity. As the temperature is lowered a "pairing peak" develops in the absence of superfluidity. Note that in most cases losses in state $|2\rangle$ were monitored as a function of the rf. The rf spectra therefore show dips where the response of the system is strongest. In the Innsbruck experiment a different normalization was chosen and the strongest response appears as a peak. The spectra were taken for the following parameters: A) $\delta = 0.87$, $E_F = h \times 260$ kHz, $T/T_F = 1.9$; B) $\delta = 0.94$, $E_F = h \times 360$ kHz, $T/T_F = 1.0$; C) $\delta = 0.94$, $E_F = h \times 360$ kHz, $T/T_F = 0.9$; D) $\delta = 0.93$, $E_F = h \times 340$ kHz, $T/T_F = 0.5$.

nevertheless discuss them in some detail. But the reader should be cautioned up front that any quantitative interpretation of the rf spectra obtained in the (1,2) mixture close to unitarity is difficult.

6.2 Rf spectroscopy and the superfluid phase transition

To study the relation between the signature of pairing in the rf spectra (in the (1,2) mixture) and the superfluid phase transition we set out to

- Obtain rf spectra in the normal phase of an imbalanced gas above the CC limit.
- Correlate the rf spectra at lower imbalances with the onset of superfluidity via the observation of fermion pair condensation as a function of temperature and imbalance

These experiments probe for the presence of pre-formed pairs at temperatures $T > T_c > 0$, as well as pairing correlations in a regime where $T_c = 0$ (at imbalances above δ_c). The experiments were carried out by preparing imbalanced Fermi gases at unitarity (833 G) and applying the rf to the *minority* component [23].

Minority rf spectra for four different temperatures at an imbalance of $\delta_N \sim 0.9$, i.e. well above the CC-limit, are displayed in Fig. 6-3. The spectra exhibit the same behavior as the ones obtained for an equal mixture in the Innsbruck experiment (fig. 6-2): As the temperature is lowered a shifted pairing peak emerges in the rf spectrum. Based on the assumptions made in the interpretation of the Innsbruck data this demonstrates the formation of fermion pairs in a regime where pairing is not a precursor to superfluidity at lower temperatures. Furthermore the experiment shows that the emergence of a pairing peak in the rf spectrum at unitarity is not necessarily related to superfluidity but yet another consequence of the strong interactions in the normal phase.

To correlate the rf spectra with the onset of superfluidity we repeated the experiments for smaller imbalances where the superfluid phase transition can be observed both as a function of temperature and population imbalance. The corresponding rf spectra are given in Fig. 6-4. Already above T_c as well as above $\delta_{N,c}$ the spectra show full pairing in the normal phase and there is now indication for the onset of superfluidity within the experimental resolution. The spectra demonstrate the presence of pre-formed pairs above T_c i.e. a $T^* > T_c$ as well as pairing above the critical population imbalance $\delta_{N,c}$ where $T_c = 0$.

These conclusions have to be scrutinized again in the light of the more recent experiments which are not subject to strong final state interactions and will be discussed below. Important questions concern a more detailed understanding of the signature of "pairs" in the rf spectrum versus other forms of "pairing". In this context it will be important to study the majority rf spectra both in the polarized superfluid and in the normal phase. This will allow us to spectroscopically distinguish unbound majority atoms (which are quasiparticles in the superfluid phase) from paired majority atoms.

It has been suggested that a single minority atom embedded in a Fermi sea of majority atoms with resonant interactions, can be described as a "polaron" [86, 71, 87] with an interaction energy on the order of $-0.6E_F$. This implies that somewhere in the phase diagram "pairs" turn into "polarons" for increasing imbalance. A spectroscopic signature of this change in the nature of the pairs might help a to improve our understanding of the relation between pairing and superfluidity.

These ideas show that it may be possible to observe a signature of the superfluid phase transition in the rf spectra. An experiment to observe such a signature must likely be performed at temperatures well below the tricritical point. This is the regime where the phase transition is first order and the minority component shows a sizable jump in density at the phase boundary. Reaching these temperatures consistently in the several hundred subsequent runs of the experiment required to obtain a high resolution rf spectrum will, however, pose a considerable challenge.

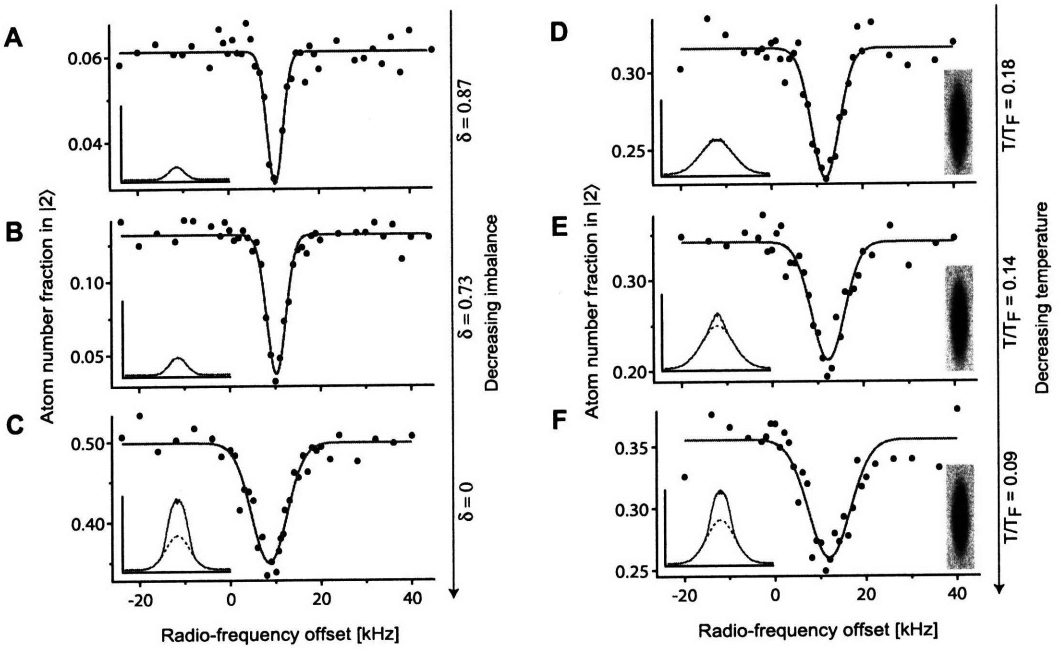

Figure 6-4: RF spectra of the minority component obtained while crossing the phase transition by reducing either the population imbalance (**A**–**C**) or temperature (**D**–**F**). The rf spectra do not reveal the phase transition within the experimental resolution. The onset of superfluidity is indirectly observed by fermion pair condensation. The spectra were taken for the following parameters **A**–**C**: A) $\delta_N = 0.87$, $E_F = h \times 27$ kHz, $T/T_F = 0.08$; B) $\delta_N = 0.73$, $E_F = h \times 27$ kHz, $T/T_F = 0.10$; C) $\delta_N = 0.00$, $E_F = h \times 23$ kHz, $T'/T_F = 0.10$. **D**–**F**: D) $\delta_N = 0.37$, $E_F = h \times 38$ kHz, $T/T_F = 0.18$; E) $\delta_N = 0.32$, $E_F = h \times 38$ kHz, $T/T_F = 0.14$; F) $\delta_N = 0.29$, $E_F = h \times 35$ kHz, $T/T_F = 0.09$.

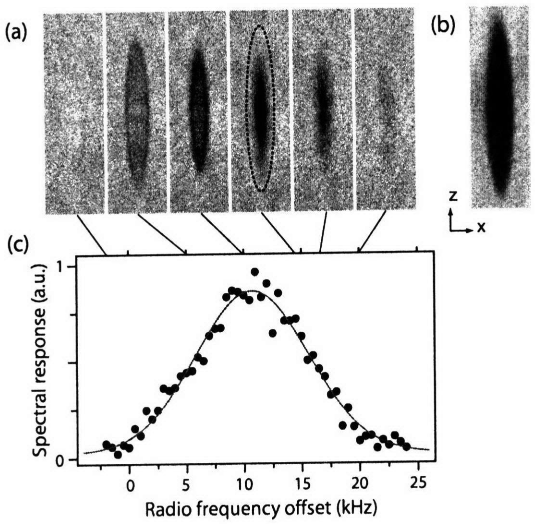

Figure 6-5: Spatially resolved rf spectroscopy in an equal (1,2) mixture at unitarity. The rf is resonant with the $|2\rangle$ to $|3\rangle$ transition thus creating a local "imbalance" in the (1,2) mixture which can be precisely detected *in situ* with the phase contrast imaging technique described in chapter 3. a) Response of the cloud to different radio frequencies: the lower density wings become excited at smaller frequencies than the high density parts in the center of the cloud. b) Absorption image of an equal mixture without rf excitation indicating the size of the cloud (see also the dashed line in a). c) Inhomogeneous rf spectrum obtained by integrating the response in the phase contrast images.

6.3 Spatially resolved rf spectroscopy

The rf spectra obtained in the previous section suffered from the problem that they were not "spatially resolved" i.e. they sampled the response of the minority atoms across the varying density of the majority component. On may argue that at high population imbalances this should not be such a serious problem as the density of the majority atoms changes only very little across the small minority cloud. In general, however, a quantitative comparison between the rf spectra and theory is straightforward only if one can spatially resolve where in the trap atoms are transferred as a function of the applied rf frequency. This is especially important if the trapped gas is in different (superfluid/normal) phases depending on the local densities in the trap.

We have been able to spatially resolve the response of an equal, superfluid mixture as a function of the applied rf (see Fig. 6-5) [24]. After 3D image reconstruction one obtains the rf signal at a given density of the system. In Fig. 6-6 the inhomogeneous signal and the response at the center of the trapped cloud are compared. The homogenous spectrum shows a clear gap from the zero offset and contributes only to the the high frequency part of the inhomogenous spectrum.

The two rf spectroscopy experiments we have discussed in this and the preceding sec-

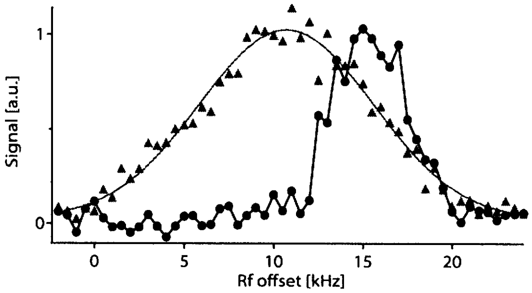

Figure 6-6: Homogenous rf spectrum from the center of the trapped cloud (black circles) and the inhomogenous spectrum from the integrated response (red triangles). The spectra are normalized to the same maximum amplitude. Compared to the inhomogenous spectrum, the central spectrum shows a reduction in width by about a factor of two and a clear gap with regard to the zero frequency offset.

tion [23, 24], have renewed theoretical interest in the interpretation of the rf spectra and their relation to fermionic pairing in the normal and superfluid phases. Final state interactions have been explicitly considered in references [112, 113, 114, 115] and rf spectroscopy in imbalanced mixtures in references [112, 116, 117, ?, 118, 119, 120].

6.4 Final state interactions and new superfluid spin mixtures

The potentially dramatic effect of final state interactions on the rf spectra obtained in the (1,2) mixture becomes apparent when one compares the observed spatially resolved spectrum with the theoretical expectations for both the BEC and BCS limits (see Fig. 6-7). While the calculated rf spectra in both limits show a lineshape typical for pair dissociation spectra, the experimentally obtained spectrum at unitarity does not: it is symmetric and narrow. Since the physics in the BEC-BCS crossover is expected to evolve smoothly from one limit to the other this is a surprising observation. Furthermore the properties of the initial state at unitarity should be universal and therefore independent of the specific system used in the experiment. Final state interactions, however, are non-universal and could very well cause this unexpected behavior.

Final state interactions arise when atoms transferred from state $|b\rangle$ (in an initial (a,b) mixture) to a third state $|c\rangle$ interact with atoms in the initial state. In rf spectroscopy experiments with fermionic atoms only interactions of atoms in state $|c\rangle$ with atoms in state $|a\rangle$ can contribute [7, 32]. A conceptually very simple and dramatic effect of final state interactions arises when (using a molecular picture for simplicity) the rf does not dissociate an (a,b) molecule but transfers it to another (a,c) molecule. If the wave function of the (a,b) and (a,c) molecules are very similar, the Franck-Condon overlap for such a transition is very high and pair dissociation is suppressed. The lineshape of such "bound-

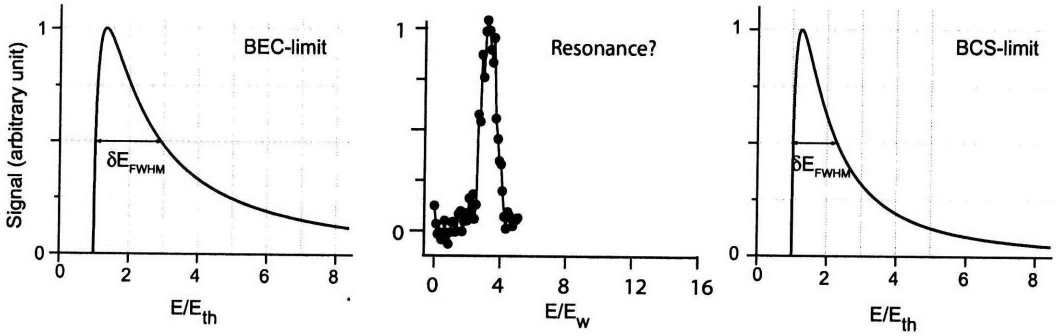

Figure 6-7: The problem: the rf spectrum of the (1,2) mixture at resonance is symmetric and narrow, while the spectra expected in both the BEC and BCS limits show a highly asymmetric pair dissociation lineshape. The frequency axis of the experimental spectrum has been scaled by the full width at half maximum since the spectral onset can be subject to shifts due to Hartree terms (see also section 6.5).

Mixture	B_0[G]	Rf transition	$a_f[a_0]$
(1,2)	834	$\|2\rangle \rightarrow \|3\rangle$	$a_{13} \approx -3300$
(2,3)	811	$\|2\rangle \rightarrow \|1\rangle$	$a_{13} \approx -3560$
(1,3)	691	$\|1\rangle \rightarrow \|2\rangle$	$a_{23} \approx +1140$
(1,3)	691	$\|3\rangle \rightarrow \|2\rangle$	$a_{12} \approx +1450$

Table 6.1: Final state scattering lengths for magnetic field insensitive rf transitions at unitarity for the (1,2), (2,3) and (1,3) mixtures. For a typical value of $k_F \approx 3000a_0$ in our experiments the final state for the (1,2) and (2,3) mixtures is strongly interacting. This is not the case for the (1,3) mixture where the two possible final scattering lengths are more than a factor of two smaller and positive. This mixture is therefore an ideal candidate for rf spectroscopy experiments.

bound" transition is symmetric and narrow in contrast to the asymmetric lineshape for pair dissociation or "bound-free" transitions.

6.4.1 Effect of final state interactions

In principle there are several ways to change the final state interactions without affecting the initial state. At unitarity the final state interaction strength can be reduced by lowering the density and therefore $k_F a_f$, while the initial state remains resonantly interacting ($1/k_F a_i \approx 0$). Decreasing the density by a large factor while maintaining the same low temperature T/T_F is, however, experimentally difficult. Alternatively one might attempt to spectroscopically access a different final state. However, the induced transition must be magnetic field insensitive to obtain the required spectral resolution in the kHz regime. The (1,2) mixture in ^{6}Li does not provide other rf transitions that fulfill this requirement. Instead we created resonantly interacting superfluids in new combinations of initial hyperfine states: (1,3) and (2,3) by utilizing the broad Feshbach exhibited by these mixtures at 691

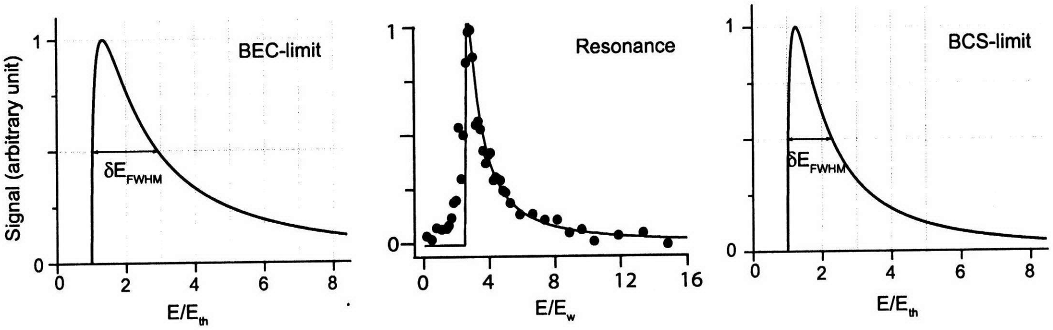

Figure 6-8: The solution: Rf spectroscopy of the (1,3) superfluid at unitarity. With negligible final state effects the rf spectrum displays the expected asymmetric lineshape. The frequency axis of the experimental spectrum has been scaled by the full width at half maximum since the spectral onset can be subject to shifts due to Hartree terms (see also section 6.5).

G and 811 G respectively. Table 6.1 summarizes the location of the Feshbach resonances together with the allowed magnetic field insensitive rf transitions and final state scattering lengths. Details about the experimental realization of these mixtures and related information are given in chapter 3. The comparison of the final state scattering lengths between the three mixtures clearly shows that the (1,3) mixture is the ideal candidate for rf spectroscopy experiments. Indeed, the rf spectra obtained with a (1,3) mixture at unitarity show the typical pair dissociation lineshape one would expect from a simple crossover picture (see Fig. 6-8).

A direct comparison between the rf spectra obtained at unitarity in the (1,2) and the (1,3) mixture reveals the dramatic effect of finite state interactions which suppress the asymmetric "tails" of the (1,2) rf spectrum and shift the spectral peak. We will discuss possible explanations for the strong effects of these interactions on the rf spectra in the context of further experiments later in this chapter.

6.4.2 (1,3) spectroscopy: $|1\rangle$ to $|2\rangle$ versus $|3\rangle$ to $|2\rangle$ transition.

As has been indicated in table 6.1 the (1,3) mixture has two magnetic field insensitive rf transitions, associated with positive final state scattering lengths (that differ by about 30%). Fig. 6-10 shows the rf spectra at unitarity for these two transitions. Apart from the asymmetric "bound-free" transition to higher energies all spectra show a second "bound-bound" transition from fermion pairs in the initial state to more deeply bound (1,2) or (2,3) molecules for the $|3\rangle$ to $|2\rangle$ and $|1\rangle$ to $|2\rangle$ transitions respectively. Note that the bound-free spectra are very similar for both $|3\rangle$ to $|2\rangle$ and $|1\rangle$ to $|2\rangle$ transitions. The bound-bound spectra, however, show different shifts indicating that the final (2,3) molecule is more strongly bound than the (1,2) molecule. This is a consequence of the smaller width of the

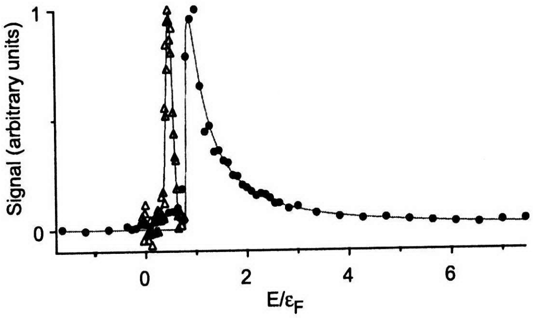

Figure 6-9: Dramatic effect of final state interactions: direct comparison of spatially resolved rf spectra obtained at unitarity from the (1,2) mixture (open triangles) [24] and from the (1,3) mixture (solid circles). The frequency axis is normalized by the local Fermi energies. While the (1,3) spectrum shows the expected asymmetric lineshape, the (1,2) spectrum is symmetric, narrow, and shifted to lower energies. All spectra in the strongly interacting regime reported in references [22, 23, 24] were subject to these significant distortions.

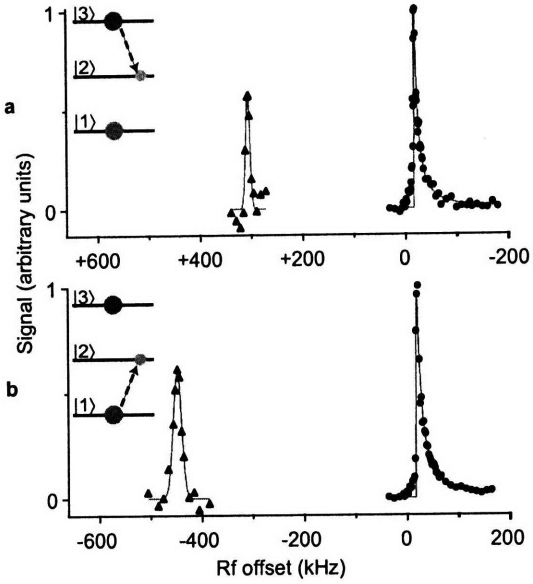

Figure 6-10: Spectroscopy on the two magnetic field insensitive rf transitions in the (1,3) mixture at unitarity. The insets in (a) and (b) schematically indicate the two rf transitions employed in the experiment. Since state $|3\rangle$ has a higher energy than state $|2\rangle$, the dissociation energy for the $|3\rangle$ to $|2\rangle$ transition is always less than the transition frequency for the atomic resonance E_0/h and therefore the $|3\rangle$ to $|2\rangle$ dissociation spectra appear at negative energies compared to E_0.

(2,3) Feshbach resonance at 811 G [44] compared to the width of the (1,2) resonance at 834 G (see Tab. 3.1 and Fig. 3-4).

The spectra also show directly that final state interactions can only weakly affect the dissociation spectrum: the distance between the bound-bound and bound-free transitions in the spectra is large compared to the linewidth of the dissociation spectrum. As discussed in detail in ref. [111] this implies that the Franck-Condon overlap between the (1,3) pair in the initial and the (1,2) or (3,2) pairs in final state is small and the bound-bound transition does not have a significant spectral weight [121, 115].

Rf spectra obtained from the (1,3) mixture are therefore the ideal starting point for experiments to probe the microscopic structure of the superfluid fermion pairs. Using the (1,3) mixture we can go ahead and record spatially resolved rf dissociation spectra (like the ones shown in Fig. 6-10) that can be directly compared to theory.

6.5 Determination of the fermion pair size in a resonantly interacting superfluid

The fermion pair size at unitarity (measured in units of $1/k_F$) is one of the fundamental, non-trivial and universal parameters characterizing the superfluid system. In contrast to other important universal parameters at unitarity like the critical temperature T_c/T_F, the Clogston limit of superfluidity δ_c, or the ratio of μ/E_F - which are more closely related to the macroscopic properties of the superfluid gas - the pair size directly describes its microscopic "building blocks".

Interestingly, small fermion pair sizes have been linked to high critical temperatures by the Uemura plot for a wide class of fermionic superfluids [122]. Since the critical temperature T_c/T_F in a balanced, resonantly interacting Fermi gas is an order of magnitude larger than for any other known fermionic superfluid (including high-temperature superconductors), it is of fundamental interest to determine the fermion pair size in this new system and to compare it to the pair size in other fermionic superfluids.

In the following we will show that both the width and the onset of the rf dissociation spectrum are directly and simply related to pair size in the entire BEC-BCS crossover. We have discussed rf spectroscopy and the rf lineshape in chapter 2 and we will repeatedly refer to these results in the discussion below.

6.5.1 Fermion pair size and rf spectroscopy

A characteristic size of the fermion pairs in the crossover can be defined via the two-particle correlation length ξ_{pair} given by:

$$\xi_{pair} = \sqrt{\frac{\langle\phi|r^2|\phi\rangle}{\langle\phi|\phi\rangle}} \tag{6.1}$$

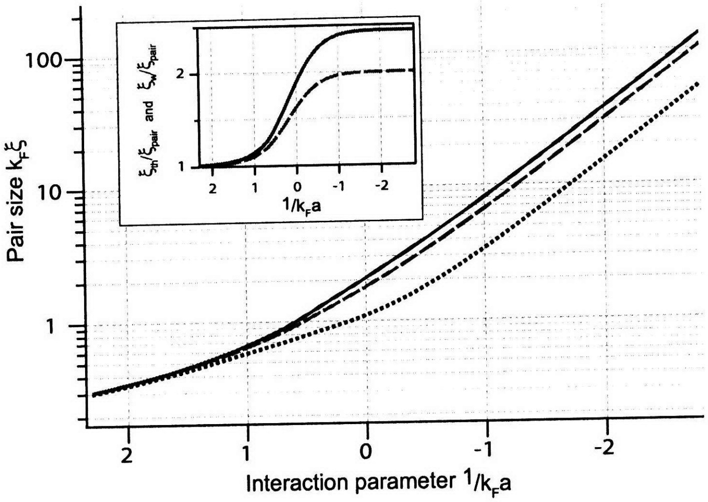

Figure 6-11: Evolution of the fermion pair size in the BEC-BCS crossover [123, 124, 31, 28]. ξ_w (solid blue), ξ_{th} (dashed red) and ξ_{pair} (dotted black) are displayed as a function of the interaction parameter $1/k_Fa$. The inset shows the ratios ξ_w/ξ_{pair} (solid blue) and ξ_{th}/ξ_{pair} (dashed red).

where ϕ is the pair wavefunction.

The weakly interacting molecules in the BEC limit are described by a wavefunction $\phi_m(r)$ proportional to $e^{-r/b}/r$, and have a binding binding energy $E_b = \hbar^2/mb^2$ [28]. For ϕ_m equation 6.1 yields a pair size of $\xi_{pair} = b/\sqrt{2}$. Both the onset energy E_{th} and the full width at half maximum E_w of the rf spectrum (see chapter 2) are proportional to E_b and we find $E_b = E_{th} \approx 1.89 \times E_w \propto 1/b^2$. The pair size can therefore be directly obtained both from the width and the onset of the rf spectrum as:

$$\xi_{th}^2 = \frac{\hbar^2}{2mE_{th}} \tag{6.2}$$

$$\xi_w^2 = \gamma \times \frac{\hbar^2}{2mE_w} \tag{6.3}$$

where we choose $\gamma = 1.89$ so that $\xi_{pair} = \xi_{th} = \xi_w$ in the BEC limit.

In the BCS limit $E_{th} = \frac{\Delta^2}{2E_F}$ which is the binding or condensation energy of the N/2 pairs in the superfluid. The fermion pair size is related to E_{th} and E_w via $E_w \approx 1.27 \times E_{th} = 1.27 \times \frac{\Delta^2}{2E_F} \propto 1/\xi_c^2$ where $\xi_c = \frac{\hbar^2 k_F}{\pi m \Delta}$ is the Pippard coherence length which is often associated with the fermion pair size[2]. We find $\xi_{th} = 2\xi_{pair}$ and $\xi_w \approx 2.44 \times \xi_{pair}$. So up to factors on the order of unity E_{th} and E_w are directly related to the fermion pair size both in the BEC and BCS limits. Figure 6-11 displays ξ_{th}, ξ_w and ξ_{pair} as a function of interaction strength.

---

[2] The value of ξ_{pair} depends on the choice of the pair wavefunction ϕ; Here we chose ϕ_P and then $\xi_{pair} = \pi/(2\sqrt{2})\xi_c$.

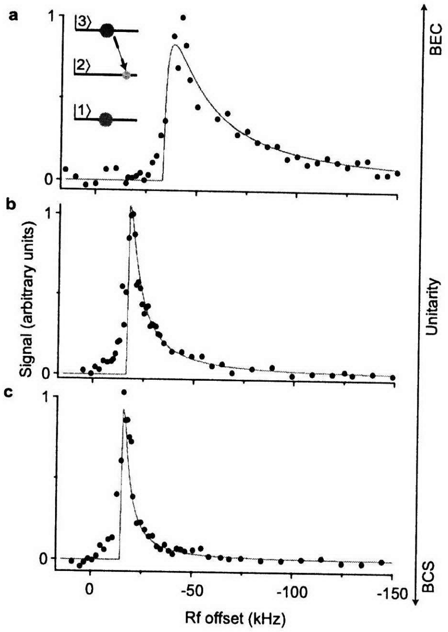

Figure 6-12: Rf dissociation spectra in the crossover. Below, at and above resonance the spectrum shows the typical asymmetric lineshape of a pair dissociation spectrum. The signal is proportional to the three dimensional local response at the center of the cloud. **(a)** 670 G (BEC side), $\epsilon_F = h \times 24$ kHz, $T/T_F \approx 0.2$, $1/k_F a_i = 0.4$; **(b)** 691 G (resonance), $\epsilon_F = h \times 21$ kHz, T/T_F=0.1, $1/k_F a_i \sim 0$; **(c)** 710 G (BCS side), $\epsilon_F = h \times 20$ kHz, T/T_F=0.1, $1/k_F a_i = -0.3$.

Although ξ_{pair} changes by orders of magnitude from the BEC to the BCS limit ξ_{th} and ξ_w show the same behavior and deviate from each other by not more than 22%. This illustrates that the pair size can be reliably determined from the rf dissociation spectrum throughout the whole BEC-BCS crossover.

Figure 6-12 shows the rf dissociation spectra obtained in the BEC-BCS crossover with the (1,3) superfluid. Three dimensional image reconstruction was applied to obtain the local spectrum at the center of the cloud. As expected, both E_{th} and E_w decrease with decreasing interaction strength $1/k_F a_i$. In chapter 2 we have seen that the rf lineshape is expected to show only small changes in the crossover regime. Indeed, when the frequency axes for the spectra in Fig. 6-12 are scaled by E_{th} and the spectra are shifted to show the same onset all spectra overlap as shown in Fig. 6-13. This confirms experimentally the "universal" lineshape of the rf dissociation spectrum. The fit to the spectra in Fig. 6-12 used the simple dissociation lineshape I_{generic}.

As discussed above the pair size can in principle be obtained from both E_{th} and E_w. However, since the whole spectrum may be subject to shifts from Hartree terms [33, 7], we focus in the following only on the width of the spectrum. At unitarity we determine the full

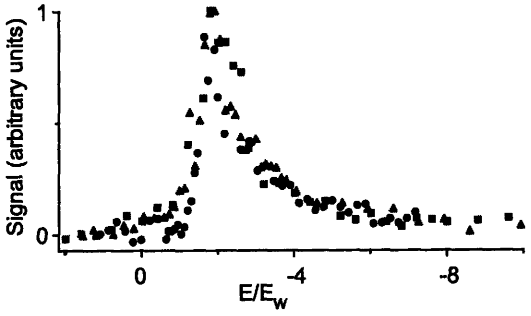

Figure 6-13: Universal rf lineshape in the crossover. Same spectra as in Fig. 6-12 but with the frequency axis scaled by the threshold energy E_{th} and shifted so that the spectral onsets overlaps with the BEC side spectrum. BEC side: black circles; Resonance: red triangles; BCS side: blue squares.

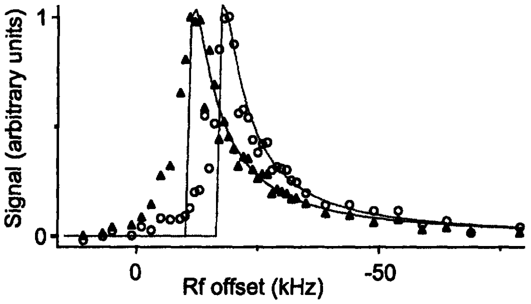

Figure 6-14: Density effects at unitarity for the (1,3) mixture at 691 G. The figure shows the spectral response in the center (open circles, same spectrum as in Fig. 6-12b) as well as the lower density wings (filled triangles) of the cloud. In this regime the cloud might have turned normal.

width at half maximum to be $E_w = 0.36(6)\epsilon_F$ corresponding to a spectroscopic pair size of $\xi_w = 2.3(2)/k_F$. Here ϵ_F is the local Fermi energy and $k_F = \sqrt{2m\epsilon_F}/\hbar$. The fermion pairs are smaller than the interparticle spacing given by $l = n^{1/3} = (3\pi^2)^{1/3}/k_F \sim 3.1/k_F$ (n is the total density) and are in units of $1/k_F$ the smallest observed in fermionic superfluids. In high-temperature superconductors the pair size ξ at optimal doping is in the range of 5 to $10/k_F$ [122]. The high temperature superfluid therefore confirms the relation between small pair size and high transitions temperatures found in many fermionic superfluids.

The strong narrowing of the spectrum in Fig. 6-12 (a) to (c) demonstrates that the fermion pair size increases from strong to weak coupling. The decreasing width corresponds to a twofold increase in the spectroscopic pair size from $\xi_w = 1.4(1)/k_F$ at 670 G to $\xi_w = 2.8(3)/k_F$ at 710 G where the extent of the pairs becomes comparable to the interparticle spacing. A change of the absolute pair size with density at unitarity can in principle be observed by comparing the spectral width in the center and the outer region of the cloud.

As the density decreases the spectrum shifts to lower energies (see Fig. 6-14). However, the spectral onset also becomes increasingly softer and the asymmetry of the pair dissociation peak less pronounced, possibly due to atomic diffusion during the excitation pulse. This prevents a reliable determination of the pair size in the spatial wings where the density is changing rapidly and the system may already be in the normal phase.

We have shown here that the (1,3) rf spectra contain detailed information about the microscopic properties of the fermion pairs at unitarity and in the crossover. In future experiments the microscopic structure of the pairs can now be studied both in the superfluid and normal phase as a function of interaction strength, temperature and spin imbalance. In the next section we will discuss rf spectra of the majority and minority component in an imbalanced Fermi gas at unitarity.

6.6 Observation of quasiparticles in a polarized superfluid

In section 6.2 we discussed the first rf spectroscopy experiment with imbalanced mixtures reported in [23]. The experiment was carried out in the (1,2) mixture and without spatial resolution. The spectra were therefore subject to strong final state effects and only rf spectra of the minority component could be obtained at a satisfactory signal to noise ratio.

At this point, however, we are in the position to take full advantage of rf spectroscopy in the (1,3) mixture [111], spatially resolved techniques [24] and our knowledge of the phase diagram for imbalanced mixtures [21]. By spectroscopically probing both the majority and the minority components it is also possible to directly correlate the spectral response of majority and minority atoms. Note, that the (1,3) mixture permits two rf transitions (from $|1\rangle$ to $|2\rangle$ and from $|3\rangle$ to $|2\rangle$, see figure 6-10) so that majority and minority spectra can be obtained from identically prepared samples.

The data obtained in this experiment are very rich and we will only provide a small "taste" of what the full analysis may yield [125]. Figure 6-15 shows three majority and minority spectra obtained at a temperature of about 0.05 T/T_F for three different spin polarizations as indicated in the phase diagram. The most impressive feature is the clear double peak structure in the *majority* cloud observed for intermediate imbalances in the vicinity of the first order normal to superfluid phase transition (Fig. 6-15 b). The spectral peak at high frequencies overlaps with the pair dissociation peak of the minority spectrum. At the second, lower frequency peak in the majority spectrum the minority component shows no spectral response. This feature in the spectrum is therefore due to unbound majority atoms, i.e. thermally excited quasiparticles.

This "double peak structure" is the first direct signature of quasiparticles in superfluid Fermi gases. The observation of quasiparticles is facilitated in imbalanced systems since the imbalance helps to "inject" a significant population of quasiparticles into the superfluid at low temperatures. While double peak structures have also been found in previous rf

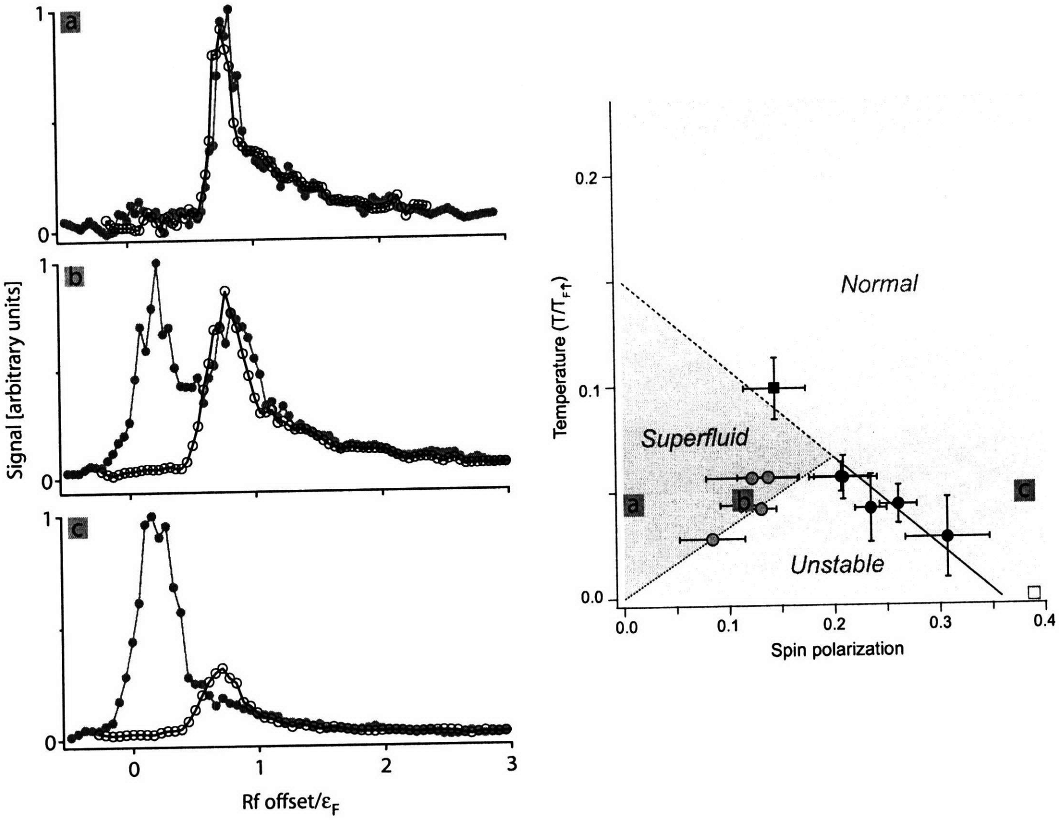

Figure 6-15: Quasiparticle peak in the rf spectrum of the majority component of an imbalanced mixture at unitarity. The majority (filled red circles) and minority (open black circles) rf spectra were obtained for three sets of parameters as indicated in the phase diagram. (a) In the balanced case both components show the rf dissociation spectra discussed in previous sections. (b) At higher spin polarizations, in the vicinity of the first order normal to superfluid phase transition, the majority spectrum has two peaks. The asymmetric pair dissociation peak at higher frequencies overlaps with the corresponding peak in the minority spectrum. The second peak at lower frequencies has no counterpart in the minority cloud and stems from "unbound" majority atoms, i.e. thermally exited quasiparticles. (c) At high imbalances above the CC limit of superfluidity the majority spectrum is dominated by the peak close to zero offset, but it shares the asymmetric high-frequency "tail" with the minority component. Importantly, the peak of the minority atoms now has contributions that exceed the signal in the majority component at the same rf frequencies, possibly indicating a state where the pairing correlations become more polaron like. The frequency axis of the rf spectra is normalized by the local Fermi energy ϵ_F.

spectroscopy experiments (see figures 6-2, 6-3 and references [22, 23]), these rf spectra were not spatially resolved and the two peaks may have originated from different locations inside the trap. In this experiment, however, the double peaks imply the *local* coexistence of pairs and quasiparticles.

Surprisingly, the quasiparticle peak appears on the same, positive side of the frequency axis as the pair dissociation peak. By removing a quasiparticle from the superfluid, energy is gained and therefore one would expect the quasiparticle peak to be located at negative frequencies. However, this description does not take Hartree terms in both the initial and final states into account, which can lead to shifts of the spectrum relative to the zero frequency offset.

At the imbalances considered so far, the pair dissociation peak of minority and majority components overlap. This changes at higher imbalances: in Fig. 6-15 c) we observe that at frequencies close to the peak in the minority cloud, the majority atoms shows a significantly weaker response. The majority spectrum is dominated by a peak close to zero frequency and only at high frequencies, in the small, asymmetric wings of the spectrum, the signal from both majority and minority components are well overlapped. The fact that the spectral weight in the minority peak is not anymore "balanced" by the spectral weight of the majority spectrum at the same frequencies could indicate the development of a more "polaronic" type of pairing.

A more detailed analysis of the data will show whether the rf spectra reveal a signature of the normal to superfluid phase transition and may also yield a better characterization of the "pair" to "polaron" transition.

6.7 Final state interactions revisited

The advances reported in the previous two sections could not have been obtained with rf spectra from the (1,2) mixture due to the dramatic effects caused by final state interactions. In this section we will try to better understand why these interactions had such a significant impact.

Figure 6-16 displays three rf spectra from the Innsbruck group taken on the BEC side of the (1,2) Feshbach resonance at 661, 695 and 764 G [121]. At 661 G the spectrum is dominated by a "bound-bound" peak from (1,2) to (1,3) molecules due to a high Franck-Condon overlap between these molecular states. The second spectrum was obtained at 695 G just on the BCS side of the (1,3) resonance. Here the final state is strongly interacting but no final bound molecular state is accessible. Accordingly the rf transition is predominantly bound-free, i.e. the (1,2) pair is dissociated by the rf pulse. Compared to regular dissociation spectra the lineshape shows modifications owing to the strongly interacting final state. As the (1,2) resonance is approached for higher magnetic fields $|a_f|$ decreases and the final state interactions therefore are expected to become *weaker*. The third rf spectrum in figure 6-

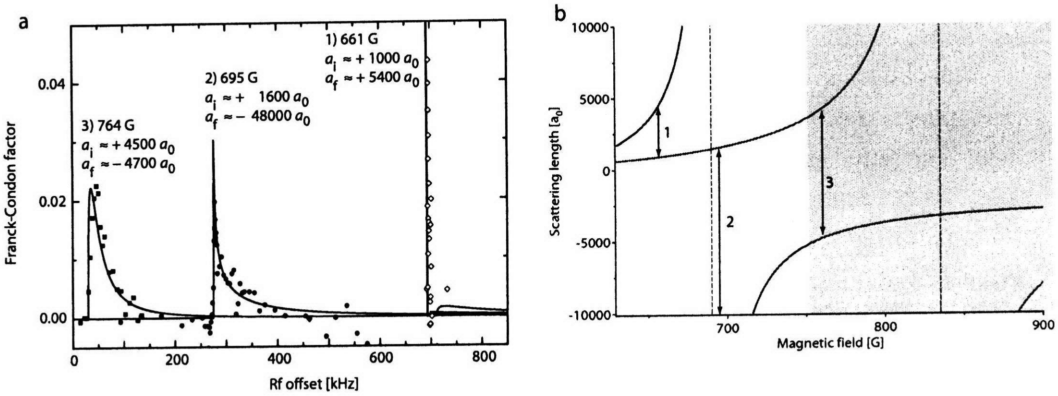

Figure 6-16: a) Rf dissociation spectra in the (1,2) mixture on the BEC side of the (1,2) Feshbach resonance. The figure has been adopted (with some modifications) from ref. [121], the data were obtained by the Innsbruck group. b) Plot of a_{12} (red) and a_{13} (blue) as a function of the magnetic field between 630 and 900 G. The dashed lines mark the resonance positions. In the shaded region *both* the (1,2) and (1,3) mixtures are strongly interacting for typical values of k_F. The arrows indicate where the rf spectra shown in a) have been obtained.

16 was observed at 764 G, where the initial (1,2) mixture enters the strongly interacting regime ($a_i \approx 4500a_0$). Interestingly, this rf spectrum is comparable, even in terms of the frequency scale, to the rf dissociation spectra we recorded in the BEC-BCS crossover of the (1,3) mixture (Fig. 6-12.) With the knowledge from the (1,3) system one would therefore conclude that the (1,2) rf spectra should actually not change significantly from 764 G towards unitarity, especially since final state interactions in terms of $|a_f|$ *continue to decrease further.* However, quite to the contrary, the observed (1,2) spectra are subject to the significant distortions discussed above (see Fig. 6-9). This indicates that a better understanding of the *interplay* between the interactions in the final and in the initial state is required.

The explanation for the strong impact of final effects must be related to the fact that at 750 G and higher fields the interactions in the initial state enter the strongly interacting regime and therefore *become comparable to the ones in final state* (see the shaded region in Fig. 6-16 b). For identical interactions in the initial and final state rf spectroscopy measures a delta function at zero frequency offset. If the interactions in the initial and final state are similar but different, one would expect a bound-bound peak with a certain offset from zero frequency to dominate the spectrum and strongly suppressed bound-free contribution to emerge. This scenario is consistent with the narrow and symmetric lineshape (characteristic for bound-bound transitions) observed in the (1,2) mixture at unitarity. Of course, the sign of a in initial and final state is different, but there is evidence that in the strongly interacting regime certain interactions are largely independent of the sign of the scattering length [126, 127, 128, 7].

The (1,3) mixture allows us to check these ideas experimentally. Figure 6-17 shows (1,3) rf spectra as the final state interactions change from weak to strong with increasing magnetic field. The initial state stays in the strongly interacting regime, but may turn normal around $k_F a_i \sim 1$. Compared to the (1,2) mixture the role of initial and final state are exchanged so that the *initial* state is always strongly interacting while the *final* state enters this regime at fields around 750 G. Here and at higher fields the bound-free transitions strongly looses in spectral weight until it cannot be resolved ay more at 833 G, where only the narrow and symmetric bound-bound peak remains. This demonstrates the dominance of bound-bound transitions in a regime where $|1/(k_F a_i) - 1/(k_F a_f)| \leq 1.5$. The spectra from the (1,3) mixture therefore provide further evidence for the dominance of bound-bound transitions in the (1,2) mixture close to unitarity.

In a recent paper bound-bound and bound-free transition have been studied theoretically in the strongly interacting regime [115]. It was found that the spectrum of the superfluid at resonance shows bound-bound peaks for positive but also for negative values of $1/k_F a_f$. The theoretical treatment in ref. [115] is in qualitative agreement with our observations in the (1,3) mixture but underestimates the region where bound-bound transitions are dominant by about a factor of two. We infer from ref. [115] that for a system in the unitarity limit it is much more difficult to spectrally resolve bound-bound and bound-free transitions if $a_f < 0$. When one approaches resonance for the (1,2) system from the BEC side the bound-free spectrum narrows and smoothly turns into a bound-bound dominated one.

We conclude that the (1,2) to (1,3) rf spectra in the vicinity of 833 G reported in ref [22, 23, 24] can therefore not be simply interpreted in terms of a pair dissociation process and a pairing gap [22, 129, 130, 131, 24, 23] and are likely to be dominated by bound-bound transitions.

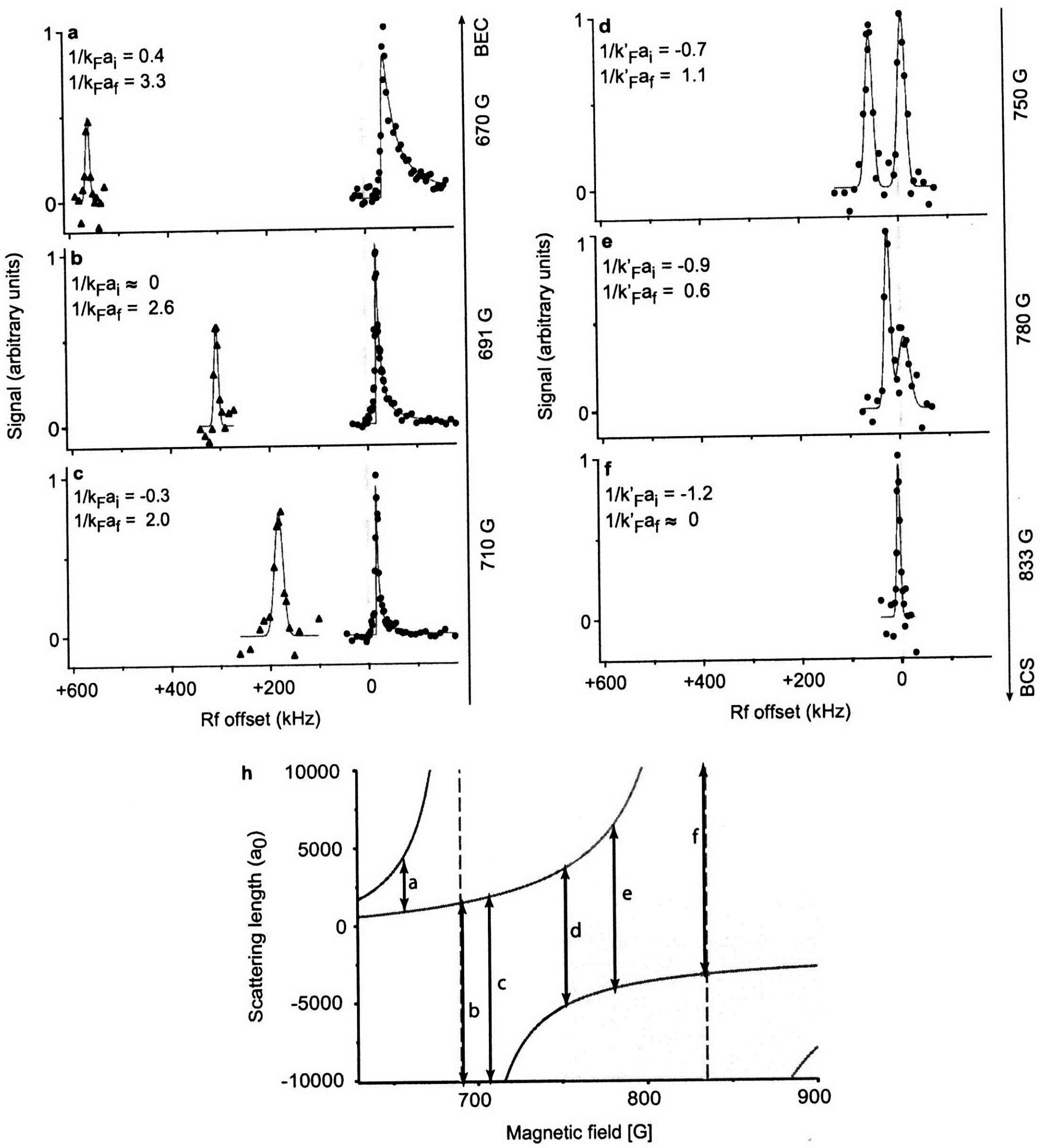

Figure 6-17: Effect of final state interactions on rf spectroscopy: bound-bound and bound-free spectra in the BEC-BCS crossover of the (1,3) mixture. While the initial (1,3) state is strongly interacting at all fields the final state interactions change from weakly (**a-c**) to strongly interacting (**d-f**). See also the diagram in **h**. At the higher magnetic fields for $1/k_F a_i \approx -1$ the initial state may have turned normal. (**a-c**) Same bound-free spectra and parameters as in Fig. 6-12. The bound-bound peaks have been fit by a Gaussian. The relative weight of the bound-bound and bound-free peaks were not determined experimentally. (**d-f**) All peaks have been fit by a Gaussian. (**d**) 750 G, $E_F = h \times 22$ kHz, T/T_F=0.09; (**e**) 780 G, $E_F = h \times 23$ kHz, T/T_F=0.09; (**f**) 833 G, $E_F = h \times 20$ kHz, T/T_F=0.06.

Chapter 7

Conclusion and Outlook

The past five years were a fantastic time to do experiments with ultracold fermionic atoms. Looking back to the early beginnings of learning about Feshbach resonances and molecule formation, which are problems that mostly concerned "atomic physics", it becomes apparent at what amazing rate the field has matured. The current experiments locally probe strongly interacting fermions in regimes that are very difficult to realize in other systems and start to study many-body problems of fundamental importance to various areas in physics.

The best part, however, is that in many ways one may still regard the field to be at a beginning. This becomes apparent when one compiles a list of just a few ideas for future experiments that are currently pursued:

- ***p*-wave Superfluidity.** All ultracold atom experiments so far have studied superfluidity with *s*-wave pairing. However *p*-wave Feshbach resonances have been observed and *p*-wave molecules have been created. In the future it might be possible to stabilize these molecules sufficiently to cool them into the superfluid state with anisotropic interactions.

- **Simulating condensed matter physics Hamiltonians with fermionic atoms.** All experiments described in this thesis studied interacting fermionic atoms in a harmonic trap. Superimposing an optical lattice allows one to explore a whole array of new phenomena closely related to condensed matter physics. A challenging goal for future experiments is to study fermions with repulsive interactions and to realize antiferromagnetic order in a lattice at half filling. This could be the first step towards observing *d*-wave superfluidity at even lower filling. Such experiments will be able to directly address some of the important open questions in condensed matter physics.

- **Two species fermion-fermion mixtures and molecular BECs with dipolar interactions.** Two species mixtures of fermions have recently been created and may allow studies of mass imbalanced fermionic superfluids. Furthermore, it could be possible to form heteronuclear bosonic molecules from two fermionic atoms by Feshbach association and then transfer them into the molecular ground state. This could lead to the creation of molecular Bose-Einstein condensates with long range dipolar interactions which are of interest not only in the context of many-body physics but also with regard to quantum computation schemes.

- **Bose-Fermi mixtures and Boson mediated pairing.** As in Fermi-Fermi mixtures also Bose-Fermi mixtures can be the starting point for the creation of heteronuclear ground state molecules with the difference that these molecules will be fermionic. Furthermore, if strongly interacting Bose-Fermi mixtures are sufficiently stable, it might be possible to observe boson-mediated fermionic pairing and superfluidity. In three-dimensional optical lattices at half filling and with weak and repulsive Bose-Fermi interactions the formation of a supersolid phase might be observable.
- **Ternary mixtures of fermions** The experiments with different spin mixtures in ^{6}Li indicate that even a ternary mixtures might prove to be sufficiently stable at least for a certain range of interactions. Such a system would allow a wide range of studies from pairing competition in multicomponent Fermi gases, to the observation of color superfluidity (analogous to a color superconducting phase in QCD) in combination with optical lattices.

Some of these ideas will likely become reality in the very near future. More than ten years after the discovery of Bose-Einstein condensation the field of ultracold atoms is still progressing at an amazing rate and in various new directions. The possibilities for future experiments based on the combination of new "tools" and techniques with different fermionic mixtures are numerous. There are exciting years ahead of us.

Appendix A

Feshbach resonances in fermionic ^{6}Li

This appendix contains a reprint of Ref. [25]: C. H. Schunck, M. W. Zwierlein, C. A. Stan, S. M. F. Raupach, W. Ketterle, A. Simoni, E. Tiesinga, C. J. Williams, and P. S. Julienne *Feshbach resonances in fermionic* ^{6}*Li*, Phys. Rev. A **71**, 045601 (2005).

PHYSICAL REVIEW A 71, 045601 (2005)

Feshbach resonances in fermionic ^{6}Li

C. H. Schunck, M. W. Zwierlein, C. A. Stan, S. M. F. Raupach, and W. Ketterle
Department of Physics, MIT-Harvard Center for Ultracold Atoms, and Research Laboratory of Electronics, MIT, Cambridge, Massachusetts 02139, USA

A. Simoni, E. Tiesinga, C. J. Williams, and P. S. Julienne
National Institute of Standards and Technology, 100 Bureau Drive stop 8423, Gaithersburg, Maryland 20899-8423, USA

(Received 14 July 2004; published 5 April 2005)

Feshbach resonances in ^{6}Li were experimentally studied and theoretically analyzed. In addition to two previously known s-wave resonances, three p-wave resonances were found. Four of these resonances are narrow and yield a precise value of the singlet scattering length. The position of the broad s-wave resonance near 83 mT is mostly sensitive to the triplet potential. It was previously determined in a molecule-dissociation experiment for which we, here, discuss systematic shifts.

DOI: 10.1103/PhysRevA.71.045601 PACS number(s): 03.75.Ss, 32.80.Pj, 34.50.Pi

Interactions in ultracold atomic gases can be magnetically tuned using Feshbach resonances [1]. A Feshbach resonance occurs when the energy of two colliding atoms is nearly degenerate to the energy of a bound molecular state. Tunable interactions have been used to explore novel phenomena in collisional and many-body physics. Recently, Feshbach resonances have been used to control pairing processes in ultracold fermionic gases. This led to the achievement of Bose-Einstein condensation (BEC) of molecules in ^{40}K [2] and ^{6}Li [3–5] and to the first studies of the BEC-BCS crossover, the continuous transition of fermion pairs from weakly bound molecules to long-range Cooper pairs [5–11].

Most experiments in ^{6}Li have been carried out in the vicinity of the s-wave Feshbach resonance near 830 G [5,7–11] ($1\ \mathrm{G}=10^{-4}\ \mathrm{T}$). The quantitative interpretation of these experiments and the characterization of the BEC-BCS crossover require a precise knowledge of the resonance location. However, its determination is not trivial since the resonance width is extremely large and the line shape is strongly affected by many-body effects. In our previous work we determined the position of this resonance by the onset of molecule dissociation to be 822 ± 3 G [8].

In this paper we report on a detailed study of Feshbach resonances in the two lowest hyperfine states of ^{6}Li with the goal of accurately characterizing the interaction potential of two ^{6}Li atoms. In addition to two previously known s-wave resonances, we find three p-wave resonances [12]. The positions of the p-wave resonances together with the location of the narrow s-wave resonance near 543 G are used for a precise determination of the singlet s-wave scattering length. These results, however, do not constrain the position of the broad resonance, which also depends on the triplet scattering length. An improved measurement of its location is presented and the magnitude and the origin of possible systematic errors are discussed.

The experimental setup has been described in Ref. [13]. Up to 4×10^7 quantum degenerate ^{6}Li atoms in the $|F,m_F\rangle=|3/2,3/2\rangle$ state were obtained in a magnetic trap by sympathetic cooling with ^{23}Na. The ^{6}Li atoms were then transferred into an optical dipole trap (ODT) formed by a focused 1064-nm laser beam with a maximum power of 9 W. In the optical trap a single radio-frequency sweep transferred the atoms to state $|1\rangle$ ($|F,m_F\rangle=|1/2,1/2\rangle$ at low field). A subsequent Landau-Zener sweep at an externally applied magnetic field of 565 G could then be used to either prepare the entire sample in state $|2\rangle$ ($|1/2,-1/2\rangle$ at low field) or create an equal mixture of atoms in states $|1\rangle$ and $|2\rangle$. Except for the measurement of the broad s-wave Feshbach resonance, all resonances were observed by monitoring magnetic-field-dependent atom losses. Atom numbers were obtained from absorption images taken at zero field. The externally applied field was calibrated by driving microwave transitions from state $|2\rangle$ to state $|5\rangle$ ($|3/2,1/2\rangle$ at low field) at several magnetic fields close to resonance positions and from state $|2\rangle$ to state $|3\rangle$ ($|3/2,-3/2\rangle$ at low field) at high magnetic fields around 800 G.

For spin-polarized samples either in state $|1\rangle$ or $|2\rangle$ s-wave scattering is forbidden by symmetry; therefore, the observed resonances occur in the p-wave channel. The same molecular state that is responsible for these two resonances also causes a p-wave resonance in the $|1\rangle+|2\rangle$ mixture. The three p-wave resonances were observed in clouds with typical temperatures $T\sim6\ \mu\mathrm{K}$ and $T/T_F\simeq0.5-1.5$, where T_F is the Fermi temperature. Radial and axial trap frequencies were typically $\omega_r=2\pi\times1.0$ kHz and $\omega_a=2\pi\times6.9$ Hz.

The position of the p-wave resonance in the collision of a pair of state $|1\rangle$ atoms was determined by first ramping the magnetic field to approximately 5 G below the resonance. Using an additional power supply to precisely change the magnetic field within a 10 G range, the field was then switched in 1 ms to a test value B_{test}. Here the atoms were kept for 200 ms before the field and the optical trap were switched off. Finally, atom number versus B_{test} was recorded. Resonantly enhanced losses due to inelastic three-body decay led to a Lorentzian shaped feature as shown in Fig. 1(a). Resonance positions and widths are summarized in Table I.

The same technique was used to determine the $|1\rangle+|2\rangle$ and $|2\rangle+|2\rangle$ p-wave resonances. The resonance line shapes are asymmetric (see Fig. 1), possibly due to threshold effects [14,15]. The splitting of a p-wave resonance due to spin-spin interactions [16] is for these resonances more than one order

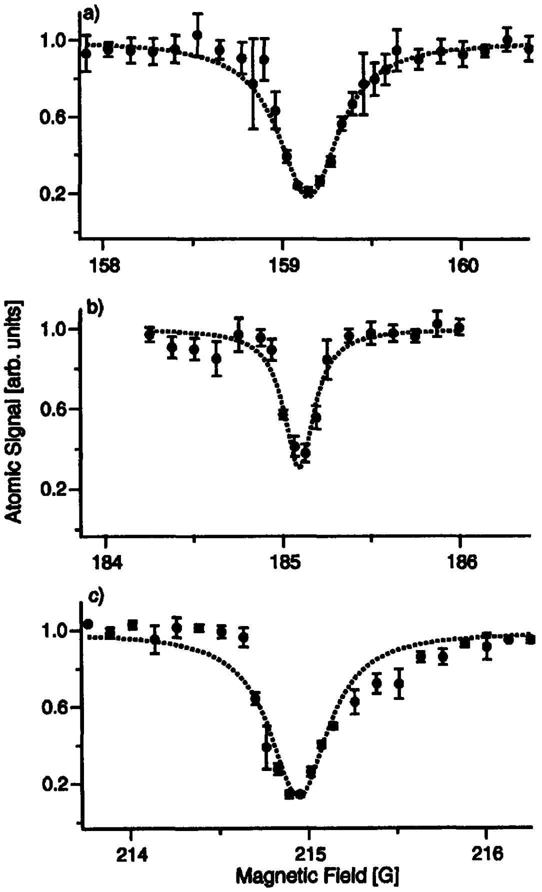

FIG. 1. p-wave resonances for $|1\rangle+|1\rangle$ (a), $|1\rangle+|2\rangle$ (b), and $|2\rangle+|2\rangle$ (c) collisions. Dashed lines are Lorentzian fits to the data. The results are summarized in Table I.

TABLE I. Position of the Feshbach resonances. Given are the experimentally and theoretically determined resonance locations B_{expt} and B_{theory}, respectively, and the measured resonance width. The uncertainties for the experimental data in the first four rows are dominated by magnetic field drifts between the measurement of the resonance and the field calibration for which we find an upper bound of 80 mG. For the $|1\rangle+|1\rangle$ resonance an additional drift was monitored. The statistical error of determining the line center and the estimated uncertainty due to asymmetric line shapes are negligible. The quoted linewidths are not corrected for source depletion due to atom loss. We estimate that this effect reduces the linewidths by 25%–40%. For the broad s-wave resonance (fifth row) only a range is given. See the text for a discussion.

States	Wave	B_{expt} [G]	B_{theory} [G]	Width [G]
$\|1\rangle+\|1\rangle$	p	159.14±0.14	159.15(4)	0.4
$\|1\rangle+\|2\rangle$	p	185.09±0.08	185.15(4)	0.2
$\|2\rangle+\|2\rangle$	p	214.94±0.08	214.90(4)	0.4
$\|1\rangle+\|2\rangle$	s	543.28±0.08	543.27(5)	0.4
$\|1\rangle+\|2\rangle$	s	822...834		

of magnitude smaller than the width and could not be discerned with our sensitivity.

The position of the s-wave resonance near 543 G in the $|1\rangle+|2\rangle$ mixture was determined as presented above in clouds with typical temperatures of 6 μK, but in a slightly deeper optical trap and with an extended holdtime of 2900 ms at B_{test}. The result of a fit to the Lorentzian lineshape is given in Table I. This s-wave resonance was first reported in [17] and calculated in [18].

To determine the position of the broad s-wave Feshbach resonance near 830 G a different method was required. The resonance was identified as the onset of molecular dissociation [6,8,19]. Molecules were first created on the repulsive (BEC) side of the Feshbach resonance and then dissociated into atoms when the magnetic field crossed the resonance. However, this method is subject to systematic shifts in the resonance position that depend on the molecular density and the speed of magnetic field ramps. To control the density-dependent shift, the molecular density was varied by using different parameters for the optical dipole trap and by performing the dissociation at different times of flight.

The starting point of the experiment was an almost pure $^6Li_2$ molecular BEC that was prepared at a magnetic field of about 780 G in the optical trap as described in Ref. [8]. The data shown in Fig. 2 were obtained by releasing the molecules from the optical trap at 780 G [20]. After 2 ms the field was ramped to a test value B_{test} in 14 ms. In these first 16 ms time of flight the peak molecular density dropped by three orders of magnitude to $n_{\text{mol}}=5\times10^9\ \text{cm}^{-3}$. The magnetic field was held at B_{test} for another 5 ms before it was ramped down. The critical field ramp, which can alter the resonance position, is the initial phase of the magnetic field ramp down in which the molecules are still in the resonance region. Here, fast ramps can dissociate weakly bound molecules. However, we could only use a limited time of flight while maintaining a good signal-to-noise ratio. Therefore the field was ramped down in two steps: at an initial rate of 100 G/ms for 2 ms to leave the resonance region, followed by an exponential decay with time constant 30 G/μs which brought the field to zero in 3 ms. To better control the effects of the field ramp, the experiment was repeated for different initial switch off speeds. Finally, the sample was imaged with light which was resonant only with unbound atoms; the possible molecular transitions are far detuned from the atomic transition at zero field. By monitoring the atom number as a function of B_{test} the onset of molecule dissociation was observed. The data in Fig. 2 show the onset at 821±1 G. The slow approach of the atomic signal to unity reflects the time constant of dissociation and the possible reconversion of atoms into molecules during the magnetic field switch off. In our analysis only the onset of the atomic signal was evaluated.

We now consider the two sources of systematic errors mentioned above in more detail. Few-body collisions might dissociate molecules when their size, which near resonance is on the order of the scattering length between the constituent atoms [21], becomes comparable to the mean distance between the molecules, $a\sim n_{\text{mol}}^{-1/3}$. The scattering length near resonance is parametrized by $a=a_{\text{bg}}[1+\Delta B/(B-B_0)] \approx a_{\text{bg}}\Delta B/(B-B_0)$, where a_{bg} is the negative background scat-

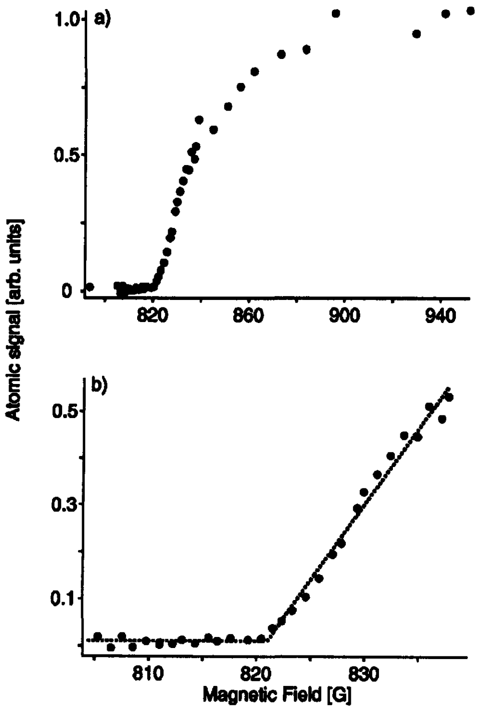

FIG. 2. Determination of the position of the broad s-wave Feshbach resonance. (a) Onset of dissociation of molecules into atoms at 821±1 G. (b) The resonance position was obtained by fitting two lines to the data points near the threshold, one horizontal through the points showing no atomic signal and a second line following the initial rise in atom number. The intersection of the two lines gives the resonance position; the estimated uncertainty of this point is ±1 G.

tering length, B_0 is the resonance position, and ΔB is the resonance width. So molecule dissociation will become important at a magnetic field B for which $a_{\mathrm{bg}}\Delta B/(B-B_0) \sim n_{\mathrm{mol}}^{-1/3}$. For the broad resonance, this density-dependent, few-body effect is expected to shift the observed resonance position to lower magnetic fields.

The second systematic error is a density-independent, single-molecule effect. Switching off the magnetic field becomes nonadiabatic close to resonance and destroys very weakly bound molecules [22]. If a molecule with binding energy $\hbar\omega=\hbar^2/(ma^2)$ is forced to change its size faster than its oscillation frequency (i.e., if $\dot{a}/a \gg \omega$), the molecule may dissociate. With the magnetic field dependence of a given above, the rate $\dot{a}/a \sim \dot{B}/(B-B_0)$ becomes comparable to $\omega \sim (B-B_0)^2$ at a magnetic field that is shifted from the resonance location B_0 by $\Delta B = B - B_0 \sim \dot{B}^{1/3}$. This expression gives the scaling of the ramp-induced systematic error with the ramp speed $\dot{B}$.

To find the order of magnitude of these shifts we have determined the resonance locations for three different ramp rates at constant density and for three different densities at constant ramp rate.

At a molecular density of $n_{\mathrm{mol}}=1.5\times 10^{10}$ the resonance positions were measured at initial ramp speeds of 30 G/μs (fastest possible switch off), 100 G/ms (fastest externally controlled ramp), and 12.5 G/ms (controlled ramp). For the fastest switch off the onset of dissociation occurs at 793±7 G, for the other two controlled ramps at 822±3 G. Assuming that no density shifts affect these data, one can extrapolate to zero ramp speed based on the $(B-B_0) \propto \dot{B}^{1/3}$ dependence. In this way we find a resonance position of 825±3 G.

For a fixed initial ramp speed of 100 G/ms the resonance locations were determined at densities of 5×10^9 cm^{-3}, 1.5×10^{10} cm^{-3}, and 1.2×10^{12} cm^{-3} to be 821±1 G, 822±3 G, and 800±8 G, respectively. Here one can use the $(B-B_0) \propto n^{1/3}$ dependence to extrapolate to a resonance position of 825±3 G, neglecting effects due to nonadiabatic magnetic field ramps.

Both systematic effects shift the maximum magnetic field value at which the molecules are stable to lower magnetic fields. In a simple picture, one would expect the total shift to be the larger of the two. However, if they are similar, as in our case, they may add or combine in a more complicated way. We have measured the threshold position at low density and slow ramp rates to be 822±3 G and determined two shifts of 3±3 G. Therefore, we expect the position of the Feshbach resonance to be between 822 and 834 G. A more accurate extrapolation requires measuring the dissociation threshold for more ramp speeds and densities. However, technical limitations in varying magnetic field ramp speeds and an unfavorable signal-to-noise ratio at lower densities precluded this.

All Feshbach resonances discussed in this paper are due to the $v=38$ vibrational state of the singlet potential with total electronic spin S equal to zero. The p-wave resonances have a total nuclear spin $I=1$, while the 543 G and broad s-wave resonances have $I=2$ and $I=0$, respectively.

The resonance locations are compared with results of scattering coupled-channel calculations. We locate the resonance from the maximum of the elastic cross section as a function of magnetic field. The collision energy is fixed at $E=k_BT$, where k_B is the Boltzmann constant and T is the experimental temperature. Our collision model, described in detail in Ref. [18], treats the singlet and triplet scattering lengths as adjustable parameters. The triplet state has a total electron spin equal to one. It turns out that all narrow resonances, which could be accurately located, are insensitive to the triplet scattering length. Only s- and p-waves are included in the calculation. Fitting the singlet scattering length a_S to the field locations given in the first four rows of Table I yields a very accurate value of $a_S=45.1591(16)a_0$, where $a_0=0.052\,917\,7$ nm. With this value, the resonance positions given in the third column of Table I were calculated at a collision energy equal to k_BT. The agreement with the experimental values is excellent. The location of the s-wave resonance is also in very good agreement with the determination of Ref. [23], 543.26(10) G.

Our theoretical uncertainties do not include contributions due to a thermal average. Moreover, there can be a discrepancy between the field values at which the observed three-body loss rate and the theoretical two-body elastic cross section are maximal. Experimental observations on ^{40}K [14] are not conclusive about the magnitude of this shift, although they suggest it is well within the linewidth of the observed loss features. As an estimate of our possible systematic error, a shift in the resonance position δ(G) will give rise to a shift from our best a_S of $(-0.0365\delta)a_0$.

The broad resonance is caused by a hyperfine-induced mixing between a singlet vibrational level and an almost-bound virtual state of the triplet potential, a situation analyzed in [24,25]. It is the virtual state that gives rise to the large and negative triplet scattering length a_T of ^{6}Li. Mixing occurs for magnetic field values above 500 G. In fact, in absence of the hyperfine mixing, the resonance would occur around 550 G. The coupling shifts the resonance by a few hundred gauss. For typical Feshbach resonances, these shifts are no more than a few gauss. A consequence of the large shift is that the resonance location depends critically on the less well known triplet potential.

In conclusion, we have found three p-wave Feshbach resonances in ^{6}Li. Together with the narrow s-wave resonance they give a precise value of the singlet scattering length. The position of the broad resonance could not be constrained using the refined singlet potential. The determination of the position of the broad resonance via molecule dissociation is subject to systematic errors, which shift the onset of dissociation to lower magnetic fields.

The MIT research is supported by NSF, ONR, ARO, and NASA. S.R. acknowledges financial support from the Dr. Jürgen Ulderup Foundation.

---

[1] E. Tiesinga, B. J. Verhaar, and H. T. C. Stoof, Phys. Rev. A **47**, 4114 (1993); W. C. Stwalley, Phys. Rev. Lett. **37**, 1628 (1976); S. Inouye *et al.*, Nature (London) **392**, 151 (1998); P. Courteille *et al.*, Phys. Rev. Lett. **81**, 69 (1998).
[2] M. Greiner, C. A. Regal, and D. S. Jin, Nature (London) **426**, 537 (2003).
[3] S. Jochim *et al.*, Science **302**, 2101 (2003).
[4] M. W. Zwierlein *et al.*, Phys. Rev. Lett. **91**, 250401 (2003).
[5] T. Bourdel *et al.*, Phys. Rev. Lett. **93**, 050401 (2004).
[6] C. A. Regal, M. Greiner, and D. S. Jin, Phys. Rev. Lett. **92**, 040403 (2004).
[7] M. Bartenstein *et al.*, Phys. Rev. Lett. **92**, 120401 (2004).
[8] M. W. Zwierlein *et al.*, Phys. Rev. Lett. **92**, 120403 (2004).
[9] J. Kinast *et al.*, Phys. Rev. Lett. **92**, 150402 (2004).
[10] M. Bartenstein *et al.*, Phys. Rev. Lett. **92**, 203201 (2004).
[11] C. Chin *et al.*, Science **305**, 1128 (2004).
[12] We presented most of the results of the present paper at the KITP workshop in Santa Barbara, 2004. Similar results were independently obtained in Paris [15].
[13] Z. Hadzibabic *et al.*, Phys. Rev. Lett. **91**, 160401 (2003).
[14] C. A. Regal *et al.*, Phys. Rev. Lett. **90**, 053201 (2003).
[15] J. Zhang *et al.*, Phys. Rev. A **70**, 030702(R) (2004).
[16] C. Ticknor *et al.*, Phys. Rev. A **69**, 042712 (2004).
[17] K. Dieckmann *et al.*, Phys. Rev. Lett. **89**, 203201 (2002).
[18] K. M. O'Hara *et al.*, Phys. Rev. A **66**, 041401(R) (2002).
[19] T. Mukaiyama *et al.*, Phys. Rev. Lett. **92**, 180402 (2004).
[20] The ODT power was 36 mW, yielding trap frequencies of $\omega_r = 2\pi \times 690$ Hz radially and $\omega_a = 2\pi \times 12.5$ Hz axially. The axial frequency is mostly due to magnetic field curvature.
[21] T. Kohler *et al.*, Phys. Rev. Lett. **91**, 230401 (2003).
[22] J. Cubizolles *et al.*, Phys. Rev. Lett. **91**, 240401 (2003).
[23] K. E. Strecker, G. B. Partridge, and R. G. Hulet, Phys. Rev. Lett. **91**, 080406 (2003).
[24] B. Marcelis *et al.*, Phys. Rev. A **70**, 012701 (2004).
[25] E. G. M.v. Kempen, B. Marcelis, and S. J. J. M. F. Kokkelmans, Phys. Rev. A **70**, 050701(R) (2004).

Appendix B

Formation Dynamics of a Fermion Pair Condensate

This appendix contains a reprint of Ref. [26]: M. W. Zwierlein, C. H. Schunck, C. A. Stan, S. M. F. Raupach, and W. Ketterle, *Formation Dynamics of a Fermion Pair Condensate*, Phys. Rev. Lett. **94**, 180401 (2005).

Formation Dynamics of a Fermion Pair Condensate

M. W. Zwierlein, C. H. Schunck, C. A. Stan, S. M. F. Raupach, and W. Ketterle
Department of Physics, MIT-Harvard Center for Ultracold Atoms, and Research Laboratory of Electronics, MIT,
Cambridge, Massachusetts 02139, USA

(Received 23 December 2004; published 9 May 2005)

The dynamics of pair condensate formation in a strongly interacting Fermi gas close to a Feshbach resonance was studied. We employed a phase-shift method in which the delayed response of the many-body system to a modulation of the interaction strength was recorded. The observable was the fraction of condensed molecules in the cloud after a rapid magnetic field ramp across the Feshbach resonance. The measured response time was slow compared to the rapid ramp, which provides final proof that the molecular condensates reflect the presence of fermion pair condensates before the ramp.

DOI: 10.1103/PhysRevLett.94.180401 PACS numbers: 03.75.Ss, 05.30.Fk

Atomic Fermi gases close to a Feshbach resonance [1] offer the unique possibility of studying many-body phenomena in a strongly interacting system with tunable interactions. Recently a major focus has been on condensates of pairs of fermionic atoms [2–8]. By changing the magnetic field, the interaction strength between atoms in two spin states can be varied. That way, condensates of either tightly bound molecules or of extended pairs of fermions can be created, whose size can become comparable or even larger than the interparticle spacing. The description of this so-called BEC-BCS crossover [9] is an active frontier in many-body physics with still controversial interpretations [10–13].

The control of interactions via magnetic fields does not only give access to very different physical regimes, it also allows one to apply a time-varying interaction strength [14,15] and to study the dynamics of a many-body system in novel ways. This was used in recent experiments in which molecular condensates were observed after a rapid field ramp from the BCS to the Bose-Einstein condensate (BEC) side of the Feshbach resonance [6,7]. It was argued that if the ramp time was faster than the formation time of a molecular condensate, its presence after the sweep necessarily reflected a preexisting condensate of fermion pairs. However, without access to that formation time, secondary evidence was gathered, namely, the invariance of the condensate fraction under variations of the sweep rate [6] or of the density immediately before the ramp [7]. This excluded simple models of the molecular condensate formation during the ramp, but left room for more sophisticated many-body effects. In particular, the time to cross the Feshbach resonance in these experiments was not faster than the unitarity limited collision time $\propto \hbar E_F^{-1}$, and therefore dynamics during the sweep could not be ruled out.

Here we present an experimental study of the formation dynamics of a fermion pair condensate on the BCS side of the Feshbach resonance [16]. We employ a novel phase-shift method, which records the delayed response of the many-body system to a modulation of the magnetic field that changes periodically its interaction strength. The observable is again the molecular condensate fraction after a rapid sweep to the BEC side of the Feshbach resonance. Its sensitivity to changes in the scattering length on the BCS side [6,7] arises through the dependence of the critical temperature for pair condensation on the interaction strength. By showing that the delayed response time of the molecular condensate fraction is long compared to the sweep times used in the present and previous experiments, we infer that the observed condensates could not have been created during the rapid transfer and thus must originate from preexisting fermion pair condensates. However, we do find evidence that condensed pairs are more likely to be transferred into molecules than thermal pairs. Therefore, in contrast to assumptions made in previous work [6,7], the molecular condensate fraction after the ramp may not equal the fraction of condensed atom pairs above resonance.

The experimental setup was the same as in our previous work [7]. A degenerate cloud of ^{6}Li, sympathetically cooled with ^{23}Na, was loaded into an optical dipole trap to access a broad Feshbach resonance at 834 G [17,18] between the two lowest hyperfine states of ^{6}Li, labeled $|1\rangle$ and $|2\rangle$. An equal mixture of these states was evaporatively cooled at 770 G using an exponential ramp-down of the optical trap to 15 mW. This resulted in an essentially pure Bose-Einstein condensate of 3×10^6 molecules. An upper limit for the temperature of the gas is $\frac{T}{T_F} < 0.2$, with the Fermi temperature T_F given by the zero-temperature, ideal gas relation $T_F = \hbar\omega(3N)^{1/3}$, $\omega/2\pi$ is the geometric mean of the trapping frequencies, and N is the total atom number. Next, the trap was recompressed to 25 mW (trap frequencies: $\nu_x = \nu_y = 580$ Hz, $\nu_z = 12.1\ \mathrm{Hz}\sqrt{0.2 + B}$ with the magnetic field B in kG) and the magnetic field was adiabatically increased in 500 ms to 1000 G, the starting point for the following experiments. Here, in the wings of the Feshbach resonance, the scattering length a was still sufficiently large and negative for the gas to be in the strongly interacting regime, with $k_F|a| = 1.6$ at a Fermi energy of $E_F = 2.0\ \mu$K and a Fermi wave number $k_F = 1/2700a_0$. The temperature at this point could therefore not be reli-

0031-9007/05/94(18)/180401(4)$23.00

ably determined, but is expected to be significantly lower than the one on the BEC side due to adiabatic cooling [19]. Subsequently, the magnetic field and thus the interaction strength in the gas were modulated at frequencies in the range of 100–500 Hz, and an amplitude of about 50 G [20]. At a variable time t after the start of the modulation, the fraction of condensed fermion pairs was recorded by time-of-flight analysis.

To identify fermionic condensates across the resonance region, we proceeded as in [6,7]. Immediately after the release of the cloud from the optical potential, the magnetic field was switched to zero field (initial ramp rate 30 G/μs), where further expansion of the cloud took place. This rapid ramp out of the resonance region transformed large fermion pairs into deeply bound molecules with high efficiency [21]. Figure 1 details the imaging procedure used to determine molecular condensate fractions and the number of unpaired atoms in each state after the ramp. In our previous work, we showed that the condensate fractions had a peak around the Feshbach resonance and fell off on either side [7]. Here, this dependence was exploited to observe the delayed response of the system to the magnetic field modulation on the BCS side.

Figure 2 shows the main result of this Letter: The condensate fraction in the molecular clouds after the rapid ramp did not follow the magnetic field modulation instantaneously, but lagged behind. At a Fermi energy of $E_F = 2\ \mu$K, the peak condensate fraction was delayed by $\tau_R = (500 \pm 100)\ \mu$s with respect to the magnetic field's closest approach to resonance [22]. This time scale was independent of the modulation frequency [compare Figs. 2 and 4(a), below]. This also rules out that our results are affected by the excitation of collective modes. τ_R equals 130 times the unitarity limited collision time, $\hbar E_F^{-1} = 3.8\ \mu$s. The rapid magnetic field ramp utilized here and in [7] traversed the Feshbach resonance in less than 10 μs, which is much smaller than τ_R.

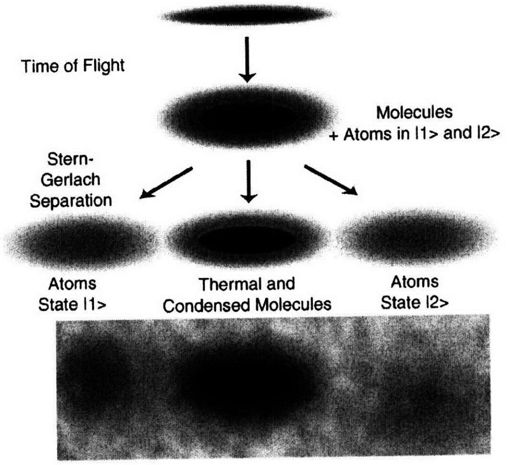

FIG. 1. Imaging of molecular condensates. The rapid ramp to zero field after release from the trap created a cloud containing both molecules and unpaired atoms. A Stern-Gerlach field gradient separated atoms (magnetic moment $\pm\frac{1}{3}\ \mu_B$ for states $|1\rangle$ and $|2\rangle$, respectively) from molecules, which are purely singlet at zero field. At the end of 5 ms of ballistic expansion, the molecules were dissociated in a fast ramp (in 3 ms to ~1200 G) across the Feshbach resonance. After another 2 ms expansion again at zero field, an absorption image of the separated clouds was taken. Condensate fractions were determined from the molecular cloud, and the numbers in each component were recorded. An absorption image is shown on the bottom, the field of view is 3 mm × 1 mm.

This delay time can be interpreted as the relaxation time of the fermionic condensate. In a normal Fermi gas of N particles at temperatures much smaller than the Fermi temperature T_F, relaxation occurs through collisions between the thermally excited particles close to the Fermi surface, whose number scales as $N_{\mathrm{th}} \simeq N \frac{k_B T}{E_F}$. The number of available scattering states again being proportional to $\frac{k_B T}{E_F}$, the relaxation time will be $\tau_R \simeq \hbar \frac{E_F}{(k_B T)^2}$. In general, if the Fermi surface is smeared out over an energy width ΔE, the relaxation time is $\simeq \hbar \frac{E_F}{(\Delta E)^2}$. This formula with $\Delta E = \Delta$ should apply also to the superfluid state [23] when the gap parameter Δ is rapidly changed to a much smaller value. Generally, one would expect ΔE to be the larger of Δ and $k_B T$. Using $\tau_R = 500\ \mu$s, we obtain the estimate $\Delta E = 0.1 E_F$ which may set an upper bound for both temperature and pairing gaps.

A decay is superimposed to the periodic modulation of the condensate fraction. It could be caused by heating due to the nonadiabaticity of the process. Another source of heating could be the excitation of the cloud via the small accompanying variation of the magnetic field curvature.

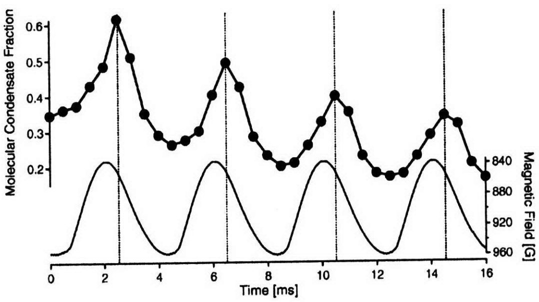

FIG. 2. Measurement of the relaxation time of fermionic pair condensates. Shown is the delayed response of the observed condensate fraction (data points and thick line to guide the eye) to a 250 Hz magnetic field modulation (thin line) on the BCS side of the Feshbach resonance at 834 G. The condensates were detected as described in Fig. 1. Three measurements per point were taken in random order, the size of the data points reflecting the standard deviation. The vertical lines indicate the points of maximum condensate fraction, which are delayed with respect to the times at which the magnetic field is closest to resonance.

Despite the decay of the condensate fraction, the relaxation time was constant for subsequent cycles of modulation, within the (limited) accuracy of our measurement.

In a compressed trap of $p = 150$ mW, at a 1.8 times higher Fermi energy of 3.6 μK, the measured delay time was $\tau_R \simeq (230 \pm 100)$ μs. BCS theory predicts that the relaxation time should scale with density like $\tau_R \propto E_F^{-1} e^{\pi/(k_F|a|)}$, giving $\tau_R \simeq 200$ μs for this experiment performed around 900 G. However, we regard this agreement with observation as fortuitous since BCS theory cannot be rigorously applied, and finite temperature effects may contribute to the relaxation.

We now discuss further observations regarding the efficiency of converting atoms into molecules. Since the relaxation time introduces some hysteresis, we observe the same condensate fraction at two different magnetic field values. Therefore, in contrast to equilibrium experiments [6,7], we can distinguish the dependence of the conversion efficiency on condensate fraction and magnetic field.

Figure 3 shows that the total number of detected atoms (in both the atom and the molecule channels) was modulated by the magnetic field. We assume that this instantaneous response reflects the two-body physics during the magnetic field sweep. In a simple two-state Landau-Zener model, the initial magnetic field and the sweep rate determine what fraction of the atoms appears as bound molecules. However, the total number of bound or unbound atoms should be constant in contrast to our observations. This is evidence for the presence of other molecular states (e.g., lower lying vibrational states) which are populated during the magnetic field sweep, and the population is larger for initial magnetic fields closer to the Feshbach resonance. Note that the determination of the condensate fraction is immune against those "disappeared" molecules, since the two-body physics does not depend on the center-of-mass motion of the atom pair.

We now look at the molecular fraction which we define as $1 - N_{\text{atom}}/N_{\text{total}}$, where N_{atom} is the number of atoms observed after the sweep and N_{total} the total number of atoms before the sweep (this definition includes the disappeared molecules) [24]. If the molecule fraction would follow the instantaneous magnetic field, it would again reflect the two-body physics during the sweep. Instead, we observe a delayed response in perfect correlation with the condensate fraction (Fig. 4). Since the delay time reflects the many-body physics of condensate formation, this is clear evidence that the molecule conversion efficiency depends on the initial many-body state.

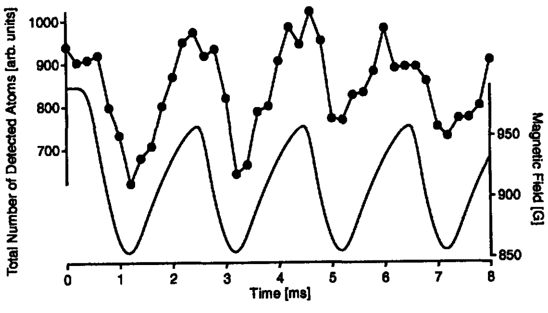

FIG. 3. Total number of detected atoms (unbound atoms and molecules) after the rapid ramp (same data set as in Fig. 4). It is modulated in phase with the magnetic field. For initial fields close to resonance, more atoms are "missing" after the rapid ramp.

One consistent explanation of these findings is that fermion pairs in the condensate are more completely transferred into tightly bound molecules than thermal pairs. With this assumption, we extrapolated the fitted line in Fig. 4(b) to a zero condensate fraction to obtain the transfer efficiency from thermal atom pairs into molecules (including the missing fraction) as $p_{\text{th}} = 75\%$ [21]. Extrapolating towards the other limit, we do not expect any unpaired atoms after the ramp already for a condensate fraction of 80% [25], suggesting a transfer efficiency for condensed fermion pairs into molecules of $p_0 = 100\%$. This effect would lead to an overestimate of the fermionic condensate fraction before the sweep. Small condensate fractions could be overestimated by as much as $\frac{p_0 - p_{\text{th}}}{p_{\text{th}}} = 33\%$. The largest absolute error occurs for an initial pair condensate

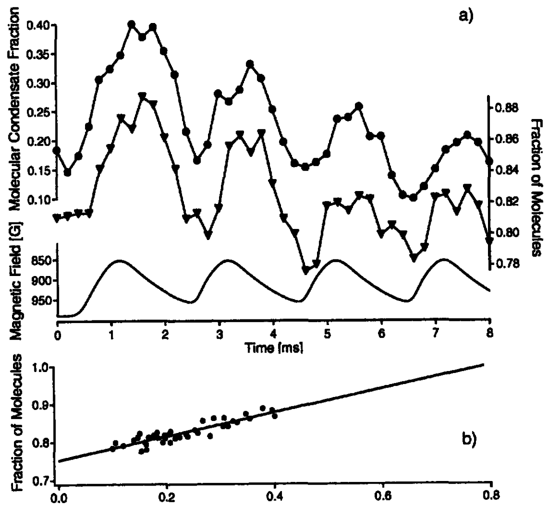

FIG. 4. Correlation between the observed condensate fraction and the molecular fraction. Shown are (a) the condensate fraction vs time during a 500 Hz field modulation (circles), the fraction of molecules (triangles) and the magnetic field. Unlike the total detected signal (Fig. 3), the molecular fraction is modulated not in phase with the magnetic field, but in complete correlation with the condensate fraction. (b) The molecular fraction vs the condensate fraction, together with a fitted line through the data.

fraction of $\frac{\sqrt{p_{\mathrm{th}}}}{\sqrt{p_0}+\sqrt{p_{\mathrm{th}}}} = 46\%$ and would be about 7% in our case.

This effect can have several possible origins: One is that the atomic separation in a condensed atom pair is smaller than that of two uncondensed atoms. Also, the presence of a large pair condensate increases the density of the cloud [26]. Finally, if there are incoherent processes involved during the rapid ramp, bosonic stimulation into the molecular condensate could play a role.

In conclusion, we have determined the intrinsic time scale for the growth of a fermion pair condensate by observing the delayed response of the system to a change in its interaction strength. For our trap parameters, the response was delayed by ≈ 500 μs. This time is far longer than the time spent within the resonance region during the conversion of fermion pairs into molecules. This provides final proof that the observed molecular condensates originated from condensates of pairs of fermions above the resonance. Regarding the two-body physics of the rapid transfer, we found that there is a missing fraction of particles after the ramp, presumably transferred into unobserved molecular states. We found evidence that condensed fermion pairs are more efficiently transformed into molecules than thermal pairs during the rapid ramp. Thus, the observed molecular condensate fractions tend to overestimate the initial fermion pair condensate fraction.

This work was supported by the NSF, ONR, ARO, and NASA. We thank Michele Saba for the critical reading of the manuscript. S. Raupach is grateful to the Dr. Jürgen Ulderup foundation for financial support.

---

[1] E. Tiesinga, B. J. Verhaar, and H. T. C. Stoof, Phys. Rev. A **47**, 4114 (1993); W. C. Stwalley, Phys. Rev. Lett. **37**, 1628 (1976); S. Inouye, M. R. Andrews, J. Stenger, H.-J. Miesner, D. M. Stamper-Kurn, and W. Ketterle, Nature (London) **392**, 151 (1998); P. Courteille, R. S. Freeland, D. J. Heinzen, F. A. van Abeelen, and B. J. Verhaar, Phys. Rev. Lett. **81**, 69 (1998).

[2] M. Greiner, C. A. Regal, and D. S. Jin, Nature (London) **426**, 537 (2003).

[3] S. Jochim, M. Bartenstein, A. Altmeyer, G. Hendl, S. Riedl, C. Chin, J. H. Denschlag, and R. Grimm, Science **302**, 2101 (2003).

[4] M. W. Zwierlein, C. A. Stan, C. H. Schunck, S. M. F. Raupach, S. Gupta, Z. Hadzibabic, and W. Ketterle, Phys. Rev. Lett. **91**, 250401 (2003).

[5] T. Bourdel, L. Khaykovich, J. Cubizolles, J. Zhang, F. Chevy, M. Teichmann, L. Tarruell, S. J. J. M. F. Kokkelmans, and C. Salomon, Phys. Rev. Lett. **93**, 050401 (2004).

[6] C. A. Regal, M. Greiner, and D. S. Jin, Phys. Rev. Lett. **92**, 040403 (2004).

[7] M. W. Zwierlein, C. A. Stan, C. H. Schunck, S. M. F. Raupach, A. J. Kerman, and W. Ketterle, Phys. Rev. Lett. **92**, 120403 (2004).

[8] J. Kinast, S. L. Hemmer, M. E. Gehm, A. Turlapov, and J. E. Thomas, Phys. Rev. Lett. **92**, 150402 (2004).

[9] D. M. Eagles, Phys. Rev. **186**, 456 (1969); A. J. Leggett, in *Modern Trends in the Theory of Condensed Matter, Proceedings of the XVIth Karpacz Winter School of Theoretical Physics, Karpacz, Poland, 1980* (Springer-Verlag, Berlin, Karpacz, Poland, 1980), pp. 13–27; P. Nozières and S. Schmitt-Rink, J. Low Temp. Phys. **59**, 195 (1985).

[10] G. M. Falco and H. T. C. Stoof, Phys. Rev. Lett. **92**, 130401 (2004).

[11] R. A. Barankov and L. S. Levitov, Phys. Rev. Lett. **93**, 130403 (2004).

[12] Roberto B. Diener and Tin-Lun Ho, cond-mat/0404517.

[13] S. Simonucci, P. Pieri, and G. C. Strinati, cond-mat/0407600.

[14] M. R. Matthews, D. S. Hall, D. S. Jin, J. R. Ensher, C. E. Wieman, E. A. Cornell, F. Dalfovo, C. Minniti, and S. Stringari, Phys. Rev. Lett. **81**, 243 (1998).

[15] M. Greiner, C. A. Regal, and D. S. Jin, Phys. Rev. Lett. **94**, 070403 (2005).

[16] We presented the main result of the present Letter at the KITP workshop in Santa Barbara, May 10–14, 2004.

[17] C. H. Schunck, M. W. Zwierlein, C. A. Stan, S. M. F. Raupach, W. Ketterle, A. Simoni, E. Tiesinga, C. J. Williams, and P. S. Julienne, Phys. Rev. A **71**, 045601 (2005).

[18] M. Bartenstein, A. Altmeyer, S. Riedl, R. Geursen, S. Jochim, C. Chin, J. H. Denschlag, R. Grimm, A. Simoni, E. Tiesinga, C. J. Williams, and P. S. Julienne, Phys. Rev. Lett. **94**, 103201 (2005).

[19] L. D. Carr, G. V. Shlyapnikov, and Y. Castin, Phys. Rev. Lett. **92**, 150404 (2004).

[20] The instantaneous magnetic field was determined by probing the atoms using a Zeeman-sensitive optical transition. For the 500 Hz modulation, the deduced field followed the modulation current with a time delay of (85 ± 5) μs and a reduced amplitude of 95% compared to the dc situation. This was due to induced eddy currents in the apparatus.

[21] The transfer probability depends on the ramp speed and on the density of the cloud. In a tighter trap with 150 mW of power we cannot discern any unpaired atoms after the ramp.

[22] This was far shorter than evaporation time scales, which were on the order of 100 ms.

[23] R. A. Barankov, L. S. Levitov, and B. Z. Spivak, Phys. Rev. Lett. **93**, 160401 (2004).

[24] N_{total} was determined in a different cycle of the experiment, for which the rapid ramp was omitted.

[25] Indeed, on resonance we observe almost pure condensates, and only a negligible amount of unpaired atoms after the ramp. Note that fitting routines, saturated absorption, and imaging noise all tend to underestimate condensate fractions.

[26] This is not true in the BCS regime, where the atomic density is independent of the presence of a condensate. Still, an additional overestimation of the condensate fraction comes from the fact that the condensed pairs are concentrated in the high density region of the cloud, where the conversion efficiency is higher. However, this does not affect the total molecular signal.

Appendix C

Direct Observation of the Superfluid Phase Transition in Ultracold Fermi Gases

This appendix contains a reprint of Ref. [19]: Martin W. Zwierlein, Christian H. Schunck, André Schirotzek & Wolfgang Ketterle, *Direct Observation of the Superfluid Phase Transition in Ultracold Fermi Gases*, Nature **442**, 56 (2006).

nature Vol 442|6 July 2006|doi:10.1038/nature04936

LETTERS

Direct observation of the superfluid phase transition in ultracold Fermi gases

Martin W. Zwierlein[1], Christian H. Schunck[1], André Schirotzek[1] & Wolfgang Ketterle[1]

Phase transitions are dramatic phenomena: water freezes into ice, atomic spins spontaneously align in a magnet, and liquid helium becomes superfluid. Sometimes, such a drastic change in behaviour is accompanied by a visible change in appearance. The hallmark of Bose–Einstein condensation and superfluidity in trapped, weakly interacting Bose gases is the sudden formation of a dense central core inside a thermal cloud[1–7]. However, in strongly interacting gases—such as the recently observed fermionic superfluids[8]—there is no longer a clear separation between the superfluid and the normal parts of the cloud. The detection of fermion pair condensates has required magnetic field sweeps[9–11] into the weakly interacting regime, and the quantitative description of these sweeps presents a major theoretical challenge. Here we report the direct observation of the superfluid phase transition in a strongly interacting gas of ^{6}Li fermions, through sudden changes in the shape of the clouds—in complete analogy to the case of weakly interacting Bose gases. By preparing unequal mixtures of the two spin components involved in the pairing[12,13], we greatly enhance the contrast between the superfluid core and the normal component. Furthermore, the distribution of non-interacting excess atoms serves as a direct and reliable thermometer. Even in the normal state, strong interactions significantly deform the density profile of the majority spin component. We show that it is these interactions that drive the normal-to-superfluid transition at the critical population imbalance of 70 ± 5 per cent (ref. 12).

The dramatic signature of Bose–Einstein condensation in weakly interacting gases in atom traps derives from a natural hierarchy of energy scales: the critical temperature for condensation, $T_C \propto n^{2/3}$ at particle density n, is much larger than the chemical potential (divided by the Boltzmann constant k_B) of a pure condensate, $\mu \propto na$, which measures the interaction strength between particles (a is the scattering length). Hence, for weak (repulsive) interactions ($a > 0$, $na^3 \ll 1$), the condensate is clearly distinguished from the cloud of uncondensed particles through its smaller size and higher density. However, as the interactions are increased, for example by tuning a using a Feshbach resonance, this hierarchy of energy scales breaks down, as μ can now become comparable to $k_B T_C$. In Fermi gases with weak attractive interaction ($a < 0$, $n|a|^3 \ll 1$), the chemical potential is given by the Fermi energy E_F and will even far exceed the superfluid transition temperature $k_B T_C \propto E_F e^{-\pi/2k_F|a|}$ (where $k_F \propto n^{1/3}$ is the Fermi wave vector). Both the normal and the condensed cloud will here be of the same size and shape, dependent only on E_F and the trapping potential.

The phase transition from the normal to the superfluid state, although dramatic in its consequences, is thus not revealed by a major change in the appearance of the gas. Indeed, in strongly interacting Fermi gases no deviation from a normal cloud's shape has so far been detected, either in the unitary regime, where a diverges, or on the attractive Bardeen–Cooper–Schrieffer (BCS) side of a Feshbach resonance. Theoretical works predicted small 'kinks'[14–16] or other slight deviations[17] in the density profiles of the gas in the superfluid regime, but after line-of-sight integration these effects have so far been too small to be observable. Condensates could only be observed via rapid magnetic field ramps to the Bose–Einstein condensate (BEC) side ($a > 0$) of the Feshbach resonance, performed during expansion[9,10]. This suddenly reduced the condensate's chemical potential, and let the thermal fraction grow beyond the condensate size. A similar ramp was used to detect vortices on resonance and on the BCS side in the demonstration of fermionic superfluidity[8]. However, these magnetic field ramps are difficult to model theoretically, and a satisfactory quantitative comparison of, for example, the condensate fraction with experiments has not been accomplished[18–21].

In this work we demonstrate that the normal-to-superfluid phase transition in a strongly interacting Fermi gas can be directly observed in absorption profiles, without the need for any magnetic field ramps. As in the case of weakly interacting BECs, preparation, expansion and detection of the sample all take place at the same, fixed magnetic field and scattering length. As for BECs, the phase transition is observed as a sudden change in the shape of the cloud during time-of-flight expansion, when the trap depth is decreased below a critical value. To clearly distinguish the superfluid from the normal component, we break the number symmetry between spin-up (majority atom number, $N_\uparrow$) and spin-down (minority atom number, $N_\downarrow$) and produce an unequal mixture of fermions (imbalance parameter $\delta = (N_\uparrow - N_\downarrow)/(N_\uparrow + N_\downarrow)$). Standard BCS superfluidity requires equal densities of the two spin components. Hence, when cooled below the phase transition the cloud should show a sudden onset of a superfluid region of equal densities. Indeed, below a critical temperature, we observe how the density distribution of the minority component becomes bimodal.

Breaking the symmetry in atom numbers thus produces a direct and striking signature of the superfluid phase transition[22–24]. A similar situation has been encountered in Bose–Einstein condensation, where breaking the symmetry of a spherical trap resulted in dramatic anisotropic expansion of the condensate, now a hallmark of the BEC phase transition.

Figure 1 shows column density profiles of the two imbalanced spin states for different points along the evaporation path corresponding to different temperatures, and for three magnetic fields that correspond to the BEC side, exact resonance and the BCS side of the resonance. For large final trap depths (upper panels in Fig. 1), the smaller cloud has the expected shape of a normal, non-superfluid gas: it is very well fitted using a single, finite temperature Thomas–Fermi-profile (with central optical density, radius and the fugacity as independent fit-parameters). However, below a critical trap depth, a second, denser feature appears in the centre of the minority component (lower panels in Fig. 1). This onset of bimodality occurs very suddenly as the trap depth is lowered, as can be seen from Fig. 2: Around the critical point, the atom number (Fig. 2a) and population

---

[1] Department of Physics, MIT-Harvard Center for Ultracold Atoms, and Research Laboratory of Electronics, MIT, Cambridge, Massachusetts 02139, USA.

imbalance (Fig. 2b) are practically constant, and the temperature (Fig. 2c) varies in a smooth linear way with the trap depth. In contrast, below the critical trap depth, the shape of the smaller cloud starts to deviate drastically from the Thomas–Fermi distribution of a normal gas, as quantified in Fig. 2d. This sudden increase in the standard deviation of a fit to a single-component fitting function is a standard way of identifying the BEC phase transition in a model-independent way[2].

Figure 2e displays the fact that below the critical trap depth a new, third radius is required to describe the two clouds. As we will see below, the appearance of this central feature coincides with the appearance of the fermion pair condensate in experiments involving the magnetic field ramp technique[10–12]. It is this condensate that contains the superfluid vortices in refs 8 and 12. We are thus naturally led to interpret the central core as the condensate of fermion pairs, and the outer wings as the normal, uncondensed part of the cloud. This constitutes, to our knowledge, the first direct observation of the normal-to-superfluid phase transition in resonantly interacting Fermi gases on resonance and on the BCS side (that is, without a magnetic field sweep that so far cannot be quantitatively accounted for).

Already at high temperatures, above the phase transition, the larger cloud's profile is strongly deformed in the presence of the smaller cloud, a direct signature of interaction. Indeed, on resonance the cloud size of the minority component is significantly smaller than that of a non-interacting sample with the same number of atoms (see Fig. 2e). At the phase transition, the outer radii of the clouds do not change abruptly. This demonstrates that interactions, not superfluidity, are the main mechanism behind the reduced cloud size of an interacting Fermi gas.

On the BEC side, the condensate is clearly visible in the larger cloud. On resonance, however, the condensate is not easily discernible in the larger component's profiles at the scale of Fig. 1. Nevertheless, we have found a very faint but reproducible trace of the condensate when analysing the curvature of these column density profiles (see Supplementary Fig. S1). On resonance and on the BCS side, the onset of bimodality in the smaller cloud can be clearly observed for imbalances larger than ~20% (but below a certain critical imbalance, see below), for which the condensate is small compared to the minority cloud size. With increasing magnetic field on the BCS side (that is, with decreasing interaction strength), the bimodality becomes less pronounced and is not clearly discerned beyond 853 G (interaction parameter $1/k_F a < -0.15$).

Thermometry of strongly interacting Fermi gases has always been a major difficulty in experiments on strongly interacting fermions[25]. A thermometer can only be reliable if the working substance is not affected by the sample to be measured. In equal mixtures of fermions, the two overlapping atomic clouds are strongly interacting throughout. Temperatures determined from a non-interacting Thomas–Fermi fit to these clouds need calibration based on approximate theoretical calculations[25]. In addition, as will be reported elsewhere, we find that those fits do not describe the profiles of a partially superfluid Fermi gas as well as they do in the normal state, in agreement with theory[14–17]. In the case of imbalanced mixtures, the wings of the larger component, where the spin-down species are absent, are non-interacting and thus serve as a direct thermometer (see Fig. 2c). For an imbalance of $\delta = 75 \pm 3\%$ we determine the critical temperature for the phase transition on the BEC side at $1/k_F a = 0.46$ to be $T/T_F = 0.18(3)$ ($k_B T_F = \hbar\omega(3(N_\uparrow + N_\downarrow))^{1/3} \equiv \hbar^2 k_F^2/2m$ is the Fermi energy of a non-interacting, equal mixture with the same total number of fermions $N_\uparrow + N_\downarrow$, $\omega/2\pi$ is the

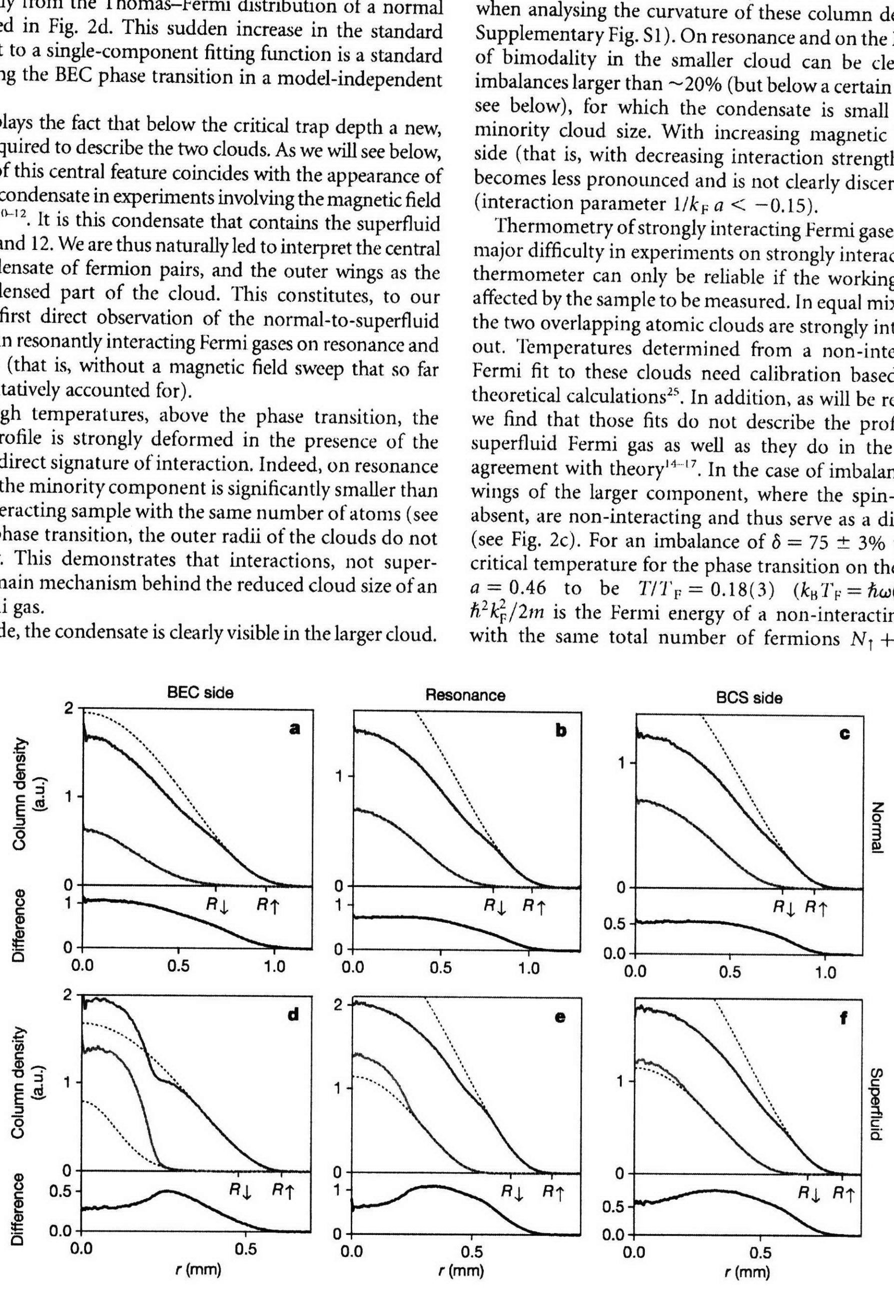

Figure 1 | Direct observation of the phase transition in a strongly interacting two-state mixture of fermions with imbalanced spin populations. Top (**a**–**c**) and bottom (**d**–**f**) rows show the normal and the superfluid state, respectively. Panels **a** and **d** were obtained in the BEC regime (at $B = 781$ G), **b** and **e** on resonance (834 G), and **c** and **f** on the BCS side of the Feshbach resonance (853 G). The profiles represent the azimuthal average of the column density after 10 ms (BEC side) or 11 ms (on resonance and BCS side) of expansion. The appearance of a dense central feature in the smaller component marks the onset of condensation. The condensate causes a clear depletion in the difference profiles (bottom of each panel). Both in the normal and in the superfluid state, interactions between the two spin states are manifest in the strong deformation of the larger component. The dotted lines show Thomas–Fermi fits to the wings of the column density. The radii $R_\uparrow$ and $R_\downarrow$ mark the Fermi radius of a ballistically expanding, non-interacting cloud with atom number $N_\uparrow$, $N_\downarrow$. The trap depth U (in μK), the atom numbers, the population imbalance δ (in %), the interaction parameter $1/k_F a$, the temperature T (in nK) and the reduced temperature T/T_F were respectively: **a**, 4.8, 1.8×10^7 and 2.6×10^6, 75, 0.42, 350, 0.20; **b**, 3.2, 1.8×10^7 and 4.2×10^6, 63, 0 (resonance), 260, 0.15; **c**, 2.5, 1.5×10^7 and 4.5×10^6, 52, −0.13, 190, 0.12; **d**, 0.8, 6.5×10^6 and 1.5×10^6, 62, 0.67, 50, ≤0.05; **e**, 1.1, 1.5×10^7 and 3.8×10^6, 60%, 0 (resonance), 70, 0.06; **f**, 1.2, 1.3×10^7 and 4.4×10^6, 50, −0.15, 100, 0.08. a.u., arbitrary units.

geometric mean of the trapping frequencies, and m is the mass of ^{6}Li). This corresponds to $T/T_{C,\downarrow} = 0.55(9)$ when comparing the temperature to the critical temperature $T_{C,\downarrow}$ for Bose condensation in a non-interacting gas with $N_\downarrow$ bosons. The reduction in the critical temperature is a direct consequence of strong repulsive interactions between the molecules. On resonance, at $\delta = 59 \pm 3\%$, we find $T/T_F = 0.12(2)$, and on the BCS side ($1/k_F a = -0.14$) for $\delta = 53 \pm 3\%$ we obtain $T/T_F = 0.11(2)$. These are, to our knowledge, the first directly measured and reliable temperatures for the superfluid transition in strongly interacting Fermi gases. They may serve as a checkpoint for theoretical models.

We note that the critical temperature will in general depend on the population imbalance. For example, for large enough imbalance on resonance or on the BCS side, no condensate will form even at zero temperature[12], as we discuss below. Here, the critical temperature for superfluidity will be zero.

An important qualitative difference distinguishes the BEC side from resonance at the lowest temperatures. On the BEC side, the gas consists of only two parts—the superfluid core surrounded by a fully polarized degenerate Fermi gas of the excess species. On resonance and on the BCS side, however, there exists a third region, a normal state in which both species are mixed. Several recent theories describe

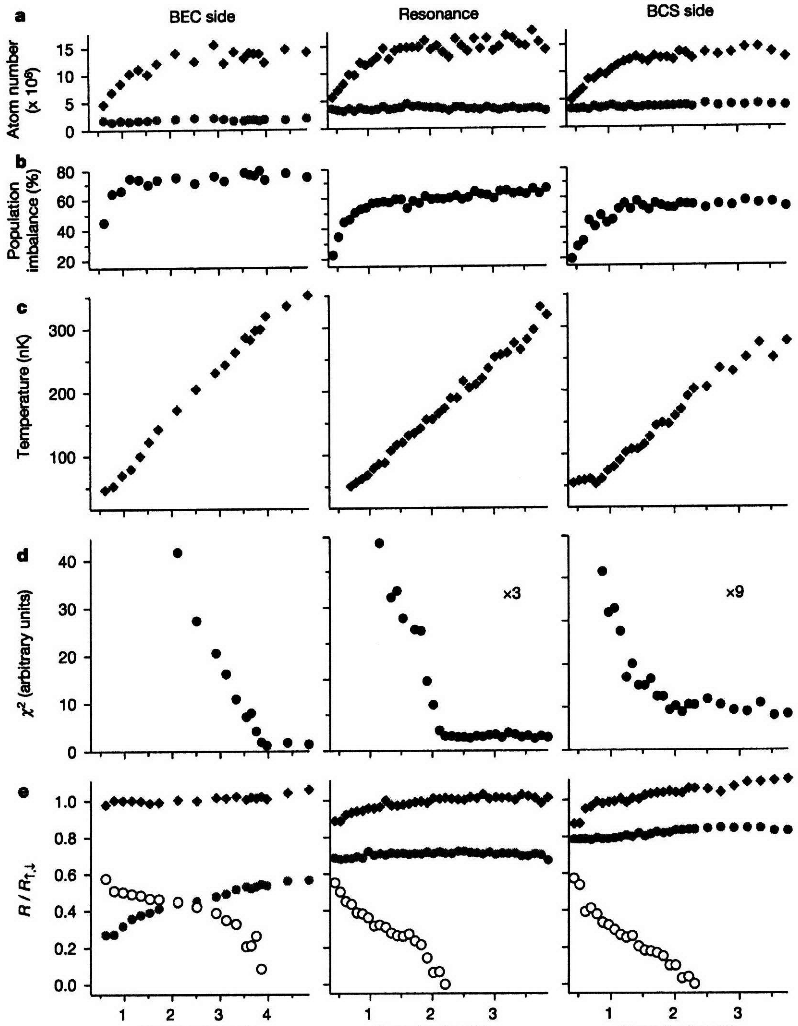

Figure 2 | Characterization of the phase transition. **a–e**, The data characterize the evolution of the fermion mixture as the cloud is evaporatively cooled by lowering the trap depth. The chosen magnetic fields are identical to those in Fig. 1. Data obtained from the majority (minority) cloud are shown as diamonds (circles). **a**, The atom number; **b**, the population imbalance between the two spin states; and **c**, the temperature of the spin mixture as determined from the non-interacting wings of the larger cloud's profile. **d**, A finite temperature Fermi–Dirac (for resonance and the BCS side) or gaussian (for the BEC side) distribution is fitted to the minority cloud; the phase transition is marked by a sudden increase in χ^2 as the condensate starts to appear. **e**, Outer radii of the majority and minority cloud (for the minority cloud on the BEC side, thermal cloud radius; all other cases, Thomas–Fermi radius) as well as the condensate radius (open circles), defined as the position of the 'kink' in the minority profile (see Fig. 1). The majority (minority and condensate) cloud size is normalized by the Fermi radius $R_\uparrow$ ($R_\downarrow$) of a non-interacting cloud with $N_\uparrow$ ($N_\downarrow$) atoms, and adjusted for ballistic (hydrodynamic) expansion. Note that the imbalance decreases during evaporation because the larger majority cloud incurs stronger evaporative losses. For the data, three (BEC and resonance) to five (BCS) independent measurements were averaged.

density profiles of imbalanced Fermi mixtures[26–32]. Mean-field theories that neglect interactions in the normal cloud and between the normal and condensed cloud are only in qualitative agreement with our results. Descriptions that exclude the mixed region or find superfluidity on resonance at all population imbalances are ruled out by our observations.

To elucidate the origin of the clear separation between condensate and normal components, we varied the population imbalance at our coldest temperatures and on resonance. Figure 3b shows several resulting profiles after 11 ms expansion from the trap. For large imbalances, $\delta > 70\%$, the minority cloud is not bimodal and well fitted by a (unconstrained) Thomas–Fermi profile. At a critical imbalance of $\delta \approx 70\%$, the condensate appears and then grows further as the imbalance is reduced (for the cloud radii, see Supplementary Fig. S2).

To characterize the appearance of the condensate for imbalances around $\delta = 70\%$, a Thomas–Fermi profile is fitted to the wings of the minority cloud. The fraction of atoms not contained in this fit is a measure of the condensate fraction (see Fig. 3). We find a critical imbalance of $\delta_c = 70(5)\%$ above which the condensate disappears. This agrees with our previous work[12], where we employed a rapid ramp method to the BEC side to extract the condensate fraction. We observed the quantum phase transition from the superfluid to the normal state as a critical population imbalance of $\delta_c = 70\%$ was exceeded. This strongly suggests that the bimodality observed here directly in the minority component, and the bimodality observed in molecular clouds after a magnetic field sweep, are signatures of the same phase transition.

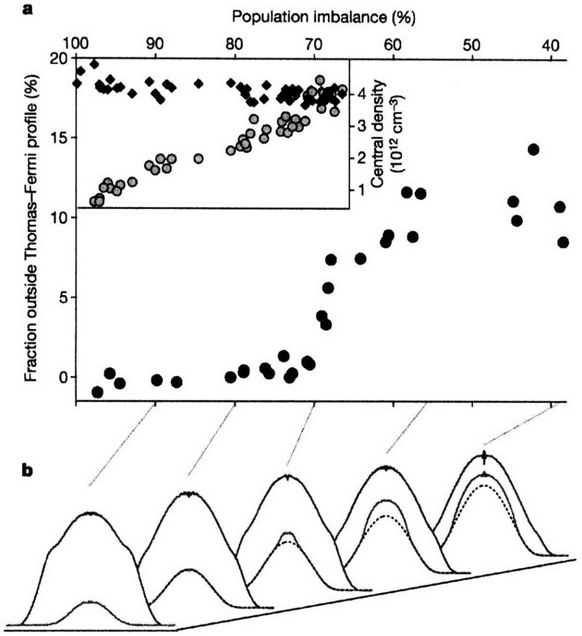

Figure 3 | Quantum phase transition to superfluidity for decreasing population imbalance. a, Main panel, the 'condensate fraction' of excess minority atoms, not contained in the Thomas–Fermi fit, versus population imbalance on resonance. **b,** Column density profiles of majority (blue) and minority (red) clouds, azimuthally averaged, for varying population imbalance. The condensate is clearly visible in the minority component as the dense central feature on top of the normal background (finite-temperature Thomas–Fermi fit, dotted lines). Below the critical imbalance $\delta_c = 70\%$, the condensate starts to form. The inset in **a** shows the central densities of the larger (black diamonds) and smaller (grey circles) cloud in the normal state above δ_c. This demonstrates that here the central densities are unequal, suppressing superfluidity. The densities were calculated from the central optical density and the fitted size of the clouds, assuming local density approximation and adjusting for ballistic (hydrodynamic) expansion of the outer radii of majority (minority) clouds. The data points for the condensate fraction show the average of several independent measurements.

The transition at δ_c is known as the Clogston limit of superfluidity[12,33], and occurs when the chemical potential difference $\delta\mu$ becomes larger than a constant times the (local) superfluid gap $\Delta(\mathbf{r})$ (see Supplementary Information). Here we present a simple picture for the character of this phase transition in a harmonic trap. Thomas–Fermi fits for the normal clouds beyond δ_c allow a simple estimate of the central three-dimensional density of the gas (with an estimated accuracy of 20% for the relative density difference), shown in the inset of Fig. 3. For large imbalances, we find that the three-dimensional densities differ significantly, as is expected for two weakly interacting Fermi clouds. As the imbalance is reduced towards the critical δ_c, the central densities approach each other and become approximately equal around δ_c. This is a direct consequence of strong interactions in the normal state. In a non-interacting Fermi mixture with an imbalance of δ_c, the central densities would differ by a factor of 2.4.

This observation now offers an intriguing insight into the nature of a fermionic superfluid on resonance or on the BCS side. Already in the normal state above T_C or beyond $\delta = \delta_c$, interactions between the two spin states are strong. Indeed, this is directly seen in the deformation of the majority cloud due to the presence of the minority species (see Figs 1, 3). However, here these interactions are not strong enough to let the central densities of the two clouds become comparable. At the critical imbalance the Clogston criterion $\delta\mu = c\Delta(\mathbf{r} = 0)$ is fulfilled in the centre of the trap (here, c is a constant that equals $\sqrt{2}$ in the BCS limit[33]). For smaller imbalance, a central superfluid region can form: the condensate. Its borders are defined by $\delta\mu < c\Delta(\mathbf{r})$. The simple density estimate in Fig. 3 suggests that in this region, the two clouds will have equal densities, although more refined techniques to measure small density differences have to be developed to finally settle this question. Outside the superfluid region there is still a normal state with unequal densities of minority and majority components. The discontinuity in the clouds' densities at the normal-to-superfluid phase boundary gives rise to the visible kink in the column density profiles. Such a density discontinuity is characteristic of a first-order phase transition.

Interestingly, most of the 'work' needed to build the superfluid state has already been done in the normal component by decreasing the density difference. Consequently, the critical population difference needed to form the superfluid is largely determined by the interactions in the normal gas.

In conclusion, we have observed the normal-to-superfluid phase transition through the direct observation of condensation in an imbalanced Fermi mixture—on the BEC side, on the BCS side, and right on the Feshbach resonance. Unequal mixtures offer a direct method of thermometry by analysing the non-interacting wings of the majority species. Strong interactions are already visible in the normal cloud as marked deformations of the majority profile. It is these interactions in the normal gas that squeeze the two components and eventually, at the critical imbalance, let them reach almost equal densities in the centre, aiding the formation of the superfluid. Our method of direct detection of the condensate is a powerful new tool to characterize the superfluid phase transition. At the current level of precision, the appearance of a condensate after magnetic field sweeps and the direct observation of the central dense core occur together, and indicate the normal-to-superfluid phase transition. An intriguing question is whether further phases are possible, including a more exotic superfluid state with unequal densities. Several theories predict that the Fulde–Ferrell–Larkin–Ovchinnikov state, a superfluid state with oscillating order parameter, should be present for imbalanced spin populations[24,26,28].

METHODS

Experimental procedure. Our experimental setup is described in previous publications[8,12]. A spin-polarized cloud of ^{6}Li fermions is cooled to degeneracy using a combination of laser cooling and sympathetic cooling with sodium atoms in a magnetic trap. After transfer into an optical trap, a variable spin mixture of the lowest two hyperfine states, labelled $|\uparrow\rangle$ and $|\downarrow\rangle$, is prepared at a magnetic bias field of 875 G. Interactions between the two spin states can be freely tuned via a 300-G-wide Feshbach resonance located at $B_0 = 834$ G. At fields below B_0, two-body physics supports a stable molecular bound state (BEC side), while at higher fields (BCS side), no such bound state exists for two isolated atoms. Our trap combines a magnetic saddle potential with a weakly focused (waist $w \approx 120\,\mu$m) infrared laser beam (wavelength $\lambda = 1{,}064$ nm), leading to a harmonic axial confinement with oscillation frequency of $\nu_z = 22.8(0.2)$ Hz and a gaussian radial potential with variable trapping frequency ν_r in the central harmonic region. The trap depth U is related to ν_r and ν_z by:

$$U = \frac{1}{4} m (2\pi \nu_r)^2 w^2 \left(1 - \frac{\nu_z^2}{2\nu_r^2} \ln\left(\frac{2(\nu_r^2 + \nu_z^2/2)}{\nu_z^2}\right)\right).$$

The initial degeneracy of the spin mixture is about $T/T_F \approx 0.3$. The strongly interacting gas is further cooled by decreasing the laser power of the optical trap over several seconds and evaporating the most energetic particles. During the first few seconds, the magnetic field is adiabatically ramped to a chosen final field in the resonance region where the last stage of the evaporation (shown in Fig. 2) takes place. For detection, the optical trap is switched off and the gas expands in the remaining magnetic saddle-point potential. After a variable time-of-flight, an absorption image of atoms either in state $|\uparrow\rangle$ or $|\downarrow\rangle$ is taken along the axial direction of the trap (the direction of the optical trapping beam). The cloud's radial symmetry allows for azimuthal averaging of the resulting column densities, leading to low-noise profiles[12].

For preparing clouds at the coldest temperatures (as shown in Fig. 3) with varying population imbalance, the spin mixture is evaporated down to a trap depth of $1\,\mu$K over several seconds on resonance, after which the trap depth is increased again to $1.4\,\mu$K for more harmonic confinement (trap frequencies: $\nu_r = 115(10)$ Hz and $\nu_z = 22.8(0.2)$ Hz). The temperature of the gas is determined to be $T/T_F \lesssim 0.06$ for all $\delta > 15\%$, and appears to smoothly rise to $T/T_F = 0.11$ for an equal mixture, although thermometry in the interacting wings is problematic. The total atom number was 1.5×10^7 and constant to within 15% for all values of δ.

Errors. The error in the critical temperature T_C/T_F for the phase transition is dominated by the uncertainty in the atom number entering the determination of T_F, which we estimate to be 30% (ref. 12). For T_F we use the harmonic approximation for the radially gaussian trapping potential, with the measured trapping frequencies reflecting the average curvature of the gaussian potential. The phase transition is observed above $U = 2\,\mu$K, where anharmonicities contribute only 3% to the error in T_F. Note that anharmonicities do not affect the temperature measurement performed on the majority wings: ballistic expansion of non-interacting atoms reveals their momentum distribution, regardless of the shape of the trap.

Received 6 March; accepted 23 May 2006.

1. Anderson, M. H., Ensher, J. R., Matthews, M. R., Wieman, C. E. & Cornell, E. A. Observation of Bose-Einstein condensation in a dilute atomic vapor. *Science* 269, 198–201 (1995).
2. Davis, K. B. *et al.* Bose-Einstein condensation in a gas of sodium atoms. *Phys. Rev. Lett.* 75, 3969–3973 (1995).
3. Greiner, M., Regal, C. A. & Jin, D. S. Emergence of a molecular Bose-Einstein condensate from a Fermi gas. *Nature* 426, 537–540 (2003).
4. Zwierlein, M. W. *et al.* Observation of Bose-Einstein condensation of molecules. *Phys. Rev. Lett.* 91, 250401 (2003).
5. Bartenstein, M. *et al.* Crossover from a molecular Bose-Einstein condensate to a degenerate Fermi gas. *Phys. Rev. Lett.* 92, 120401 (2004).
6. Bourdel, T. *et al.* Experimental study of the BEC-BCS crossover region in lithium 6. *Phys. Rev. Lett.* 93, 050401 (2004).
7. Partridge, G. B., Strecker, K. E., Kamar, R. I., Jack, M. W. & Hulet, R. G. Molecular probe of pairing in the BEC-BCS crossover. *Phys. Rev. Lett.* 95, 020404 (2005).
8. Zwierlein, M. W., Abo-Shaeer, J. R., Schirotzek, A., Schunck, C. H. & Ketterle, W. Vortices and superfluidity in a strongly interacting Fermi gas. *Nature* 435, 1047–1051 (2005).
9. Regal, C. A., Greiner, M. & Jin, D. S. Observation of resonance condensation of fermionic atom pairs. *Phys. Rev. Lett.* 92, 040403 (2004).
10. Zwierlein, M. W. *et al.* Condensation of pairs of fermionic atoms near a Feshbach resonance. *Phys. Rev. Lett.* 92, 120403 (2004).
11. Zwierlein, M. W., Schunck, C. H., Stan, C. A., Raupach, S. M. F. & Ketterle, W. Formation dynamics of a fermion pair condensate. *Phys. Rev. Lett.* 94, 180401 (2005).
12. Zwierlein, M. W., Schirotzek, A., Schunck, C. H. & Ketterle, W. Fermionic superfluidity with imbalanced spin populations. *Science* 311, 492–496 (2006). Published online 21 December 2005 (doi:10.1126/science.1122318).
13. Partridge, G. B., Li, W., Kamar, R. I., Liao, Y. & Hulet, R. G. Pairing and phase separation in a polarized Fermi gas. *Science* 311, 503–505 (2006). Published online 21 December 2005 (doi:10.1126/science.1122876).
14. Chiofalo, M. L., Kokkelmans, S. J. J. M. F., Milstein, J. N. & Holland, M. J. Signatures of resonance superfluidity in a quantum Fermi gas. *Phys. Rev. Lett.* 88, 090402 (2002).
15. Ho, T.-L. Universal thermodynamics of degenerate quantum gases in the unitarity limit. *Phys. Rev. Lett.* 92, 090402 (2004).
16. Perali, A., Pieri, P., Pisani, L. & Strinati, G. C. BCS-BEC crossover at finite temperature for superfluid trapped Fermi atoms. *Phys. Rev. Lett.* 92, 220404 (2004).
17. Stajic, J., Chen, Q. & Levin, K. Density profiles of strongly interacting trapped Fermi gases. *Phys. Rev. Lett.* 94, 060401 (2005).
18. Diener, R. B. & Ho, T.-L. Projecting fermion pair condensates into molecular condensates. Preprint at ⟨http://arxiv.org/cond-mat/0404517⟩ (2004).
19. Perali, A., Pieri, P. & Strinati, G. C. Extracting the condensate density from projection experiments with Fermi gases. *Phys. Rev. Lett.* 95, 010407 (2005).
20. Altman, E. & Vishwanath, A. Dynamic projection on Feshbach molecules: A probe of pairing and phase fluctuations. *Phys. Rev. Lett.* 95, 110404 (2005).
21. Chen, Q., Regal, C. A., Greiner, M., Jin, D. S. & Levin, K. Understanding the superfluid phase diagram in trapped Fermi gases. *Phys. Rev. A* 73, 041603 (2006).
22. Bedaque, P. F., Caldas, H. & Rupak, G. Phase separation in asymmetrical fermion superfluids. *Phys. Rev. Lett.* 91, 247002 (2003).
23. Caldas, H. Cold asymmetrical fermion superfluids. *Phys. Rev. A* 69, 063602 (2004).
24. Sheehy, D. E. & Radzihovsky, L. BEC-BCS crossover in "magnetized" Feshbach-resonantly paired superfluids. *Phys. Rev. Lett.* 96, 060401 (2006).
25. Kinast, J. *et al.* Heat capacity of a strongly-interacting Fermi gas. *Science* 307, 1296–1299 (2005).
26. Mizushima, T., Machida, K. & Ichioka, M. Direct imaging of spatially modulated superfluid phases in atomic fermion systems. *Phys. Rev. Lett.* 94, 060404 (2005).
27. Pieri, P. & Strinati, G. C. Trapped fermions with density imbalance in the Bose-Einstein condensate limit. *Phys. Rev. Lett.* 96, 150404 (2006).
28. Kinnunen, J., Jensen, L. M. & Törmä, P. Strongly interacting Fermi gases with density imbalance. *Phys. Rev. Lett.* 96, 110403 (2006).
29. De Silva, T. N. & Mueller, E. J. Profiles of near-resonant population-imbalanced trapped Fermi gases. *Phys. Rev. A* 73, 051602(R) (2006).
30. Yi, W. & Duan, L.-M. Trapped fermions across a Feshbach resonance with population imbalance. *Phys. Rev. A* 73, 031604(R) (2006).
31. Chevy, F. Density profile of a trapped strongly interacting Fermi gas with unbalanced spin populations. *Phys. Rev. Lett.* 96, 130401 (2006).
32. Haque, M. & Stoof, H. T. C. Pairing of a trapped resonantly-interacting fermion mixture with unequal spin populations. Preprint at ⟨http://arxiv.org/cond-mat/0601321⟩ (2006).
33. Clogston, A. M. Upper limit for the critical field in hard superconductors. *Phys. Rev. Lett.* 9, 266–267 (1962).

Supplementary Information is linked to the online version of the paper at www.nature.com/nature.

Acknowledgements We thank the participants of the Aspen winter conference on strongly interacting fermions for discussions. This work was supported by the NSF, ONR and NASA.

Author Information Reprints and permissions information is available at npg.nature.com/reprintsandpermissions. The authors declare no competing financial interests. Correspondence and requests for materials should be addressed to M.W.Z. (zwierlei@mit.edu).

Direct Observation of the Superfluid Phase Transition in Ultracold Fermi Gases

Martin W. Zwierlein, Christian H. Schunck, André Schirotzek, and Wolfgang Ketterle

Supplementary Information

Supplementary Figures

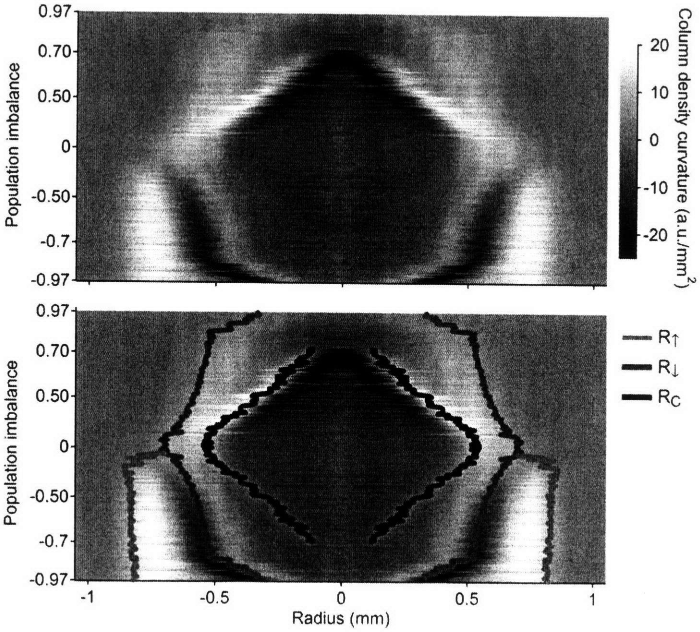

Supplementary Figure 1: (Color online) Signatures of the condensate on resonance in the spatial profiles. The curvature of the observed column density is encoded in shades of gray with white (black) corresponding to positive (negative) curvature. The outer radii of the two components and the condensate radius are shown as an overlay in the lower panel. As a direct consequence of strong interactions, the minority component causes a pronounced bulge in the majority density that is reflected in the rapid variation of the profile's curvature. The condensate is clearly visible in the minority component ($\delta > 0$), but also leaves a faint trace in the majority component ($\delta < 0$). The image was composed out of 216 individual azimuthally averaged column density profiles, smoothed to reduce technical noise. Data close to the cloud's center suffer from larger noise due to the lower number of averaged points. The central feature of about 50μm width is an artefact of smoothing in this region of increased noise.

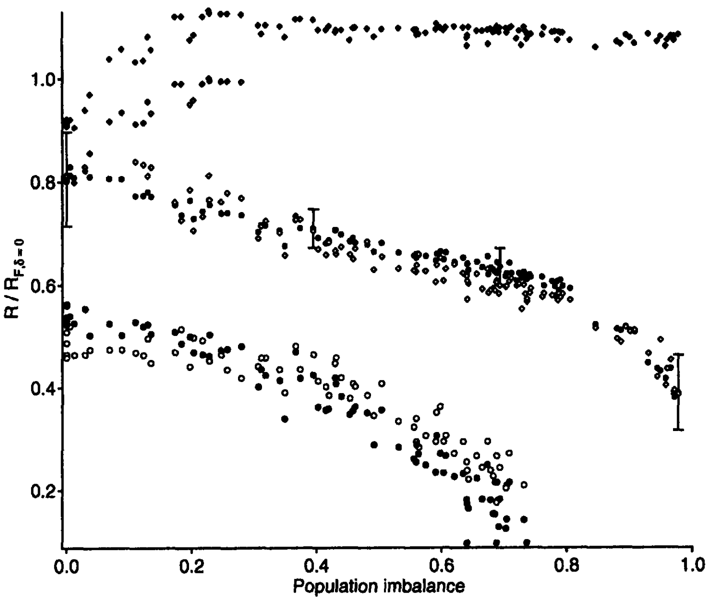

Supplementary Figure 2: Outer radii of the two cloud profiles and condensate radius versus population imbalance. Data obtained from the majority (minority) cloud are shown as diamonds (circles). The outer radii of the clouds (black) are determined from Thomas-Fermi fits to the profiles' wings, where the results of a zero-temperature and a finite temperature fit were averaged. For the minority cloud, the representative error bars indicate the difference between these two results. The position of the "bulge" in the majority profile (white diamonds) naturally follows the outer minority radius. The condensate radius is defined as the position of the "kink" in the minority profiles. It was obtained by a) fitting an increasing portion of the minority wings until a significant increase in χ^2 was observed (grey circles), and b) the position of the minimum in the profile's derivative (white circles). All sizes are scaled by the Fermi-radius of a non-interacting equal mixture. The minority radii were adjusted for the observed hydrodynamic expansion (expansion factor 11.0). The non-interacting wings of the majority cloud expand ballistically (expansion factor 9.7), as long as they are found a factor $11/9.7 = 1.13$ further out than the minority radius. For small imbalances ($\delta < 20\%$), also the majority wing's expansion will be affected by collisions. The grey diamonds give the majority cloud's outer radius if hydrodynamic expansion is assumed.

Supplementary Methods

Hydrodynamic vs. ballistic expansion

A non-interacting cloud of atoms simply expands ballistically from a trap. However, strongly interacting equal Fermi mixtures, above and below the phase transition, are collisionally dense and therefore expand according to hydrodynamic scaling laws [1–3]. These scaling laws only depend on the equation of state of the gas, $\epsilon \propto n^\gamma$, with $\gamma = 1$ for the BEC-side, $\gamma = 2/3$ for resonance (a direct consequence of unitarity) and $\gamma = 2/3$ for the BCS-side, away from resonance. In an unequal spin mixture of fermions, the expansion does not follow a simple scaling law. The minority cloud is always in contact with majority atoms and thus strongly interacting throughout the expansion, which is therefore hydrodynamic. The excess atoms in the wings of the larger cloud are non-interacting and will expand ballistically, as we have checked experimentally. The absorption images after expansion are taken along the axial direction of the trap (the direction of the optical trapping beam). In order to compare the expanded cloud sizes to the in-trap Fermi radii of non-interacting clouds (see Fig. 2 and Fig. S2 below) we scale the majority cloud with the ballistic factor for the radial direction

$$\sqrt{\cosh^2\left(2\pi\nu_z t/\sqrt{2}\right) + (\sqrt{2}\nu_r/\nu_z)^2 \sinh^2\left(2\pi\nu_z t/\sqrt{2}\right)},$$

where t is the expansion time and $\nu_z/\sqrt{2}$ gives the radial anti-trapping curvature of the magnetic saddle-point potential. The scaling factor for the hydrodynamic expansion of an equal mixture is given by the solution to a differential equation [2,3]. A priori, the minority cloud in unequal mixtures could expand with a different scaling, since the equation of state now depends on *two* densities. However, by imaging the cloud in trap and at different times during expansion, we found that the minority cloud's expansion is very well described by the scaling law for an equal mixture. In particular, the aspect ratio of the minority cloud did not change as a function of population imbalance (within our experimental error of 5%), and was equal to that of a balanced mixture.

For the data on resonance in Figs. 3, S1 and S2, which were obtained after 11 ms expansion out of a trap with radial (axial) frequency of $\nu_r = 113(10)$ Hz ($\nu_z = 22.8(0.2)$ Hz), the ballistic (hydrodynamic) expansion factor for the radial direction is 9.7 (11.0).

Supplementary Discussion

Signature of the condensate

Fig. S1 demonstrates that on resonance, the condensate is visible not only in the minority component, but also in the larger cloud as a small change in the profile's curvature. In the condensate region, the majority profile is slightly depleted when compared to the shape of a normal Fermi cloud. This effect is still significant on the BCS-side (see Fig. 1): Although here, the condensate is less visible in the smaller component than on resonance, the larger cloud's central depletion still produces a clear dip in the difference profile.

Radii in the unequal Fermi mixture

Fig. S2 shows the outer radii of the majority and minority cloud, together with the condensate radius (on resonance, for the deepest evaporation compatible with constant total atom number versus imbalance). As was the case for the phase transition at finite temperature, the outer cloud sizes change smoothly with imbalance. No drastic change is seen at the critical population imbalance. The radii are obtained by fitting the profiles' wings to the Thomas-Fermi expression for the radial column density $n(r)$:

$$n(r) = n_0 \frac{\mathrm{Li}_2\left(-\lambda^{1-r^2/R^2}\right)}{\mathrm{Li}_2\left(-\lambda\right)},$$

with the central column density n_0, the fugacity λ and the Thomas-Fermi radius R as the free parameters. $\mathrm{Li}_2(x)$ is the Dilogarithm. The zero-temperature expression reduces to $n(r) = n_0(1 - r^2/R^2)^2$.

Lower and upper bounds for the critical chemical potential difference at δ_c

For the clouds at the critical imbalance δ_c, we now want to extract a lower and upper bound for the difference in chemical potentials $\delta\mu_c$ of the majority and minority component. This difference allows us to conclude that BCS-type superfluidity with imbalanced densities is not possible.

The chemical potential difference $\delta\mu \equiv 2h = (\mu_\uparrow - \mu_\downarrow)$ measures the energy cost, relative to $\mu = (\mu_\uparrow + \mu_\downarrow)/2$, to add a particle to the cloud of excess fermions. Δ, the pairing gap, is the energy cost for this additional majority particle to enter the superfluid. Both the critical temperature T_C and the critical chemical potential difference $\delta\mu_c$ provide a measure of the superfluid gap: The superfluid can be either destroyed by raising the temperature or by increasing the population imbalance. If $h_c \equiv \delta\mu_c/2 < \Delta$, excess atoms will always stay outside the superfluid, in the phase separated normal state. For $h_c > \Delta$, excess atoms can enter the superfluid for $h_c > h > \Delta$. Hence, superfluidity with unequal densities, if allowed via $h_c > \Delta$, would be favored at large population imbalance, contrary to the interpretation in [4], where such a state was proposed for small population imbalance. A recent Monte-Carlo calculation [5] for the Clogston limit on resonance gives $h_c = 1.00(5)\Delta = 0.50(5)E_F$ and can thus not decide on the question of superfluidity with imbalanced densities.

We can attempt to extract the chemical potential from the cloud sizes $R_{\uparrow,\downarrow}$ - taking into account hydrodynamic expansion for the minority cloud and ballistic expansion for the excess fermions. For the majority cloud, we find $\mu_{c,\uparrow} = 1/2\, m\omega_r^2 R_\uparrow^2 = 1.21(6)E_F$. For the minority cloud, we find $1/2\, m\omega_r^2 R_\downarrow^2 = 0.39(10)E_F$. Throughout the smaller cloud, minority atoms are always strongly attracted by majority atoms. This strong attractive interaction likely reduces their chemical potential from the above upper limit. The difference of the chemical potentials $\delta\mu_c \equiv 2h_c$ is thus given by $h_c = (\mu_{c,\uparrow} - \mu_{c,\downarrow})/2 \geq 0.41(6)E_F = 0.51\mu$, our lower bound. Another condition on h_c concerns whether the normal state can be mixed, $h_c < \mu$, (minority and majority atoms in the same spatial region) or whether the normal state is always completely polarized $h_c > \mu$. Our observation of the mixed region in Fig. 1 immediately results in $h_c < \mu$, the upper bound.

On resonance, $\Delta = 1.16\mu$ in BCS-theory, while a recent Monte-Carlo study [5] obtains $\Delta = 1.2\mu$. If $\Delta > \mu$ holds true, our finding of the upper bound on h_c would imply $h_c < \Delta$ and hence would exclude a superfluid with unequal spin densities (at least on the basis of BCS-theory, see [6] for a recent suggestion which goes beyond BCS).

Supplementary Notes

1. O'Hara, K. M., Hemmer, S. L., Gehm, M. E., Granade, S. R. & Thomas, J. E. Observation of a strongly interacting degenerate fermi gas of atoms. *Science* **298**, 2179 (2002).
2. Menotti, C., Pedri, P. & Stringari, S. Expansion of an Interacting Fermi gas. *Phys. Rev. Lett.* **89**, 250402 (2002).
3. Castin, Y. Exact scaling transform for a unitary quantum gas in a time dependent harmonic potential. *Comptes Rendus Physique* **5**, 407–410 (2004).
4. Partridge, G. B., Li, W., Kamar, R. I., a. Liao, Y. & Hulet, R. G. Pairing and Phase Separation in a Polarized Fermi Gas. *Science* **311**, 503 (2006). Published online 21 December 2005 (10.1126/science.1122876).
5. Carlson, J. & Reddy, S. Asymmetric Two-Component Fermion Systems in Strong Coupling. *Phys. Rev. Lett.* **95**, 060401 (2005).
6. Ho, T.-L. & Zhai, H. Homogeneous Fermion Superfluid with Unequal Spin Populations. Preprint at <http://arxiv.org/cond-mat/0602568> (2006).

Appendix D

Superfluid Expansion of a Rotating Fermi Gas

This appendix contains a reprint of Ref. [17]: C. H. Schunck, M.W. Zwierlein, A. Schirotzek, and W. Ketterle, *Superfluid Expansion of a Rotating Fermi Gas*, Phys. Rev. Lett. **98**, 050404 (2007).

PRL 98, 050404 (2007) PHYSICAL REVIEW LETTERS week ending 2 FEBRUARY 2007

Superfluid Expansion of a Rotating Fermi Gas

C. H. Schunck, M. W. Zwierlein, A. Schirotzek, and W. Ketterle
Department of Physics, MIT-Harvard Center for Ultracold Atoms, and Research Laboratory of Electronics, MIT, Cambridge, Massachusetts 02139, USA

(Received 11 July 2006; published 1 February 2007)

We study the expansion of a rotating, superfluid Fermi gas. The presence and absence of vortices in the rotating gas are used to distinguish the superfluid and normal parts of the expanding cloud. We find that the superfluid pairs survive during the expansion until the density decreases below a critical value. Our observation of superfluid flow in the expanding gas at $1/k_F a = 0$ extends the range where fermionic superfluidity has been studied to densities of 1.2×10^{11} cm^{-3}, about an order of magnitude lower than any previous study.

DOI: 10.1103/PhysRevLett.98.050404 PACS numbers: 03.75.Ss, 03.75.Hh, 03.75.Kk, 03.75.Lm

Ultracold atomic gases have been used to create novel quantum many-body systems ranging from Bose-Einstein condensates and Mott insulators in optical lattices to high-temperature superfluids of strongly interacting fermions. These systems offer a high degree of control over physical parameters including interaction strength and density. Many important features in these gases have a spatial scale too small to be resolved while the gas is trapped. A standard technique to reveal this physics is to switch off the confining potential and release the gas. A noninteracting gas expands ballistically and the expansion reveals its momentum distribution. The expansion dynamics of an interacting gas is modified by the effect of collisions. This can result in classical hydrodynamic flow and in this case the expansion serves as a (not necessarily linear) magnifying glass for the trapped state. In contrast to classical hydrodynamics, superfluid hydrodynamic flow does not rely on collisions. When a weakly interacting Bose-Einstein condensate (BEC) is released from an anisotropic trapping potential, superfluid hydrodynamics leads to an inversion of the aspect ratio, often regarded as a hallmark of Bose-Einstein condensation [1].

The expansion dynamics of strongly interacting Fermi gases have been the subject of a long-standing debate. For a weakly interacting ultracold Fermi gas anisotropic expansion has been proposed as a probe for superfluidity, analogous to the case of weakly interacting BECs [2]. Anisotropic expansion has been experimentally observed in strongly interacting Fermi gases [3–5]. In this case, however, the inversion of the aspect ratio can occur due to collisions between the expanding atoms even if they were initially at zero temperature [6,7]. So far experiments have not been able to discriminate between superfluid and collisional hydrodynamics in expansion and indeed one would expect both effects to contribute: In the BCS regime, the superfluid transition temperature T_C depends exponentially on the density. Starting at $T < T_C$, the superfluid gas expands according to superfluid hydrodynamics. As the density drops, T approaches T_C and superfluidity cannot be maintained. From this point on, the gas should expand according to collisional hydrodynamics or enter a regime intermediate between collisional hydrodynamic and collisionless expansion.

In this Letter we study the expansion of a superfluid Fermi gas, in the regime where pairing is purely a many-body effect. We have observed superfluid flow even after 5 ms of expansion, when the cloud size had increased by more than a factor of 4 and the peak density had dropped by a factor of 17 compared to the in-trap values.

Superfluidity in Fermi gases has previously been established through the observation of vortex lattices [8,9]. To detect vortices in a rotating fermion-pair condensate the pairs are transferred into stable molecules by sweeping an external magnetic field across a Feshbach resonance shortly after the gas is released from the trap. Vortices can be observed only when the gas is still a superfluid at the moment of the magnetic field sweep [10]. At the final magnetic field (on the BEC side of the Feshbach resonance) the interactions are much weaker. Therefore the vortex core has higher contrast and is larger than near resonance. If the gas is no longer superfluid at the time of the field ramp, we expect the vortex core to fill in quickly and disappear. The observed vortex cores therefore serve as markers for the regions which are superfluid at the time of the magnetic field ramp.

Our experimental setup has been described earlier [11,12]. ^{6}Li fermion-pair condensates containing 5×10^6 fermions were created in an optical dipole trap at a magnetic field of 812 G. This is on the BEC side of a Feshbach resonance at $B_0 = 834$ G. At magnetic fields below (above) B_0, on the BEC (BCS) side, the scattering length a is positive (negative) and a nearby molecular bound state exists (does not exist). The radial and axial trapping frequencies were $\omega_r = 2\pi \times 120$ Hz and $\omega_a = 2\pi \times 23$ Hz, respectively. To observe vortices as a probe of superfluid flow, the gas was set in rotation: two blue-detuned laser beams were rotated symmetrically around the cloud for 1 s at an angular frequency of $2\pi \times 80$ Hz [8]. We allowed 500 ms of equilibration before the magnetic field was ramped (in 500 ms) to several probe fields on the BCS side of the resonance. Finally, we studied the expansion of the rotating superfluid: The gas was released

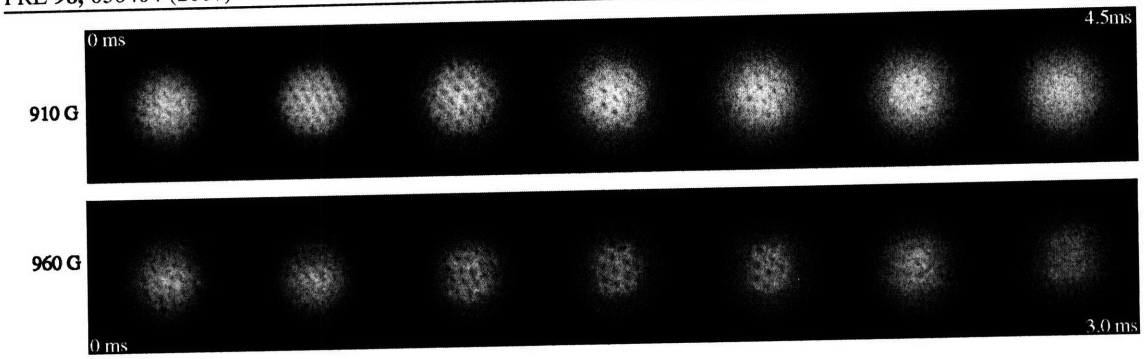

FIG. 1. Superfluid expansion of a strongly interacting rotating Fermi gas. Shown are absorption images for different expansion times on the BCS side of the Feshbach resonance at 910 G (0.0, 1.0, 2.0, 3.0, 3.5, 4.0, and 4.5 ms) and 960 G (0.0, 0.5, 1.0, 1.5, 2.0, 2.5, and 3 ms), before the magnetic field was ramped to the BEC side for further expansion. The vortices served as markers for the superfluid parts of the cloud. Superfluidity survived the expansion for several milliseconds and was gradually lost from the low density edges of the cloud towards its center. Compared to 910 G ($a = -7200a_0$), superfluidity decayed faster at 960 G ($a = -5000a_0$) due to the reduced interaction strength. The total expansion time remained constant [14]. The field of view of each image is 1.2 mm × 1.2 mm.

from the optical trap and expanded at the probe field for a variable "BCS-expansion" time t_{BCS}, that was increased in 500 μs steps. To transfer the remaining fermion pairs into stable molecules the magnetic field was then lowered in 400 μs to 680 G [13]. Here, the cloud was given several milliseconds of "BEC expansion." For absorption imaging the magnetic field was raised to 730 G in 500 μs before the last 2 ms of time of flight. For most of the data the total time of flight was chosen to be 11 ms [14]. An absorption image of the gas was obtained separately at t_{BCS} to determine the peak density and the peak Fermi momenta k_F before the magnetic field sweep.

Figure 1 shows absorption images taken as outlined above for seven different BCS-expansion times at both 910 and 960 G. The presence of vortices proves that superfluid fermion pairs survived in the expanding gas. As the density of the gas dropped during the BCS expansion the vortices were gradually lost from the low density edges of the cloud towards its center. After 4.5 ms time of flight at 910 G and 3 ms at 960 G all of the vortices had decayed. If we regard the number of vortices as an indicator of the superfluid fraction of the gas, we can draw the "phase diagram" of Fig. 2. Here the number of vortices is shown as a function of the inverse scattering length $1/a$ and the inverse peak Fermi momentum $1/k_F$. As $1/k_F$ increases at a given magnetic field, corresponding to the decrease in density during time of flight, vortices are lost. The reduction in the number of vortices for decreasing $|a|$ reflects the decrease of the superfluid fraction for smaller attractive interactions at a given temperature. In addition, the increase in the normal fraction leads to higher damping of the remaining vortex number [8]. Most importantly, however, we see that vortices are lost earlier in time of flight as the interactions are reduced.

At all magnetic fields the peak interaction strength at the point where all vortices were lost is about constant, $k_F a \sim -0.8$ (Fig. 3). As shown in Fig. 1 the loss of vortices occurred gradually and the surviving vortices were located within a circle of decreasing radius. We assume that the critical value of $k_F a$ for which superfluidity was lost, was first reached at the edge of the cloud and subsequently further inward. However, we were not able to confirm this

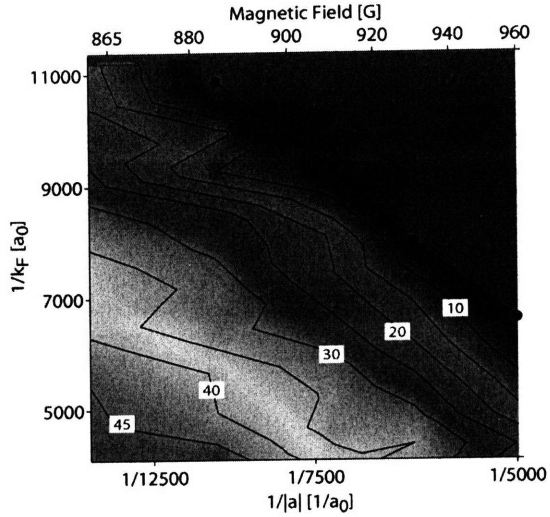

FIG. 2 (color online). "Phase diagram" of an expanding, rotating Fermi gas: At a given magnetic field the number of vortices served as a measure for the size of the superfluid region in the gas. The number of vortices is plotted versus $1/k_F$ and $1/|a|$. The contour plot was created from a total of 53 data points. In this diagram lines of constant $k_F a$ correspond to hyperbolas. The vortices decayed when the density (increasing $1/k_F$) or the scattering length (increasing $1/|a|$) was reduced. For weaker interactions, at smaller scattering lengths $|a|$, vortices were lost already at higher densities. The four data points shown mark the breakdown of superfluidity and are the same as the squares in Fig. 3.

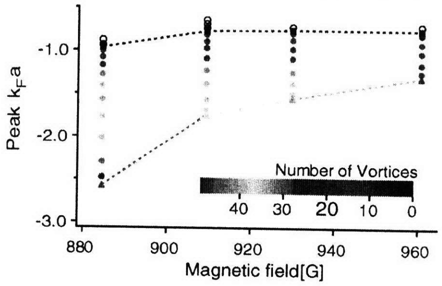

FIG. 3 (color online). The peak interaction strength during superfluid expansion. Starting at a peak k_Fa in the optical trap (triangles) vortices survived up to a critical peak k_Fa of -0.8 ± 0.1 (squares), almost independent of the magnetic field (scattering length). Solid circles correspond to partially superfluid, open circles to normal clouds. The observed number of vortices is color coded. The critical k_Fa was obtained for each magnetic field separately by taking the average of the peak k_F of the last partially superfluid and the first completely normal cloud. The error in k_Fa is about 10% and dominated by the systematic error in the atom number.

picture quantitatively without a model that describes how the shape of the cloud and the bimodality develop during and after the magnetic field sweep.

It is remarkable that the observation of superfluidity and fermion-pair condensation for *trapped* gases has also been limited to values of $k_F|a|$ larger than 1 on the BCS side [8,12,15]. This suggests that the underlying reason for this limitation is the same for a trapped and an expanding gas. One obvious scenario for the decay of the vortex lattice during expansion is the breakdown of superfluidity due to finite temperature when a critical interaction strength is reached. As the density decreases, T_C/T_F drops while T/T_F remains constant (since the phase space density $n \times T^{-3/2}$ is invariant during expansion). Therefore T_C eventually becomes smaller than T everywhere in the cloud. The critical interaction strength can be estimated by equating $1 \equiv T/T_C = (T/T_F)(T_F/T_C) = 1.76(T/T_F)(E_F/\Delta)$. Here $\Delta = (2/e)^{7/3}E_F \exp(-\pi/2k_F|a|)$ is the pairing gap in the BCS limit (valid for $k_F|a| \lesssim 1$) [16], where the peak Fermi energy $E_F = \hbar^2 k_F^2/2m$ and k_F are density dependent. For an estimate of our lowest temperatures of $T/T_F = 0.05$ [17] this gives $k_Fa = -0.9$ close to the observed value. This finite-temperature scenario implies that the superfluid state evolves adiabatically during expansion, which is plausible: Even when the critical k_Fa is reached, the pair binding energy changes at a slower rate, $\dot{\Delta}/\Delta$, than the rate at which the pairs can respond to this change, $\Delta/\hbar$ [18]. For weakly interacting BECs, the decay of vortex lattices at finite temperature was studied theoretically [19], and similar structures are found.

In analogy to the critical magnetic field H_{c2} in type-II superconductors, superfluidity can also break down in response to rapid rotation [20,21]. However, Ref. [21] predicts that superfluidity is stable in the strongly interacting regime ($k_F|a| > 1.029$) at all rotation frequencies up to the trap frequency. Since our estimated rotation frequencies are much smaller [22] we believe that the observed breakdown of superfluidity at $k_F|a| = 0.8$ is mainly due to finite temperature, and only weakly affected by rotation. This is consistent with the observation that vortices disappear in rotating clouds at approximately the same k_Fa at which fermion-pair condensates disappeared in experiments with nonrotating clouds.

Another explanation for the loss of vortices is a failure of the transfer of correlated fermion pairs into molecules since the size of the fermion pairs increases with decreasing density. When the fermion-pair size becomes larger than the interparticle spacing, molecules might be formed out of uncorrelated nearest neighbors rather than out of correlated pairs. The magnetic field sweep then destroys the coherent many-body wave function.

Vortices [8,9] and bimodal density distributions [12,15] are indicators for superfluidity and pair condensation, respectively. If a fermion-pair condensate is transferred to the BEC side before its interaction energy has been converted into kinetic energy, it continues to expand with the drastically reduced mean-field energy of a molecular BEC at 680 G. This results in a clear separation of condensate and thermal cloud after further BEC expansion. If the transfer of fermion pairs into molecules is delayed after releasing the gas from the trap, the fermion-pair condensate initially expands just like the normal part of the cloud. This eventually leads to a loss of bimodality in the density profiles after the transfer. We can now study how the two indicators, vortices and bimodality, are related in this experiment. For short BCS expansion t_{BCS} our data showed bimodality as well as vortices. However, bimodality was gradually lost and could not be discerned after longer BCS

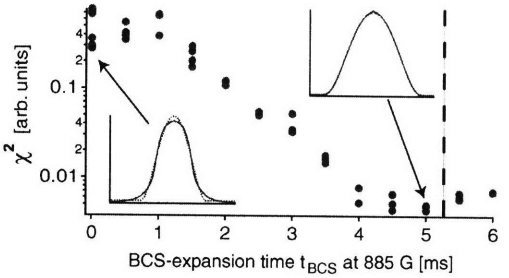

FIG. 4 (color online). Disappearance of bimodality. Zero temperature Thomas-Fermi profiles (dotted) were fit to density profiles (solid) obtained after BCS expansion at 885 G and subsequent BEC expansion at 680 G. The χ^2 of the fit was monitored as a function of the BCS-expansion time t_{BCS}. A high χ^2 indicates a bimodal density distribution. Vortices were still observed after 5 ms of expansion (indicated by the dashed line in the figure) while bimodality had already disappeared (for χ^2 values smaller than 0.01 bimodality cannot be discerned). Hence, the absence of bimodality does not imply an absence of superfluidity.

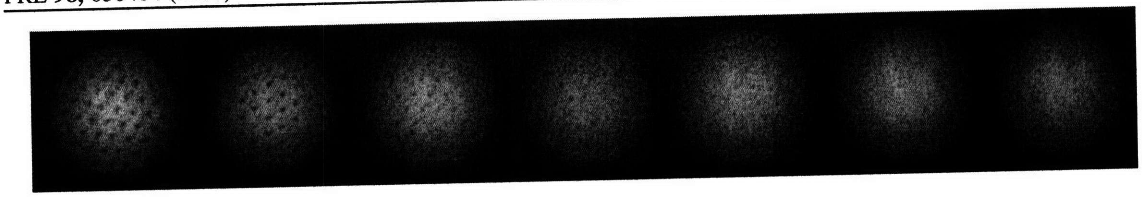

FIG. 5. Loss of vortex contrast on resonance at 834 G. Shown are absorption images after a fixed total time of flight, but for different expansion times on resonance (2, 2.5, 3, 3.5, 4, 5, and 6 ms) before the magnetic field was swept to the BEC side for further expansion. A gradual loss of the vortex contrast from about 15% (after 2 ms of expansion on resonance) to 3% (after 5 ms) was observed across the whole cloud. The field of view of each image is 1.2 mm × 1.2 mm.

expansion although vortices were still visible (see Fig. 4 for details). The absence of bimodality therefore does not indicate a breakdown of superfluidity.

So far we have studied the expanding gas on the BCS side of the Feshbach resonance. On the BEC side and on resonance, T_C is proportional to T_F so that T/T_C is constant during expansion. Therefore, one would not expect to observe a breakdown of superfluidity. Figure 5 shows absorption images obtained after initial expansion of the cloud on resonance at 834 G. In contrast to the situation on the BCS side of the resonance no vortices were lost. Instead, the vortex contrast decreased uniformly across the cloud for longer expansion times. Vortices have been detected at total densities as low as 1.2×10^{11} cm^{-3} in the wings of the expanded cloud. Here the critical temperature T_C of approximately $0.2T_F$ [23,24] was below 20 nK ($k_B T_F$ is the local Fermi energy). We believe that the decrease in vortex contrast is due to the low density of the gas after long expansion on resonance: after the magnetic field sweep the vortex cores cannot adjust quickly enough to the high contrast and large size they would have in equilibrium on the BEC side. This reduction of contrast limited our study of the breakdown of superfluidity to magnetic fields above 880 G.

In conclusion, we have shown that superfluid pairs can survive during the expansion of a strongly interacting Fermi gas. This is the first observation of nonequilibrium superfluid flow in such systems. It has allowed us to observe fermionic superfluidity at total densities as low as 1.2×10^{11} cm^{-3}. Our results show that future experiments with expanding, superfluid Fermi gases can be carried out *in situ*, i.e., without magnetic field sweeps to the BEC side. An intriguing question is whether fermion pairs expanding from two clouds can coherently interfere.

We thank Gretchen Campbell for a critical reading of the manuscript. This research was supported by the NSF, ONR, and NASA.

---

[1] W. Ketterle *et al.*, in *Bose-Einstein Condensation in Atomic Gases* (IOS Press, Amsterdam, 1999), pp. 67–176.
[2] C. Menotti *et al.*, Phys. Rev. Lett. **89**, 250402 (2002).
[3] K. M. O'Hara *et al.*, Science **298**, 2179 (2002).
[4] C. A. Regal *et al.*, Phys. Rev. Lett. **90**, 230404 (2003).
[5] T. Bourdel *et al.*, Phys. Rev. Lett. **91**, 020402 (2003).
[6] S. Gupta *et al.*, Phys. Rev. Lett. **92**, 100401 (2004).
[7] B. Jackson *et al.*, Europhys. Lett. **67**, 524 (2004).
[8] M. W. Zwierlein *et al.*, Nature (London) **435**, 1047 (2005).
[9] M. W. Zwierlein *et al.*, Science **311**, 492 (2006).
[10] The sweep time is much faster than the formation time of a vortex lattice in the trap, which is several hundred milliseconds. Detection of vortices after the ramp therefore proves their presence before the ramp [8].
[11] Z. Hadzibabic *et al.*, Phys. Rev. Lett. **91**, 160401 (2003).
[12] M. W. Zwierlein *et al.*, Phys. Rev. Lett. **92**, 120403 (2004).
[13] The ramp time was 200 μs for the data taken at 834, 865, and 885 G. We have checked that the rate of the magnetic field sweep to 680 G had no influence on the number of observed vortices within our measurement accuracy.
[14] To increase the visibility of the vortices for $t_{\mathrm{BCS}} = 0$ and 500 μs the total time of flight was increased to up to 15 ms and/or the power of the optical trap was increased by a factor of 4.5 during the last 2 ms of trapping [8].
[15] C. A. Regal *et al.*, Phys. Rev. Lett. **92**, 040403 (2004).
[16] L. P. Gor'kov *et al.*, Sov. Phys. JETP **13**, 1018 (1961).
[17] M. W. Zwierlein *et al.*, Nature (London) **442**, 54 (2006).
[18] We find $\frac{\hbar\dot{\Delta}}{\Delta^2} = \frac{\hbar}{\Delta} \times \frac{\dot{n}}{n} \times (\frac{2}{3} + \frac{\pi}{6k_F|a|})$. Because the gas expands to a very good approximation only radially, we assume that the density varies as $n(t) = n_0/(1 + \omega_r^2 t^2)$, and obtain $|\frac{\hbar\dot{\Delta}}{\Delta^2}| = \frac{\hbar}{\Delta} \frac{2\omega_r^2 t}{1+\omega_r^2 t^2} (\frac{2}{3} + \frac{\pi}{6k_F|a|})$. For the experimental parameters when the vortices in the center of the cloud are lost we find that $\hbar\dot{\Delta}/\Delta^2 \leq 0.4$.
[19] S. Kragset *et al.*, Phys. Rev. Lett. **97**, 170403 (2006).
[20] M. Y. Veillette *et al.*, Phys. Rev. Lett. **97**, 250401 (2006).
[21] H. Zhai *et al.*, Phys. Rev. Lett. **97**, 180414 (2006).
[22] At resonance we find an in-trap rotation frequency of about $\nu = 15$ Hz, assuming that the condensate and the Thomas-Fermi radii are approximately equal (see Fig. 5). Because of the complicated expansion dynamics during the magnetic field sweep we can only estimate the in-trap rotation frequencies at higher magnetic fields to lie in the range of $\nu = 6$ to $\nu = 15$ Hz, small compared to the radial trapping frequency of $\nu = 120$ Hz. During expansion, the rotation will slow down further.
[23] A. Bulgac *et al.*, Phys. Rev. Lett. **96**, 090404 (2006).
[24] E. Burovski *et al.*, Phys. Rev. Lett. **96**, 160402 (2006).

Appendix E

Pairing Without Superfluidity: The Ground State of an Imbalanced Fermi Mixture

This appendix contains a reprint of Ref. [23]: C. H. Schunck, Y. Shin, A. Schirotzek, M. W. Zwierlein, W. Ketterle, *Pairing Without Superfluidity: The Ground State of an Imbalanced Fermi Mixture*, Science **316**, 867 (2007).

Pairing Without Superfluidity: The Ground State of an Imbalanced Fermi Mixture

C. H. Schunck,* Y. Shin, A. Schirotzek, M. W. Zwierlein,† W. Ketterle

We used radio-frequency spectroscopy to study pairing in the normal and superfluid phases of a strongly interacting Fermi gas with imbalanced spin populations. At high spin imbalances, the system does not become superfluid even at zero temperature. In this normal phase, full pairing of the minority atoms was observed. Hence, mismatched Fermi surfaces do not prevent pairing but can quench the superfluid state, thus realizing a system of fermion pairs that do not condense even at the lowest temperature.

Fermionic superfluidity has many manifestations in nature; it occurs in such diverse systems as superconducting materials, liquid ^{3}He, neutron stars, and ultracold quantum gases. At its heart lies the formation of fermion pairs. Although the Pauli principle forbids identical fermions to occupy the same quantum state, pairs of fermions can condense and thus become superfluid. Superconductivity, the flow of electrical current without resistance, is a manifestation of fermionic superfluidity in a condensed-matter system. Superconductors are characterized by a temperature T^* where electrons start to pair and a critical temperature T_c for the onset of superconductivity. In conventional superconductors, understood within the framework of Bardeen-Cooper-Schrieffer (BCS) theory, fermion pairs form and condense simultaneously (i.e., $T^* = T_c$). In high-temperature superconductors, strongly correlated electrons exist in the normal phase, that is, $T^* > T_c$. The interactions that mediate pairing and ultimately lead to superconductivity in these complex systems are still subject to debate (*1*). Another strongly interacting but comparatively simple fermion system is an ultracold gas of neutral fermionic atoms. High-temperature superfluidity was recently observed in these gases (*2*), opening a new approach to explore the highly correlated normal phase of strongly interacting fermions and its relation to the onset of superfluidity.

Ultracold atomic Fermi mixtures of two spin states close to a Feshbach resonance constitute a highly controllable model system for strongly interacting fermions. By resonantly changing the interaction strength between the fermionic atoms, the crossover from BCS superfluidity of loosely bound pairs to Bose-Einstein condensation (BEC) of tightly bound molecules can be explored. BEC-BCS crossover theory at finite temperature contains pairing in the normal phase below a temperature $T^* > T_c$ (*1*, *3*–*5*). Evidence for pairing above T_c in ultracold Fermi gases was found in (*6*, *7*) via radio-frequency (rf) spectroscopy. Here, we use rf spectroscopy to study primarily the normal state of an imbalanced spin mixture. An imbalance in the spin populations of the two-state Fermi system leads to a qualitative change of the phase diagram: Above a certain interaction-dependent population imbalance, the transition to the superfluid state is suppressed even at zero temperature. This is known as the Chandrasekhar-Clogston (CC) or Pauli paramagnetic limit of superfluidity (*8*, *9*). In several works, the CC limit is assumed to imply pair dissociation and is referred to as "Pauli pair breaking" (*10*–*12*), that is, T^* and T_c are assumed to vanish simultaneously. The CC limit has been observed and characterized in ultracold atomic gases (*13*).

We report on the observation of a gap in a single-particle excitation spectrum (representing a spin response function) of a highly imbalanced sample. This implies that the system is in a correlated state and that the minority component is paired. Pairing of fermions is thus not necessarily a precursor to superfluidity: T^* is finite even when T_c vanishes. The CC limit of superfluidity, at least for strong interactions, is not associated with breaking of fermion pairs but only with the quenching of the superfluid state. Another and probably very different system with finite T^* and vanishing T_c has been discussed in strongly underdoped cuprates (*1*).

The rf spectra presented in this work were also correlated with an indirect signature for superfluidity by determining pair condensate fractions (*14*, *15*). We conclude that rf spectra cannot distinguish, at present experimental resolution, between normal and superfluid states.

In our experiment, a strongly interacting, imbalanced spin mixture of ^{6}Li fermions in the two lowest hyperfine states, labeled $|1\rangle$ and $|2\rangle$ (corresponding to the $|F = {}^1\!/_2, m_F = {}^1\!/_2\rangle$ and $|F = {}^1\!/_2, m_F = -{}^1\!/_2\rangle$ states at low magnetic field) was created in an optical dipole trap at 833 G, the center of the $|1\rangle$-$|2\rangle$ Feshbach resonance [see (*15*, *16*) for details]. On resonance, all interactions in the $|1\rangle$-$|2\rangle$ mixture are universal, as the Fermi energy E_F and the inverse Fermi wavenumber $1/k_F$ are the only relevant energy and length scales. The imbalance δ of the mixture was controlled as reported in (*13*, *17*), where $\delta = (N_1 - N_2)/(N_1 + N_2)$ and N_1 and N_2 are the atom numbers in states $|1\rangle$ and $|2\rangle$, respectively. Here, E_F, k_F, and the Fermi temperature T_F are given for a noninteracting Fermi gas with the same atom number as the majority component. To access a broader range of temperatures, we used two optical traps with different waists, characterized by the axial and radial trapping frequencies ω_a and ω_r (as given in the figure captions of the rf spectra).

The interactions were spectroscopically probed in a three-level system (*18*). A 2-ms rf pulse resonant with the transition from state $|2\rangle$ (the minority component) to a third state, labeled $|3\rangle$ ($|F = {}^3\!/_2, m_F = -{}^3\!/_2\rangle$ at low field) was applied. Immediately after the rf pulse, the optical trap was switched off and the cloud was allowed to expand for absorption imaging. Two absorption images of atoms in states $|2\rangle$ and $|1\rangle$ were taken successively, and the atom number fraction $N_2/(N_1 + N_2)$ was obtained as a function of the applied rf. The rf spectra at the highest imbalances were taken with a population transfer smaller than 3% of the total number of atoms. The data points in all spectra are the average of three

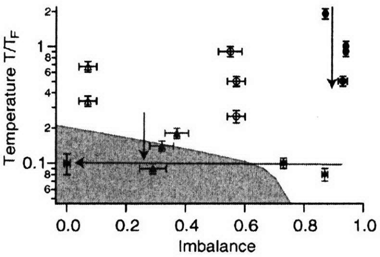

Fig. 1. The temperature-imbalance diagram shows where the rf spectra presented in Fig. 2 (black circles), Fig. 4, A to C (blue diamonds), and Fig. 4, D to F (red triangles) were taken. All spectra were obtained on resonance at 833 G. The arrows indicate the order in which the spectra are displayed in the figures. The shaded region indicates the superfluid phase. The spectra corresponding to the open circles and triangles are similar to the spectra of Fig. 2, A to C, and are shown in (*19*). Except for the data close to zero imbalance, for which the interacting temperature T' is given, temperatures have been determined from the noninteracting wings of the majority cloud (*25*).

Department of Physics, MIT-Harvard Center for Ultracold Atoms, and Research Laboratory of Electronics, Massachusetts Institute of Technology, Cambridge, MA 02139, USA.

*To whom correspondence should be addressed. E-mail: chs@mit.edu

†Present address: Institut für Physik, AG Quantum, Staudinger Weg 7, 55128 Mainz, Germany.

independent measurements. Temperature was adjusted by evaporation to different depths of the optical trap, followed by recompression. Spectra presented as a data set were taken with the same final trap depth. Figure 1 provides an overview of the imbalances and temperatures at which the rf spectra were obtained. Specific details are given in the figure captions and in (*19*). All radio frequencies were referenced to the |2⟩-|3⟩ resonance recorded in the absence of atoms in state |1⟩.

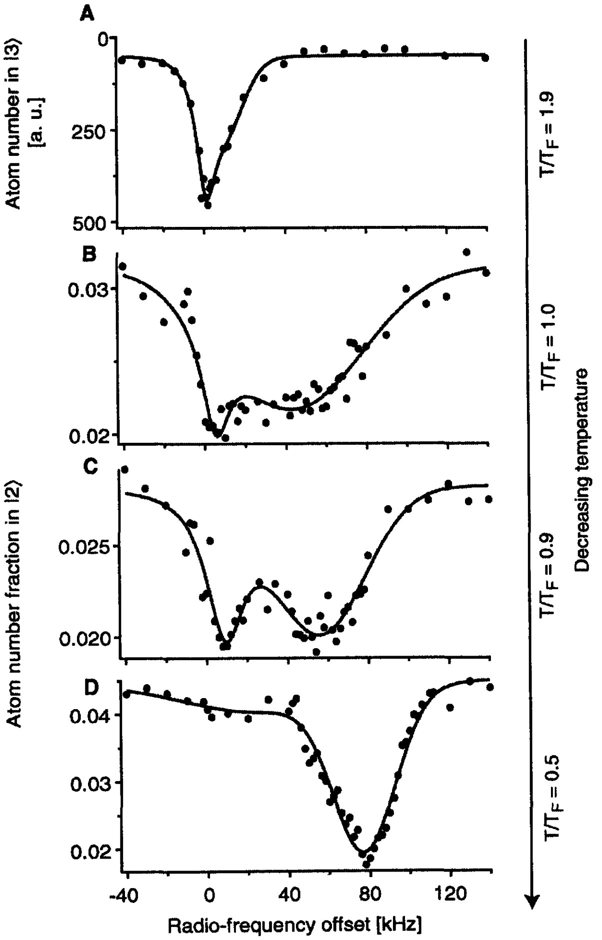

Fig. 2. Radio-frequency spectroscopy of the minority component in an imbalanced ($\delta \sim 0.9$), strongly interacting mixture of fermionic atoms above the CC limit of superfluidity. As the temperature is lowered, full pairing develops in the absence of superfluidity. **(A)** An asymmetric and broad peak centered at the position of the atomic line is observed. The asymmetry and the large width might be caused by the presence of pairing correlations already at T/T_F = 1.9. For this spectrum only, heating was applied and the atom number in state |3⟩ was recorded (*19*). **(B** and **C)** The pairing peak emerges. **(D)** At T/T_F = 0.5, the pairing peak remains and the minority atoms are almost fully paired (see also Fig. 4A). As a guide to the eye, a double-peak line consisting of a Lorentzian fit to the atomic peak and a Gaussian fit to the pairing peak is included. Spectra were taken for the following parameters (see also the solid black circles in Fig. 1): (A) $\delta = 0.87$, $E_F = h \times 260$ kHz, $T/T_F = 1.9$; (B) $\delta = 0.94$, $E_F = h \times 360$ kHz, $T/T_F = 1.0$; (C) $\delta = 0.94$, $E_F = h \times 360$ kHz, $T/T_F = 0.9$; (D) $\delta = 0.93$, $E_F = h \times 340$ kHz, $T/T_F = 0.5$. The trapping frequencies were $\omega_r = 2\pi \times 3.5$ kHz and $\omega_a = 2\pi \times 77$ Hz.

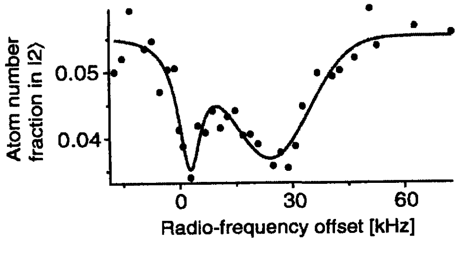

Fig. 3. Radio-frequency spectrum of the minority component obtained at a magnetic field of 937 G ($1/k_Fa_{12} = -0.18$) and imbalance $\delta = 0.88$, demonstrating strong pairing above the CC limit on the BCS side of the Feshbach resonance (a_{12} is the s-wave scattering length in the |1⟩-|2⟩ mixture). The rf spectrum was taken for the parameters $E_F = h \times 280$ kHz and T/T_F = 0.3. The trapping frequencies were $\omega_r = 2\pi \times 2.9$ kHz and $\omega_a = 2\pi \times 64$ Hz.

The rf spectroscopy measures a single-particle spin excitation spectrum for the minority component of the mixture (*20*–*23*). To understand the expected rf spectra, one can use a simplified description of the gas as a mixture of free atoms and molecule-like pairs, which is strictly valid only in the BEC limit. Transferring an unbound atom from state |2⟩ into state |3⟩ requires an energy ΔE_{23}. As the |1⟩-|3⟩ mixture is also strongly interacting because of a |1⟩-|3⟩ Feshbach resonance located at 690 G (*18*), we first assume, as in (*6*, *7*), that mean-field shifts (i.e., shifts corresponding to Hartree terms) are absent in the rf spectrum. Then ΔE_{23} and the width of the atomic |2⟩-|3⟩ transition are independent of the density of atoms in state |1⟩. However, if an atom in state |2⟩ is paired with an atom in state |1⟩, the rf photon must provide the binding energy E_B required to break the pair in addition to ΔE_{23}. Therefore, if pairing is present in the system, a second peak emerges in the minority rf spectrum that is separated from the atomic line and associated with pairing (*6*, *7*). In a Fermi cloud, pairing is strong only near the Fermi surface. Because the rf photons can excite atoms in the whole Fermi sea, the observed spectral gap $\Delta\nu$ may have to be interpreted as a pair-binding energy averaged over the Fermi sea. Indeed, in the BCS limit one has $h\Delta\nu \propto \Delta^2/E_F$, where h is Planck's constant and Δ is the BCS pairing gap (*23*). Under these working assumptions, we interpret the emergence of a gap in the spectrum as a pairing effect.

The presence of pairing in the normal phase has been observed in the rf spectra for a highly imbalanced mixture, with $\delta \sim 0.9$, on resonance at 833 G (Fig. 2) and on the BCS side at 937 G (Fig. 3). At high temperature, only the atomic peak was present, and as the temperature was lowered, a second peak—the pairing peak—emerged and separated from the atomic peak. At sufficiently low temperatures, essentially only the pairing peak remained. This behavior is qualitatively similar to what has been observed in an equal mixture (*6*). The spectral gap $\Delta\nu$ (i.e., the shift of the pairing peak relative to the atomic line) increases as the temperature is lowered. At the lowest temperature of $0.08T/T_F$ (Fig. 4A), we measured a shift of $0.38E_F$.

All the spectra in Figs. 2 and 3 were obtained at high imbalances above the CC limit of superfluidity. Here the system cannot undergo a phase transition to the superfluid state even at zero temperature. For a trapped gas on resonance the CC limit is reached at a critical imbalance of $\delta_{c,\mathrm{exp}} = 0.74 \pm 0.05$ (*13*, *17*), in agreement with a calculated value of $\delta_{c,\mathrm{theory}}$ = 0.77 (*24*). On the BCS side of the Feshbach resonance, at an interaction strength of $1/k_Fa_{12}$ = −0.18, the critical imbalance is $\delta_{c,\mathrm{exp}} = 0.6 \pm 0.1$, as previously measured around this interaction strength (*13*).

Because we observed full pairing in the normal phase of the strongly interacting gas, one might not expect the rf spectra to reveal the onset of superfluidity. We recorded rf spectra covering the phase transition from the normal to the superfluid state by varying imbalance (Fig. 4, A to C) as well as temperature (Fig. 4, D to F). In both cases, no signature of the phase transition was resolved, although both the emergence of fermion pair condensates and sudden changes in the density profiles (*13*, *17*) showed the phase transition. In our previous work (*2*, *13*), these indirect indicators of superfluidity were correlated with the presence of quantized vortices (i.e., superfluid flow).

Figure 4, A to C, illustrates that working with high imbalances has the advantage of reducing line-broadening effects that arise from averaging over the inhomogeneous density distribution of the sample. The narrowest line was observed at the highest imbalance (Fig. 4A), where the minority is considerably smaller than the majority cloud. The homogeneous linewidth should reflect the wave function of a single fermion pair. The observed narrow linewidth indicates localization in momentum space well below the Fermi momentum k_F, and hence a pair size on the order of the interparticle spacing.

We now examine the assumptions underlying our interpretation of the peaks in the rf spectra. In particular, we address the question of whether our observations can distinguish between pairing correlations and mean-field effects. Indeed, mean-field–like shifts were observed, for example, in the rf spectrum of Fig. 2C where the atomic line shows a shift of $0.03E_F$ to higher energy. Although the $|1\rangle$-$|3\rangle$ interactions are in the unitary regime for a typical value of $k_F a_{13} \approx -3.3$ (varying, for example, from –3 to –3.6 across the minority cloud in Fig. 2C), they may not have fully converged to their value at unitarity and thus may have caused the observed shifts (a_{13} is the *s*-wave scattering length in the $|1\rangle$-$|3\rangle$ mixture). However, all shifts of the atomic line are small relative to the size of the spectral gap of up to $0.38E_F$ and are only seen in the presence of the pairing peak (fig. S3 displays all observed shifts of atomic and pairing peaks versus temperature). Although the shifts of the atomic line are small at all temperatures, the shifts associated with the pairing peak start rising below $T/T_F \sim 1$, accompanied by a decrease in the weight of the atomic line. In the intermediate temperature range, where the rf spectra show a double-peak structure, the pairing peak should originate primarily from the higher-density region in the center of the cloud, and the atomic peak should originate from the low-density wings. Therefore, if one were to normalize the data according to the local density of majority atoms, the data points for the atom peaks would shift up in T/T_F by a factor of between 1.5 and 5, the smaller factor reflecting the cases of large imbalance, where the minority cloud is considerably smaller than the majority cloud. As a result, near $T/T_{F(\mathrm{local})} = 0.5$, we have observed both atomic peaks and pairing peaks, which is an indication for the local coexistence of unpaired and paired minority atoms. However, in this possible coexistence region, either the peak separation is small or one peak has very small weight. Therefore, more work is needed to study the possibility of coexistence. An alternative interpretation assumes single local peaks and a sudden onset of peak shifts below $T/T_F \sim 1$. This appears to be incompatible with a local mean-field approximation as well: The mean field in the unitarity limit should saturate when T approaches T_F and not vary strongly for $T < T_F$, because the relative momentum of two particles in this regime is dominated by the Fermi momentum and not by the thermal

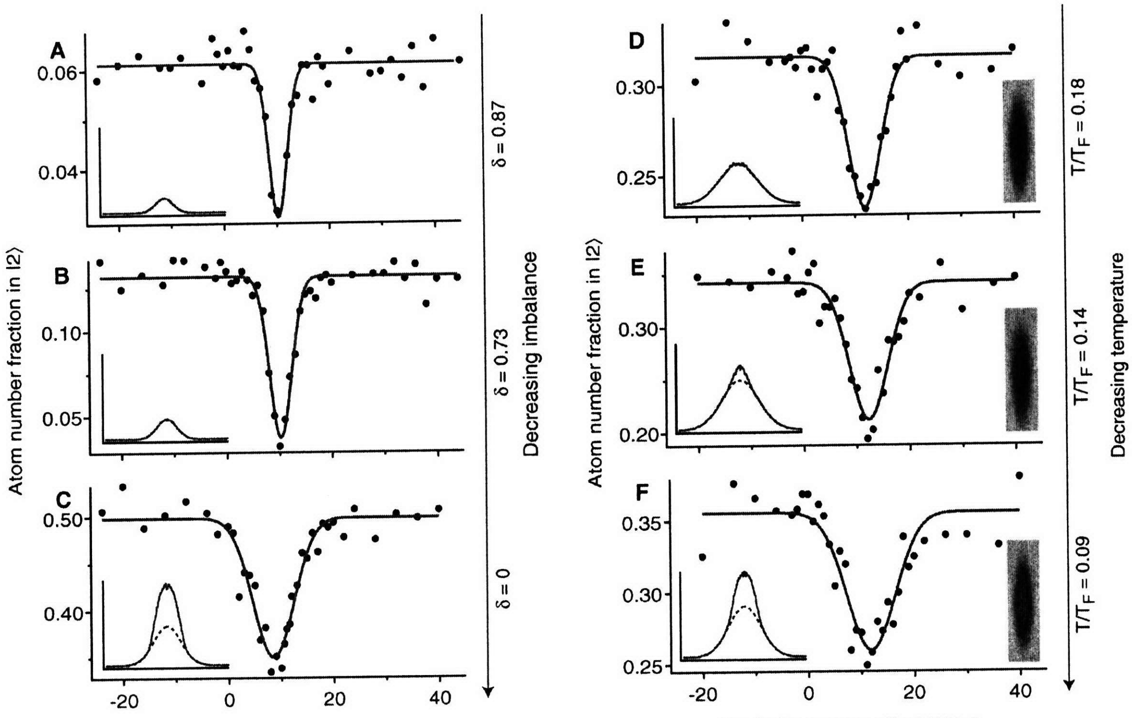

Fig. 4. Radio-frequency spectra of the minority component obtained while crossing the phase transition by reducing imbalance (**A** to **C**) and temperature (**D** to **F**). The rf spectra do not reveal the phase transition. The onset of superfluidity is indirectly observed by fermion pair condensation. The condensate fractions are zero in (A) and (B) and 35 ± 2% in (C). The onset of superfluidity as a function of temperature occurs between (D) and (F), with condensate fractions of 0% in (D), 3 ± 2% in (E), and 17 ± 3% in (F). The insets in (A) to (F) show the column density profile (red) of the minority cloud after a rapid magnetic field ramp to the BEC side and further expansion (*19*); the blue dashed line is a Gaussian fit to the thermal background. The additional insets in (D) to (F) show phase-contrast images for a trapped cloud, obtained at imbalances of the opposite sign. Spectra were taken for the following parameters in (A) to (C) (see also the blue diamonds in Fig. 1): (A) $\delta = 0.87$, $E_F = h \times 27$ kHz, $T/T_F = 0.08$; (B) $\delta = 0.73$, $E_F = h \times 27$ kHz, $T/T_F = 0.10$; (C) $\delta = 0.00$, $E_F = h \times 23$ kHz, $T'/T_F = 0.10$. The trapping frequencies were $\omega_r = 2\pi \times 143$ Hz and $\omega_a = 2\pi \times 23$ Hz. For the spectrum in (C) we quote the temperature T' obtained from a fit to the interacting Fermi gas (*19*). Spectra were taken for the following parameters in (D) to (F) (see also the solid red triangles in Fig. 1): (D) $\delta = 0.37$, $E_F = h \times 38$ kHz, $T/T_F = 0.18$; (E) $\delta = 0.32$, $E_F = h \times 38$ kHz, $T/T_F = 0.14$; (F) $\delta = 0.29$, $E_F = h \times 35$ kHz, $T/T_F = 0.09$. The trapping frequencies were $\omega_r = 2\pi \times 192$ Hz and $\omega_a = 2\pi \times 23$ Hz.

momentum. Furthermore, a sudden onset of interactions would likely affect the density distribution of the minority atoms. However, the minority clouds observed in expansion are well fit by a single Thomas-Fermi profile (*25*).

The BEC-side picture of a mixture of single atoms and molecules seems to extend into the resonance region, in the sense that fermion pairs form high above the superfluid transition temperature and possibly coexist locally with unpaired atoms. However, the fermion pairs on resonance behave differently from "real" molecules: Their binding energy increases with lower temperature and higher atomic density. Most important, fermion pairs above the CC limit do not condense at low temperature as bosonic molecules would do at any imbalance. Although some extensions of BCS mean-field theories to the imbalanced case do not predict pairing at imbalances δ above the CC limit (*26*), a survival of Cooper pairs "far from the transition region" has been predicted (*27*) for a superconducting system that is driven into the normal, paramagnetic phase by Zeeman splitting.

The observed spectral gaps appear to be insensitive to the density of the minority atoms (Fig. 4, A to C). At very high imbalances, one should indeed approach the limit of one minority atom immersed in a fully polarized Fermi sea. In (*24*, *28*, *29*) the ground-state energy for this scenario has been calculated to be about $-0.6E_F$, for example, by using a modified Cooper-pair wave function ansatz (*28*). These calculations do not provide an excitation spectrum and do not distinguish between pairing (correlation) energies and mean-field (Hartree) terms. Therefore, the theoretical result cannot be directly compared to our spectroscopic measurement of $h\Delta\nu = -0.38E_F$ at $T/T_F = 0.08$.

Whether superfluidity can occur for large imbalances and low atom numbers in highly elongated geometries remains a subject of debate (*30*). In light of our findings, it may be important to clearly distinguish between the effects of pairing and of superfluidity. It has also been suggested that the presence of an atomic peak next to the pairing peak in the minority cloud at zero temperature and high imbalance could provide evidence for exotic forms of superfluidity, such as the Fulde-Ferrel-Larkin-Ovchinnikov state (*31*). However, for the parameters studied here, the atomic peak is seen to disappear as the temperature is reduced (Figs. 2 and 4A).

Working with imbalanced Fermi gases, we were able to study and characterize pairing in a situation where no superfluidity occurs even at zero temperature. The spectral gap $\Delta\nu$ appears to be only weakly dependent on the imbalance. This finding suggests that near unitarity, certain pairing correlations in the superfluid state are similar to those in a dilute cloud of minority atoms immersed into the Fermi sea of the majority. Moreover, it implies that the energetics that drive the normal-to-superfluid phase transition involve more than the observed pairing energy. Further studies of the strongly correlated normal state might yield new insights into the microscopic physics of the superfluid state.

References and Notes

1. P. A. Lee, N. Nagaosa, X.-G. Wen, *Rev. Mod. Phys.* **78**, 17 (2006).
2. M. W. Zwierlein, J. R. Abo-Shaeer, A. Schirotzek, C. H. Schunck, W. Ketterle, *Nature* **435**, 1047 (2005).
3. N. Trivedi, M. Randeria, *Phys. Rev. Lett.* **75**, 312 (1995).
4. A. Perali, P. Pieri, G. C. Strinati, C. Castellani, *Phys. Rev. B* **66**, 024510 (2002).
5. Q. Chen, J. Stajic, S. Tan, K. Levin, *Phys. Rep.* **412**, 1 (2005).
6. C. Chin *et al.*, *Science* **305**, 1128 (2004); published online 22 July 2004 (10.1126/science.1100818).
7. J. Kinnunen, M. Rodríguez, P. Törmä, *Science* **305**, 1131 (2004); published online 22 July 2004 (10.1126/science.1100782).
8. B. S. Chandrasekhar, *Appl. Phys. Lett.* **1**, 7 (1962).
9. A. M. Clogston, *Phys. Rev. Lett.* **9**, 266 (1962).
10. K. Capelle, *Phys. Rev. B* **65**, 100515 (2002).
11. M. Maśka, *Phys. Rev. B* **66**, 054533 (2002).
12. K. Kumagai *et al.*, *Phys. Rev. Lett.* **97**, 227002 (2006).
13. M. W. Zwierlein, A. Schirotzek, C. H. Schunck, W. Ketterle, *Science* **311**, 492 (2006); published online 21 December 2005 (10.1126/science.1122318).
14. C. A. Regal, M. Greiner, D. S. Jin, *Phys. Rev. Lett.* **92**, 040403 (2004).
15. M. W. Zwierlein *et al.*, *Phys. Rev. Lett.* **92**, 120403 (2004).
16. Z. Hadzibabic *et al.*, *Phys. Rev. Lett.* **91**, 160401 (2003).
17. Y. Shin, M. W. Zwierlein, C. H. Schunck, A. Schirotzek, W. Ketterle, *Phys. Rev. Lett.* **97**, 030401 (2006).
18. S. Gupta *et al.*, *Science* **300**, 1723 (2003); published online 8 May 2003 (10.1126/science.1085335).
19. See supporting material on *Science* Online.
20. J. Kinnunen, M. Rodríguez, P. Törmä, *Phys. Rev. Lett.* **92**, 230403 (2004).
21. Y. Ohashi, A. Griffin, *Phys. Rev. A* **72**, 063606 (2005).
22. Y. He, Q. Chen, K. Levin, *Phys. Rev. A* **72**, 011602 (2005).
23. Z. Yu, G. Baym, *Phys. Rev. A* **73**, 063601 (2006).
24. C. Lobo, A. Recati, S. Giorgini, S. Stringari, *Phys. Rev. Lett.* **97**, 200403 (2006).
25. M. W. Zwierlein, C. H. Schunck, A. Schirotzek, W. Ketterle, *Nature* **442**, 54 (2006).
26. C. Chien, Q. Chen, Y. He, K. Levin, *Phys. Rev. Lett.* **98**, 110404 (2007).
27. I. L. Aleiner, B. L. Altshuler, *Phys. Rev. Lett.* **79**, 4242 (1997).
28. F. Chevy, *Phys. Rev. A* **74**, 063628 (2006).
29. A. Bulgac, M. M. Forbes, *Phys. Rev. A* **75**, 031605(R) (2007).
30. G. B. Partridge *et al.*, *Phys. Rev. Lett.* **97**, 190407 (2006).
31. J. Kinnunen, L. M. Jensen, P. Törmä, *Phys. Rev. Lett.* **96**, 110403 (2006).

32. We thank W. Zwerger, P. Lee, K. Levin, and Q. Chen for stimulating discussions and D. Miller for critical reading of the manuscript. Supported by NSF and the Office of Naval Research.

Supporting Online Material

www.sciencemag.org/cgi/content/full/316/5826/867/DC1
Materials and Methods
Figs. S1 to S3
References

2 February 2007; accepted 29 March 2007
10.1126/science.1140749

The Process of Tholin Formation in Titan's Upper Atmosphere

J. H. Waite Jr.,[1*] D. T. Young,[1] T. E. Cravens,[2] A. J. Coates,[3] F. J. Crary,[1] B. Magee,[1*] J. Westlake[4]

Titan's lower atmosphere has long been known to harbor organic aerosols (tholins) presumed to have been formed from simple molecules, such as methane and nitrogen (CH_4 and N_2). Up to now, it has been assumed that tholins were formed at altitudes of several hundred kilometers by processes as yet unobserved. Using measurements from a combination of mass/charge and energy/charge spectrometers on the Cassini spacecraft, we have obtained evidence for tholin formation at high altitudes (~1000 kilometers) in Titan's atmosphere. The observed chemical mix strongly implies a series of chemical reactions and physical processes that lead from simple molecules (CH_4 and N_2) to larger, more complex molecules (80 to 350 daltons) to negatively charged massive molecules (~8000 daltons), which we identify as tholins. That the process involves massive negatively charged molecules and aerosols is completely unexpected.

Methane and nitrogen in Titan's atmosphere are supplied with free energy from solar ultraviolet (UV) radiation and energetic particles in Saturn's magnetosphere. These circumstances make Titan, a prolific source of complex organic compounds, unparalleled in the solar system. Hydrocarbon chemistry is further enhanced by the escape of hydrogen from the exosphere, which accelerates the conversion of methane to unsaturated hydrocarbon-nitrile species by circumventing the buildup of molecular hydrogen, thus promoting unsaturated hydrocarbon formation (*1*, *2*). Sagan and Khare (*3*) have suggested that the penultimate result of the formation of these large compounds is the generation of hydrocarbon-nitrile aerosols (tholins) thought to populate haze layers in Titan's stratosphere (*4*, *5*). Similar organic chemistry occurs during soot formation in Earth's troposphere (*6*–*8*) and may have taken place in the

[1]Space Science and Engineering Division, Southwest Research Institute (SWRI), 6220 Culebra Road, San Antonio, TX 78238, USA. [2]Department of Physics and Astronomy, University of Kansas, Lawrence, KS 66045, USA. [3]Department of Space and Climate Physics, Mullard Space Science Laboratory, University College London, Holmbury St. Mary, Dorking RH5 6NT, UK. [4]Department of Physics and Astronomy, University of Texas, San Antonio, TX 78249, USA.

*To whom correspondence should be addressed. E-mail: hwaite@swri.edu (J.H.W.); bmagee@swri.edu (B.M.)

Science
AAAS

www.sciencemag.org/cgi/content/full/316/5826/867/DC1

Supporting Online Material for

Pairing Without Superfluidity:

The Ground State of an Imbalanced Fermi Mixture

C. H. Schunck,* Y. Shin, A. Schirotzek, M. W. Zwierlein, W. Ketterle

*To whom correspondence should be addressed. E-mail: chs@mit.edu

Published 11 May 2007, *Science* **316**, 867 (2007)
DOI: 10.1126/science.1140749

This PDF file includes:

Materials and Methods

Figs. S1 to S3

References

Experimental details

1. **Determination of the atomic reference line:** For the data taken at the center of the $|1\rangle - |2\rangle$ Feshbach resonance the resonance frequency of the $|2\rangle - |3\rangle$ transition in the absence of atoms in state $|1\rangle$ was determined to be 81.700 MHz ± 1 kHz, corresponding to a magnetic field of about 833 G. The FWHM of a Lorentzian fit to the resonance peak was less than 1 kHz. These values reflect day to day fluctuations and correspond to a magnetic field stability better than 0.2 G. The resonance frequency of the $|2\rangle - |3\rangle$ transition on the BCS-side of the Feshbach resonance (Fig. 3) was 81.187 MHz ± 1 kHz (corresponding to a magnetic field of 936.5 G), determined in the absence of atoms in state $|1\rangle$.

2. **Rf pulse**: For all data a rf pulse of 2 ms was applied. This pulse duration is optimized in terms of precision and minimizing a dynamic response of the system during the rf pulse. For each spectrum the rf power was adjusted to give an adequate signal-to-noise ratio.

3. **Determination of the atom number fraction in state $|2\rangle$:** To obtain the atom number fraction $N_2/(N_1+N_2)$ two absorption images, one of the minority component in state $|2\rangle$ and the other of the majority component in state $|1\rangle$, were taken successively. The time-of-flight before the first absorption image as well as the delay time between the absorption

images were adjusted depending on the imbalance δ of the mixture, final temperature and the trapping frequency of the optical dipole trap. The time-of-flight before the absorption image of the minority varied between 200 μs and 8 ms, the delay time between the images was in the range of 500 μs and 2 ms.

4. **Imaging atoms transferred to state $|3\rangle$; Fig. 2A**: For the rf spectrum in Fig. 2A, T/T_F was increased by shortly switching off the optical dipole trap and allowing for subsequent equilibration before the rf pulse. The number of atoms transferred to state $|3\rangle$ was recorded for a better signal-to-noise ratio . The absorption image had to be taken within 200 μs after applying the rf pulse. After longer time-of-flight atoms in state $|3\rangle$ decayed through collisions. This precluded imaging atoms in state $|3\rangle$ at lower temperatures where longer time-of-flights were required before absorption imaging to avoid saturation.

5. **Weight of the atomic peak as function of imbalance**: The population imbalance affects the weight of the atomic peak in rf spectra obtained at the same T/T_F (compare Fig. 2D, S1C and S2B). As the imbalance decreases, the weight of the atomic peak increases. This is likely due to the higher relative temperature compared to the local binding energy in the the lower density region of the majority could. That effect will result in a higher fraction of unpaired atoms at small imbalances.

6. **Temperature determination**: Except for equal and nearly equal mixtures ($\delta < 20\%$), temperatures were determined from the *non-interacting* wings of the majority cloud after expansion (*S3*). In ref. (*S3*) it was found that for imbalances $\delta > 20\%$ the non-interacting wings of the majority cloud expand ballistically and are not affected by the hydrodynamic expansion of the interacting component. For equal or nearly equal mixtures the temperature T' was determined from a finite-temperature Thomas-Fermi fit to the whole density profile of the majority cloud.

7. **Clogston-Chandrasekhar limit**: The experimental value quoted of $\delta_{\mathrm{c,exp}} = 0.74(5)$ on resonance was obtained with the following probes for superfluidity: vortices and condensate fractions (*S2*), bimodal density distributions of the minority cloud in time-of-flight (*S3*). We would like to emphasize, that the previous experimental determination of the critical imbalance included a measurement of its *temperature dependence*, which was found to be weak at low temperatures (*S2*).

8. **Condensate fractions**: Condensate fractions were obtained as previously described in ref. (*S1*) and (*S2*). The samples were prepared as in the rf experiment, but the rf pulse was not applied. Instead the gas was released from the trap and the magnetic field was switched in 200 μs to 690 G, where the cloud expanded for several ms. Then the magnetic field was ramped in 1 ms to 720 G for absorption imaging. Condensate fractions were determined from bimodal fits to the minority component. Condensates were only observed when condensate fractions are explicitly stated (Fig. 4 of the letter).

References and Notes

S1. M. W. Zwierlein *et al.*, *Phys. Rev. Lett.* **92**, 120403 (2004).

S2. M. W. Zwierlein, A. Schirotzek, C. H. Schunck, W. Ketterle, *Science* **311**, 492 (2006).

S3. M. W. Zwierlein, C. H. Schunck, A. Schirotzek, W. Ketterle, *Nature* **442**, 54 (2006).

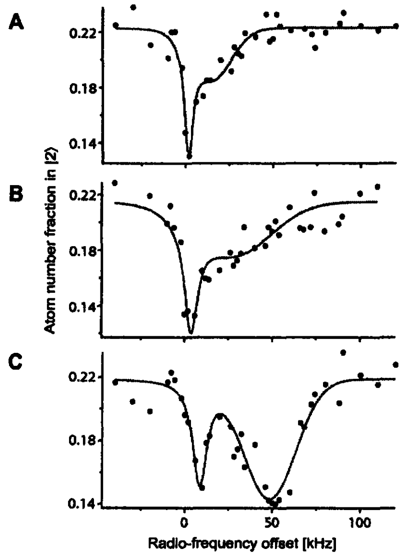

Fig. S1. Rf spectra of the minority component on resonance at 833 G. The spectra correspond to the open triangles shown in Fig. 1 of the letter and were obtained for the following parameters: A) $\delta = 0.55$, $E_F = h \times 230$ kHz, $T/T_F = 0.9$; The trapping frequencies for **A** were $\omega_r = 2\pi \times 3.4$ kHz and $\omega_a = 2\pi \times 76$ Hz. B) $\delta = 0.57$, $E_F = h \times 230$ kHz, $T/T_F = 0.5$; C) $\delta = 0.57$, $E_F = h \times 220$ kHz, $T/T_F = 0.25$. The trapping frequencies for **B** and **C** were $\omega_r = 2\pi \times 2.9$ kHz and $\omega_a = 2\pi \times 64$ Hz.

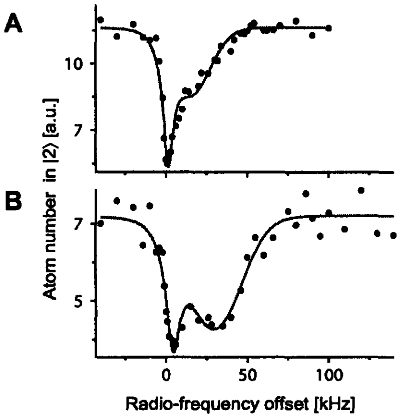

Fig. S2. Rf spectra of the minority component on resonance at 833 G. Since the majority component of the nearly equal mixture also suffered significant losses after the rf pulse (probably due to inelastic collisions), we report here the un-normalized atom number in state $|2\rangle$ as a function of the applied radio frequency. The spectra correspond to the open circles shown in Fig. 1 of the letter and were obtained for the following parameters: A) $\delta = 0.07$, $E_F = h \times 210$ kHz, $T'/T_F = 0.67$; B) $\delta = 0.07$, $E_F = h \times 180$ kHz, $T'/T_F = 0.34$. The trapping frequencies were $\omega_r = 2\pi \times 2.9$ kHz and $\omega_a = 2\pi \times 64$ Hz.

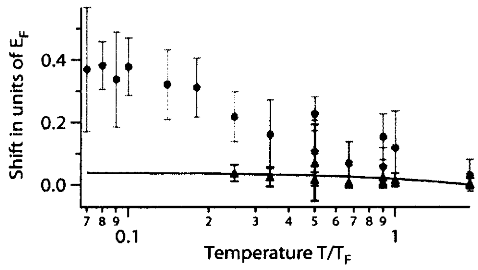

Fig. S3. Normalized shifts of the atomic peaks (black triangles) and pairing peaks (red circles) as a function of T/T_F (for equal mixture data as a function of T'/T_F). E_F (T_F) is the Fermi energy (temperature) of a non-interacting Fermi gas with the same number of atoms as the majority component. The black line is a linear fit to the atomic peak shifts. The error bars reflect the full width at half maximum of a Gaussian fit to the peaks.

Appendix F

Tomographic rf Spectroscopy of a Trapped Fermi Gas at Unitarity

This appendix contains a reprint of Ref. [24]: Y. Shin, C. H. Schunck, A. Schirotzek, and W. Ketterle, *Tomographic rf Spectroscopy of a Trapped Fermi Gas at Unitarity*, Phys. Rev. Lett. **99**, 090403 (2007).

Tomographic rf Spectroscopy of a Trapped Fermi Gas at Unitarity

Y. Shin,* C. H. Schunck, A. Schirotzek, and W. Ketterle
Department of Physics, MIT-Harvard Center for Ultracold Atoms, and Research Laboratory of Electronics,
Massachusetts Institute of Technology, Cambridge, Massachusetts, 02139, USA

(Received 25 May 2007; published 31 August 2007)

We present spatially resolved radio-frequency spectroscopy of a trapped Fermi gas with resonant interactions and observe a spectral gap at low temperatures. The spatial distribution of the spectral response of the trapped gas is obtained using *in situ* phase-contrast imaging and 3D image reconstruction. At the lowest temperature, the homogeneous rf spectrum shows an asymmetric excitation line shape with a peak at $0.48(4)\varepsilon_F$ with respect to the free atomic line, where ε_F is the local Fermi energy.

DOI: 10.1103/PhysRevLett.99.090403 PACS numbers: 03.75.Ss, 03.75.Hh, 32.30.Bv

Ultracold Fermi gases near a Feshbach resonance provide new insight into fermionic superfluidity, allowing the study of the crossover from Bardeen-Cooper-Schrieffer (BCS) superfluids of Cooper pairs to Bose-Einstein condensates (BECs) of dimer molecules. Many aspects of the BCS-BEC crossover, including superfluidity [1], have been experimentally investigated [2]. The properties of Fermi gases on resonance at unitarity, where the scattering length between the fermionic atoms diverges and the system shows universal behavior [3], are of great importance to understand the crossover physics. Measurements of the critical temperature [4], the interaction energy [5], and collective excitations [6] have presented stringent quantitative test to the theoretical description of strongly interacting Fermi gases.

Radio-frequency (rf) spectroscopy has been a successful method to probe the strongly interacting Fermi gas. It allows us to measure an excitation spectrum by inducing transitions to different hyperfine spin states. This method on Fermi gases has led to the observation of unitarity limited interactions [7,8], molecule formation on the BEC side of the Feshbach resonance [9], as well as pairing in the crossover regime [10,11]. rf spectroscopy provides valuable information on the nature of the pairs. Since an rf photon can dissociate bound molecules or fermion pairs into the free atom continuum, the binding energy of the pairs or the excitation gap can be determined. Furthermore the excitation line shape is related to the wave function of the pairs; e.g., larger pairs have narrower lines. However, currently all experimental measurements on the excitation spectrum in strongly interacting Fermi gases [10,12] have been performed with samples confined in a harmonic trapping potential so that the spectral line shape is broadened due to the inhomogeneous density distribution of the trapped samples, preventing a more stringent comparison with theoretical predictions [13–16].

In this Letter, we demonstrate spatially resolved rf spectroscopy of a trapped, spin-balanced Fermi gas at unitarity at very low temperature. The spatial distribution of the rf-induced excited region in the trapped gas was recorded with *in situ* phase-contrast imaging [17] and the local rf spectra were compiled after 3D image reconstruction. In contrast to the inhomogeneous rf spectrum, the homogeneous local rf spectrum shows a clear spectral gap with an asymmetric line shape. We observe that the peak of the spectrum shifts by $0.48(4)\varepsilon_F$ to higher energy and that the spectral gap is $0.30(8)\varepsilon_F$ with respect to the free atomic reference line, where ε_F is the local Fermi energy. This new spectroscopic method overcomes the line broadening problem for inhomogeneous samples and provides homogeneous rf spectra of a resonantly interacting Fermi gas revealing the microscopic physics of fermion pairs.

We prepared a degenerate Fermi gas of spin-polarized ^{6}Li atoms in an optical trap, using laser cooling and sympathetic cooling with ^{23}Na atoms, as described in Ref. [18]. An equal mixture of the two lowest hyperfine states $|1\rangle$ and $|2\rangle$ (corresponding to the $|F = 1/2, m_F = 1/2\rangle$ and $|F = 1/2, m_F = -1/2\rangle$ states at low magnetic field) was created at a magnetic field $B = 885$ G. A broad Feshbach resonance located at $B_0 = 834$ G strongly enhanced the interactions between the two states. The final evaporative cooling by lowering the trap depth and all spectroscopic measurements were performed at $B = 833$ G. The total atom number was $N_t = 1.0 \pm 0.1 \times 10^7$ and the radial (axial) trap frequency was $f_r = 129$ Hz ($f_z = 23$ Hz). The Fermi energy (temperature) of a noninteracting equal mixture with the same total atom number is $E_F = h(f_r^2 f_z)^{1/3}(3N_t)^{1/3} = h \times 22.3$ kHz ($T_F = E_F/k_B = 1.07$ μK), where h is Planck's constant and k_B is Boltzmann's constant. The ratio of the sample temperature T to T_F of ≈ 0.06 was determined by fitting a finite temperature Thomas-Fermi (TF) distribution to the whole cloud after expansion [4].

rf spectroscopy was performed by driving atoms in state $|2\rangle$ to the next lowest hyperfine state $|3\rangle$ (corresponding to $|F = 3/2, m_F = -3/2\rangle$ at low field) that was initially empty. After applying an rf pulse of 1 ms, we directly measured the *in situ* distribution of the density difference

0031-9007/07/99(9)/090403(4)

$n_d \equiv n_1 - n_2$ in the excited sample, using a phase-contrast imaging technique [17], where n_1 and n_2 are the densities of atoms in the states $|1\rangle$ and $|2\rangle$, respectively. The frequency of the imaging beam was set to make the net phase shift in the sample proportional to the density difference n_d, which was done by zeroing the optical signal in an equal mixture without applying an rf pulse [17]. Since the initial atom densities in states $|1\rangle$ and $|2\rangle$ are equal, the density difference n_d represents the atom number depletion in state $|2\rangle$, i.e., the spectral response I [19].

The total spectral response, obtained by integrating over the phase-contrast images, reproduces earlier results [10,11]. The phase-contrast images now reveal the nature of the observed line shape (Fig. 1). The spectral response strongly depends on position. The inner region of the cloud, which is at higher density, shows a higher resonance frequency. The integrated inhomogeneous spectrum peaks at the rf offset $\Delta\nu_i \approx 10$ kHz [20]. The spatially resolved images reveal that at this frequency, no excitations occur in the center of the cloud, but rather in a spatial shell. The rf offset $\Delta\nu$ is measured with respect to the resonance frequency of the $|2\rangle - |3\rangle$ transition in the absence of atoms in state $|1\rangle$ [21].

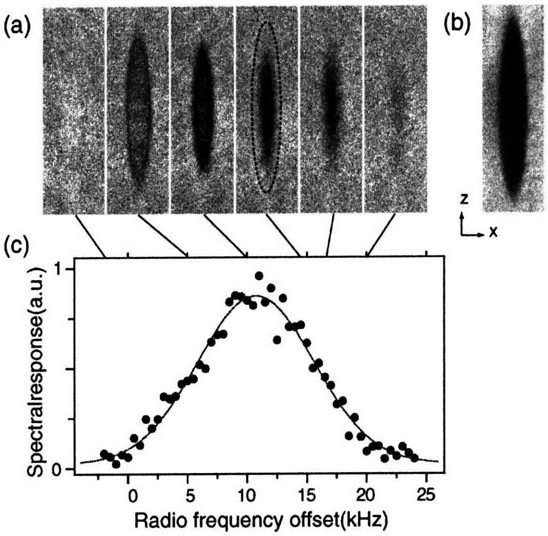

FIG. 1 (color online). Radio-frequency (rf) spectroscopy of a Fermi gas with *in situ* phase-contrast imaging. (a) After applying an rf pulse, the spatial distribution of the density difference between state $|1\rangle$ and $|2\rangle$ is recorded with the phase-contrast imaging technique [17]. The density depletion reflects the spin excitation induced by the rf pulse. The dashed line indicates the size of the trapped sample. (b) An absorption image of an equal mixture without applying an rf pulse. The field of view for each image is 205 μm × 680 μm. (c) rf spectrum of the inhomogeneous sample is obtained by integrating the signal in the phase-contrast images. The red (or gray) line is a Gaussian fit to the spectrum.

Local rf spectra $I(r, \Delta\nu)$ are compiled from the reconstructed 3D radial profiles of the density difference. A phase-contrast image contains the 2D distribution of the column density difference integrated along the imaging line, $n_{d,2\mathrm{D}}(x, z) \equiv \int n_d(\vec{r})dy$. The excited regions have an elliptical shape with the same aspect ratio as the trap, $\lambda = f_z/f_r$, showing the validity of the local density approximation. Therefore, we can use elliptically averaged profiles of the column density difference, $n_{d,2\mathrm{D}}(r)$, to improve the signal-to-noise ratio, where the ellipse for averaging is defined as $x^2 + \lambda^2 z^2 = r^2$ for a given radial position r. The 3D radial profile $n_d(r)$ is calculated using the inverse Abel transformation of $n_{d,2\mathrm{D}}(r)$ [22] and gives the spectral intensity via $I(r, \Delta\nu) \propto n_d(r; \Delta\nu)$. The spatial resolution of our imaging system is about 1.4 μm.

With this technique, we obtain homogeneous rf spectra as a function of the 3D radial position, shown in Fig. 2. These spectra are the main result of this paper and we now discuss their features and implications for our system. The local homogeneous rf spectra show a spectral gap. The peak of the spectrum is shifted away from the atomic reference line by much more than its line width. Such a gap is not observed in the inhomogeneous rf spectrum [Fig. 1(c)] where the Gaussian wings overlap with the position of the free atomic line. Furthermore, the local rf spectrum reveals an asymmetric line shape of the excitation spectrum. For the central region, the peak is located at $\Delta\nu_p \approx 15$ kHz and the spectral gap, defined as the minimum energy offset for excitation, is $h\Delta\nu_g \approx h \times 10$ kHz.

The spectral peak position $\Delta\nu_p$ in the local rf spectra shows a parabolic dependence on the radial position [Fig. 2(a)]. This can be explained by unitarity, which demands that all energetic quantities scale with the Fermi energy. At unitarity, the only relevant energy scale in the system is the Fermi energy $\varepsilon_F \equiv \hbar^2(6\pi^2 n)^{2/3}/2m$ [3,23], where n is the atom density in one spin state and m is the atomic mass. All energetic quantities such as the chemical potential μ and the pairing gap energy Δ are proportional to ε_F, i.e., $\mu = \xi\varepsilon_F$ and $\Delta = \eta\varepsilon_F$ with the universal parameters ξ and η. Therefore, the excitation spectrum might also scale with the Fermi energy. In an external harmonic potential $V(r) \propto r^2$, the local Fermi energy $\varepsilon_F(r) = \mu(r)/\xi = (\mu_0 - V(r))/\xi = \varepsilon_{F0}(1 - r^2/R^2)$, where μ_0 is the global chemical potential, ε_{F0} is the local Fermi energy at the center, R is the radius of the trapped sample, and $\varepsilon_{F0} = \mu_0/\xi = V(R)/\xi$. The spectral peak position $\Delta\nu_p(r)$ thus simply reflects the parabolic radial dependence of the local Fermi energy $\varepsilon_F(r)$.

The local Fermi energy at the center is determined from $\varepsilon_{F0} = (R/R_{\mathrm{TF}})^{-2}E_F$, where R_{TF} is the radial Thomas-Fermi radius for a noninteracting Fermi gas with the same atom number. We obtain $R_{\mathrm{TF}} = 67.3 \pm 1.1$ μm for the measured total atom number and trap frequencies. The radius of the trapped sample was measured to be $R = 56.6 \pm 1.8$ μm, using absorption images like in Fig. 1(b)

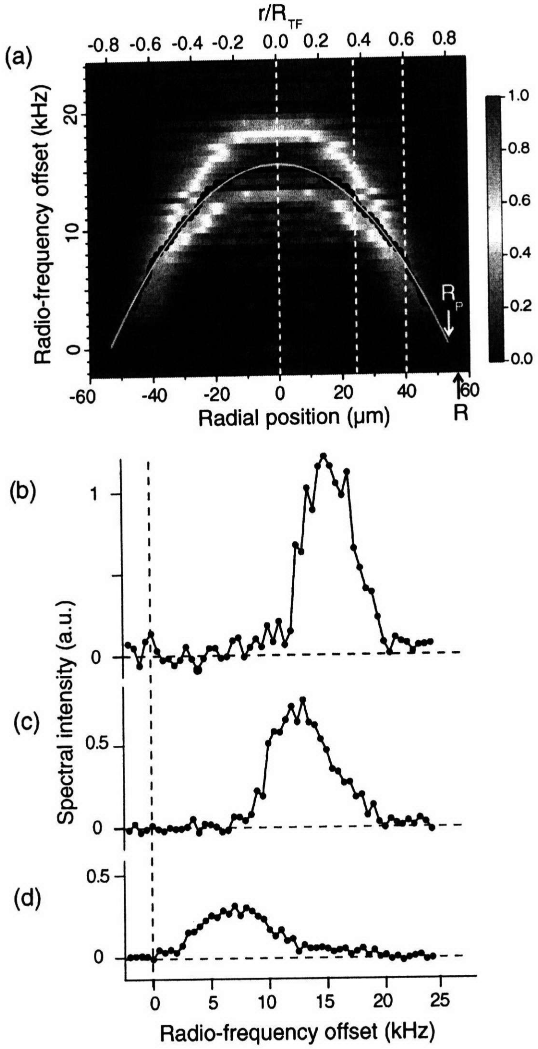

FIG. 2 (color online). Spatially resolved rf spectroscopy of a trapped Fermi gas. (a) The spectral intensity $I(r, \Delta\nu)$ was obtained from the reconstructed 3D profiles of the density difference. See text for the description of the reconstruction method. Local rf spectra are shown for (b) $r = 0$ μm, (c) $r = 24$ μm, and (d) $r = 40$ μm, whose positions are marked by vertical dashed lines in (a). Each spectrum is obtained by spatially averaging over 2.5 μm. R_{TF} is the radial Thomas-Fermi radius for a noninteracting Fermi gas with the same atom number. The peak position $\Delta\nu_p(r)$ in the local rf spectra is determined from the moderately smoothed spectra and marked by the black line in (a). The determination of $\Delta\nu_p$ is limited to $|r| < 48$ μm due to the signal-to-noise ratio. The yellow (or light gray) line is a parabolic fit to $\Delta\nu_p(r)$. The radius determined by extrapolating the fit to zero rf offset is $R_p = 53.6$ μm indicated by the white down arrow. The black up arrow indicates the radius of the trapped sample, $R = 56.6$ μm, measured independently from absorption images like Fig. 1(b).

and fitting the nonsaturated outer wing profile to a zero-temperature TF distribution, giving $\varepsilon_{F0} = h \times 31.5 \pm 2.5$ kHz. We estimate the universal parameter $\xi = (R/R_{\mathrm{TF}})^4 = 0.50 \pm 0.07$, which is in good agreement with previous measurements [4,5,24–28] and quantum Monte Carlo calculations [29–31] ($\xi \equiv 1 + \beta$ in some references).

The local spectrum at the center of our sample shows the spectral peak at $h\Delta\nu_p = 0.48(4)\varepsilon_{F0}$ and the spectral gap of $h\Delta\nu_g = 0.30(8)\varepsilon_{F0}$. We can determine a radius R_p such that $\Delta\nu_p(R_p) = 0$, extrapolating the parabolic curve fit of $\Delta\nu_p$ to zero rf offset [Fig. 2(a)]. $R_p = 53.6$ μm is slightly smaller than the measured radius R, which we attribute to finite temperature effects. Previous studies of rf spectroscopy of Fermi gases [10,11] demonstrated that the spectral peak shifts to higher energy at lower temperature, which is interpreted as the increase of the pairing gap energy. In the outer region of lower density, the local T/T_F becomes higher, consequently reducing $h\Delta\nu_p/\varepsilon_F$. The observation of R_p being close to R implies that our experiment is very close to the zero-temperature limit. From the relation $T/T_F(r) \propto (1 - r^2/R^2)^{-1}$, we can estimate $T/T_F(R_p) \approx 15T/T_F(0)$. If we assume that the pairing gap energy starts emerging at $T/T_F \approx 0.6$ [14], we might infer the local $T/T_F < 0.05$ at the center, close to our estimated temperature. Although $h\Delta\nu_p/\varepsilon_F$ is almost constant over the whole sample, the line width increases in the outer region.

The conventional picture of rf spectroscopy of a strongly interacting Fermi gas is a photodissociation process: the initial $|1\rangle - |2\rangle$ bound state, which can be molecules or fermion pairs, breaks into free particles in state $|1\rangle$ and $|3\rangle$. In a BCS superfluid, the free particle in state $|1\rangle$ is regarded as a quasiparticle, so after the spin transition the whole system can be described as the excited BCS state with one quasiparticle and one free particle in state $|3\rangle$. Since an rf photon changes the spin state while imparting negligible momentum, rf spectroscopy measures a single-particle spin excitation spectrum. With the assumption of no interactions between state $|1\rangle$ and $|3\rangle$, the rf photon energy offset would be $h\Delta\nu = -\mu + E_{-k} + \hbar^2k^2/2m$, where the first term accounts for removing one atom in state $|2\rangle$, the second term E_{-k} is the energy cost for generating one quasiparticle excitation with momentum $-k$, and the last term is the kinetic energy of the atom in state $|3\rangle$ with momentum k.

The homogeneous rf spectra measured in our experiment allow a direct comparison with theoretical predictions. However, a comprehensive theoretical interpretation of the rf spectrum including the effects of $|1\rangle - |3\rangle$ interactions is not available yet. The mean-field (Hartree) energies due to $|1\rangle - |2\rangle$ and $|1\rangle - |3\rangle$ interactions have been empirically assumed to have the same unitarity limited value because of the proximity of a $|1\rangle - |3\rangle$ Feshbach resonance at $B = 690$ G [10,13]. The recent experiments with imbalanced mixtures and higher densities showed some deviations from this assumption [11]. The line shape of the rf spectrum should be affected by $|1\rangle - |3\rangle$ interactions, e.g., when $a_{13} = a_{12}$ (a_{ij} is the s-wave scattering length for two atoms in state $|i\rangle$ and $|j\rangle$), the rf spectrum will be the same as the free atomic spectrum regardless of the initial many-body state of a $|1\rangle$–$|2\rangle$ mixture.

A localized spin excitation, induced by an rf pulse, eventually diffuses over the sample. This ultimately limits the pulse duration and therefore the spatial resolution. Using phase-contrast imaging, we monitored the evolution of the spatial structure in the excited sample with various delay times after applying an rf pulse. The shell structure was well preserved even after 5 ms and only some broadening was observed, showing that during the 1-ms pulse the dynamic evolution of the density difference profiles is not significant.

We found that atoms in state $|3\rangle$ rapidly decayed in the sample, although the total atom number difference between state $|1\rangle$ and $|2\rangle$ did not change over time. At the center of the sample, where the total atom density is about 8×10^{12} cm^{-3}, the lifetime of atoms in state $|3\rangle$ was measured to be less than 0.4 ms. Since a $|1\rangle$–$|3\rangle$ mixture and a $|2\rangle$–$|3\rangle$ mixture are stable at $B = 833$ G [32], the decay should be associated with exoergic molecule formation via three-body collisions involving one atom from each spin state. We observed that the loss of one atom in state $|3\rangle$ was accompanied by loss of one atom in state $|1\rangle$ and one atom in state $|2\rangle$, supporting the three-body loss mechanism [33].

Our new technique of spatially resolved rf spectroscopy should be able to address several important questions also at finite temperature. One question is whether the observed double peak structure [10,11] of an atomic line and a pairing peak is purely inhomogeneous, or whether it is possible to have local coexistence of paired and unpaired atoms. This is of course possible on the BEC side of the Feshbach resonance where in a certain temperature range, bound molecules and thermally dissociated free atoms locally coexist, but it is an open question, how this picture will change in the BEC-BCS crossover.

In conclusion, we present spatially resolved rf spectroscopy of a trapped Fermi gas, using an *in situ* phase-contrast imaging technique. The homogeneous rf spectra of a Fermi gas at unitarity provide a benchmark for a complete theoretical description, which should reveal microscopic details of the paired states.

We thank M. Zwierlein and R. Grimm for stimulating discussions and T. Pasquini for critical reading of the manuscript. This work was supported by the NSF and ONR.

Note added.—Recently, Punk and Zwerger [34], and Baym *et al.* [35] showed that the average shift of the rf spectrum is proportional to $\sqrt{\varepsilon_F}/a_{13}$ near the resonance. We could not clearly distinguish the ε_F dependence of the average shift in our data.

*yishin@mit.edu

[1] M. W. Zwierlein *et al.*, Nature (London) **435**, 1047 (2005).
[2] R. Grimm, arXiv:cond-mat/0703091 (*Proceedings of the International School of Physics "Enrico Fermi," Course CLXIV*).
[3] T.-L. Ho, Phys. Rev. Lett. **92**, 090402 (2004).
[4] J. Kinast *et al.*, Science **307**, 1296 (2005).
[5] J. T. Stewart *et al.*, Phys. Rev. Lett. **97**, 220406 (2006).
[6] A. Altmeyer *et al.*, Phys. Rev. Lett. **98**, 040401 (2007).
[7] C. A. Regal and D. S. Jin, Phys. Rev. Lett. **90**, 230404 (2003).
[8] S. Gupta *et al.*, Science **300**, 1723 (2003).
[9] C. A. Regal *et al.*, Nature (London) **424**, 47 (2003).
[10] C. Chin *et al.*, Science **305**, 1128 (2004).
[11] C. Schunck *et al.*, Science **316**, 867 (2007).
[12] M. Greiner, C. A. Regal, and D. S. Jin, Phys. Rev. Lett. **94**, 070403 (2005).
[13] J. Kinnunen, M. Rodríguez, and P. Törmä, Science **305**, 1131 (2004).
[14] Y. He, Q. Chen, and K. Levin, Phys. Rev. A **72**, 011602(R) (2005).
[15] Y. Ohashi and A. Griffin, Phys. Rev. A **72**, 063606 (2005).
[16] Z. Yu and G. Baym, Phys. Rev. A **73**, 063601 (2006).
[17] Y. Shin *et al.*, Phys. Rev. Lett. **97**, 030401 (2006).
[18] Z. Hadzibabic *et al.*, Phys. Rev. Lett. **91**, 160401 (2003).
[19] Note that also atoms in state $|3\rangle$ contribute to the optical signal. However, since their density is proportional to n_d, the signal is still proportional to n_d.
[20] The measured $h\Delta\nu_i/E_F \approx 0.45$ is higher than the values reported in Refs. [10,11], which we attribute to lower temperature and less heating over the short pulse duration.
[21] The magnetic field was calibrated by determining the resonance frequency ν_0 of the $|2\rangle - |3\rangle$ transition in the absence of atoms in state $|1\rangle$. $\nu_0 = 81.700(1)$ MHz corresponds to a magnetic field of about 833.0(2) G.
[22] R. N. Bracewell, *The Fourier Transform and Its Applications* (McGraw-Hill, New York, 1986).
[23] H. Heiselberg, Phys. Rev. A **63**, 043606 (2001).
[24] K. M. O'Hara *et al.*, Science **298**, 2179 (2002).
[25] M. E. Gehm *et al.*, Phys. Rev. A **68**, 011401(R) (2003).
[26] M. Bartenstein *et al.*, Phys. Rev. Lett. **92**, 120401 (2004).
[27] T. Bourdel *et al.*, Phys. Rev. Lett. **93**, 050401 (2004).
[28] G. B. Partridge *et al.*, Science **311**, 503 (2006).
[29] J. Carlson *et al.*, Phys. Rev. Lett. **91**, 050401 (2003).
[30] G. E. Astrakharchik *et al.*, Phys. Rev. Lett. **93**, 200404 (2004).
[31] J. Carlson and S. Reddy, Phys. Rev. Lett. **95**, 060401 (2005).
[32] R. Grimm (private communication).
[33] In our experiment, the maximum fractional atom loss in state $|2\rangle$ ($|1\rangle$) was about 30% (15%) at $\Delta\nu \approx 10$ kHz, which could not be reduced further due to limits in our signal-to-noise ratio. Including the spatial width of the excitation region, we estimate that the local density depletion was about 45%.
[34] M. Punk and W. Zwerger, arXiv:0707.0792.
[35] G. Baym *et al.*, arXiv:0707.0859.

Appendix G

Phase diagram of a two-component Fermi gas with resonant interactions

This appendix contains a reprint of Ref. [21]: Y. Shin, C. H. Schunck, A. Schirotzek & W. Ketterle, *Phase diagram of a two-component Fermi gas with resonant interactions*, Nature **451**, 689 (2008).

Vol 451 | 7 February 2008 | doi:10.1038/nature06473

nature

LETTERS

Phase diagram of a two-component Fermi gas with resonant interactions

Yong-il Shin[1], Christian H. Schunck[1], André Schirotzek[1] & Wolfgang Ketterle[1]

The pairing of fermions lies at the heart of superconductivity and superfluidity. The stability of these pairs determines the robustness of the superfluid state, and the quest for superconductors with high critical temperature equates to a search for systems with strong pairing mechanisms. Ultracold atomic Fermi gases present a highly controllable model system for studying strongly interacting fermions[1]. Tunable interactions (through Feshbach collisional resonances) and the control of population or mass imbalance among the spin components provide unique opportunities to investigate the stability of pairing[2–4]—and possibly to search for exotic forms of superfluidity[5,6]. A major controversy has surrounded the stability of superfluidity against an imbalance between the two spin components when the fermions interact resonantly (that is, at unitarity). Here we present the phase diagram of a spin-polarized Fermi gas of ^{6}Li atoms at unitarity, experimentally mapping out the superfluid phases versus temperature and density imbalance. Using tomographic techniques, we reveal spatial discontinuities in the spin polarization; this is the signature of a first-order superfluid-to-normal phase transition, and disappears at a tricritical point where the nature of the phase transition changes from first-order to second-order. At zero temperature, there is a quantum phase transition from a fully paired superfluid to a partially polarized normal gas. These observations and the implementation of an *in situ* ideal gas thermometer provide quantitative tests of theoretical calculations on the stability of resonant superfluidity.

When the two spin components resonantly interact, the behaviour of the system becomes independent of the nature of the interactions. This case of unitarity has become a benchmark for experimental and theoretical studies over the last few years. However, there is an ongoing debate about the stability of resonant superfluidity, reflected in major discrepancies in predicted transition temperatures for the balanced spin mixture[7–9], and an even more dramatic discrepancy for the critical imbalance of the two spin components, called the Chandrasekhar–Clogston limit of superfluidity[2,3]. Recent quantum Monte Carlo calculations predicted that superfluidity would be quenched by a density imbalance around 40% (ref. 10), whereas other studies predicted a critical imbalance above 90% (refs 11–16). Our earlier work[17–19] suggested the lower limit but other experiments[20,21] were interpreted to be consistent with the absence of the Chandrasekhar–Clogston limit. This huge discrepancy reveals that even qualitative aspects, such as the role of interactions in the normal phase, are still controversial. The lack of reliable thermometry for strongly interacting systems limits the full interpretations of experimental results.

Here we resolve this long-standing debate by presenting the phase diagram of a spin-polarized Fermi gas at unitarity. We observe that the normal-to-superfluid phase transition changes its nature. At low temperature, the phase transition occurs with a jump in the spin polarization as the imbalance increases, which we interpret as a first-order phase transition. The local spin polarization or local density imbalance is defined as $\sigma = (n_\uparrow - n_\downarrow)/(n_\uparrow + n_\downarrow)$, where ↑ and ↓ refer to the two spin components with densities $n_{\uparrow,\downarrow}$. At high temperature, the phase transition is smooth and therefore of second order. The two regimes are connected by a tricritical point[4,22] and we estimate its position to be $(\sigma_{\mathrm{tc}}, T_{\mathrm{tc}}/T_{\mathrm{F}\uparrow}) \approx (0.2, 0.07)$, where $k_{\mathrm{B}} T_{\mathrm{F}\uparrow} = \hbar^2 (6\pi^2 n_\uparrow)^{2/3}/2m$ is the Fermi energy of the majority component of density $n_\uparrow$ (k_{B} is the Boltzmann constant, $\hbar$ is the Planck constant divided by 2π and m is the atomic mass of ^{6}Li). Our low-temperature results confirm a zero-temperature quantum phase transition at a critical polarization $\sigma_{\mathrm{c}0} \approx 36\%$.

This work required the introduction of several techniques. A tomographic reconstruction of local Fermi temperatures and spin polarization allowed us to obtain the phase diagram for the homogeneous system, no longer affected by the inhomogeneous density of the trapped samples. Furthermore, absolute temperatures were obtained using *in situ* thermometry applied to the non-interacting fully polarized Fermi gas in the outer part of the trapped samples, an ideal thermometer with exactly known thermal properties. Unlike previous work[18,23], this is a direct measurement without any approximations.

Our experiments are carried out in a trapping potential $V(\mathbf{r})$. The local chemical potential of each spin component is given as $\mu_{\uparrow,\downarrow}(\mathbf{r}) = \mu_{\uparrow 0,\downarrow 0} - V(\mathbf{r})$, where $\mu_{\uparrow 0,\downarrow 0}$ are the global chemical potentials. When $\mu_{\uparrow 0} \neq \mu_{\downarrow 0}$, owing to imbalanced populations, the chemical potential ratio $\eta(\mathbf{r}) = \mu_\downarrow/\mu_\uparrow$ varies spatially over the trapped sample and so, under the local density approximation, the trapped inhomogeneous sample is represented by a line in the phase diagrams of the homogeneous system. Figure 1 illustrates the spatial structure of a strongly interacting Fermi mixture in a harmonic trap. In the inner region, where η is closer to unity, a superfluid with zero (or small) spin polarization will form at zero (or low) temperatures, having a sharp phase boundary against the partially polarized normal gas in the outer region. The spin polarization shows a discontinuity at the boundary of the superfluid core at $r = R_{\mathrm{c}}$, a signature of the phase separation of a superfluid and a normal gas[24]. The critical polarization $\sigma_{\mathrm{c}} = \lim_{r \to R_{\mathrm{c}}^+} \sigma(r)$ represents the minimum spin polarization for a stable normal gas; $\sigma_{\mathrm{s}} = \lim_{r \to R_{\mathrm{c}}^-} \sigma(r)$ represents the maximum spin polarization for a stable superfluid gas. At higher temperatures, the discontinuity in the density imbalance disappears. The main result of this paper is the observation and quantitative analysis of such density profiles. Because we have no experimental evidence, we are not discussing the exotic partially polarized phases[25] which could exist only in the transition layer between the superfluid core and the normal outer region.

We prepared a variable spin mixture of the two lowest hyperfine states of ^{6}Li atoms, labelled $|\uparrow\rangle$ and $|\downarrow\rangle$, at a magnetic field of 833 G. A

---

[1] Department of Physics, MIT-Harvard Center for Ultracold Atoms, and Research Laboratory of Electronics, MIT, Cambridge, Massachusetts, 02139, USA.

broad Feshbach resonance at 834 G enhances the interactions between the two spin states. Our sample was confined in a three-dimensional harmonic trap with cylindrical symmetry. The *in situ* density distributions of the majority (spin ↑) and minority (spin ↓) components were determined using a phase-contrast imaging technique[19] (Fig. 2). We obtained the low-noise profiles $\tilde{n}$ by averaging the column density distribution along the equipotential line and determined the three-dimensional density profiles $n(r)$ using the inverse Abel transformation of the column densities $\tilde{n}(r)$ (see Methods Summary). Most of our measurements were performed at a total population imbalance of $\delta \approx 50\%$, where $\delta = (N_\uparrow - N_\downarrow)/(N_\uparrow + N_\downarrow)$ refers to the total numbers of atoms in the sample, $N_\uparrow$ and $N_\downarrow$ of the spin ↑ and ↓ components, respectively.

Figure 3 displays the radial profiles of the densities $n_{\uparrow,\downarrow}(r)$ and the corresponding spin polarization $\sigma(r)$ for various temperatures. The discontinuity in the spin polarization, clearly shown at very low temperatures, demonstrates the phase separation of the inner superfluid of low polarization and the outer normal gas of high polarization. At low temperature, the core radius R_c is determined as the kink (and/or peak) position in the column density difference profile. At high temperature (but still in the superfluid regime), the discontinuity in $\sigma(r)$ disappears. At our lowest temperature, the radii of the minority cloud and the core region were measured as $R_\downarrow = 0.73(1)R_\uparrow$ and $R_c = 0.430(3)R_\uparrow$ (at $\delta = 44(4)\%$), respectively, and these values agree with recent theoretical calculations[10,25] within the experimental uncertainties due to the determination of δ. Here, $R_\uparrow$ is the radius of the majority cloud, and the uncertainty of the final digit is indicated by parentheses.

We determined temperature from the *in situ* majority wing profiles. The outer part of the majority component, forming a non-interacting Fermi gas, fulfils the definition of an ideal thermometer, namely a substance with exactly understood properties in contact with the target sample. This new *in situ* method avoids the modification of the ideal gas profile caused by the collision with the inner core during ballistic expansion (ref. 18, see Supplementary Information). The outer part of the averaged column density difference profile $(r > R_\downarrow)$ was fitted to a finite temperature Fermi–Dirac distribution in a harmonic trap (Fig. 4) and the relative temperature $T' \equiv T/T_{F0}$ was determined, where $k_B T_{F0} = \hbar^2(6\pi^2 n_0)^{2/3}/2m$ is the Fermi energy of the non-interacting Fermi gas, which has the same density distribution in the outer region as the majority cloud (n_0 is the central density of the non-interacting Fermi gas at zero temperature). We verified that anharmonicity of the trapping potential does not affect the fitted temperature (see Methods).

The critical lines of the phase diagram of a homogeneous spin-polarized Fermi gas were obtained by determining the local temperature and spin polarization at the phase boundary. The local relative temperature $T'_{\mathrm{local}} \equiv T/T_{F\uparrow}$ was derived from the local density $n_\uparrow(R_c)$ according to $T'(R_c) = T/T_{F0} \times (n_0/n_\uparrow(R_c))^{2/3}$. Because we observe no jump in the majority density within our resolution, $T_{F\uparrow}$ is well-defined at the boundary. The critical polarizations σ_c and σ_s were measured as $\sigma_c = \sigma(R_c)$ and $\sigma_s = \sigma(R_c - 0.05R_\uparrow)$ (this criterion for σ_s was more robust than a fitting procedure, but excludes the possibility that σ_s will be equal to σ_c at high temperature. Therefore, the measured σ_s should be regarded as a lower bound for the polarization of

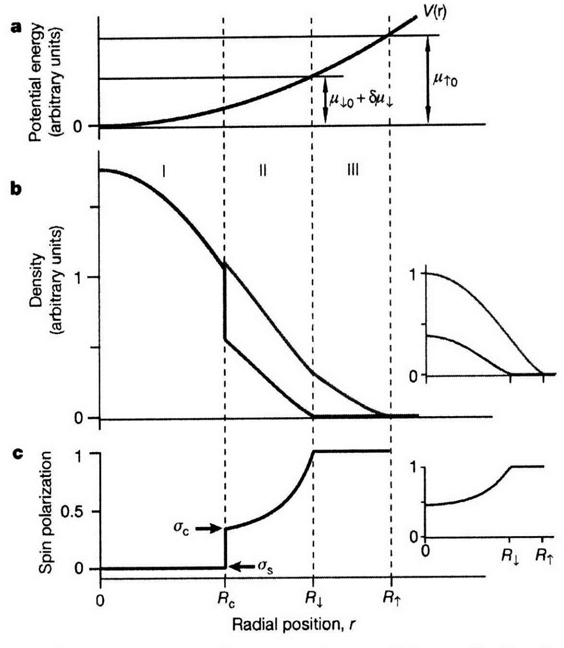

Figure 1 | Schematic of spatial structure of a strongly interacting Fermi gas in a harmonic trap. a, A two-component (spin ↑ and ↓) Fermi mixture is confined in an external potential $V(r) \propto r^2$ with the chemical potential $\mu_{\uparrow0,\downarrow0}$ of each spin component ($\delta\mu_\downarrow$ is the shift for the spin ↓ component owing to interactions). **b,** Density distributions of the majority component $n_\uparrow(r)$ (red line) and the minority component $n_\downarrow(r)$ (blue line). **c,** Spin polarization $\sigma(r) = (n_\uparrow - n_\downarrow)/(n_\uparrow + n_\downarrow)$. At zero temperature, the sample has a three-layer radial structure: (I), the core region $(0 \leq r < R_c)$ of a fully paired superfluid with $n_\uparrow = n_\downarrow$; (II), the intermediate region $(R_c < r < R_\downarrow)$ of a partially polarized normal gas; and (III), the outer region $(R_\downarrow < r < R_\uparrow)$ of a fully polarized normal gas. The critical polarization σ_c (or σ_s) is defined as the minimum (or maximum) spin polarization of the normal (or superfluid) region. The non-interacting case is shown in the insets. The insets have the same axes as the main figure.

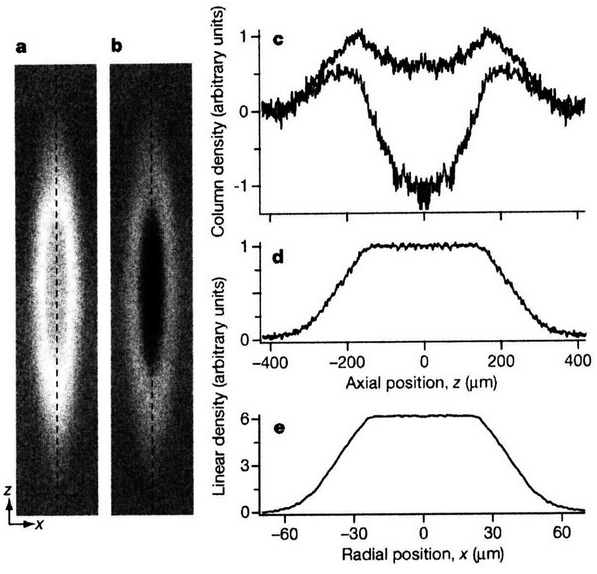

Figure 2 | Double *in situ* phase-contrast imaging of a trapped Fermi mixture. Two phase-contrast images of one sample were taken using different probe frequencies of the imaging beam, measuring the density difference $n_{d1} = n_\uparrow - n_\downarrow$ (**a**) and the weighted density difference $n_{d2} = 0.76 n_\uparrow - 1.43n_\downarrow$ (**b**), respectively. The images show the two-dimensional distribution of the column density difference, $\tilde{n}_{d1,2}(x,z) \equiv \int n_{d1,2}(\mathbf{r})dy$, owing to the line-of-sight integration. The field of view for each image is 150 μm × 820 μm. **c**, The distributions of the column density difference $\tilde{n}_{d1}$ (black line) and $\tilde{n}_{d2}$ (red line) along the central line (the dashed lines in **a** and **b**). The profiles of the integrated linear density difference, $\bar{n}_{d1,z} \equiv \int \tilde{n}_{d1}(x,z)dx$ (**d**) and $\bar{n}_{d1,x} \equiv \int \tilde{n}_{d1}(x,z)dz$ (**e**), show the identical flat-top feature except scaling. The aspect ratio of the trapping potential was $\lambda = 6.15$, the majority atom number was $N_\uparrow = 5.9(5) \times 10^6$, the population imbalance was $\delta = 44(4)\%$, and the relative temperature was $T' = T/T_{F0} = 0.03(1)$ (see text for definitions).

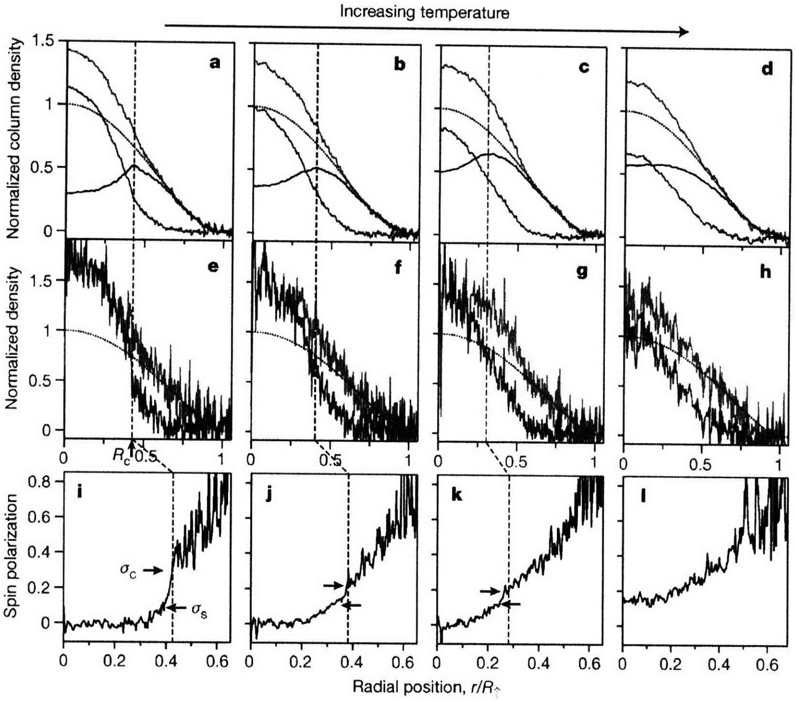

Figure 3 | Density profiles of trapped Fermi mixtures with imbalanced populations. The top row (**a–d**) shows the averaged column density profiles for various temperatures (red, majority; blue, minority; black, difference). The majority radius $R_\uparrow$ was determined from the outer region ($r > R_\downarrow$, where $R_\downarrow$ is the radius of the minority cloud) of the majority profiles using a fit to a zero-temperature Thomas–Fermi distribution (black dotted lines). The column densities are normalized by the central value of the fitted Thomas–Fermi distribution. The middle row (**e–h**) and the bottom row (**i–l**) show the reconstructed three-dimensional profiles and the spin polarization profiles $\sigma(r)$ corresponding to the profiles in **a–d**. The core radius R_c was determined as the peak (and/or kink) position in the column density difference (only for **a–c**), indicated by the vertical dashed lines. The two spin polarizations σ_c at $r = R_c$ and σ_s at $r = R_c - 0.05R_\uparrow$ are marked by the right and left arrows, respectively. The values for T', σ_c, $R_c/R_\uparrow$, $R_\uparrow$ (in μm), $N_\uparrow$, δ (in %) and λ were, respectively: for **a**, **e** and **i**, 0.03(1), 0.34, 0.43, 385, $5.9(5) \times 10^6$, 44(4), 6.15; for **b**, **f** and **j**, 0.05(2), 0.24, 0.39, 416, $1.0(1) \times 10^7$, 48(4), 6.5; for **c**, **g** and **k**, 0.07(1), 0.21, 0.29, 443, $1.2(2) \times 10^7$, 54(4), 6.5; for **d**, **h** and **l**, 0.10(1), not determined, not determined ($\sigma_{r=0} = 0.15$ and condensate fraction = 2(1)%), 398, $5.3(4) \times 10^6$, 54(4), 7.7.

the superfluid at the boundary). The discontinuity in the spin polarization profile implies that there is a thermodynamically unstable window, $\sigma_s < \sigma < \sigma_c$, leading to a first-order superfluid-to-normal phase transition. As the temperature increases, the unstable region reduces with decreasing σ_c and increasing σ_s. For high temperature when the bimodal feature in the spin polarization profile disappears, we recorded the condensate fraction as an indicator of superfluidity, using the rapid field-ramp technique[17]. As the temperature decreases, the condensate fraction gradually increases with a finite central polarization[19]. Such smooth variations of the density profile and condensate fraction across the phase transition are characteristic of a second-order phase transition.

The phase diagram is characterized by three distinct points: the critical temperature T_{c0} for a balanced mixture, the critical polarization σ_{c0} of a normal gas at zero temperature, and the tricritical point (σ_{tc}, T_{tc}) at which the nature of the phase transition changes. Owing to the lack of a predicted functional form for the phase transition line in the σ–T plane, we apply a linear fit to the measured critical points, suggesting $T_{c0}/T_{F\uparrow} \approx 0.15$, $\sigma_{c0} \approx 0.36$ and $(\sigma_{tc}, T_{tc}/T_{F\uparrow}) \approx (0.20, 0.07)$. The value for σ_{c0} agrees well with the prediction (from the quantum Monte Carlo calculation) of 0.39 (ref. 10). The extrapolation of the phase diagram to $\sigma = 0$ is tentative, because the *in situ* thermometry could not be applied to small population imbalances owing to the narrowness of the non-interacting outer region.

The Chandrasekhar–Clogston limit reflects the energetic competition between a superfluid state and a partially polarized normal state, and occurs at a critical value of $2h_c$ for the chemical potential difference $\delta\mu = \mu_\uparrow - \mu_\downarrow$. In Bardeen–Cooper–Schrieffer theory, which is valid for weak interactions, $h_c = \Delta/\sqrt{2}$ (ref. 3). Here, Δ is the pairing gap. With the assumption of no interactions in a normal gas, quantum Monte Carlo studies predict $h_c = 1.00(5)\Delta \approx 1.2\mu$ at unitarity[11], where $\mu = (\mu_\uparrow + \mu_\downarrow)/2$. The condition $\mu_{\downarrow c} = \mu - h_c < 0$ requires $n_\downarrow = 0$ for a non-interacting normal gas, implying the absence of a partially polarized normal phase and consequently $\sigma_{c0} = 100\%$. Mean-field approaches[12–16], which cannot treat the interactions in the normal phase accurately, also predict a high critical imbalance $\sigma_{c0} > 90\%$. Strong interactions in the normal phase, however, have been observed through the compressed shape of the minority cloud[18] and the shift in the radio frequency excitation spectrum[26]. The data in Fig. 5 clearly establish a zero-temperature Chandrasekhar–Clogston limit for σ_{c0} in the range 30% to 40%. By analysing the *in situ* density profiles[25,27], we obtained $h_c \approx 0.95\mu$ (see Methods). Since theory clearly predicts $\mu < \Delta$ at unitarity[9,11], we have $h_c < \Delta$. If h_c were larger than Δ, polarized quasi-particles would have negative energies and would already form at zero temperature. Therefore, up to our observed value of h_c, the fully paired

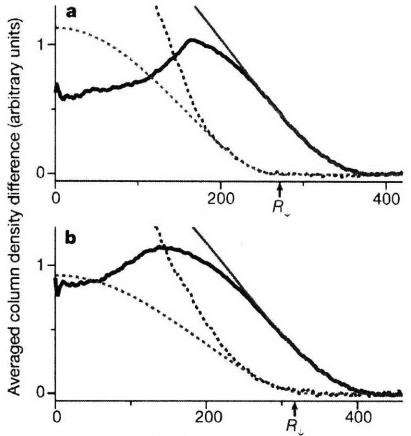

Figure 4 | Temperature determination using *in situ* density profiles. The relative temperature $T' = T/T_{F0}$ (see text for definition) was determined from the outer region ($r > R_\downarrow$) of the averaged column density difference profile (black line) fitted to a finite temperature Fermi–Dirac distribution (red line). The radius of the minority cloud $R_\downarrow$ was determined from a fit of the wing profile of the minority component (black dashed line) to a zero-temperature Thomas–Fermi distribution (red dashed line). **a**, $T' = 0.03(1)$ and $\delta = 44(4)\%$. **b**, $T' = 0.08(1)$ and $\delta = 46(4)\%$.

superfluid state is stable, and a polarized superfluid exists only at finite temperature.

The interface between two immiscible fluids involves a surface energy, leading to at least a small violation of the local density approximation. However, the observed sharp interface along an equipotential line and the flat-top structure of the linear density difference profiles (Fig. 2d and e) imply that corrections to the local density approximation are smaller than the resolution of our experiment. These observations are inconsistent with the interpretations given for the experimental results reported in refs 20 and 21, where it has been shown that highly elongated small samples are deformed by surface tension[28,29]. The scaling of those surface effects to our parameters predicted a deviation of the aspect ratio of the superfluid core of about 15% from the trap aspect ratio[29], whereas our data gives an upper bound of 2%. We note that surface tension would add energy in the phase-separated superfluid regime and would shift the Chandrasekhar–Clogston limit to smaller values. Refs 20 and 21 concluded that the Chandrasekhar–Clogston limit should be $\delta_{c0} > 95\%$, which is ruled out by our observations. We are not aware of any suggested effect that can reconcile the data of refs 20 and 21 with our phase diagram for a resonant superfluid. To identify this finite size effect and to understand fully the nature of the normal state[26], more work on imbalanced Fermi gases is needed.

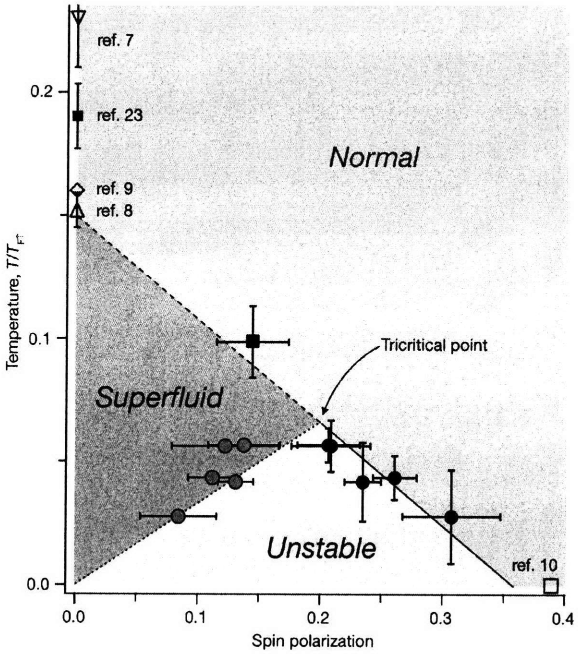

Figure 5 | The σ–T phase diagram for a homogeneous spin-polarized Fermi gas with resonant interactions. The critical polarizations σ_c (black solid circles and square) and σ_s (grey solid circles) are displayed along the local $T/T_{F\uparrow}$ at the phase boundary. The yellow area ($\sigma_s < \sigma < \sigma_c$) represents a thermodynamically unstable region, leading to the phase separation. Above the tricritical point, the phase transition in the centre of the cloud was observed by the onset of pair condensation. For this, a cloud was evaporatively cooled, until it crossed the phase transition on a trajectory almost perpendicular to the phase transition line (see Supplementary Information). The critical spin polarization and temperature were obtained by interpolating between points without and with small condensates (black solid square). The linear fit to the σ_c values is shown as a guide to the eye for the normal-to-superfluid phase transition line. Each data point consists of five independent measurements and error bars indicate standard deviation. The blue open symbols show theoretical predictions for the critical temperature of a homogeneous equal mixture[7–9] and the critical polarization at zero temperature[10]. The blue solid square is the measured critical temperature of ref. 23, multiplied by $\sqrt{\xi}$ with $\xi = 0.42$ (ref. 11) to obtain local T/T_F at the centre. Finite temperature correction may increase the effective value of ξ.

In conclusion, we have established the phase diagram of a homogeneous spin-polarized Fermi gas with resonant interactions in the σ–T plane. This includes the identification of a tricritical point at which the critical lines for first-order and second-order phase transitions meet, and the final confirmation of a zero-temperature quantum phase transition—the Chandrasekhar–Clogston limit of superfluidity—for a gas at unitarity. So far, predicted exotic superfluid states such as the breached-pair state in a stronger coupling regime (Bose–Einstein condensate side)[13] and the Fulde–Ferrell–Larkin–Ovchinnikov state in a weaker coupling regime (Bardeen–Cooper–Schrieffer side)[5,6,12,16,30] have not been observed, but the novel methods of tomography and thermometry will be important tools in the search for those states.

METHODS SUMMARY

The experimental procedure has been described in our previous publications[17–19]. A degenerate Fermi gas of ^{6}Li atoms was first prepared in an optical trap, using laser cooling and sympathetic cooling with ^{23}Na atoms. A variable spin mixture of the two lowest hyperfine states $|\uparrow\rangle$ and $|\downarrow\rangle$ (corresponding to the $|F=1/2, m_F=1/2\rangle$ and $|F=1/2, m_F=-1/2\rangle$ states at low magnetic field) was created at a magnetic field $B = 885$ G. The final evaporative cooling was achieved by lowering the trap depth and all measurements were performed at $B = 833$ G. The temperature of the cloud was controlled by the lowest value of the trap depth in the evaporative cooling process. The oscillation frequency in the axial direction was $f_z = 23$ Hz. The two transverse oscillation frequencies f_ρ are equal to within less than 2%. Two phase-contrast images of the same sample were taken consecutively with different probe frequencies, ν_1 and ν_2 (Fig. 2). The time interval between the two images was 10 μs, and the pulse duration of each probe beam was 15 μs. Because the probe beam was off-resonant, no heating effect of the first pulse was observed in the second image. The trapped sample was observed to have an elliptical shell structure of the same aspect ratio $\lambda = f_\rho/f_z$ as the trapping potential over our entire temperature range, and we obtained the low-noise profiles $\tilde{n}$ by averaging the column density distribution along the equipotential line defined as $\lambda^2x^2 + z^2 = r^2$ for a given radial position r. The region for averaging was restricted depending on the type of analysis. Deviations from the trap aspect ratio were only found for the outer thermal wings. Details of the phase-contrast imaging technique and the data analysis are given in Methods and Supplementary Information.

Full Methods and any associated references are available in the online version of the paper at www.nature.com/nature.

Received 19 September; accepted 8 November 2007.

1. Giorgini, S., Pitaevskii, L. P. & Stringari, S. Theory of ultracold Fermi gases. Preprint at ⟨http://arxiv.org/abs/0706.3360⟩ (2007).
2. Chandrasekhar, B. S. A note on the maximum critical field of high-field superconductors. *Appl. Phys. Lett.* **1**, 7–8 (1962).
3. Clogston, A. M. Upper limit for the critical field in hard superconductors. *Phys. Rev. Lett.* **9**, 266–267 (1962).
4. Sarma, G. On the influence of a uniform exchange field acting on the spins of the conduction electrons in a superconductor. *J. Phys. Chem. Solids* **20**, 1029–1032 (1963).
5. Fulde, P. & Ferrell, R. A. Superconductivity in a strong spin-exchange field. *Phys. Rev.* **135**, A550–A563 (1964).
6. Larkin, A. I. & Ovchinnikov, Y. N. Inhomogeneous state of superconductors. *Sov. Phys. JETP* **20**, 762–769 (1965).
7. Bulgac, A., Drut, J. E. & Magierski, P. Spin 1/2 fermions in the unitary regime: a superfluid of a new type. *Phys. Rev. Lett.* **96**, 090404 (2006).
8. Burovski, E., Prokofev, N., Svistunov, B. & Troyer, M. Critical temperature and thermodynamics of attractive fermions at unitarity. *Phys. Rev. Lett.* **96**, 160402 (2006).
9. Haussmann, R., Rantner, W., Cerrito, S. & Zwerger, W. Thermodynamics of the BCS-BEC crossover. *Phys. Rev. A.* **75**, 023610 (2007).
10. Lobo, C., Recati, A., Giorgini, S. & Stringari, S. Normal state of a polarized Fermi gas at unitarity. *Phys. Rev. Lett.* **97**, 200403 (2006).
11. Carlson, J. & Reddy, S. Asymmetric two-component fermion systems in strong coupling. *Phys. Rev. Lett.* **95**, 060401 (2005).
12. Sheehy, D. E. & Radzihovsky, L. BEC-BCS Crossover in "magnetized" Feshbach-resonantly paired superfluids. *Phys. Rev. Lett.* **96**, 060401 (2006).
13. Yi, W. & Duan, L.-M. Phase diagram of a polarized Fermi gas across a Feshbach resonance in a potential trap. *Phys. Rev. A* **74**, 013610 (2006).
14. Gubbels, K. B., Romans, M. W. & Stoof, H. T. Sarma phase in trapped unbalanced Fermi gases. *Phys. Rev. Lett.* **97**, 210402 (2006).

15. Chien, C.-C., Chen, Q., He, Y. & Levin, K. Superfluid phase diagrams of trapped Fermi gases with population imbalance. *Phys. Rev. Lett.* **98**, 110404 (2007).
16. Parish, M. M., Marchetti, F. M., Lamacraft, A. & Simons, B. D. Finite-temperature phase diagram of a polarized Fermi condensate. *Nature Phys.* **3**, 124–128 (2007).
17. Zwierlein, M. W., Schirotzek, A., Schunck, C. H. & Ketterle, W. Fermionic superfluidity with imbalanced spin populations. *Science* **311**, 492–496 (2006).
18. Zwierlein, M. W., Schunck, C. H., Schirotzek, A. & Ketterle, W. Direct Observation of the superfluid phase transition in ultracold Fermi gases. *Nature* **442**, 54–58 (2006).
19. Shin, Y., Zwierlein, M. W., Schunck, C. H., Schirotzek, A. & Ketterle, W. Observation of phase separation in a strongly interacting imbalanced Fermi gas. *Phys. Rev. Lett.* **97**, 030401 (2006).
20. Partridge, G. B., Li, W., Karmar, R. I., Liao, Y. & Hulet, R. G. Pairing and phase separation in a polarized Fermi gas. *Science* **311**, 503–505 (2006).
21. Partridge, G. B., Li, W., Karmar, R. I., Liao, Y. & Hulet, R. G. Deformation of a trapped Fermi gas with unequal spin populations. *Phys. Rev. Lett.* **97**, 190407 (2006).
22. Griffiths, R. B. Thermodynamics near the two-fluid critical mixing point in He^3-He^4. *Phys. Rev. Lett.* **24**, 715–717 (1970).
23. Luo, L., Clancy, B., Joseph, J., Kinast, J. & Thomas, J. E. Measurement of the entropy and critical temperature of a strongly interacting Fermi gas. *Phys. Rev. Lett.* **98**, 080402 (2007).
24. Bedaque, P. F., Caldas, H. & Rupak, G. Phase separation in asymmetrical fermion superfluids. *Phys. Rev. Lett.* **91**, 247002 (2003).
25. Bulgac, A. & Forbes, M. M. Zero-temperature thermodynamics of asymmetric Fermi gases at unitarity. *Phys. Rev. A* **75**, 031605(R) (2007).
26. Schunck, C. H., Shin, Y., Schirotzek, A., Zwierlein, M. W. & Ketterle, W. Pairing without superfluidity: the ground state of an imbalanced Fermi mixture. *Science* **316**, 867–870 (2007).
27. Chevy, F. Universal phase diagram of a strongly interacting Fermi gas with unbalanced spin populations. *Phys. Rev. A* **74**, 063628 (2006).
28. De Silva, T. N. & Mueller, E. J. Surface tension in unitary Fermi gases with population imbalance. *Phys. Rev. Lett.* **97**, 070402 (2006).
29. Haque, M. & Stoof, H. T. C. Trapped fermionic clouds distorted from the trap shape due to many-body effects. *Phys. Rev. Lett.* **98**, 260406 (2006).
30. Machida, K., Mizushima, T. & Ichioka, M. Generic phase diagram of fermion superfluids with population imbalance. *Phys. Rev. Lett.* **97**, 120407 (2006).

Supplementary Information is linked to the online version of the paper at www.nature.com/nature.

Acknowledgements We thank M. W. Zwierlein and A. Keshet for a critical reading of the manuscript. This work was supported by NSF, ONR, MURI and DARPA.

Author Information Reprints and permissions information is available at www.nature.com/reprints. Correspondence and requests for materials should be addressed to Y.S. (yishin@mit.edu).

METHODS

Phase-contrast imaging. The optical signal in the phase-contrast imaging is proportional to the net phase shift of the imaging beam passing through a Fermi mixture, that is, it is proportional to $n_\uparrow/(\nu-\nu_\uparrow^0)-n_\downarrow/(\nu-\nu_\downarrow^0)$, where ν is the probe frequency of the imaging beam, and $\nu_\uparrow{}^0$ and $\nu_\downarrow{}^0$ are the resonance frequencies of the optical transition for the states $|\uparrow\rangle$ and $|\downarrow\rangle$, respectively. When the probe beam is tuned to the middle of the two transitions, that is, to $\nu=\nu_0=(\nu_\uparrow^0+\nu_\downarrow^0)/2$, the optical signal reflects the density difference $n_d = n_\uparrow - n_\downarrow$. In our experiment, two phase-contrast images of the same sample were taken consecutively with different probe frequencies, ν_1 and ν_2 (Fig. 2). The two images record the density difference $n_{d1} = n_\uparrow - n_\downarrow$ and the weighted density difference $n_{d2} = \alpha_\uparrow n_\uparrow - \alpha_\downarrow n_\downarrow$. The first probe frequency ν_1 was determined by zeroing the optical signal with an equal mixture and $\alpha_{\uparrow,\downarrow}$ was determined by the signal ratio between the first and the second image for a highly imbalanced Fermi mixture with $|\delta|>95\%$ (an almost fully polarized gas). Finally, we obtained $n_\uparrow = (\alpha_\downarrow n_{d1} - n_{d2})/(\alpha_\downarrow - \alpha_\uparrow)$ and $n_\downarrow = (\alpha_\uparrow n_{d1} - n_{d2})/(\alpha_\downarrow - \alpha_\uparrow)$. The difference between ν_1 and ν_2 was chosen to lie between 8 and 13 MHz.

Data analysis. Low-noise profiles were obtained by averaging the column density distribution of phase-contrast images along elliptical equipotential lines ($\lambda^2x^2+z^2=r^2$). For the measurement of the critical spin polarization, the averaging region was restricted to $|x|<12\,\mu\text{m}$ to preserve the sharp features at the phase boundary. The diffraction limit for our imaging system was about 2 μm. For the determination of local quantities in the profiles, we averaged over ±5 μm around a given position. For temperature determination, the averaging region was restricted to an axial sector of ±60° to avoid corrections due to transverse anharmonicities (see below). The relative temperature T' is determined as $T'\equiv T/T_{F0}=(-6\mathrm{Li}_3(-\zeta))^{-1/3}$, where ζ is the fugacity obtained from the fit ($\mathrm{Li}_s(z)\equiv\sum_{k=1}^{\infty} z^k/k^s$ is the polylogarithmic function of order s).

Anharmonicity of the trapping potential. For the determination of temperatures from the spatial *in situ* profiles it was necessary to address the anharmonicity of the trapping potential. Our trap is generated by a weakly focused (beam waist $w\approx 125\,\mu\text{m}$) infrared gaussian laser beam (wavelength 1,064 nm) near the saddle point of a magnetic potential. The total trapping potential is given as

$$V(\rho,z)=U_0\exp\left(-\frac{2\rho^2}{w^2}\right)+\frac{m(2\pi f_z)^2}{2}\left(-\frac{\rho^2}{2}+z^2\right),$$

where $\rho^2=x^2+y^2$. We note that gravity has been compensated by a magnetic field gradient. The axial confinement comes mainly from the magnetic potential with oscillation frequency of f_z = 23 Hz. The transverse magnetic potential is anti-trapping and limits the trap depth according to:

$$U=\frac{1}{4}m(2\pi f_\rho)^2w^2\left[1-\frac{f_z^2}{2f_\rho^2}\ln\left(\frac{2f_\rho^2+f_z^2}{f_z^2}\right)\right] \tag{1}$$

where f_ρ is the transverse oscillation frequency in the central harmonic region. When the trap depth is comparable to the Fermi energy of a sample, the transverse anharmonicity will affect the shape of the cloud. Although in our experiments the inner core and the outer cloud had the same aspect ratio as the trapping potential, anharmonicities were not negligible in the spatial wings used to determine the temperature.

This issue was addressed by adjusting the angular averaging region (Supplementary Fig. 3). Because the trapping potential is only anharmonic for large ρ, we could reduce the effect by decreasing the angle of the averaging sector around the axial z-direction. Both the experimental data and an exact simulation for an ideal Fermi gas show that the fitted temperature remains almost constant up to a certain angle and then increases when the averaging sector includes more of the transverse outer region. In our temperature determination, we chose the averaging sector to be ±60°, which was large enough to create low-noise profiles, but kept the effect of the anharmonicities to below 10%. The one-dimensional fit to angularly averaged profiles was computationally more efficient than a two-dimensional fit to a selected region of the image. In a two-dimensional fit, one could also include anharmonic terms in the fitting function.

Critical chemical potential ratio η_c. In a harmonic trap, the chemical potential of the majority and minority components are given as $\mu_\uparrow(r)=\mu_{\uparrow0}(1-r^2/R_\uparrow^2)$ and $\mu_\downarrow(r)=\mu_{\uparrow0}(\eta_0-r^2/R_\uparrow^2)$, respectively. At unitarity, the global chemical potential of a fully paired superfluid in the core is given as $\mu_{s0}=\xi\varepsilon_F=\zeta\hbar^2(6\pi^2n_{s0})^{2/3}/2m$ where $n_{s0}=n_{\uparrow,\downarrow}(r=0)$ is the central density. The thermodynamic equilibrium requires $\mu_{s0}=(\mu_{\uparrow0}+\mu_{\downarrow0})/2$, where $\mu_{\uparrow0}=\hbar^2(6\pi^2n_0)^{2/3}/2m$. From $\mu_{s0}/\mu_{\uparrow0}=\xi(n_{s0}/n_0)^{2/3}$, we obtain the chemical potential ratio as:

$$\eta(r)=\frac{\eta_0-r^2/R_\uparrow^2}{1-r^2/R_\uparrow^2}=2\frac{\xi(n_{s0}/n_0)^{2/3}-1}{1-r^2/R_\uparrow^2}+1$$

In our coldest sample ($\delta\approx 44\%$), the normalized central density and the radius for the phase boundary were measured to be $n_{s0}/n_0 = 1.72(4)$ and $R_c/R_\uparrow = 0.430(3)$, respectively, yielding the critical chemical potential ratio $\eta_c=\eta(R_c)\approx 0.03$ with $\xi=0.42$ (ref. 11). The critical difference is $h_c/\mu=(1-\eta_c)/(1+\eta_c)\approx 0.95$.

doi: 10.1038/nature06473

Phase diagram of a two-component Fermi gas with resonant interactions

Yong-il Shin, Christian H. Schunck, André Schirotzek & Wolfgang Ketterle

Supplementary Information

Supplementary Figures

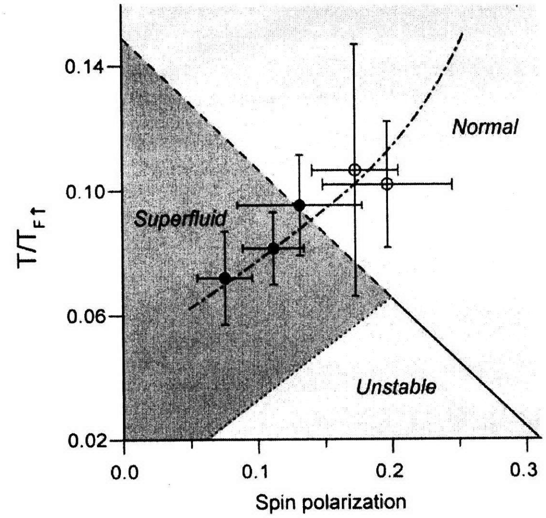

Supplementary Figure 1: (Color online) Trajectory of the center of a cloud in the phase diagram during the cooling process. Above the tricritical point, the normal-to-superfluid phase transition was observed by the onset of pair condensation in the evaporative cooling process. The local spin polarization and temperature at the center of the cloud was measured (black solid (open) circles with (without) condensate fraction), and the critical point was obtained by linearly interpolating with the condensate fraction. The dashed-dot line shows a guide line for the trajectory of the cloud center. The population imbalance of the sample was $\delta \approx 55\%$. A non-interacting mixture with this imbalance has a spin polarization $\sigma \approx 30\%$ at the center at zero temperature.

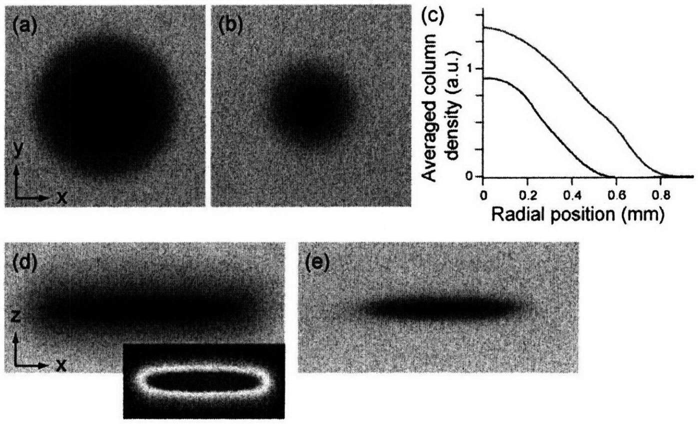

Supplementary Figure 2: (Color online) Expansion of a population-imbalanced Fermi mixture. The absorption images of (a, d) the majority and (b, e) minority components were taken along (a, b) the axial *z* and (d, e) transverse *y* directions after expansion. (c) The azimuthally averaged column density profiles of the majority (red) and the minority (blue) cloud are obtained from (a) and (b), respectively. The excess majority atoms in the outer region interact with the core during expansion. The contour lines of the outer part of the majority cloud (color inset) are not elliptical and have the shape of a horse-track. This shows that the minority cloud pushes the outer majority atoms in the transverse direction, which is also indicated by the hump of the majority profile at the edge of the minority cloud. The population imbalance was $\delta \approx 55\%$

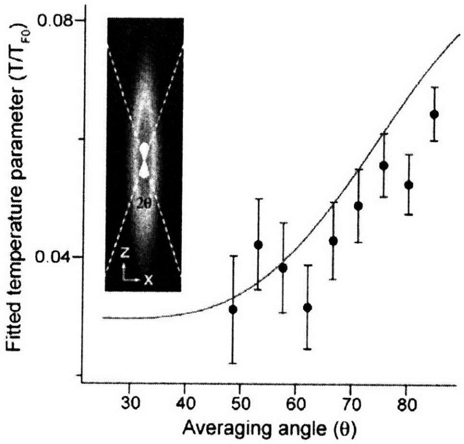

Supplementary Figure 3: (Color online) The temperature of the cloud was determined for various angles θ of the averaging sector. For a large angle, the large-*x* region is included in the averaged profile, resulting in a broadening of the spatial wings and consequently higher value of the fitted temperature. The red line shows the results of a simulation using the same parameters as the experiment ($\lambda = f_\rho/f_z = 6.15$, $T_{F0} = 1$ μK and the trap depth $U/k_B = 2$ μK).

Supplementary Discussion

Thermometry of ultracold Fermi gases

In our previous work[1,2], temperatures have been determined by fitting the spatial wings of the majority component after expansion. However, we found that one can neglect collisions with the minority atoms in the core only for large population imbalances. In a simplified picture, one can regard collisions with the inner core as collisions with a moving wall, which moves outward radially and inward axially (due to the magnetic trapping potential). This results in different average kinetic energies (transversely and axially) of the free majority atoms in the outer region. Figure S2 shows the density distribution of the majority and minority components after expansion. Although the temperature has been overestimated by only 20% for typical experimental conditions ($\delta \approx 60\%$) in refs [1,2], we do not regard this technique as well-calibrated absolute thermometry.

One other concept for thermometry determines temperature as the derivative of entropy with energy. So far, this concept could be implemented only for balanced fermion mixtures with certain approximations, and due to the need of determining a derivative, could only be used to obtain temperatures averaged over a certain range[3].

Polarized superfluid at finite temperature

When the two spin components have a chemical potential difference $2h$, the BCS-type superfluid has two branches of quasiparticles with excitation energies $\sqrt{(\varepsilon_k - \mu)^2 + \Delta^2} \pm h$ where $\varepsilon_k = \hbar^2 k^2 / 2m$. At finite temperature, the superfluid is polarized due to the large thermal population of the lower branch compared to the upper branch. An interesting situation arises when h becomes larger than Δ, i.e. the lower branch has negative energy quasiparticles, implying that even at zero temperature the superfluid state would have a finite polarization. Our experiments show $h_c < \Delta$ at very low temperature, suggesting that a polarized superfluid state exists only at finite temperature. The breached-pair state with $h_c > \Delta$ at zero temperature has been predicted in a stronger coupling regime (on the BEC side of the Feshbach resonance). Since Δ gradually decreases with higher temperature, it might be possible to have $h_c > \Delta$ at finite temperature, at least in the weakly-interacting BCS limit where Δ smoothly approaches zero at a second order phase transition point. One interesting problem is identifying this gapless region of $h > \Delta$ in the phase diagram for various coupling regimes.

Supplementary Notes

1. Zwierlein, M. W., Schunck, C. H., Schirotzek, A. & Ketterle, W. Direct Observation of the superfluid phase transition in ultracold Fermi gases. *Nature* **442**, 54-58 (2006).
2. Shin, Y., Zwierlein, M. W., Schunck, C. H., Schirotzek A. & Ketterle, W. Observation of phase Separation in a strongly interacting imbalanced Fermi gas. *Phys. Rev. Lett.* **97**, 030401 (2006).
3. Luo, L., Clancy, B., Joseph, J., Kinast, J. & Thomas, J. E. Measurement of the entropy and critical temperature of a strongly interacting Fermi gas. *Phys. Rev. Lett.* **98**, 080402 (2007).

Appendix H

Determination of the fermion pair size in a resonantly interacting superfluid

This appendix contains an updated version of Ref. [111]: C. H. Schunck, Y. Shin, A. Schirotzek & W. Ketterle, *Determination of the fermion pair size in a resonantly interacting superfluid.* Preprint, arXiv:0802.0341v1 [cond-mat.supr-con].

Determination of the fermion pair size in a resonantly interacting superfluid

Christian H. Schunck, Yong-il Shin, André Schirotzek, and Wolfgang Ketterle
Department of Physics, MIT-Harvard Center for Ultracold Atoms, and Research Laboratory of Electronics, MIT, Cambridge, MA 02139

(Dated: February 4, 2008)

Fermionic superfluidity requires the formation of pairs. The actual size of these fermion pairs varies by orders of magnitude from the femtometer scale in neutron stars and nuclei to the micrometer range in conventional superconductors. Many properties of the superfluid depend on the pair size relative to the interparticle spacing. This is expressed in BCS-BEC crossover theories [1–3], describing the crossover from a Bardeen-Cooper-Schrieffer (BCS) type superfluid of loosely bound and large Cooper pairs to Bose-Einstein condensation (BEC) of tightly bound molecules. Such a crossover superfluid has been realized in ultracold atomic gases where high temperature superfluidity has been observed [4, 5]. The microscopic properties of the fermion pairs can be probed with radio-frequency (rf) spectroscopy. Previous work [6–8] was difficult to interpret due to strong and not well understood final state interactions. Here we realize a new superfluid spin mixture where such interactions have negligible influence and present fermion-pair dissociation spectra that reveal the underlying pairing correlations. This allows us to determine the spectroscopic pair size in the resonantly interacting gas to be $2.3(2)/k_F$ (k_F is the Fermi wave number). The fermions pairs are therefore smaller than the interparticle spacing and the smallest pairs observed in fermionic superfluids. This finding highlights the importance of small fermion pairs for superfluidity at high critical temperatures [9]. We have also identified transitions from fermion pairs into bound molecular states and into many-body bound states in the case of strong final state interactions.

The properties of pairs are revealed in a dissociation spectrum, where pair dissociation is monitored as a function of the applied energy E. The spectrum has a sharp onset at the pair's binding energy E_b, where the fragments have zero kinetic energy, and then spreads out to higher energy. Since a rf photon has negligible momentum, the allowed momenta for the fragments reflect the Fourier transform $\Phi(k)$ of the pair wavefunction $\phi(r)$, which has a width on the order of $1/\xi$ where ξ is the pair size. Thus the pair size can be estimated from the spectral line width E_w as $\xi^2 \sim \hbar^2/mE_w$ (m is the mass of the particles and $\hbar$ is Planck's constant h divided by 2π).

The conceptually simplest pairs in the BCS-BEC crossover are the weakly bound molecules in the BEC limit, which are described by a spatial wavefunction $\phi_m(r) \propto e^{-r/b}/r$ with a binding energy $E_b = \hbar^2/mb^2$. When the molecules are dissociated into non-interacting free particles, the spectral response is $I_m \propto \sqrt{E-E_b}/E^2$, showing a highly asymmetric line shape with a steep rise at the molecular binding energy E_b and a long "tail" to higher energies (Fig. 1a) [5, 10].

This general behavior of the dissociation spectrum holds also in the BCS limit where pairing is a many-body effect [5, 11]. The rf dissociation process discussed below, in the limit of negligible final state interactions, can be considered as breaking a Cooper pair into one quasiparticle and one free particle. The rf spectrum in the BCS limit has an onset at $\Delta^2/2E_F$ and the same dependence of $E^{-3/2}$ at high energy as in the BEC limit (Fig. 1b; here E_F is the Fermi energy and Δ is the gap) [12]. Since the rf excitation takes place throughout the whole Fermi sea it is most natural to interpret the BCS state as $N/2$ pairs with condensation energy $\Delta^2/2E_F$ where N is the total number of fermions [5].

A spectroscopic pair size can be defined both from the onset and the width of the rf spectrum as $\xi_{th}^2 = \hbar^2/2mE_{th}$ and $\xi_w^2 = \gamma \times \hbar^2/2mE_w$. Here E_{th} is the onset/threshold energy, E_w is the full width at half maximum, and $\gamma = 1.89$ is a numerical constant chosen for convenience (see caption of Fig. 1). The pair sizes ξ_{th} and ξ_w which can be directly obtained from the rf spectrum capture the evolution of the pair size from the BCS limit to the BEC limit (see Fig. 1c).

Since the rf spectra show a similar behavior in both limiting cases of the BEC-BCS crossover, one would expect comparable spectra within the crossover regime. Surprisingly, the rf spectra obtained in previous rf experiments did not fit into this picture: the lineshape did not show any pronounced asymmetry and the linewidth was narrow [6–8] (see also Fig. 7). These experiments could therefore not be simply interpreted in terms of pairing energy and pair size. We will show that this is caused by strong final state interactions and transitions to bound states.

In the previous and our new experiments, the fermion pairs consist of two atoms in different hyperfine states $|a\rangle$ and $|b\rangle$. The rf transfers atoms in state $|b\rangle$ to an initially unoccupied third state $|c\rangle$. In addition to "pair dissociation", also referred to as a "bound-free" transition and characterized by the asymmetric lineshape discussed above, rf spectroscopy can induce a second kind of transition to another bound state, i.e. the transfer of a pair (a,b) to a pair (a,c) (also referred to as a "bound-bound" transition). The latter spectra have a narrow and symmetric lineshape.

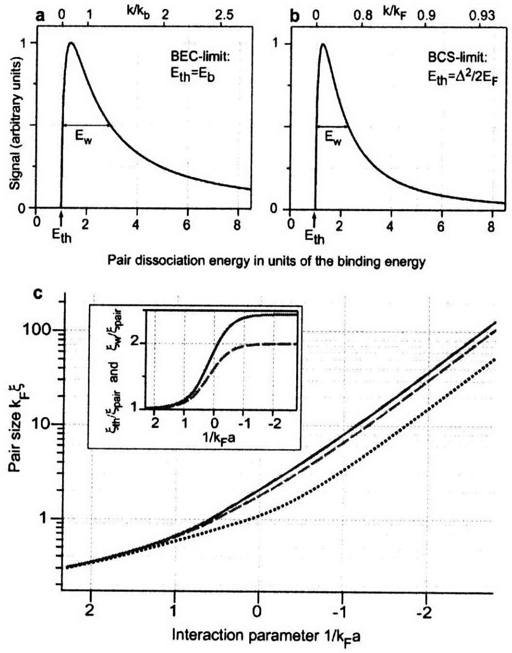

FIG. 1: Line shape of the pair dissociation spectrum in the BEC (**a**) and BCS limit (**b**) and the evolution of the fermion pair size in the BEC-BCS crossover [5, 11, 20]. (**a**) and (**b**): Simulated rf dissociation spectra in the BEC and BCS limits. The momentum k of the free particles after dissociation is indicated in the top axes, where $\hbar^2 k_b^2/m = E_b$. Apart from an offset, the spectra in the BEC and BCS limits show almost indistinguishable lineshapes. The molecular dissociation lineshape I_m with an additional offset parameter can therefore serve as a generic, model independent fit function for pair dissociation spectra (see Methods and Fig. 6). (**c**) The fermion pair sizes ξ_w (solid blue) and ξ_{th} (dashed red) are displayed as a function of the interaction parameter $1/k_F a$ (a is the s-wave scattering length). Also shown is the two-particle correlation length ξ_{pair} (dotted black) given by $\xi_{pair} = \sqrt{\langle\phi|r^2|\phi\rangle/\langle\phi|\phi\rangle}$, where $\phi(r) = \langle\psi|\Psi_\alpha^\dagger(r)\Psi_\beta^\dagger(0)|\psi\rangle$. Here ψ is the generalized BCS wavefunction and α and β refer to the two components [2]. In the BEC limit, the value for the molecular size is $\xi_m = b/\sqrt{2} = \xi_{pair}$. We chose $\gamma = 1.89$ in the definition of ξ_w, so that $\xi_m = \xi_{th} = \xi_w$. In the BCS limit, $\xi_{pair} = \pi/(2\sqrt{2})\xi_c$ where $\xi_c = \hbar^2 k_F/(\pi m\Delta)$ is the Pippard coherence length and we have $\xi_{th} = 2\xi_{pair}$, $\xi_w = 2.44\xi_{pair}$. The inset shows the ratios ξ_w/ξ_{pair} (solid blue) and ξ_{th}/ξ_{pair} (dashed red). Although ξ_{pair} changes by orders of magnitude, ξ_{th} and ξ_w show the same behavior as ξ_{pair} deviating from each other by not more than 22 %. This illustrates that the pair size can be reliably determined from the rf dissociation spectrum throughout the whole BEC-BCS crossover.

Final state effects arise when the dissociated atom in state $|c\rangle$ interacts with atoms in state $|a\rangle$. The interaction strength is measured by the dimensionless parameter $k_F a$. Here a is the s-wave scattering length and we use a_i (a_f) for the initial (a,b) (final (a,c)) interactions. As discussed in detail below, final state interactions severely affect the rf dissociation spectra when $|k_F a_f| > 1$ [13–15]. To overcome this problem, one has to change the interactions in the final state without changing those in the initial one. Our solution is the realization of a new high temperature superfluid in ^{6}Li using a different combination of hyperfine states for which rf excitation with reduced final state interactions is possible (see Methods). As a result, we were able to resolve the bound-bound and bound-free contributions to the rf spectrum, and to determine the size of fermion pairs from the asymmetric fermion pair dissociation spectra.

We have taken advantage of the fact that any two state mixture (1,2), (1,3), and (2,3) of the three lowest hyperfine states of ^{6}Li (labeled in the order of increasing hyperfine energy as $|1\rangle$, $|2\rangle$ and $|3\rangle$) exhibits a broad Feshbach resonance [16, 17]. So far, all experiments with strongly interacting fermions in ^{6}Li have been carried out in the vicinity of the (1,2) Feshbach resonance located at about $B_{12} \sim 834$ G. Surprisingly, inelastic collisions including allowed dipolar relaxation are not enhanced by the (1,3) and (2,3) Feshbach resonances. We observe that at both the (1,3) and (2,3) Feshbach resonances superfluids can be created as well (see Methods). This doubles the number of high temperature superfluids available for experimental studies.

The newly created (1,3) superfluid is the best choice for rf spectroscopy experiments since the final state scattering length a_f at the (1,3) resonance position $B_{13} \sim 691$ G is small and positive ($0 < k_F a_f < 1$ for typical values of k_F). Therefore the accessible final states are either a molecule of a well defined binding energy or two free, only weakly interacting atoms. The actual final state interactions depend on whether one drives the rf transitions from $|1\rangle$ to $|2\rangle$ or from $|3\rangle$ to $|2\rangle$ allowing the comparison between spectra taken from the same sample but with different a_f (see Methods and Supplementary Information). After preparing the (1,3) superfluid a rf pulse resonant with the $|3\rangle$ to $|2\rangle$ transition is applied. Then either the losses in state $|3\rangle$ or the atoms transferred to state $|2\rangle$ are monitored (see Methods). All spectra are plotted versus frequency or energy relative to the atomic resonance, i.e. relative to the energy E_0 required to transfer an atom from $|3\rangle$ to $|2\rangle$ in the *absence* of atoms in state $|1\rangle$.

The main result of this paper are the spectra observed in the (1,3) BEC-BCS crossover between 670 and 710 G (Fig. 2). The spectra have the asymmetric lineshape characteristic for pair dissociation and are indeed well fit by a generic pair dissociation lineshape (see Fig. 1 and Methods). If the frequency axis is scaled by E_w

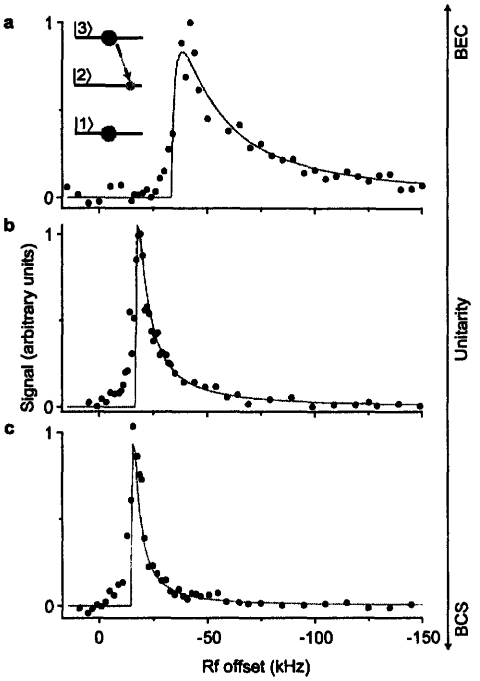

FIG. 2: Rf dissociation spectra in the BEC-BCS crossover. Below, at, and above resonance, the spectrum shows the typical asymmetric lineshape of a pair dissociation spectrum. The signal is proportional to the three dimensional local response at the center of the cloud (see Methods). Since state $|3\rangle$ has a higher energy than state $|2\rangle$ (see the schematic inset in (a)), the dissociation energy is always less than the transition frequency for the atomic resonance E_0/h and therefore the dissociation spectra appear at negative energies compared to E_0. The inverted frequency axis ensures that the dissociation spectrum is always on the right (or "positive") side of the origin. The magnetic field (in G), the local Fermi energy ϵ_F (in kHz), the temperature T in units of the Fermi temperature T/T_F and the interaction strength $1/k_F a_i$ are (a), 670, $h \times 24$, ≈ 0.2, 0.4; (b), 691, $h \times 21$, 0.1, ~ 0; (c), 710, $h \times 20$, 0.1, -0.3.

and the spectra are shifted to show the same onset all three spectra overlap as shown in Fig. 3a. At the level of our experimental resolution the dissociation lineshape is therefore not sensitive to a change in interactions. As illustrated in Fig. 1, the pair size can in principle be obtained from both E_{th} and E_w. However, since the whole spectrum may be subject to shifts from Hartree terms [16, 18], we focus in the following only on the width of the spectrum.

At unitarity we determine the full width at half maximum to be $E_w = 0.36(6)\epsilon_F$ corresponding to a spectroscopic pair size of $\xi_w = 2.3(2)/k_F$ (here ϵ_F is the local Fermi energy and $k_F = \sqrt{2m\epsilon_F}/\hbar$). The pairs are therefore smaller than the interparticle spacing l given by $l = n^{1/3} = (3\pi^2)^{1/3}/k_F \sim 3.1/k_F$ (where n the total density) and in units of $1/k_F$ the smallest reported so far for fermionic superfluids. In high-temperature superconductors the reported values for ξ at optimal doping are in the range of 5 to $10/k_F$ [9].

In the simple BEC-BCS crossover model the ratio ξ_{pair}/ξ_w varies from 1 to 1/2.4. The fact that ξ_w is smaller than l suggests the use of the molecular ratio, i.e. $\xi \equiv \xi_{pair} = \xi_w = 2.3/k_F$. Before we compare with theoretical predictions we note that various definitions of the pair size differ by factors on the order of unity [19]. With this in mind, we find that our observed ξ is larger than a predicted pair size of about $1/k_F$ based on a functional integral formulation of the BEC-BCS crossover [20]. Small fermion pair sizes have been explicitly linked to high critical temperatures via the relation $T_c/T_F \approx 0.4/(k_F\xi_{pair})$ which applies for weak coupling [9]. Inserting the observed ξ this relation yields an estimate of $T_c/T_F \approx 0.2$ which is in the range of the predicted values between 0.15 to 0.23 (here T_F is the local Fermi temperature) [21]. If we use the asymptotic BCS relation $\Delta = \frac{\hbar^2 k_F}{\pi m}\frac{1}{\xi_c} = \frac{1}{\sqrt{2}}\frac{1}{k_F\xi_{pair}}\epsilon_F$, valid at weak coupling, and our observed ξ at unitarity we find $\Delta \approx 0.3\epsilon_F$ smaller than the value of $0.5\epsilon_F$ predicted by Monte Carlo

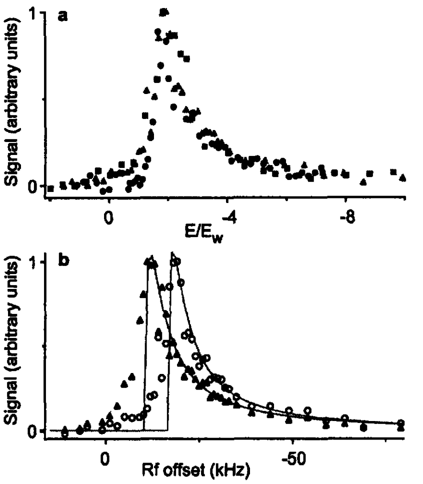

FIG. 3: Comparison of lineshapes and density effects. (a) Same spectra as in Fig. 2 but with the frequency axis scaled by E_w and shifted so that the spectral onsets overlap with the BEC side spectrum: BEC side (black circles), resonance (red triangles), and BCS side (blue squares). (b) Density effects at unitarity for the (1,3) mixture at 691 G. The figure shows the tomographically reconstructed spectral response in the center (open circles, same spectrum as in Fig. 2b) as well as the lower density wings (filled triangles) of the cloud. In this regime the cloud might have turned normal.

simulations [22].

The strong narrowing of the spectral line in Fig. 2 (a) to (c) demonstrates that the fermion pair size increases from strong to weak coupling. The decreasing width corresponds to a twofold increase in the spectroscopic pair size from $\xi_w = 1.4(1)/k_F$ at 670 G to $\xi_w = 2.8(3)/k_F$ at 710 G where the extent of the pairs becomes comparable to the interparticle spacing. A change of the absolute pair size with density at unitarity can in principle be observed by comparing the spectral width in the center and the outer region of the cloud. As the density decreases the spectrum shifts to lower energies (see Fig. 3b). However, the sharp spectral onset also becomes increasingly softer and the asymmetry of the pair dissociation peak less pronounced, possibly due to atomic diffusion during the excitation pulse. This prevents a reliable determination of the pair size in the spatial wings where the density is changing rapidly.

We now consider the effect of final state interactions in more detail. First we would like to point out that the increase in a_f by about a factor of two from 670 G to 710 G has not affected the lineshape of the spectra in Fig. 3a within the experimental resolution. This suggests that final state effects are small for these spectra. Additional information is obtained from the previously intro-

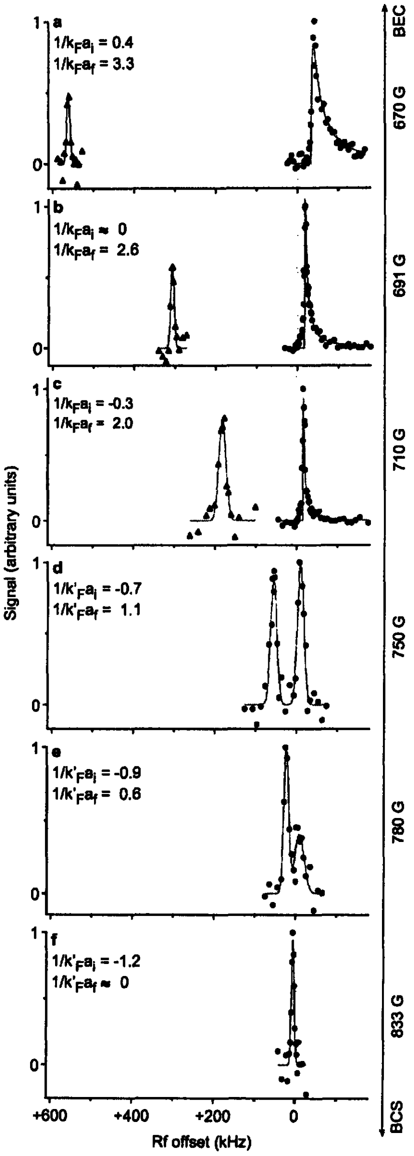

FIG. 4: Effect of final state interactions on rf spectroscopy: bound-bound (BB) and bound-free (BF) spectra in the BEC-BCS crossover of the (1,3) mixture (only the BF spectra in (a-c) were tomographically reconstructed). While the initial (1,3) state is strongly interacting at all fields the final state interactions change from weak (a-c) to strong (d-f). See ref. [17] for a plot of the Feshbach resonances. At the higher magnetic fields for $1/k_F a_i \approx -1$ the initial state may have turned normal. (a-c), Same BF spectra and parameters as in Fig. 2. The relative weight of the BB and BF peaks could not be determined experimentally (see Methods).(d), 750 G, $E_F = h \times 22$ kHz, T/T_F=0.09; (e), 780 G, $E_F = h \times 23$ kHz, T/T_F=0.09; (f), 833 G, $E_F = h \times 20$ kHz, T/T_F=0.06.

duced bound-bound (BB) transitions which are outside the range plotted in Fig. 2. On the BEC side of the resonance the (1,3) molecule can be transferred also to a more deeply bound (1,2) molecule (see Fig. 4a). The BB peak is still present at unitarity and also on the BCS side at 710 G (Fig. 4b and c) and results from the transition of a many-body bound fermion pair to a (1,2) molecule. The strong overlap of the pair wavefunction and the molecule in the final state is another indication for the "molecular" character of the fermions pairs in the strongly interacting regime.

The spectra start to change significantly at higher fields. As the magnetic field is increased the (1,3) mixture remains in the unitarity limited regime with the interaction strength approaching $1/|k_F a_i| \approx 1$ at $B_{12} = 833$ G. The final state interactions, however, change from weak to strong causing the pair dissociation peak to decrease in weight and the BB peak to become dominant (Fig. 4d-f). This single peak apparently corresponds to a BB transition from many-body bound (1,3) pairs to a highly correlated final state of an atom in state $|2\rangle$ interacting with the paired atoms in state $|1\rangle$.

A narrow BB peak is predicted both in the molecular (two-body) and many-body case, when initial and final state interactions are identical or similar. The spectra in Fig. 4 show that BB transitions dominate when $|1/(k_F a_i) - 1/(k_F a_f)| \leq 1.5$. In our opinion a recent theoretical treatment [23] agrees qualitatively with these results but underestimates the region where BB transitions are dominant by about a factor of two. Our observations allow a reinterpretation of the rf spectra obtained from the (1,2) superfluid with resonant interactions [6–8] (see the Supplementary Information for an extended discussion). The spectra have been taken in a regime where $|1/(k_F a_i) - 1/(k_F a_f)| \leq 1$ where strong BB transitions are expected. Together with the very narrow and symmetric lineshape (see Fig. 7), this suggests that the (1,2) to (1,3) rf spectra at 833 G are dominated by such BB transitions and cannot be simply interpreted in terms of a pair dissociation process and a pairing gap [6–8, 24–26].

In conclusion we have determined the pair size of resonantly interacting fermions using new superfluid spin mixtures in ^{6}Li. The (1,3) mixture is ideally suited for rf spectroscopy since final state interactions do not significantly affect the spectra. Our measurements are the first to clearly reveal the microscopic structure of the fermion pairs in the strongly interacting regime. The small fermion pair size and high critical temperatures observed in our system show a relation similar to the one suggested by the Uemura plot for a wide class of fermionic superfluids [9]. Our results also explain why the rapid ramp method used to observe fermion pair condensation in the crossover has been successful [27, 28]. The small pair size facilitated the efficient transfer of the many-body bound fermion pairs into more strongly bound molecules while preserving the momentum distribution of the pairs.

This work opens ample opportunities for future research. The microscopic structure of the pairs can now be studied both in the superfluid and normal phase as a function of interaction strength, temperature and spin imbalance between the two components [7]. Increased spectral resolution may reveal interesting deviations of the spectral shape from the generic lineshape discussed here. Furthermore, the predicted universality of a resonantly interacting Fermi mixture can now be tested in ^{6}Li for three different systems. The lifetimes of all three two-state combinations of the three lowest hyperfine states in ^{6}Li are on the order of 10 s in the strongly interacting regime. The three-body decay rates, however, decrease by more than an order of magnitude between 690 and 830 G for a ternary mixture, which may reflect interesting three-body physics. The lifetime of 30 ms at 691 G might be sufficient for studies involving all three hyperfine states [29] with the potential for experiments on pairing competition in multi-component Fermi gases and spinor Fermi superfluids.

We thank M. Zwierlein, W. Zwerger, E. Mueller and S. Basu for stimulating discussions and A. Keshet for the experiment control software. This work was supported by the NSF and ONR, through a MURI program, and under ARO Award W911NF-07-1-0493 with funds from the DARPA OLE program.

Methods Summary

Creation of the (1,3) superfluid. As described previously [5] a spin polarized sample of ultracold ^{6}Li in state $|1\rangle$ is obtained in an an optical dipole trap after sympathetic cooling with ^{23}Na in a magnetic trap. The equal (1,3) mixture is prepared at 568 G, close to the zero crossing of a_{13}. Here a non-adiabatic Landau-Zener rf sweep, creating an equal (1,2) mixture, is followed by an adiabatic Landau-Zener sweep that transfers the atoms in state $|2\rangle$ to state $|3\rangle$. To induce strong interactions the magnetic field is adjusted in 100 ms to 730 G and then ramped to values between 660 and 833 G. After evaporative cooling in the optical trap, superfluidity is indirectly established via the observation of fermion pair condensates [27, 28]. Under comparable conditions quantized vortex lattices, a direct proof for superfluidity, have been observed in the rotating (1,2) mixture of ^{6}Li [4]. $E_F = h(\nu_r^2 \nu_{ax})^{1/3}(3N)^{1/3}$ with radial (axial) trapping frequencies $\nu_r = 140$ ($\nu_{ax} = 22$) Hz and $k'_F = \sqrt{2mE_F}/\hbar$. The temperature was determined from the shape of the expanded cloud.

Recording the (1,3) rf spectra. The rf dissociation spectra at 670, 691 and 710 G spectra have been obtained by applying a 200 μs long rf pulse to the (1,3) mixture monitoring the atoms transferred into state $|2\rangle$. Three-dimensional image reconstruction via the inverse Abel transformation was used to obtain local rf dissociation

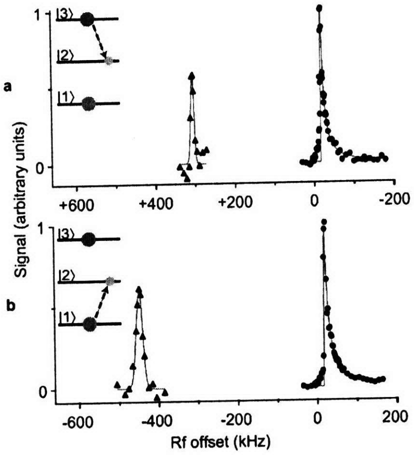

FIG. 5: Rf spectra at unitarity for the (1,3) mixture at 691 G. For all spectra the number of atoms transferred to state $|2\rangle$ has been recorded. In the (1,3) mixture rf transitions to the final state $|2\rangle$ are possible from both states $|1\rangle$ and $|3\rangle$. The final states can therefore be either bound (2,3) or (1,2) molecules respectively or a dissociated free atom in state $|2\rangle$. Note that the bound-free (BF) spectra are very similar for both $|3\rangle$ to $|2\rangle$ (**a**) and $|1\rangle$ to $|2\rangle$ (**b**) transitions. The bound-bound (BB) spectra, however, show different shifts indicating that the final (2,3) molecule is more strongly bound than the (1,2) molecule. This is a consequence of the smaller width of the (2,3) Feshbach resonance at 811 G [17] compared to the width of the (1,2) resonance at 834 G. (**a**) $|3\rangle$ to $|2\rangle$ transition; $\epsilon_F = 21$ kHz, T/T_F=0.1 (**b**) $|1\rangle$ to $|2\rangle$ transition; $\epsilon_F = 22$ kHz, T/T_F=0.14.

spectra [8]. The pulse length was chosen to be shorter than 1/4 trapping period to minimize atomic diffusion during the excitation pulse. The rf power was adjusted to transfer less than 10% of the total number of atoms. A further reduction of the rf power only affected the signal to noise ratio but not the spectral width. All BB spectra and the spectra at fields at and above 750 G are not spatially resolved and were obtained with about 1 ms long rf pulses.

Full methods

Creation of new superfluid spin mixtures for rf spectroscopy. For the well established (1,2) mixture, only the $|2\rangle$ to $|3\rangle$ transition has been used for rf spectroscopy. The final state s-wave scattering length a_{13} at B_{12} is large and negative leading to strong final state interactions with $1/k_F a_f < -1$ ($a_{13} \approx -3300\ a_0$, a_0 the Bohr radius and a_{ij} the magnetic field dependent scattering length between atoms in states $|i\rangle$ and $|j\rangle$). The strength of the final state interactions can in principle be changed in several ways without affecting the initial state. The density could be lowered to reduce the interaction strength in the final state while the initial state remains resonantly interacting. It is, however, experimentally difficult to decrease the density by a large factor and maintain the same low temperature T/T_F. One might also try to spectroscopically access a different final state. However, in ^{6}Li there are no other allowed magnetic field insensitive transitions. Magnetic field insensitivity is crucial to obtain the required spectral resolution in the kHz regime.

Since other mixtures of hyperfine states in ^{6}Li also exhibit broad Feshbach resonances we attempted to create resonantly interacting superfluids in new combinations of initial hyperfine states: (1,3) and (2,3). The lifetimes of these spin mixtures at resonance exceed 10 s implying inelastic collision rates smaller than $10^{-14}\ \mathrm{cm}^{-3}\,\mathrm{s}^{-1}$. While for the (2,3) superfluid the final state interactions are also large and negative, the final state scattering lengths at B_{13} are either $a_{23} \approx 1140\ a_0$ and $a_{12} \approx 1450\ a_0$ (depending on the rf transition employed) and therefore considerably smaller and positive.

Creation of the (2,3) superfluid. To prepare a (2,3) superfluid we follow essentially the same procedure as previously described for the (1,2) mixture [4, 5]. The only difference is that instead of applying a Landau-Zener transfer that creates an equal (1,2) mixture a complete transfer into state $|2\rangle$ is followed by a second sweep creating an equal (2,3) mixture. The final magnetic field at the center of the (2,3) resonance is $B_{23} \approx 811$ G. As in the other spin mixtures we observe fermion pair condensation after evaporation in the optical trap.

Recording the (1,3) spectra: stability of the mixture after the rf pulse Recording the atoms transferred to state $|2\rangle$ is advantageous because there is no background without rf pulse, but it requires that their lifetime with respect to three-body recombination is sufficiently long.

For fields below $\sim$ 710 G, we found that the lifetime of the $|2\rangle$ atoms after the rf pulse was short when they formed a molecule with an $|1\rangle$ atom as the result of a BB transition. Therefore, in some cases, the BB part of the spectra was recorded by observing atom number loss in the initial state. After BF (bound-free) excitation, the lifetime of atoms in state $|2\rangle$ was 30 ms (determined at 691 G) sufficiently long to observe the atoms directly. As a result of the different decay times and recording methods the relative signal strength between the BB and BF parts of the spectrum could not be determined.

At fields above $\sim$ 750 G, we found similar and strong losses after both BF and BB excitations. Therefore all data were taken by monitoring losses in the initial state $|3\rangle$ and the spectra reflect the relative strength between BB and BF transitions.

Fitting the (1,3) spectra The fit to the (1,3) rf dissociation spectra in Figures 2, 3, 4(a-c), 5, and 7 uses a generic, model independent pair dissociation lineshape based on I_m with an additional parameter E_{offset}:

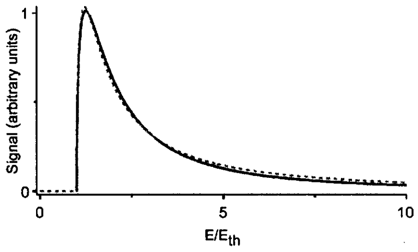

FIG. 6: Generic pair dissociation lineshape. A simulated rf dissociation spectrum in the BCS limit (black solid line) [5] is fit with I_{generic} (red dashed line) which is the molecular lineshape I_m with an additional offset parameter E_{offset} (see Methods).

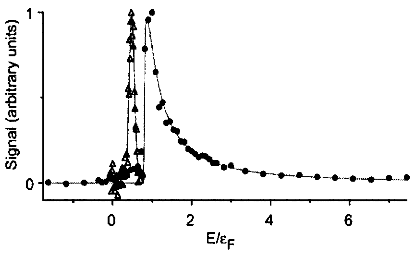

FIG. 7: Comparison of the rf spectra of the (1,2) and (1,3) superfluids at unitarity, showing dramatic final state effects for the (1,2) mixture. Open circles: same rf dissociation data as in Fig. 5b. Solid diamonds: rf spectra at unitarity for the (1,2) mixture at 833 G from ref. [8]. The frequency axis is normalized by the local Fermi energies. In the (1,2) mixture final state effects lead to a strong suppression of the asymmetric "tails" of the rf spectrum and a shift of the peak to lower energies.

$I_{\text{generic}}(E) \propto \sqrt{(E - E_{th}}/(E - E_{\text{offset}})^2$. This lineshape provides an excellent fit to simulated rf dissociation spectra both in the BEC and BCS limits [5] (see Fig 6). Also the experimentally obtained spectra are well fit by I_{generic} (Fig. 2). In some of the spectra deviations appear close to threshold where the onset is smoother than given by the fit. The smooth onset could have been caused by residual atomic diffusion during the excitation pulse which was significantly shorter than a quarter trapping period. The generic fit function contains no corrections for final state interactions. In the BEC limit (where $E_{\text{offset}} = 0$ and $E_{th} = E_b$) such corrections can be included by a multiplicative factor of $1/(E+\hbar^2/(ma_f^2)-E_{th})$ [30]. When applied to the dissociation spectra in the crossover this correction factor changes the fit only by a negligible amount. All BB and BF spectra in Fig. 4(d-f) have been fit by a Gaussian.

(1,3) mixture: $|3\rangle$ to $|2\rangle$ vs $|1\rangle$ to $|2\rangle$ transition The (1,3) superfluid gives us the opportunity to record two different (magnetic field insensitive) rf spectra: from state $|3\rangle$ to state $|2\rangle$ (the transition used for all the spectra shown in the paper) and from state $|1\rangle$ to state $|2\rangle$. This allows us to compare rf spectra of the same system but for somewhat different final state interactions. The final state scattering lengths at B_{13} are $a_{23} \approx 1140\ a_0$ for the $|1\rangle$ to $|2\rangle$ transition and $a_{12} \approx 1450\ a_0$ for the $|3\rangle$ to $|2\rangle$ transition. Figure 5 shows the spectra at 691 G. Note that the fermion pair size obtained from the spectra agrees for both rf transitions within the experimental uncertainty.

Supplementary Information

Final state interactions in the rf spectroscopy experiments with the (1,2) and (1,3) mixtures. Figure 7 shows the dramatic effect of final state interactions in the (1,2) mixture at unitarity. The narrow and symmetric lineshape observed in the (1,2) to (1,3) rf spectrum suggests that this spectral peak is dominated by a bound-bound (BB) transition from (1,2) pairs to a (1,3) correlated state.

In the molecular case final state interactions can be included in an analytical model [30]. The final states for dissociation are two atoms with momentum $\hbar k$ in an s-wave scattering state with scattering length a_f. For a large and positive $a_i \approx b$ and an increasing a_f ($0 < a_f < a_i \approx b$) the dissociation spectrum looses in weight and narrows as $(1 - a_f/a_i)/(1 + k^2 a_f^2)$ until it disappears when a_f/a_i approaches one. At this point the spectrum consists of a delta function for the BB transition between molecular states of equal size.

A very similar behavior of the BB and bound-free (BF) parts of the spectrum is expected for a superfluid with resonant interactions [23]: for $|a_f|, |a_i| \gg 1/k_F$ the spectrum is reduced to a delta function. Here, the initial state is a fermion pair condensate described by the BEC-BCS crossover wavefunction [5, 23]. In contrast to the molecular case, the spectrum of the superfluid at resonance shows a BB peak even for negative values of $1/k_F a_f$, i.e. in a regime where binding is only due to many-body effects [23]. The spectra in Fig. 4 show that BB transitions dominate when $|1/(k_F a_i) - 1/(k_F a_f)| \leq 1.5$ (a region that is about a factor of two larger than obtained in ref. [23]). We also infer from [23] that it is much more difficult to spectrally resolve BB and BF transitions for a system in the unitarity limit if $a_f < 0$. When one approaches resonance for the (1,2) system from the BEC side the BF spectrum narrows and smoothly turns into a BB dominated spectrum.

Compared to the (1,2) superfluid, a_f in the (1,3) system is up to three times smaller and positive. This leads, both in the molecular model (due to the quadratic dependence on $k_F a_f$) and in the resonant case [23], to a dramatic change in the dissociation spectrum towards the limit of negligible final state interactions. Fits to the (1,3) dissociation spectrum both with and without a correction factor for final state interactions (see Methods) [30] show negligible differences, indicating the small influence of final state interactions. In fact the (1,3) spectra in Fig. 4(a-c) show the absence of final state corrections without any detailed analysis. The splitting between BB and BF parts given by $\hbar^2/ma_f^2$ is considerably larger than the width of the BF spectrum (which is approximately $\hbar^2/mb^2$). Therefore the condition $a_f < b$ is fulfilled implying the absence of strong final state corrections to the dissociation spectrum.

[1] Eagles, D. M. Possible pairing without superconductivity at low carrier concentrations in bulk and thin-film superconducting semiconductors. *Phys. Rev.* **186**, 456-463 (1969).

[2] Leggett, A. J. *Modern Trends in the Theory of Condensed Matter*, (eds Pekalski, A. & Przystawa, J.) 13-27 (Proc. XVIth Karpacz Winter School of Theoretical Physics, Springer, Berlin, 1980).

[3] Noziéres, P. & Schmitt-Rink, S. Bose condensation in an attractive fermion gas: from weak to strong coupling superconductivity. *J. of Low Temp. Phys.* **59**, 195–211 (1985).

[4] Zwierlein, M. W., Abo-Shaeer, J. R., Schirotzek, A., Schunck, C. H. & Ketterle, W. Vortices and superfluidity in a strongly interacting Fermi gas. *Nature* **435**, 1047–1051 (2005).

[5] Ketterle, W. & Zwierlein, M. W. *Ultracold Fermi Gases*, (eds Inguscio, M., Ketterle, W. & Salomon, C.) 95-287 (Proc. International School of Physics Enrico Fermi, Course CLXIV (IOS Press, Amsterdam, SIF Bologna, 2008).

[6] Chin, C. *et al.* Observation of the pairing gap in a strongly interacting Fermi gas. *Science* **305**, 1128–1130 (2004).

[7] Schunck, C. H., Shin, Y., Schirotzek, A., Zwierlein, M. W. & Ketterle, W. Pairing without superfluidity: The ground state of an imbalanced Fermi mixture. *Science* **316**, 867–870 (2007).

[8] Shin, Y., Schunck, C. H., Schirotzek, A. & Ketterle, W. Tomographic rf spectroscopy of a trapped Fermi gas at unitarity. *Phys. Rev. Lett.* **99**, 090403 (2007).

[9] Pistolesi, F. & Strinati, G. C. Evolution from BCS superconductivity to Bose condensation: Role of the parameter $k_F\xi$. *Phys. Rev. B* **49**, 6356–6359 (1994).

[10] Regal, C. A., Ticknor, C., Bohn, J. L. & Jin, D. S. Creation of ultracold molecules from a Fermi gas of atoms. *Nature* **424**, 47–50 (2003).

[11] Diener, R. B. & Ho, T.-L. The condition for universality at resonance and direct measurement of pair wavefunctions using rf spectroscopy. Preprint, arXiv:cond-mat/0405174v2.

[12] Yu, Z. & Baym, G. Spin-correlation functions in ultracold paired atomic-fermion systems: Sum rules, self-consistent approximations, and mean fields. *Phys. Rev. A* **73**, 063601 (2006).

[13] Baym, G., Pethick, C. J., Yu, Z. & Zwierlein, M. W. Coherence and clock shifts in ultracold Fermi gases with resonant interactions. *Phys. Rev. Lett.* **99**, 190407 (2007).

[14] Punk, M. & Zwerger, W. Theory of rf-spectroscopy of strongly interacting fermions. *Phys. Rev. Lett.* **99**, 170404 (2007).

[15] Perali, A., Pieri, P. & Strinati, G. C. Competition between final-state and pairing-gap effects in the radiofrequency spectra of ultracold Fermi atoms. *Phys. Rev. Lett.* **100**, 010402 (2008).

[16] Gupta, S. *et al.* Rf spectroscopy of ultracold fermions. *Science* **300**, 1723–1726 (2003).

[17] Bartenstein, M. *et al.* Precise determination of ^{6}Li cold collision parameters by radio-frequency spectroscopy on weakly bound molecules. *Phys. Rev. Lett.* **94**, 103201 (2004).

[18] Regal, C. A. & Jin, D. S. Measurement of positive and negative scattering lengths in a Fermi gas of atoms. *Phys. Rev. Lett.* **90**, 230404 (2003).

[19] Ortiz, G. & Dukelsky, J. BCS-to-BEC crossover from the exact BCS solution. *Phys. Rev. A* **72**, 043611 (2005).

[20] Engelbrecht, J. R., Randeria, M. & Sá de Melo, C. A. R. BCS to Bose crossover: Broken-symmetry state. *Phys. Rev. B* **55**, 15153 – 15156 (1997).

[21] Burovski, E., Prokof'ev, N., Svistunov, B. & Troyer, M. Critical temperature and thermodynamics of attractive fermions at unitarity. *Phys. Rev. Lett.* **96**, 160402 (2006).

[22] Carlson, J., Chang, S.-Y., Pandharipande, V. R. & Schmidt, K. E. Superfluid Fermi gases with large scattering length. *Phys. Rev. Lett.* **91**, 050401 (2003).

[23] Basu, S. & Mueller, E. J. Final-state effects in the radio frequency spectrum of strongly interacting fermions. Preprint, arXiv:0712.1007v1 & private communication.

[24] Kinnunen, J., Rodríguez, M. & Törmä, P. Pairing gap and in-gap excitations in trapped fermionic superfluids. *Science* **305**, 1131–1133 (2004).

[25] Ohashi, Y. & Griffin, A. Single-particle excitations in a trapped gas of Fermi atoms in the BCS-BEC crossover region. II. Broad Feshbach resonance. *Phys. Rev. A* **72**, 063606 (2005).

[26] He, Y., Chen, Q. & Levin, K. Radio-frequency spectroscopy and the pairing gap in trapped Fermi gases. *Phys. Rev. A* **72**, 011602 (2005).

[27] Regal, C. A., Greiner, M. & Jin, D. S. Observation of resonance condensation of fermionic atom pairs. *Phys. Rev. Lett.* **92**, 040403 (2004).

[28] Zwierlein, M. W. *et al.* Condensation of pairs of fermionic atoms near a Feshbach resonance. *Phys. Rev. Lett.* **92**, 120403 (2004).

[29] Honerkamp, C. & Hofstetter, W. Ultracold fermions and the SU(N) Hubbard model. *Phys. Rev. Lett.* **92**, 170403 (2004).

[30] Chin, C. & Julienne, P. S. Radio-frequency transitions on weakly bound ultracold molecules. *Phys. Rev. A* **71**, 012713 (2005).

Bibliography

[1] D. M. Eagles. Possible pairing without superconductivity at low carrier concentrations in bulk and thin-film superconducting semiconductors. *Physical Review*, 186:456463, 1969.

[2] A. J. Leggett. Modern trends in the theory of condensed matter, proceedings of the XVIth Karpacz winter school of theoretical physics. pages 13–27. Springer, Berlin, 1980.

[3] P. Nozires and S. Schmitt-Rink. Bose condensation in an attractive fermion gas: from weak to strong coupling superconductivity. *Journal of Low Temperature Physics*, 59:195–211, 1985.

[4] M. W. Zwierlein, J. R. Abo-Shaeer, A. Schirotzek, C. H. Schunck, and W. Ketterle. Vortices and superfluidity in a strongly interacting Fermi gas. *Nature*, 435:1047–1051, 2005.

[5] T.-L. Ho. Universal thermodynamics of degenerate quantum gases in the unitarity limit. *Physical Review Letters*, 92:090402, 2004.

[6] K. Dieckmann, C. A. Stan, S. Gupta, Z. Hadzibabic, C. Schunck, and W. Ketterle. Decay of ultracold fermionic lithium gas near a Feshbach resonance. *Physical Review Letters*, 89:203201, 2002.

[7] S. Gupta, Z. Hadzibabic, M. W. Zwierlein, C. A. Stan, K. Dieckmann, C. H. Schunck, E. G. M. van Kempen, B. J. Verhaar, and W. Ketterle. Rf spectroscopy of ultracold fermions. *Science*, 300:1723–1726, 2003.

[8] J. Cubizolles, T. Bourdel, S. J. J. M. F. Kokkelmans, G. V. Shlyapnikov, and C. Salomon. Production of long-lived ultracold Li_2 molecules from a Fermi gas. *Physical Review Letters*, 91:240401, 2003.

[9] S. Jochim, M. Bartenstein, A. Altmeyer, G. Hendl, C. Chin, J. H. Denschlag, and R. Grimm. Pure gas of optically trapped molecules created from fermionic atoms. *Physical Review Letters*, 91:240402, 2003.

[10] K. E. Strecker, G. B. Partridge, and R. G. Hulet. Conversion of an atomic Fermi gas to a long-lived molecular Bose gas. *Physical Review Letters*, 91:080406, 2003.

[11] C. A. Regal, M. Greiner, and D. S. Jin. Lifetime of molecule-atom mixtures near a Feshbach resonance in ^{40}K. *Physical Review Letters*, 92:083201, 2004.

[12] M. Greiner, C. A. Regal, and D. S. Jin. Emergence of a molecular BoseEinstein condensate from a Fermi gas. *Nature*, 426:537–540, 2003.

[13] S. Jochim, M. Bartenstein, A. Altmeyer, G. Hendl, S. Riedl, C. Chin, J. Hecker Denschlag, and R. Grimm. Bose-Einstein condensation of molecules. *Science*, 302:2101–2103, 2003.

[14] M. W. Zwierlein, C. A. Stan, C. H. Schunck, S. M. F. Raupach, S. Gupta, Z. Hadzibabic, and W. Ketterle. Observation of Bose-Einstein condensation of molecules. *Physical Review Letters*, 91:250401, 2003.

[15] C. A. Regal, M. Greiner, and D. S. Jin. Observation of resonance condensation of fermionic atom pairs. *Physical Review Letters*, 92:040403, 2004.

[16] M. W. Zwierlein, C. A. Stan, C. H. Schunck, S. M. F. Raupach, A. J. Kerman, and W. Ketterle. Condensation of pairs of fermionic atoms near a Feshbach resonance. *Physical Review Letters*, 92:120403, 2004.

[17] C. H. Schunck, M. W. Zwierlein, A. Schirotzek, and W. Ketterle. Superfluid expansion of a rotating Fermi gas. *Physical Review Letters*, 98:050404, 2007.

[18] M. W. Zwierlein, A. Schirotzek, C. H. Schunck, and W. Ketterle. Fermionic superfluidity with imbalanced spin populations. *Science*, 311:492–496, 2006.

[19] M. W. Zwierlein, C. H. Schunck, A. Schirotzek, and W. Ketterle. Direct observation of the superfluid phase transition in ultracold Fermi gases. *Nature*, 442:54, 2006.

[20] Y. Shin, M. W. Zwierlein, C. H. Schunck, A. Schirotzek, and W. Ketterle. Observation of phase separation in a strongly interacting imbalanced Fermi gas. *Physical Review Letters*, 97:030401, 2006.

[21] Y. Shin, C. H. Schunck, A. Schirotzek, and W. Ketterle. Phase diagram of a two-component Fermi gas with resonant interactions. *Nature*, 451:689, 2008.

[22] C. Chin, M. Bartenstein, A. Altmeyer, S. Riedl, S. Jochim, J. H. Denschlag, and R. Grimm. Observation of the pairing gap in a strongly interacting Fermi gas. *Science*, 305:1128–1130, 2004.

[23] C. H. Schunck, Y. Shin, A. Schirotzek, M. W. Zwierlein, and W. Ketterle. Pairing without superfluidity: The ground state of an imbalanced Fermi mixture. *Science*, 316:867–870, 2007.

[24] Y. Shin, C. H. Schunck, A. Schirotzek, and W. Ketterle. Tomographic rf spectroscopy of a trapped Fermi gas at unitarity. *Physical Review Letters*, 99:090403, 2007.

[25] C. H. Schunck, M. W. Zwierlein, C. A. Stan, S. M. F. Raupach, W. Ketterle, A. Simoni, E. Tiesinga, C. J. Williams, and P. S. Julienne. Feshbach resonances in fermionic ^{6}Li. *Physical Review A*, 71:045601, 2005.

[26] M. W. Zwierlein, C. H. Schunck, C. A. Stan, S. M. F. Raupach, and W. Ketterle. Formation time of a fermion pair condensate. *Physical Review Letters*, 94:180401, 2005.

[27] S. Giorgini, L. P. Pitaevskii, and S. Stringari. arXiv:0706.3360v1.

[28] W. Ketterle and M. W. Zwierlein. Ultracold Fermi Gases, Proc. of the International School of Physics Enrico Fermi, Course CLXIV. pages 95–287. IOS Press, Amsterdam, SIF Bologna, 2008.

[29] I. Bloch, J. Dalibard, and W. Zwerger. Preprint, arXiv:0704.3011v2.

[30] D. S. Petrov, C. Salomon, and G. V. Shlyapnikov. preprint cond-mat/0309010.

[31] G. Ortiz and J. Dukelsky. BCS-to-BEC crossover from the exact BCS solution. *Physical Review A*, 72:043611, 2005.

[32] M. W. Zwierlein, Z. Hadzibabic, S. Gupta, and W. Ketterle. Spectroscopic insensitivity to cold collisions in a two-state mixture of fermions. *Physical Review Letters*, 91:250404, 2003.

[33] C. A. Regal and D. S. Jin. Measurement of positive and negative scattering lengths in a Fermi gas of atoms. *Physical Review Letters*, 90:230404, 2003.

[34] C. Stan. *Experiments with Interacting Bose and Fermi Gases*. PhD thesis, Massachusetts Institute of Technology, 2005.

[35] C. A. Stan and W. Ketterle. Multiple species atom source for laser-cooling experiments. *Review of Scientific Instruments*, 76:063113, 2005.

[36] D. M. Stamper-Kurn. *Peeking and poking at a new quantum fluid: Studies of gaseous Bose-Einstein condensates in magnetic and optical traps.* PhD thesis, Massachusetts Institute of Technology, 1999.

[37] Z. Hadzibabic. *Studies of a Quantum Degenerate Fermionic Lithium Gas.* PhD thesis, Massachusetts Institute of Technology, 2003.

[38] C. H. Schunck. *Study of an Ultracold Cloud of Fermionic* ^{6}*Li Atoms Near a Feshbach Resonance.* PhD thesis, University of Heidelberg, 2002.

[39] M. W. Zwierlein. *High-Temperature Superfluidity in an Ultracold Fermi Gas.* PhD thesis, Massachusetts Institute of Technology, 2006.

[40] E. W. Streed, A. P. Chikkatur, T. L. Gustavson, M. Boyd, Y. Torii, D. Schneble, G. K. Campbell, D. E. Pritchard, and W. Ketterle. Large atom number Bose-Einstein condensate machines. *Rev. Sci. Instrum.*

[41] Z. Hadzibabic, S. Gupta, C. A. Stan, C. H. Schunck, M. W. Zwierlein, K. Dieckmann, and W. Ketterle. Fifty-fold improvement in the number of quantum degenerate fermionic atoms. *Physical Review Letters*, 91:160401, 2003.

[42] S. Inouye, M. R. Andrews, J. Stenger, H.-J. Miesner, D. M. Stamper-Kurn, and W. Ketterle. Observation of Feshbach resonances in a Bose-Einstein condensate. *Nature*, 392:151–154, 1998.

[43] J. Stenger, S. Inouye, M. R. Andrews, H.-J. Miesner, D. M. Stamper-Kurn, and W. Ketterle. Strongly enhanced inelastic collisions in a Bose-Einstein condensate near Feshbach resonances. *Physical Review Letters*, 82:2422–2425, 1999.

[44] M. Bartenstein, A. Altmeyer, S. Riedl, R. Geursen, S. Jochim, C. Chin, J. Hecker Denschlag, R. Grimm, A. Simoni, E. Tiesinga, C. J. Williams, and P. S. Julienne. Precise determination of ^{6}Li cold collision parameters by radio-frequency spectroscopy on weakly bound molecules. *Physical Review Letters*, 94:103201, 2004.

[45] J. Zhang, E. G. M. V. Kempen, T. Bourdel, L. Khaykovich, J. Cubizolles, F. Chevy, M. Teichmann, L. Tarruell, S. J. J. M. F. Kokkelmans, and C. Salomon. P-wave Feshbach resonances of ultra-cold ^{6}Li. *Physical Review A*, 70:030702, 2004.

[46] A. Simoni. Private communication.

[47] Y. Inada, M. Horikoshi, S. Nakajima, M. Kuwata-Gonokami, M. Ueda, and T. Mukaiyama. Preprint, arXiv:0803.1405v2.

[48] D. Blume, S. T. Rittenhouse, J. v. Stecher, and C. H. Greene. Stability of inhomogeneous multicomponent Fermi gases. *Physical Review A*, 77:033627, 2008.

[49] T. Paananen, J.-P. Martikainen, and P. Trm. Pairing in a three-component Fermi gas. *Physical Review A*, 73:053606, 2006.

[50] H. Zhai. Superfluidity in three-species mixtures of Fermi gases across Feshbach resonances. *Physical Review A*, 75:031603, 2007.

[51] T. Luu and A. Schwenk. Three-fermion problems in optical lattices. *Physical Review Letters*, 98:103202, 2007.

[52] A. Rapp, G. Zarnd, C. Honerkamp, and W. Hofstetter. Color superfluidity and baryon formation in ultracold fermions. *Physical Review Letters*, 98:160405, 2007.

[53] X.-J. Liu, H. Hu, and P. D. Drummond. Multicomponent strongly attractive Fermi gas: A color superconductor in a one-dimensional harmonic trap. *Physical Review A*, 77:013622, 2008.

[54] L. Luo, B. Clancy, J. Joseph, J. Kinast, and J. E. Thomas. Measurement of the entropy and critical temperature of a strongly interacting Fermi gas. *Physical Review Letters*, 98:080402, 2007.

[55] C. A. Regal, C. Ticknor, J. L. Bohn, and D. S. Jin. Creation of ultracold molecules from a Fermi gas of atoms. *Nature*, 424:47–50, 2003.

[56] J. Herbig, T. Kraemer, M. Mark, T. Weber, C. Chin, H.-C. Ngerl, and R. Grimm. Preparation of a pure molecular quantum gas. *Science*, 301:1510, 2003.

[57] K. Xu, T. Mukaiyama, J. R. Abo-Shaeer, J. K. Chin, D. E. Miller, and W. Ketterle. Formation of quantum-degenerate sodium molecules. *Physical Review Letters*, 91:210402, 2003.

[58] S. Drr, T. Volz, A. Marte, and G. Rempe. Observation of molecules produced from a Bose-Einstein condensate. *Physical Review Letters*, 92:020406–4, 2004.

[59] R. B. Diener and T.-L. Ho. Preprint, arXiv:cond-mat/0404517v1.

[60] A. Perali, P. Pieri, and G. C. Strinati. Extracting the condensate density from projection experiments with Fermi gases. *Physical Review Letters*, 95:010407, 2005.

[61] E. Altman and A. Vishwanath. Dynamic projection on Feshbach molecules: A probe of pairing and phase fluctuations. *Physical Review Letters*, 95:110404, 2005.

[62] Q. Chen, C. A. Regal, M. Greiner, D. S. Jin, and K. Levin. Understanding the superfluid phase diagram in trapped Fermi gases. *Physical Review A*, 73:041601, 2006.

[63] K. M. O'Hara, S. L. Hemmer, M. E. Gehm, S. R. Granade, and J. E. Thomas. Observation of a strongly interacting degenerate Fermi gas of atoms. *Science*, 298:2179–2182, 2002.

[64] M. Bartenstein, A. Altmeyer, S. Riedl, S. Jochim, C. Chin, J. H. Denschlag, and R. Grimm. Collective excitations of a degenerate gas at the BEC-BCS crossover. *Physical Review Letters*, 92:203201, 2004.

[65] J. Kinast, S. L. Hemmer, M. E. Gehm, A. Turlapov, and J. E. Thomas. Evidence for superfluidity in a resonantly interacting Fermi gas. *Physical Review Letters*, 92:150402, 2004.

[66] J. Kinast, A. Turlapov, J. E. Thomas, Q. Chen, J. Stajic, and K. Levin. Heat capacity of a strongly-interacting Fermi gas. *Science*, 307:1296–1299, 2005.

[67] H. Zhai and T.-L. Ho. Critical rotational frequency for superfluid fermionic gases across a Feshbach resonance. *Physical Review Letters*, 97:180414, 2006.

[68] A. Turlapov, J. Kinast, B. Clancy, L. Luo, J. Joseph, and J. E. Thomas. Is a gas of strongly interacting atomic fermions a nearly perfect fluid? *Journal of Low Temperature Physics*, 150:567–576, 2008.

[69] B. S. Chandrasekhar. A note on the maximum critical field in high-field superconductors. *Applied Physics Letters*, 1:7, 1962.

[70] A. M. Clogston. Upper limit for the critical field in hard superconductor. *Physical Review Letters*, 9:266, 1962.

[71] C. Lobo, A. Recati, S. Giorgini, and S. Stringari. Normal state of a polarized Fermi gas at unitarity. *Physical Review Letters*, 97:200403, 2006.

[72] P. F. Bedaque, H. Caldas, and G. Rupak. Phase separation in asymmetrical fermion superfluids. *Physical Review Letters*, 91:247002, 2003.

[73] Y. Shin. Determination of the equation of state of a polarized Fermi gas at unitarity. *Physical Review A*, 77:041603, 2008.

[74] A. Bulgac, J. E. Drut, and P. Magierski. Spin 1/2 fermions in the unitary regime: A superfluid of a new type. *Physical Review Letters*, 96, 2006.

[75] J. Carlson and S. Reddy. Asymmetric two-component fermion systems in strong coupling. *Physical Review Letters*, 95:060401, 2005.

[76] R. Haussmann, W. Rantner, S. Cerrito, and W. Zwerger. Thermodynamics of the BCS-BEC crossover. *Physical Review A*, 75:023610, 2007.

[77] E. Burovski, N. Prokof'ev, B. Svistunov, and M. Troyer. Critical temperature and thermodynamics of attractive fermions at unitarity. *Physical Review Letters*, 96:160402, 2006.

[78] K. B. Gubbels and H. T. C. Stoof. Renormalization group theory for the imbalanced Fermi gas. *Physical Review Letters*, 100:140407, 2008.

[79] D. E. Sheehy and L. Radzihovsky. BEC-BCS crossover in "Magnetized" Feshbach-resonantly paired superfluids. *Physical Review Letters*, 96:060401, 2006.

[80] W. Yi and L.-M. Duan. Phase diagram of a polarized Fermi gas across a Feshbach resonance in a potential trap. *Physical Review A*, 74:013610, 2006.

[81] K. B. Gubbels, M. W. J. Romans, and H. T. C. Stoof. Sarma phase in trapped unbalanced Fermi gases. *Physical Review Letters*, 97:210402, 2006.

[82] C. Chien, Q. Chen, Y. He, and K. Levin. Superfluid phase diagrams of trapped Fermi gases with population imbalance. *Physical Review Letters*, 98:110404, 2006.

[83] M. M. Parish, F. M. Marchetti, A. Lamacraft, and B. D. Simons. Finite-temperature phase diagram of a polarized Fermi condensate. *Nature Physics*, 3:124–128, 2007.

[84] G. B. Partridge, W. Li, R. I. Kamar, Y. a. Liao, and R. G. Hulet. Pairing and phase separation in a polarized Fermi gas. *Science*, 311:503 – 505, 2006.

[85] G. B. Partridge, W. Li, Y. A. Liao, R. G. Hulet, M. Haque, and H. T. C. Stoof. Deformation of a trapped Fermi gas with unequal spin populations. *Physical Review Letters*, 97:190407, 2006.

[86] F. Chevy. Universal phase diagram of a strongly interacting Fermi gas with unbalanced spin populations. *Physical Review A*, 74:063628, 2006.

[87] R. Combescot, A. Recati, C. Lobo, and F. Chevy. Normal state of highly polarized Fermi gases: Simple many-body approaches. *Physical Review Letters*, 98:180402, 2007.

[88] N. Prokof'ev and B. Svistunov. Fermi-polaron problem: Diagrammatic Monte Carlo method for divergent sign-alternating series. *Physical Review B*, 77:020408, 2008.

[89] A. Recati, C. Lobo, and S. Stringari. Preprint, arXiv:0803.4419v1.

[90] T. N. D. Silva and E. J. Mueller. Surface tension in unitary Fermi gases with population imbalance. *Physical Review Letters*, 97:070402, 2006.

[91] M. Haque and H. T. C. Stoof. Trapped fermionic clouds distorted from the trap shape due to many-body effects. *Physical Review Letters*, 98:260406, 2006.

[92] A. Bulgac, J. E. Drut, P. Magierski, and G. Wlazlowski. Preprint, arXiv:0801.1504v1.

[93] Y. Shin, A. Schirotzek, C. H. Schunck, and W. Ketterle. Preprint, arXiv:0805.0623v1.

[94] G. V. Skorniakov and K. A. Ter-Martirosian. Three body problem for short range forces. I. scattering of low energy neutrons by deuterons. *Sov. Phys. JETP*, 4:648–661, 1957.

[95] M. Bartenstein, A. Altmeyer, S. Riedl, S. Jochim, C. Chin, J. Hecker Denschlag, and R. Grimm. Crossover from a molecular Bose-Einstein condensate to a degenerate Fermi gas. *Physical Review Letters*, 92:120401, 2004.

[96] T. Bourdel, J. Cubizolles, L. Khaykovich, K. M. F. Magalhes, S. J. J. M. F. Kokkelmans, G. V. Shlyapnikov, and C. Salomon. Measurement of the interaction energy near a Feshbach resonance in a ^{6}Li Fermi gas. *Physical Review Letters*, 91:020402, 2003.

[97] N. V. Sarma. *Philosophical Magazine*, 17:1233, 1968.

[98] W. V. Liu and F. Wilczek. Interior gap superfluidity. *Physical Review Letters*, 90:047002, 2003.

[99] P. Fulde and R. A. Ferrell. Superconductivity in a strong spin-exchange field. *Physical Review*, 135:A550, 1964.

[100] A. I. Larkin and Y. N. Ovchinnikov. *Soviet Physics JETP*, 20:762, 1965.

[101] R. Combescot and C. Mora. The low-temperature Fulde-Ferrell-Larkin-Ovchinnikov phases in 3 dimensions. *Europhysics Letters*, 68:79–85, 2004.

[102] T. Mizushima, K. Machida, and M. Ichioka. Direct imaging of spatially modulated superfluid phases in atomic fermion systems. *Physical Review Letters*, 94:060404, 2005.

[103] A. Sedrakian, J. Mur-Petit, A. Polls, and H. Mther. Pairing in a two-component ultracold Fermi gas: Phases with broken-space symmetries. *Physical Review A*, 72:013613, 2005.

[104] T. D. Lee, K. Huang, and C. N. Yang. Eigenvalues and eigenfunctions of a Bose system of hard spheres and its low-temperature properties. *Physical Review*, 106:1135–1145, 1957.

[105] A. Altmeyer, S. Riedl, C. Kohstall, M. J. Wright, R. Geursen, M. Bartenstein, C. Chin, J. H. Denschlag, and R. Grimm. Precision measurements of collective oscillations in the BEC-BCS crossover. *Physical Review Letters*, 98:040401, 2007.

[106] K. Capelle. Exchange-correlation effects in magnetic-field-induced superconductivity. *Physical Review B*, 65:100515, 2002.

[107] M. M. Maka. Reentrant superconductivity in a strong applied field within the tight-binding model. *Physical Review B*, 66:054533, 2002.

[108] K. Kumagai, M. Saitoh, T. Oyaizu, Y. Furukawa, S. Takashima, M. Nohara, H. Takagi, and Y. Matsuda. Fulde-Ferrell-Larkin-Ovchinnikov state in a perpendicular field of quasi-two-dimensional CeCoIn5. *Physical Review Letters*, 97:227002, 2006.

[109] M.-O. Mewes, M. R. Andrews, D. M. Kurn, D. S. Durfee, C. G. Townsend, and W. Ketterle. Output coupler for Bose-Einstein condensed atoms. *Physical Review Letters*, 78:582–585, 1997.

[110] I. Bloch, T. W. Hnsch, and T. Esslinger. An atom laser with a cw output coupler. *Physical Review Letters*, 82:3008, 1999.

[111] C. H. Schunck, Y. Shin, A. Schirotzek, and W. Ketterle. Preprint, arXiv:0802.0341v1.

[112] M. Punk and W. Zwerger. Theory of rf-spectroscopy of strongly interacting fermions. *Physical Review Letters*, 99:170404, 2007.

[113] G. Baym, C. J. Pethick, Z. Yu, and M. W. Zwierlein. Coherence and clock shifts in ultracold Fermi gases with resonant interactions. *Physical Review Letters*, 99:190407, 2007.

[114] A. Perali, P. Pieri, and G. C. Strinati. Competition between final-state and pairing-gap effects in the radio-frequency spectra of ultracold Fermi atoms. *Physical Review Letters*, 100:010402, 2008.

[115] S. Basu and E. J. Mueller. Preprint, arXiv:0712.1007v1.

[116] F. Fumarola, I. L. Aleiner, and B. L. Altshuler. Preprint, arXiv:cond-mat/0703003v2.

[117] F. Fumarola and E. J. Mueller. Preprint, arXiv:0706.1205v1.

[118] Y. He, C.-C. Chien, Q. Chen, and K. Levin. Radio-frequency spectroscopy of trapped Fermi gases with population imbalance. *Physical Review A*, 77:011602, 2008.

[119] P. Massignan, G. M. Bruun, and H. T. C. Stoof. Twin peaks in rf spectra of Fermi gases at unitarity. *Physical Review A*, 77:031601, 2008.

[120] M. Veillette, E. G. Moon, A. Lamacraft, L. Radzihovsky, S. Sachdev, and D. E. Sheehy. Preprint, arXiv:0803.2517v1.

[121] C. Chin and P. S. Julienne. Radio-frequency transitions on weakly bound ultracold molecules. *Physical Review A*, 71:012713, 2005.

[122] F. Pistolesi and G. C. Strinati. Evolution from BCS superconductivity to Bose condensation: Role of the parameter $k_F\xi$. *Physical Review B*, 49:6356–6359, 1994.

[123] J. R. Engelbrecht, M. Randeria, and C. A. R. S. Melo. BCS to Bose crossover: Broken-symmetry state. *Physical Review B*, 55:15153 – 15156, 1997.

[124] R. B. Diener and T.-L. Ho. Preprint, arXiv:cond-mat/0405174v2.

[125] A. Schirotzek. In preparation.

[126] J. V. Steele. Preprint, arXiv:nucl-th/0010066v2.

[127] H. Heiselberg. Fermi systems with long scattering lengths. *Physical Review A*, 63:043606, 2001.

[128] R. Combescot. Feshbach resonance in dense ultracold Fermi gases. *Physical Review Letters*, 91:120401, 2003.

[129] J. Kinnunen, M. Rodrguez, and P. Trm. Pairing gap and in-gap excitations in trapped fermionic superfluids. *Science*, 305:1131–1133, 2004.

[130] Y. Ohashi and A. Griffin. Single-particle excitations in a trapped gas of Fermi atoms in the BCS-BEC crossover region. II. Broad Feshbach resonance. *Physical Review A*, 72:063606, 2005.

[131] Y. He, Q. Chen, and K. Levin. Radio-frequency spectroscopy and the pairing gap in trapped Fermi gases. *Physical Review A*, 72:011602, 2005.